Technische Universität München
Institut für Energietechnik MW7

Lehrstuhl für Fluidmechanik

Numerical simulation of pressure oscillations in large Francis turbines at partial and full load operating conditions and their effects on the runner structural behaviour and fatigue life

Marcelo Vinicius Magnoli

Vollständiger Abdruck der von der Fakultät für Maschinenwesen der Technischen Universität München zur Erlangung des akademischen Grades eines

Doktor-Ingenieurs

genehmigten Dissertation.

Vorsitzender: Univ.-Prof. Dr.-Ing. M. Hajek
Prüfer der Dissertation:
1. Univ.-Prof. Dr.-Ing. Dr.-Ing. habil. Dr. h.c. R. Schilling (i.R.)
2. Univ.-Prof. Dr.-Ing. Th. Sattelmayer

Die Dissertation wurde am 06.02.2014 bei der Technischen Universität München eingereicht und durch die Fakultät für Maschinenwesen am 01.07.2014 angenommen.

Preface

This text is the result of my research work, during four years, at the Institute for Fluid Mechanics (FLM) of the Technische Universität München (TUM), under the supervision of Prof. Schilling. The first two research years were supported by the Deutscher Akademischer Austausch Dienst (DAAD) and the last two years were spent as research assistant at the Institute, financed by the Land Bayern and Voith. During the elaboration of this text, I could also count with the previous work experience of five years at the hydraulic turbines manufacturer Voith, at which I am currently employed again since three years.

The numerical simulation methods for hydraulic turbines have experienced great and fast advances in the recent years, so that simulation procedures and numerical methods can easily become part of the past. This research work has mainly concentrated on numerical simulation methods for Francis turbines. Still it also brings new knowledge about the dynamic behaviour of hydraulic machines and, from this point of view, it should still remain relevant during the next years.

For the elaboration of this work, I want to sincerely thank Prof. Schilling. With his technical competence and experience in the field of hydraulic turbines, he has brought valuable ideas and knowledge to this research work through our technical discussions. His attitude to let his assistants assume important responsibilities towards the projects and his thrust on our work have been very motivating to me. His engagement, after so many years as head of the Institute, serves as an inspiring example. From the personal point of view, my contact and relationship with him have been very pleasant.

Thanks to Prof. Hajek, who conducted the examination, as well as to Prof. Sattelmayer, who also took part in the evaluation. The relation with the other assistants at our Institute has always been extremely enjoyable. Besides the valuable technical exchange, we developed great friendship. This surely contributed for the nice years spent in München. Among all the great colleagues, I want to thank Hr. Thalhamer and Hr. Rosenberger, who contributed with discussions, suggestions and proof reading.

To my parents my many thanks for all the support that they gave me along the many years.

Contents

Symbols and Abbreviations

Abbreviations

BCGSTAB	Bi-conjugate gradient stabilised method
BD	Band
BEP	Best efficiency point
BSL	Baseline
CAD	Computer aided design
CDS	Central difference scheme
CFD	Computational fluid dynamics
CR	Crown
CSA	Computational structural analysis
CSD	Computational structure dynamics
DES	Detached eddy simulation
DNS	Direct numerical simulation
DOF	Degree of freedom
DT	Draft tube
DTI	Draft tube instabilities
EASM	Explicit algebraic stress model
FE	Finite element
FEA	Finite element analysis
FEM	Finite element method
FLI	Full load instability
FLM	Lehrstuhl für Fluidmechanik (Institute of Fluid Mechanics)
FSI	Fluid-structure interaction
FVM	Finite volume method
GV	Guide vane
HCF	High cycle fatigue
HOS	Higher order scheme
HOT	Higher order terms
HPL	Higher part load
HW	Head water
HWL	Head water level
IEC	International Electrotechnical Commission
LCF	Low cycle fatigue
LCL	Turbulence model according to Lien, Chen and Leschziner [84]

LE	Leading edge
LEC	Leading edge separation
LES	Large eddy simulation
MINMOD	Interpolation scheme according to HARTEN [62]
NS3D	Three-dimensional Navier-Stokes flow computation
OPPT	Operating point
PCG	Preconditioned conjugate gradient
PS	Pressure side
QUICK	Quadratic upwind interpolation
RANS	Reynolds-averaged Navier-Stokes equations
RCV	Runner channel vortex
RSI	Rotor-stator interaction
RSM	Reynolds stress model
RU	Runner
SAS	Scale adaptive simulation
SC	Spiral case
SGS	Sub-grid scale
SIMPLE	Semi-implicit method for pressure linked equations
SIP	Strongly implicit procedure
SMART	Sharp and monotonic algorithm for realistic transport, GASKELL AND LAU [50]
SNL	Speed-no-load
SRT	Stress relief triangle
SS	Suction side
SST	Shear stress transport
STD	Standard k-ϵ model
SV	Stay vane
TE	Trailing edge
TUM	Technische Universität München (Munich University of Technology)
TW	Tail water
TWL	Tail water level
UDS	Upwind difference scheme
URANS	Unsteady Reynolds-averaged Navier-Stokes equations
VSE	Vortex shedding effects
WF	Wall function

Software

ANSYS	Ansys Inc., ANSYS-Structural Release 11.0
CATIA	Dassault Systèmes, CATIA V5
CFX	Ansys Inc., ANSYS-CFX Release 11.0
ICEM	Ansys Inc., ICEM-CFD Release 11.0
NS3D	TUM FLM, Three-dimensional Navier-Stokes flow computation

Dimensionless Numbers

CFL	Courant number
Fr	Froude number
Pe	Peclet number
Pr	Prandtl number
Re	Reynolds number
σ	Thoma number

Latin Letters

A	Area; Turbulence model constant; Coefficient matrix
B	Fluid bulk modulus
BF	Blend function multiplier
C	Wall law constant; Turbulence model constant; Constraint; Palmgren-Miner constant
C_{ij}	Cross-term stress
C_{ijk}	Turbulent transport tensor
C_{ijkl}	Material law tensor
C_p	Pressure coefficient
C_S	Smagorinsky coefficient
D	Diameter; Fatigue damage
D_{1_a}	Blade inlet diameter at the band
D_{1_i}	Blade inlet diameter at the crown
D_{2_a}	Blade outlet diameter at the band
D_{2_i}	Blade outlet diameter at the crown
D_3	Runner outlet diameter
D_4	Inlet diameter of the draft tube cone
$D_{k\omega}$	Turbulence model constant
D_{T_i}	Inner diameter of stay vanes
D_{T_a}	Outer diameter of stay vanes
D_z	Guide vanes pitch circle diameter
E	Elasticity (Young) modulus
$E(\kappa)$	Turbulent energy spectral density
F	Flux; Blend function; Limiter; Force
F_1	SST first blend function
F_2	SST second blend function
F^c	Convective flux
F^d	Diffusive flux; DES limiter
F_{DES}	DES limiter
F_{ext}	External loads
F_{SAS}	SAS limiter
F_{SST}	Chosen SST blend function
G	LES filter function
H	Net head

H_E	Euler head
H_{E_1}	Euler head at the runner inlet
H_{E_2}	Euler head at the runner outlet
H_s	Suction head
K	Specific load; Constant
L_{char}	Characteristic length
L_{ij}	Leonard stress
L_T	Turbulence length scale
L_{vK}	Von Kármán length scale
M	Moment
N	Number of steps; Shape function; Fatigue life
N_f	Fatigue life under low cycle fatigue (LCF)
P	Power
P_1'	Dimensionless power
P_m	Mechanical power at the turbine shaft
P_k	Specific turbulent kinetic energy production term
Q	Volume flow; Source flux; Source vector
Q_1'	Dimensionless volume flow
Q_z	Transformation matrix
R	Radius; Reference Radius; Gas law constant
R_{inner}	Inner iterations residuum
R_{ij}	SGS Reynolds stress
R_{outer}	Outer iterations residuum
Re	Reynolds number
Re_T	Turbulence Reynolds number
Re_y	Near-wall turbulence Reynolds number
S	Fluid strain rate; Sutherland constant; Source term
S_y	Yield stress
S_u	Ultimate stress
S_{ij}	Fluid strain tensor
T	Torque; Period; Temperature
T_{ij}	Transformation matrix
T_T	Turbulence time scale
T_1'	Dimensionless runner torque
Tu	Turbulence intensity
U	Peripheral velocity; Potential energy
V	Volume
W	Work; Gauß integration weighting factor
W_{ex}	External loads work
W_{in}	Internal loads work

a	Absolute acceleration; Sound velocity
arg	Turbulence model constant
b	Material specific damping factor; Fatigue strength exponent; Nodes
b_0	Height of the distributor
b_2	Height of the runner inlet

b_{ij}	Anisotropy tensor
b_T	Height of the stay vanes
c	Absolute velocity; Turbulence model constant; Fatigue ductility exponent
c_m	Absolute velocity meridional component
c_u	Absolute velocity tangential component
e	Specific internal energy
e_t	Specific total internal energy
f	Frequency; Turbulence model constant; Distributed body force
f_e	Excitation frequency
f_n	Rotation frequency
g	Gravity acceleration; DES parameter
h	Specific enthalpy; Local head; Harmonic
h_t	Specific total enthalpy
h_{amb}	Ambient pressure
h_{va}	Vapour pressure
i	First index direction; Mode number
j	Second index direction
k	Specific turbulent kinetic energy; Third index direction; Nodal diameters
k_t	Thermal conductivity
ℓ	Conformal length coordinate
ℓ_{mix}	Mixing-length
m	Mass; Meridional coordinate; Outer iteration counter
$\dot{m}$	Mass flow
n	Normal direction; Rotation speed; Inner iteration counter; Number of stress cycles reversal
n'_1	Dimensionless rotation speed
n'_{1_D}	Dimensionless runaway speed
n_D	Runaway speed
n_q	Turbine specific speed
p	Pressure; Surface load
p_E	Piezometric pressure
p_t	Total pressure
q	Heat transfer rate; General coordinate
r	Radial coordinate; Local cell coordinate
r_1	Radius at blade inlet
r_2	Radius at blade outlet
r_d	DES parameter
s	Arc-length; Local cell coordinate; Dimensionless coordinate running along the blade from the leading edge to the trailing edge
t	Time; Tangential direction; Local cell coordinate
t_{ij}	Viscous stress
u	Velocity component; Dimensionless coordinate running along the blade from the pressure side trailing edge to the suction side trailing edge

u^+	Dimensionless sublayer-scaled velocity
u_r	Radial displacement
u_t	Velocity component tangent to the wall
u_τ	Friction velocity
v	Velocity component; Dimensionless coordinate running along the blade from crown to band
w	Velocity component; Relative velocity
x	x coordinate
y	y coordinate; Wall distance
y_2	Distance from the first cell centre to the wall boundary
y^+	Dimensionless sublayer-scaled distance
z	z coordinate; Axial coordinate
z_0	Number of guide vanes
z_2	Number of blades or buckets
z_T	Number of stay vanes
$\mathscr{F}$	Rayleigh dissipation functional; Fourier transform
$\mathbf{B}$	Strain-displacement matrix
$\mathbf{C}$	Damping matrix
$\mathbf{D}$	Stress-strain matrix
$\mathbf{I}$	Identity matrix
$\mathbf{J}$	Jacobian matrix
$\mathbf{F}$	Load vector
$\mathbf{K}$	Stiffness matrix
$\mathbf{M}$	Mass matrix
$\mathbf{N}$	Shape function matrix
$\mathbf{P}$	Punctual load vector; Discrete pressure vector
$\mathbf{R}$	Load vector
$\mathbf{S}$	Source term vector
$\mathbf{T}$	Transformation matrix
$\mathbf{U}$	Discrete displacement vector
$\mathbf{a}$	Absolute acceleration vector
$\mathbf{c}$	Absolute velocity vector
$\mathbf{f}$	Body load vector
$\mathbf{n}$	Unitary normal vector
$\mathbf{p}$	Surface load vector
$\mathbf{r}$	Position vector
$\mathbf{t}$	Unitary tangential vector
$\mathbf{u}$	Absolute velocity vector; Tangential velocity vector; Displacement vector
$\mathbf{w}$	Relative velocity vector
$\mathbf{x}$	Solution vector; Position vector

Greek Letters

Γ	Diffusive coefficient
Δ	Difference; Length; Filter width; Oscillation amplitude, i.e. half peak-to-peak value
ΔH	Head losses; Head oscillation amplitude
ΔP	Pressure oscillation amplitude
ΔV	Cell volume
Δh	Head oscillation
Δp	Pressure oscillation
Δt	Time step size
$\Delta\gamma$	Distributor opening
$\Delta\eta$	Efficiency losses
Φ	General variable in Reynolds and Favré decompositions; Length scale
Π	Total energy potential
Π_{ij}	Pressure-strain correlation tensor
Ω	Vorticity; Rotation frequency; Angular velocity
Ω_{ij}	Rotation tensor
α	Turbulence model constant; Under-relaxation parameter; Rayleigh damping mass coefficient; Newmark coefficient; Angle
β	Turbulence model constant; Rayleigh damping stiffness coefficient
β_1	Flow inlet angle at the runner
β_{1_S}	Blade inlet angle
β_2	Flow outlet angle at the runner
β_{2_S}	Blade outlet angle
γ	Turbulence model constant; Interpolation scheme blending factor; Structural damping factor
δ	Kronecker delta; Newmark coefficient; Deviation; Displacement
δ_i	Flow incidence angle
δ_d	Flow deviation angle
ϵ	Dissipation rate; Mechanical strain
ϵ_a	Alternating strain amplitude
ϵ'_f	Fatigue ductility coefficient
ϵ_{ij}	Dissipation tensor; Mechanical strain tensor
ζ	Body oriented coordinate; Turbulence model constant; Damping factor
η	Efficiency; Body oriented coordinate; Turbulence model constant
θ	Angle; Angle coordinate
κ	Von Kármán constant
λ	Turbulent wave length; Interpolation factor; Lamé constant; Laplace multiplier
μ	Dynamic viscosity; Lamé constant
ν	Kinematic viscosity; Poisson coefficient
ξ	Body oriented coordinate; Meridional orthogonal coordinate

ρ	Density
σ	Thoma number; Mechanical stress; Turbulence model constant; Interpolation blend factor
σ_0	Residual mechanical stress
σ_a	Alternate mechanical stress
σ_e	Equivalent or von Mises stress
σ'_f	Fatigue strength coefficient
σ_I	Mechanical stress intensity
σ_{ij}	Mechanical stress tensor
σ_L	Fatigue limit
σ_m	Time-average mechanical stress
σ_s	Static mechanical stress
τ	Viscous normal stress; Shear stress
τ_{ij}	Specific Reynolds stress tensor; SGS stress
ϕ	General variable
φ	Tangential coordinate
χ	Conformal tangential coordinate
ω	Turbulence dissipation frequency; Circular frequency; Angular velocity
ω_d	Damped natural frequency
ω_n	Natural frequency
$\mathbf{\Phi}$	Mode shape matrix
$\mathbf{\Phi}_i$	Mode shape
$\mathbf{\Omega}$	Angular velocity vector
$\boldsymbol{\epsilon}$	Mechanical strain vector
$\boldsymbol{\sigma}$	Mechanical stress vector

Subscripts

$_0$	Distributor; Reference value; Initial condition
$_1$	Runner blade inlet; Unitary value; Principal
$_2$	Runner blade outlet; Principal
$_3$	Runner outlet; Principal
$_4$	Draft tube inlet
$_{Cor}$	Coriolis
$_{DES}$	Detached eddy simulation
$_D$	Runaway
$_E$	Euler head
$_{HW}$	Head water
$_M$	Model
$_P$	Prototype; Cell centre
$_{Rh}$	Rheingans
$_S$	Blade

SAS	Scale adaptive simulation
SGS	Sub-grid scale
SST	Shear stress transport
T	Turbulence; Stay vane
TW	Tail water
w	Wall
a	Outer; Band; Alternate; Air
amb	Ambient
b	Bottom face
c	Coriolis
$char$	Characteristic
e	Element; East face; Equivalent or von Mises
eff	Effective
ext	External
i	Index; Inner; Crown; Incipient
in	Inlet boundary condition; Internal
$inner$	Inner iterations
j	Index
k	Index; Specific turbulent kinetic energy
m	Meridional plane; Meridional component; Average; Index
max	Maximum
min	Minimum
mix	Mixture
n	Normal component; Rotation speed; North face; Node index; Iteration; Natural
opt	Optimum operation point
out	Outlet boundary condition
$inner$	Outer iterations
p	Pressure
pl	Plant
q	Flow
r	Radial component
ref	Reference
s	Vector component normal to the normal and tangential directions; South face; Suction
t	Tangential; Total; Top face; Thermal
$turb$	Turbulent
u	Tangential component
v	Volume
va	Vapour
vK	Von Kármán
w	Relative velocity; West face; Water
x	x component
y	y component; Wall distance; Near-wall
z	z component; Axial direction; Centrifugal

ϵ	Dissipation rate
μ	Viscous
ρ	Density
τ	Shear stress
ϕ	General variable
ω	Turbulence dissipation frequency

Superscripts

$+$	Dimensionless sublayer-scaled
$*$	Alternative variable; Dimensionless value
$\prime$	Oscillatory value in Reynolds decomposition; Dimensionless
$\prime\prime$	Oscillatory value in Favré decomposition
CDS	Central difference scheme
HOS	Higher order scheme
HOT	Higher order terms
P	Pressure
UDS	Upwind difference scheme
mod	Modified
n	Iteration
new	New value
rel	Relative
rot	Rotational

Overhead Symbols

$\bar{}$	Reynolds-average, i.e. time-average; Area-average
$\tilde{}$	Favré-average, i.e. mass-average

Abstract

With the increase of the power density of hydraulic turbines and the extension of their operating range over the last decades, the fluid and mechanical dynamic effects in the machine became significantly more pronounced. Under severe operating conditions, the fluid flow pressure oscillations and the consequent dynamic mechanical stresses may lead to the fatigue failure of the turbine runner, with the occurrence of cracks. This has to be avoided in the early design phases, through the correct and accurate prediction of the transient fluid flow, dynamic structural motion, mechanical stresses and fatigue assessment.

The current dynamic simulation methods, for the Francis runners structure, are very limited and do not offer the required accuracy for safe and competitive design. They rely basically on extrapolated test data, numerous theoretical assumptions, simplifications and experience. The numerical simulation method proposed here intends to supply an accurate tool to predict the transient flow phenomena and the dynamic mechanical stresses for the fatigue analysis.

The main part of the process concentrates on the computational fluid dynamics (CFD) simulation of the transient fluid flow through the entire turbine. The numerical model reproduces the complete turbine geometry and counts with sophisticated hybrid turbulence models, as detached eddy simulation (DES) and scale adaptive simulation (SAS). The turbulence modelling showed up to be decisive for the proper turbine flow simulation. The transient pressure field history, provided by the CFD analysis, constitutes the input for the runner mechanical stress calculation. The structural simulation is carried out with the finite element method (FEM), making use of the direct time integration method for the transient solution of the runner structural motion for all time steps. The calculated dynamic mechanical stresses in the runner are used for the subsequent fatigue life prediction.

As an example of application of the method, a Francis turbine, with high specific speed and whose prototype is currently in operation, was simulated. Several operating points were chosen for the calculations, including full load, higher part load (HPL), part load and deep part load. These points were representative for different types of dynamic phenomena taking place during the machine operation, as rotor-stator interaction (RSI), draft tube instabilities (DTI), with the presence of rotating vortex rope, and runner channel vortices (RCV).

The numerical results of the transient fluid flow simulation were compared to experimental results from model tests and achieved very tight agreement, showing the high accuracy and advantages of the proposed method. The accurate numerical simulation of the transient fluid flow through the hydraulic machine and the computational calculation of the runner structural response, as well as the fatigue assessment, offered the possibility to gain new knowledge about the dynamic behaviour of Francis turbines.

Chapter 1

Introduction

For more than 150 years, waterpower has been significantly contributing to energy generation. In the last decades, thanks to advanced engineering development and due to the pressure for cost reduction, brought by the strong market competition, the hydraulic turbines have experienced the astonishing increase of their power density. The maximum power of individual generating units has increased and their rotational speed has become faster, while their structure has got more slender and lighter in comparison with the past. Table 1.1 illustrates this evolution. The current demand for energy and grid regulation services also take the energy producers to enlarge the machine operating range, pushing the turbine into operating conditions, which were not experienced in past years.

With the extended operating range and with the increasing power density, several dynamic phenomena, which were not clearly noticeable in the past, because of the robust structure construction, became decisive for the smooth and safe operation of modern hydraulic power plants. Among the many transient phenomena, which take place in the generating unit, the pressure oscillations in the fluid flow through the turbine and its impact on the mechanical structure are of main importance, for assuring the machine reliable operation.

In normal operation, the pressure pulsations in Francis turbines arise typically from the rotor-stator interaction (RSI) and from the draft tube instabilities (DTI). The vortex shedding effect (VSE) at the trailing edge of the runner blades can, in some cases, cause local pressure fluctuations. At extreme operating conditions, which are though typically avoided, vortices in the runner channels (RCV) and leading edge separation (LEC) can take place as well.

The oscillating pressure field over the runner blades leads to dynamic loads on the runner structure, which produce dynamic mechanical stresses. The dynamic structural stresses add up to the static stresses, caused by the mean pressure field, and, in severe cases, material fatigue can initiate and propagate structural cracks, damaging the runner seriously. Such cases have been extensively reported, as for example by Fisher et al. [44], Coutu et al. [28], Brekke [21] and Bhave,

Table 1.1: Power evolution of hydraulic generating units, adapted from Ulith [157] and Henry [64].

Power Plant	Country	Year	Units	Rated Power (MW / Unit)	Maximum Power (MW / Unit)
Bai He Tan	China	2020	16	1 015	1 015
Wu Dong De	China	2019	12	862	1 015
Xi Luo Du	China	2012	18	784	784
Long Tan	China	2007	9	714	790
Three Gorges	China	2003	26	710	852
Xingó	Brazil	1994	6	527	535
Guri II	Venezuela	1986	10	610	767
Itaipu	Brazil	1984	20	740	740
Sayano-Shushenskaya	Russia	1978	10	650	735
Grand Coulee III	USA	1975	3	716	827
Cabora Bassa	Mozambique	1975	5	415	432
Mica	Canada	1973	4	435	443
Dworshak	USA	1973	3	294	294
Krasnoyarsk	Russia	1972	5	508	508
Gokcekaya	Turkey	1972	3	103	103
Churchill Falls	Canada	1971	11	480	494
Estreito	Brazil	1969	6	175	184
Paulo Afonso II	Brazil	1961	3	93	93
Noxon Rapids	USA	1960	4	108	108
Niagara Falls II	Canada	1954	16	76	76

Murthy and Goyal [15]. Figure 1.1 shows examples of cracks at the runner blade trailing edge, near to the crown and band.

Even minor damages to the runner structure need to be immediately repaired, implying in unexpected outage periods of the machine. For the turbine owner, it means energy generation reduction and financial losses, while the turbine manufacturer can be charged with contractual penalties and must assume the repair costs, besides the consequent weakened market position. Also from the engineering point of view and with view to the turbine development improvement, fatigue failures in Francis runners shall be completely eliminated. Safe design shall also offer the possibility to operate the machine in diverse operating conditions, eventually extending the turbine operating range.

The objective of this study is to provide the understanding and the method to numerically predict the pressure oscillations, in the early stages of the turbine design, with computational fluid dynamics (CFD), to calculate the stresses with the finite element method (FEM) and to estimate the runner fatigue life, in order to prevent mechanical failures.

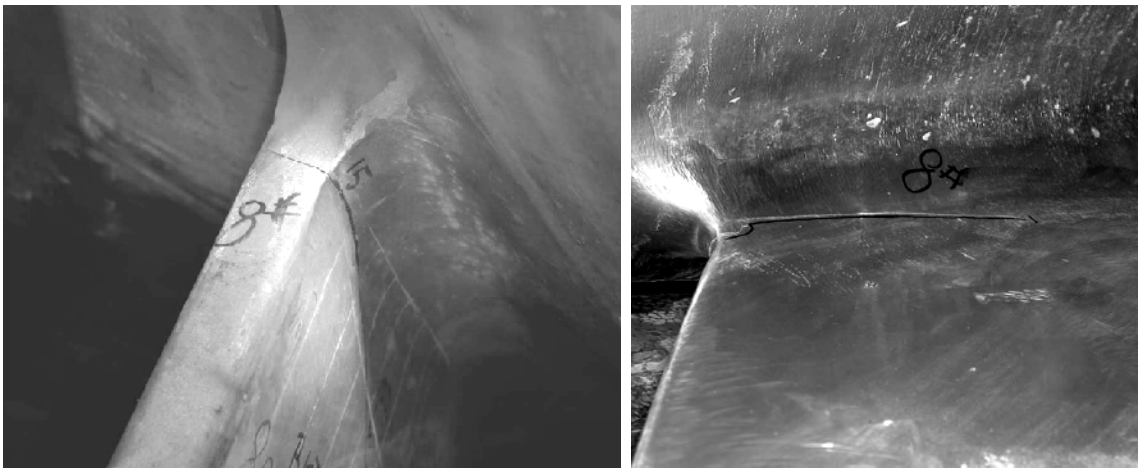

Figure 1.1: Typical fatigue cracks at the runner blade trailing edge, near to the crown (left) and near to the band (right).

The numerical simulation of the dynamic fluid flow through the hydraulic turbine involves sophisticated transient calculations and requires refined turbulence models. It constitutes an important part of this study. The application of the transient fluid simulation results as input for the structural calculation receives great attention as well.

Design Process

The fatigue calculation, for the estimation of the runner life before the initiation of cracks, requires as input the static and dynamic mechanical stresses actuating on it. The procedure for obtaining the mean stresses is well established and they can be numerically derived, as shown by numerous references, as done by Wicksström [165]. The mean pressure field on the turbine runner can be accurately evaluated, with respect to the subsequent structural analysis, by means of stationary CFD simulations, as done since years as by e.g. Keck, Drtina and Sick [71] and Ruprecht and Maihöfer [132]. The static finite element analysis (FEA) also relies on precise numerical models and delivers accurate results for the static mechanical stresses, as seen in Magnoli, Galvani and Poll [89].

On the other hand, still today, for the determination of the dynamic stresses on Francis runners, no method has made its way to standard, accurate and reliable procedure. The dynamic phenomena in the fluid flow through the complete machine, e.g. DTI, are highly instationary and their accurate numerical simulation with CFD poses several difficulties, which will be discussed in detail further on. The numerical prediction of the dynamic pressure is beyond the current standard procedures. The solution of this problem makes part of this study.

With no numerical data available for the pressure fluctuations on the runner, experiments could, in theory, offer the solution to the problem. However, dynamic

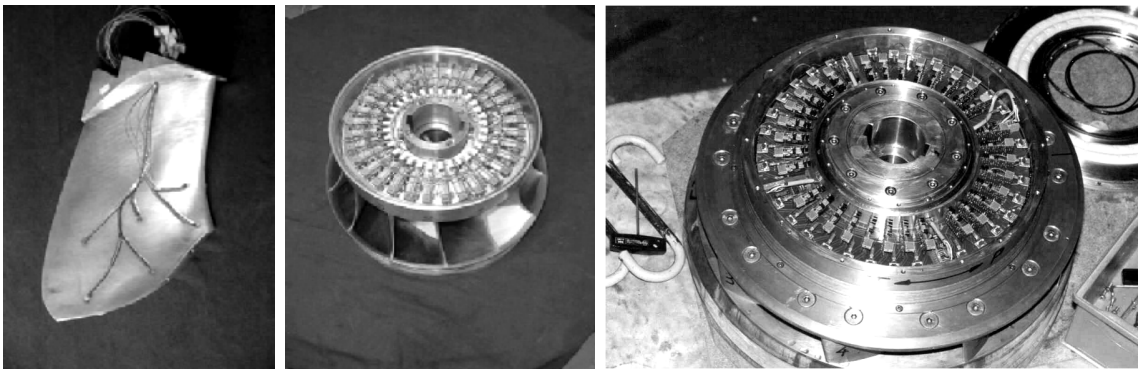

Figure 1.2: Typical experimental arrangement for measuring the pressure oscillations in Francis model runners. Pressure transducers at the blade (left) and acquisition equipment on the crown (centre, right). Reproduced from Avellan et al. [12].

pressure measurements in Francis model runners are seldom conducted. At present, it constitutes no regular practice for ordinary model tests and it has mainly been performed, e.g. by Kuntz et al. [77] and Nennemann, Vu and Farhat [109] in specific research projects. The complicated experimental arrangement, as exemplified by Avellan et al. [12] and reproduced in Figure 1.2, with pressure transducers at the blades and the data acquisition unit mounted on the crown, makes such tests extremely expensive and long. In addition, in this kind of test, the number of pressure probes at the blades is also considerably limited. Attempts to directly measure the stresses on the model machine are very disputable, since the mechanical construction of the model and prototype runners are very different and, therefore, also their dynamic mechanical properties.

Another experimental possibility would be to use strain-gauges to directly measure the mechanical stresses on the prototype runner, as done by Fischer et al. [44], Bjørndal, Moltubakk and Aunemo [16] and Gagné and Coulson [48]. Figure 1.3 shows the strain-gauges at the runner trailing edge near to crown and the acquisition system mounted under the runner cone. The complexity level of this procedure is even greater than to measure the model runner. It involves the unavailability of tested generating unit, during the measurements, for energy production and incurs in significant costs. In addition, for the prototype being tested, the objective to predict the fatigue life in the design stage cannot be achieved any more. The extrapolation of the measured data for other similar machines can be interpreted as coarse approximation, since the operating points are seldom the same and the hydraulic and mechanical designs could be eventually different.

Being aware of the difficulties for determining the instationary mechanical stresses, for the fatigue calculation, they are, in practice, estimated from the data from the scarce experiments, from empirical factors and from the turbine manufacturers experience. The estimation of the fatigue life, based on this current process, is schematically depicted in Figure 1.4. The accuracy and scientific validity of this method is disputable and the need for improvement is present. In the eventuality of mechanical failures in the prototype runner, the mitigation solutions also rely on

Figure 1.3: Typical experimental arrangement for measuring the pressure oscillations in Francis prototype runners. Strain-gauges at the blade trailing edge near to crown (left). Acquisition system mounted under the runner cone (right). Reproduced from Fischer et al. [44].

weak theoretical background, as the installation of fins at the walls of the draft tube cone, or on palliative solutions, as the welding of stress relief triangles (SRT) at the blade trailing edges, near to the crown and band. Even if such solutions work, they come anyway much too late, after the failure has already occurred in the prototype.

In order to improve the design process, it is proposed here to develop the guide lines to numerically predict the fatigue life of Francis runners. The first step consists on the accurate simulation of the dynamic flow phenomena in the complete turbine with CFD and adequate turbulence models. With the time history from the numerically calculated pressure field on the runner, the full transient FE simulations can yield the dynamic mechanical stresses. These are used, in combination with the static stresses, for the evaluation of the runner fatigue life. The scheme of the proposed procedure is represented in Figure 1.5.

To systematically simulate the dynamic pressure field and to use it as input for the structural analysis offers the advantage to predict the runner fatigue life at early stages of the machine design, allowing avoiding fatigue cracks in the prototype. Besides, with the appropriate numerical tools, it can provide accurate solutions for the instationary pressure field and dynamic mechanical stresses, with low costs in comparison to experiments.

At present, the instationary CFD and FE simulations, as proposed here, are considerably time consuming and their integration in the development of the hydraulic design, when numerous profile alternatives are compared, is still difficult. However, such simulations can be carried out for the final hydraulic design, before the prototype goes into manufacturing. In this way, fatigue failures in the prototype should be avoided. With increasing computational capacity and eventually moderated size of numerical models, the numerical prediction of the

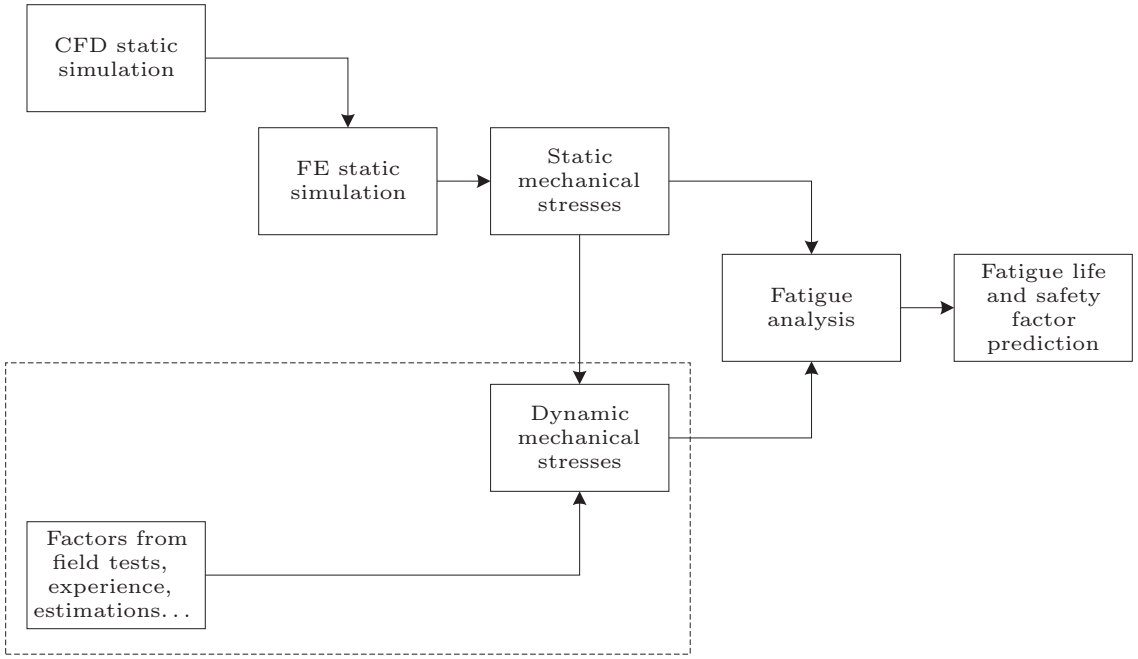

Figure 1.4: Current procedure in the turbine runner analysis.

fatigue life can possibly be performed, in the future, for the hydraulic design alternatives.

Numerical Approach

The dynamic fluid flow through the hydraulic turbine is highly instationary in many operating conditions and it can develop complex flow patterns and topology, regarding the transient pressure field, velocity distribution and streamlines.

For the accurate CFD simulation of the transient flow, the numerical model has to be able to capture the dynamic details of the fluid flow and to precisely approximate the reality, not only qualitatively but also quantitatively, as long as the reliability of the fatigue life prediction depends on all calculation steps, starting with the instationary flow simulation. In the specific case of hydraulic machines, deciding factors for the success of the dynamic fluid simulation are the reproduction of the actual physical configuration of the turbine, with all its components, and to employ proper turbulence models.

In the specific case of hydraulic turbines, the most important transient phenomena, i.e. RSI, DTI and, to some extent, LEC, come from the interaction between the different machine components. This interaction is mainly caused by the relative motion between the rotating and stationary parts, i.e. between the runner and the spiral case, stay vanes, guide vanes and draft tube. So the first difficulty in the turbine CFD simulation is to properly reproduce the flow domain, including the relative motion of the parts. For example, Wunderer [170] adopted sophisticated

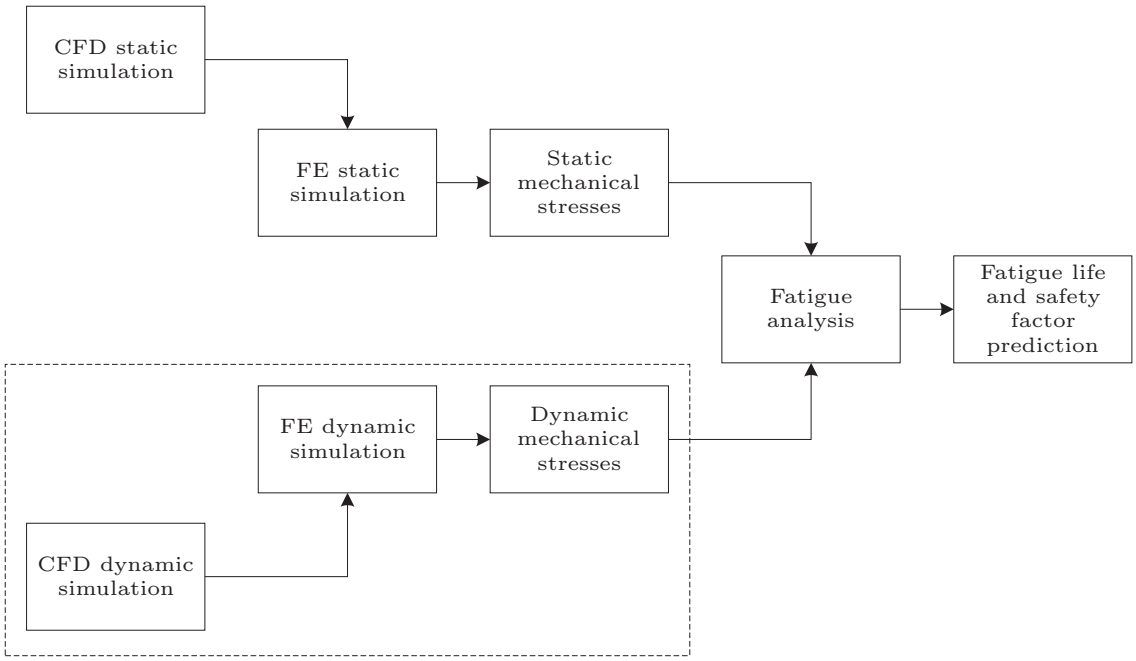

Figure 1.5: Proposed procedure for the turbine runner analysis.

turbulence models for the flow calculation. However, his numerical simulation counted only with the turbine runner, without, other components, thus limiting the extensibility of his results for real machines.

The second important aspect is the utilisation of adequate turbulence models. The current industrial standard for CFD simulations, as pointed out by Spalart [145], is to employ the unsteady Reynolds averaged Navier-Stokes (URANS) equations, based on k-ϵ or k-ω turbulence models. Through the averaging process of the fluid motion equations, URANS presents the tendency to deliver values for the turbulent viscosity, which are considerably large. It leads to the undesirable effect, in the numerical simulation, of excessively damping the dynamic flow phenomena, which develop in the reality.

One alternative to solve this limitation of URANS, with moderate computational resources, is the utilisation of hybrid turbulence models, which are the combination of URANS and large eddy simulation (LES), like the detached eddy simulation (DES) and scale adaptive simulation (SAS), see respectively Strelets [149] and Menter and Egorov [100]. These hybrid methods are capable to identify regions of the computational fluid domain, where the grid accuracy is enough to directly simulate the eddies motion, without the introduction of additional artificial damping through the turbulent viscosity, similar to LES. In other regions, where the grid is not so fine, it assumes the URANS behaviour. This approach avoids the excessive numerical damping of the transient fluid phenomena, delivering more accurate results.

Ruprecht et al. [130] were some of the first to identify this problem with the turbulence modelling in the transient simulation of hydraulic turbines and to try

to solve it. They realised the influence of the excessive numerical damping on the simulation of DTI effects in Francis turbines and proposed the very large eddy simulation (VLES). It also consisted in trying to preserve the dynamic characteristics of the flow through the reduction of the turbulent viscosity. They achieved acceptable results in the simulation of DTI. More recently, Benigni [14] employed the SAS to calculate the DTI effects in bulb turbines.

The RSI effects have been simulated more often than DTI, as shown by Keck et al. [72] for example. Since the RSI is mainly induced by the kinematic interaction between runner and spiral case, stay vanes and guide vanes, the influence of the turbulence modelling is moderate, but still present. Numerical research on the VSE in Francis runners is still very limited, being restricted to extrapolations of very simplified geometry simulations, as done by Antonsen [7], Ausoni [10] and Ruprecht et al. [131]. RCV and LEC have seldom been investigated with transient calculations.

The fluid simulations conducted here concentrate on the utilisation of DES and SAS for the numerical evaluation of the different transient effects in the Francis turbine. As reference for the numerical results accuracy, experimental results are used. The simulated transient results obtained for selected operating points are presented and discussed. They are also used as input for the transient structural simulation, needed for the fatigue assessment.

Text Organisation

The text is divided into the fluid and turbulence theory, the finite volume method (FVM) for CFD, structure and fatigue theory, the finite element method (FEM) for structural analysis and, finally, the principal part of it is dedicated to the application of these theories and methods for the flow and structural simulation and fatigue life prediction of real Francis turbines.

Chapter 2 presents the fundamentals of fluid mechanics, needed for understanding the flow through the turbine and the numerical simulation method. It also describes the turbulence modelling for CFD in detail, as long as the turbulence models are of great importance for the accurate simulation of the transient flow phenomena in the turbine. The traditional methods for instationary calculating the turbulence effect, i.e. URANS and LES, as well as hybrid turbulence models, DES and SAS, receive great attention.

Chapter 3 describes the FVM. This method constitutes the current industry standard for numerical fluid simulations. Its theory fundamentals, as well as the mathematical development, are explained. The discretisation techniques for the physical domain, for the fluid motion equation, application of boundary conditions and their numerical implementation are covered in the chapter.

In Chapter 4 the basics of structure theory are addressed. It concentrates on dynamic motion and on the aspects needed for the development of the FEM. Concepts of elasticity are also discussed, in view to the mechanical stresses. The chapter ends up by presenting the fatigue calculation method employed in the study. The aspects of the FEM, with the discretisation process of the physical space and of the motion equations and with the formulation of finite elements and boundary conditions, are described in Chapter 5.

Fundamentals of hydraulic turbines, concerning definitions, conventions, geometric characteristics and energy conversion mechanism can be found in the first part of Chapter 6. The second part of this chapter explains concepts of hydraulic turbines dynamics and contains an overview of the transient effects.

Chapter 7 brings the instationary flow simulation and its results for real Francis turbines. The model machine taken as example for the application of the proposed calculation method is presented, together with its main technical data and the chosen operating conditions for the simulation. The numerical model and calculation steps are described in detail. Numerical results, for which measuring data is available, are compared with the experimental results, for validating and checking the accuracy of the proposed procedure. In the second part of the chapter, the results for operating conditions with RSI and for the ones with DTI are presented and discussed.

In Chapter 8 the dynamic pressure field in the turbine, obtained from the instationary flow simulation, is applied to the runner structure for the FE simulation. The dynamic mechanical stresses are evaluated for the different operating conditions and employed for the fatigue life prediction of the turbine runner.

Those interested only in the turbine calculation results can proceed directly to Chapters 7 and 8, where the turbine simulation can be found. If the fluid and turbulence modelling theory and CFD techniques are the main point, Chapters 2 and 3 should be read. On the other hand, if the structure and fatigue theory and the FEM are of interest, Chapters 4 and 5 should be considered. If the reader is familiar with the theory, Chapters 2 and 4 can be left aside. Though, the theory behind the hybrid turbulence models, at the end of Chapter 2 could be worth reading. If the numerical calculation techniques are already well dominated, Chapters 3 and 5 are not imperative.

Chapter 2

Fluid Dynamics Theory

2.1 Basic Equations

The analysis of fluid flow problems, e.g. the instationary flow through hydraulic turbines, has its fundamentals on the study and solution of the basic equations for the fluid motion.

For incompressible flows, the fluid motion is fully characterised by the flow velocity components, c_i, and the pressure value, p, at every spatial coordinate, x_i, of the control volume and at every time instant, t. In compressible flows of perfect gases, the density, ρ, and one more thermodynamic variable, e.g. the internal energy, e, at every spatial and time coordinate are also needed.

At every infinitesimal control volume, the fluid motion must respect the conservation laws for the mass, moment and internal energy. Their expression can also be referred to as the transport equations for the variables in question. The solution of the corresponding differential equations allows the complete description of the fluid flow.

The mass conservation law, for compressible and incompressible flows, is represented by the following formula:

$$\frac{\partial \rho}{\partial t} + \frac{\partial \left(\rho c_i\right)}{\partial x_i} = 0 \tag{2.1}$$

The moment conservation law, even more commonly known as the Navier-Stokes equation, is given by:

$$\frac{\partial \left(\rho c_i\right)}{\partial t} + \frac{\partial \left(c_j \rho c_i\right)}{\partial x_j} = -\frac{\partial p}{\partial x_i} + \frac{\partial t_{ij}}{\partial x_j} \tag{2.2}$$

This expression is valid in the absence of field forces, otherwise, the field force vector, f_i, has to be added to the right hand-side. The first term represents the instantaneous moment variation, the second is the convective term, the third involves the pressure gradient, which can be thought as the source term in transport equations, and the last is the diffusion term. The viscous stress tensor, t_{ij}, involves the deformation tensor, s_{ij}, and is evaluated with the following expression:

$$t_{ij} = 2\mu s_{ij} - \frac{2}{3}\mu \frac{\partial c_k}{\partial x_k}\delta_{ij} \tag{2.3}$$

This formula is valid for Newtonian fluids and assumes the Stokes hypothesis for the second viscosity, $\lambda = -2/3\ \mu$, which is correct for monoatomic gases and almost always adopted in computational fluid dynamics (CFD). The deformation tensor depends only on the velocity gradients.

$$s_{ij} = \frac{1}{2}\left(\frac{\partial c_i}{\partial x_j} + \frac{\partial c_j}{\partial x_i}\right) \tag{2.4}$$

The energy conservation law is constituted by a more complex expression, in which the internal energy, e, the enthalpy, h, and the heat flux, q_j, appear. The viscous stress tensor, t_{ij}, is also present, representing the way that part of the moment is dissipated by the fluid viscosity in internal energy.

$$\frac{\partial\left(\rho e_t\right)}{\partial t} + \frac{\partial\left(c_j \rho h_t\right)}{\partial x_j} = -\frac{\partial q_j}{\partial x_j} + \frac{\partial\left(c_i t_{ij}\right)}{\partial x_j} \tag{2.5}$$

The total internal energy and the total enthalpy are defined as $e_t = e + 1/2\ c_i c_i$ and $h_t = h + 1/2\ c_i c_i$. The internal energy and the enthalpy are related by $h = e + p/\rho$. The heat flux, q_j, in the internal energy transport equation is obtained from the Fourier heat flux law, where k_t is the thermal conductivity.

$$q_j = -k_t \frac{\partial T}{\partial x_j} \tag{2.6}$$

For determination of the thermodynamic state and the closure of the differential equation system, the equation of state is needed. It relates the density, ρ, the pressure, p and the temperature, T. Considering the caloric properties of the gas in question, the internal energy, e, and the enthalpy, h, can be related to the temperature, T. In several cases, the gas properties depends on temperature, as it may be the case e.g. for the dynamic viscosity, μ.

Incompressible Fluids

Incompressible fluids are quite common in fluid flow problems and allow the simplification of the basic equations. In hydraulic turbines, the water is at its liquid state, allowing it to be considered as incompressible. The only exception would be in cavitating portions of the flow, whose occurrence is mostly avoided in normal turbine operation. For incompressible fluids, the density is constant and the divergent of the velocity vector is zero. In addition, the energy conservation equation can be discarded, as long as, in this case, the pressure and velocity fields are fully described just by the mass and moment conservation equations.

$$\frac{\partial \left(\rho c_i\right)}{\partial x_i} = 0 \tag{2.7}$$

$$\frac{\partial \left(\rho c_i\right)}{\partial t} + \frac{\partial \left(c_j \rho c_i\right)}{\partial x_j} = -\frac{\partial p}{\partial x_i} + \frac{\partial}{\partial x_j}\left[\mu\left(\frac{\partial c_i}{\partial x_j} + \frac{\partial c_j}{\partial x_i}\right)\right] \tag{2.8}$$

2.2 Averaging of the Basic Equations

2.2.1 Reynolds Average

Turbulence is present in almost all flows with practical interest in engineering applications, as observed by Tennekes and Lumley [153]. Turbulence is characterised by random fluctuations, which interact with the main flow, and whose time and length scales spectra are so broad that the numerical solution of the exact basic equations with the current technology would require prohibitive computational resources for practical problems. This difficulty can be avoided with averaging procedures for the Navier-Stokes equations. In the case of incompressible fluids, the averaging relies on the method from Reynolds [120].

In turbulent flows, the variables can be separated in a stable, $\overline{\Phi}$, and a stochastic oscillating term, Φ', superimposed to the flow mean value.

$$\Phi\left(x_i, t\right) = \overline{\Phi}\left(x_i\right) + \Phi'\left(x_i, t\right) \tag{2.9}$$

The stationary part is defined as the mean value over the complete fluid motion duration:

$$\overline{\Phi}\left(x_i\right) = \lim_{\Delta t \to \infty} \frac{1}{\Delta t} \int_t^{t+\Delta t} \Phi\left(x_i, t\right) dt \tag{2.10}$$

For unsteady flows, this variable splitting can also be done, provided that the characteristic time scale of the mean flow unsteady motion is far larger than the one of the turbulent eddies motion, $\Delta t \gg T_T$. This is normally the case, since the turbulent time scales are extremely short, and the unsteady mean value can also be defined as $\Phi(x_i,t) = \overline{\Phi}(x_i,t) + \Phi'(x_i,t)$, where $\Phi'(x_i,t)$ is defined in the same way as $\Phi'(x_i,t)$ just droping the limit calculation and taking Δt as finite.

Once the averaging procedure has been established, it can be applied to the mass and momentum conservation equations to obtain the Reynolds averaged Navier-Stokes (RANS) equations.

$$\frac{\partial(\rho\bar{c}_i)}{\partial x_i} = 0 \tag{2.11}$$

$$\frac{\partial(\rho\bar{c}_i)}{\partial t} + \frac{\partial(\bar{c}_j\rho\bar{c}_i)}{\partial x_j} = -\frac{\partial\overline{p}}{\partial x_i} + \frac{\partial}{\partial x_j}\left(\bar{t}_{ij} - \rho\overline{c_i'c_j'}\right) \tag{2.12}$$

The mean viscous stress tensor, $\bar{t}_{ij}$, is calculated with help from the mean strain-rate tensor, S_{ij}.

$$\bar{t}_{ij} = 2\mu S_{ij}, \quad S_{ij} = \frac{1}{2}\left(\frac{\partial\bar{c}_i}{\partial x_j} + \frac{\partial\bar{c}_j}{\partial x_i}\right) \tag{2.13}$$

Through the averaging process of the convective term, a new component in the momentum conservation equation appears, $\tau_{ij} = -\rho\overline{c_i'c_j'}$, which is identified as the Reynolds stress tensor. The turbulence kinetic energy is defined with the turbulent velocity fluctuations as $k = 1/2\ \overline{c_i'c_i'}$.

The Reynolds stress tensor, τ_{ij}, is symmetric and brings six new unknown variable fields to the equation system. Therefore, additional equations are needed to mathematically close the system. Multiplying the Navier-Stokes by c_i' and c_j', adding the two new equations together and time averaging the result, one obtains the tensorial transport equation for the Reynolds stress.

$$\frac{\partial\tau_{ij}}{\partial t} + \frac{\partial(\bar{c}_k\tau_{ij})}{\partial x_k} = -\tau_{ik}\frac{\partial\bar{c}_j}{\partial x_k} - \tau_{jk}\frac{\partial\bar{c}_i}{\partial x_k} + \epsilon_{ij} - \Pi_{ij} + \frac{\partial}{\partial x_k}\left[\nu\frac{\partial\tau_{ij}}{\partial x_k} + C_{ijk}\right] \tag{2.14}$$

The dissipation tensor is represented by ϵ_{ij}, the pressure-strain correlation tensor corresponds to Π_{ij} and C_{ijk} is the turbulent transport tensor. They are defined by:

$$\Pi_{ij} = \overline{p'\left(\frac{\partial c_i'}{\partial x_j} + \frac{\partial c_j'}{\partial x_i}\right)}, \quad \epsilon_{ij} = \overline{2\mu\frac{\partial c_i'}{\partial x_k}\frac{\partial c_j'}{\partial x_k}}, \quad C_{ijk} = \overline{\rho c_i'c_j'c_k'} + \overline{p'c_i'}\delta_{jk} + \overline{p'c_j'}\delta_{ik} \tag{2.15}$$

Although the expression for the transport equation for the Reynolds stress could be written, adding six more equations to the system, it introduced new pressure and velocity correlations. The tensors ϵ_{ij}, Π_{ij} and C_{ijk} bring 22 new unknowns to the problem. Further mathematical manipulations will not help to close the equation system and its closure is only possible with the introduction of turbulence models, to model the new terms in the RANS equations.

With exception of the stress transport turbulence models, almost all others models take the Boussinesq approximation to simplify the Reynolds stress tensor expression. Boussinesq [19] postulates that the turbulent and the molecular diffusivities have the same nature. This assumption allows the Reynolds stress tensor to be expressed as function of the mean strain-rate tensor, S_{ij}, in the same way as the viscous stress.

$$\tau_{ij} = 2\mu_T S_{ij} - \frac{2}{3}\rho k \delta_{ij} \tag{2.16}$$

The first term is proportional to S_{ij} and has exactly the same form as the viscous stress tensor. The coefficient μ_T is the dynamic eddy viscosity. It is the only difference between the viscous and the Reynolds stress tensors. The expression of μ_T is needed for the closure of the differential equation system and must be determined by the chosen turbulence model. It must be able to reflect the influence of turbulence on the Navier-Stokes equations.

The second term in the simplified expression for the Reynolds stress tensor is needed to guarantee the mathematical coherence of the relation between its trace and the turbulence kinetic energy, $\tau_{ii} = -2\rho k$.

For the numerical computations, the first term is aggregated to the viscous stress tensor, resulting in the diffusive term $\partial\left(2\mu_{\mathit{eff}} S_{ij}\right)/\partial x_j$, where the effective dynamic viscosity is $\mu_{\mathit{eff}} = \mu + \mu_T$. The second term can be added to the pressure component. With this procedure, the RANS equations take the same mathematical form as the original basic equations and the general numerical methods for transport equations can be directly employed.

The Boussinesq approximation is relative simple and might show limitations to predict flows with strong strain-rate gradients, secondary circulation or separation. Some turbulence models try to suppress these limitation with higher order approximations for τ_{ij} or with the stress transport equations.

The turbulence kinetic energy, k, is an important parameter for the turbulence models and its differential equation can be derived taking the trace of the Reynolds stress transport equation.

$$\frac{\partial\left(\rho k\right)}{\partial t} + \frac{\partial\left(\overline{c}_j \rho k\right)}{\partial x_j} = P_k - \rho\epsilon + \frac{\partial}{\partial x_j}\left(\mu\frac{\partial k}{\partial x_j} - \frac{\rho}{2}\overline{c_i' c_i' c_j'} - \overline{p' c_j'}\right) \tag{2.17}$$

The turbulence kinetic energy production term, P_k, and the dissipation rate, ϵ, are given by:

$$P_k = -\rho\overline{c_i'c_j'}\frac{\partial \overline{c}_i}{\partial x_j}, \quad \epsilon = \overline{2\mu\frac{\partial c_i'}{\partial x_j}\frac{\partial c_i'}{\partial x_j}} \tag{2.18}$$

Concerning the modelling, almost all turbulence models group the turbulent transport and the pressure diffusion and approximate them by a diffusive term, as it is done for the Reynolds stress tensor.

$$-\frac{\rho}{2}\overline{c_i'c_i'c_j'} - \overline{p'c_j'} = \frac{\mu_T}{\sigma_k}\frac{\partial k}{\partial x_j} \tag{2.19}$$

The Reynolds stress tensor simplification can also be introduced into the turbulence kinetic energy production term, leading to:

$$P_k = \mu_T S^2 - \frac{2}{3}\rho k\frac{\partial \overline{c}_i}{\partial x_j}\delta_{ij}, \quad S = \sqrt{2S_{ij}S_{ij}} \tag{2.20}$$

The definition of the mean rotation tensor, Ω_{ij}, and the mean vorticity, Ω, will be useful for the upcoming development of some turbulence models.

$$\Omega_{ij} = \frac{1}{2}\left(\frac{\partial \overline{c}_i}{\partial x_j} - \frac{\partial \overline{c}_j}{\partial x_i}\right), \quad \Omega = \sqrt{2\Omega_{ij}\Omega_{ij}} \tag{2.21}$$

2.2.2 Favré Average

Since the fluid density is not constant in compressible flows, the Reynolds averaging procedure cannot be directly applied to the basic equations. Otherwise, numerous new correlations would appear and it would extremely increase the mathematical complexity and the modelling difficulties. In the case of compressible flows, the mass averaging, suggested by Favré [41] is used. Again the general unknown variable Φ can be split in a stable and in an oscillatory component.

$$\Phi\left(x_i, t\right) = \tilde{\Phi}\left(x_i\right) + \Phi''\left(x_i, t\right) \tag{2.22}$$

The mean value, $\tilde{\Phi}$, is now defined by the mass averaging. It consists in using the density, ρ, as a weighting factor for the time average. The overline symbol denotes the Reynolds averaging as before.

$$\tilde{\Phi}\left(x_i\right) = \frac{\overline{\rho\Phi}}{\overline{\rho}} = \frac{1}{\overline{\rho}} \lim_{\Delta t \to \infty} \frac{1}{\Delta t} \int_t^{t+\Delta t} \rho\left(x_i, t\right) \Phi\left(x_i, t\right) dt \tag{2.23}$$

With some extensive mathematical manipulation combining the Reynolds and the Favré average for different terms, using the assumptions introduced by HUANG, COLEMAN AND BRADSHAW [65] for the mean viscous stress tensor and the approximation proposed by SARKAR ET AL. [135] for the pressure dilatation term, the Favré averaged basic equations for subsonic flows can be written as:

$$\frac{\partial \overline{\rho}}{\partial t} + \frac{\partial\left(\overline{\rho}\tilde{c}_i\right)}{\partial x_i} = 0 \tag{2.24}$$

$$\frac{\partial\left(\overline{\rho}\tilde{c}_i\right)}{\partial t} + \frac{\partial\left(\tilde{c}_j \overline{\rho}\tilde{c}_i\right)}{\partial x_j} = -\frac{\partial \overline{p}}{\partial x_i} + \frac{\partial}{\partial x_j}\left(\tilde{t}_{ij} - \overline{\rho c_i'' c_j''}\right) \tag{2.25}$$

$$\frac{\partial\left(\overline{\rho}\tilde{e}_t\right)}{\partial t} + \frac{\partial\left(\tilde{c}_j \overline{\rho}\tilde{h}_t\right)}{\partial x_j} = \frac{\partial}{\partial x_j}\left[\left(\frac{\mu}{Pr} + \frac{\mu_T}{Pr_T}\right)\frac{\partial \tilde{h}}{\partial x_j}\right] + \frac{\partial}{\partial x_j}\left[\tilde{c}_i\left(\tilde{t}_{ij} - \overline{\rho c_i'' c_j''}\right)\right] \tag{2.26}$$

In the expression above, Pr is the Prandtl number. The turbulence kinematic energy equation is also expressed with the Favré averaging:

$$\frac{\partial\left(\overline{\rho}k\right)}{\partial t} + \frac{\partial\left(\tilde{c}_j \overline{\rho}k\right)}{\partial x_j} = P_k - \overline{\rho}\epsilon + \frac{\partial}{\partial x_j}\left[\left(\mu + \frac{\mu_T}{\sigma_k}\right)\frac{\partial k}{\partial x_j}\right] \tag{2.27}$$

The Favré averaged equations are coherent with the Reynolds formulation. If the fluid density is taken to be constant with the mass averaged equations, the Reynolds averaged equations are exactly recovered.

2.3 Turbulence Modelling with the Averaged Equations

The traditional turbulence models are developed based on the averaged basic equations. They are closure models for the Navier-Stokes equations, allowing the estimation of the turbulence kinetic energy, k, and of the Reynolds stress tensor, τ_{ij}, through the determination of the turbulence eddy viscosity, ν_T, for the Boussinesq approximation. They normally do not rely only on theoretical considerations, but also on empirical evidence and test cases, used for calibrating the model parameters. The physical nature of the transport process is also considered, dictating that the turbulence differential equations shall provide time variation, convective, production, dissipation and diffusive terms.

There are turbulence models, which count just with an algebraic relation for defining the eddy viscosity, ν_T, they are also called zero-equation turbulence models and have nowadays limited application. There are also one-equation models, based on the k equation or, more recently, on the turbulence eddy viscosity, ν_T. However, they have limited accuracy for flows with complicated patterns, e.g. strong gradients, recirculation or separation. Two-equation models are more accurate and can deal with different flow types without the need of calibration for each individual problem. They usually count with the k transport equation and one additional equation for the turbulence dissipation rate, ϵ, turbulence dissipation frequency, ω, or turbulence length scale, ℓ. At present, the most common two-equation models are the k-ϵ, k-ω and their variants.

As long as the turbulence models count much more on physical insight than on mathematical derivations, the dimensional analysis constitutes a useful method for the turbulence fundamentals. The turbulence eddy viscosity can be related to turbulence kinetic energy and dissipation.

$$\mu_T = C_\mu \rho \frac{k^2}{\epsilon} \tag{2.28}$$

The need for the proportionality constant, C_μ, comes from the dimensional analysis and its exact value is part of the turbulence modelling.

A similar expression for the eddy viscosity, which involves the dissipation frequency, ω, instead of the dissipation rate, ϵ, can also be derived from the dimensional analysis.

$$\mu_T = \rho \frac{k}{\omega} \tag{2.29}$$

The dissipation rate and the dissipation frequency are both related by $\epsilon = \beta^* k\omega$, with $\beta^* = 0{,}09$.

The turbulence length scale is an important physical characteristic of turbulent flows and is required by some models. It can be expressed in terms of the turbulence kinetic energy, dissipation rate and frequency as well.

$$L_T = \frac{k^{3/2}}{\epsilon} = \frac{\sqrt{k}}{\beta^* \omega} \tag{2.30}$$

Different definitions for the turbulence length scale can be found in the literature. Most of them are equal, except for a multiplier constant. Strelets [149] follows the same definition above, $L_T = k^{3/2}/\epsilon$, while Wilcox [167] prefers $\ell = C_\mu k^{3/2}/\epsilon$ and Menter and Egorov [100] adopt $L = C_\mu^{3/4} k^{3/2}/\epsilon$.

2.3.1 k-ϵ Model

The currently still most widely spread turbulence model in industrial applications is the so called standard k-ϵ model, developed by LAUNDER and SPALDING [80]. Especially in the application field of hydraulic turbines, it enjoys great popularity, as commented by RODI [127]. It is a two-equation turbulence model, which is based on the specific turbulence kinetic energy, k, and specific turbulent dissipation rate, ϵ, transport equations, (2.31) and (2.32).

$$\frac{\partial(\rho k)}{\partial t} + \frac{\partial(\bar{c}_j \rho k)}{\partial x_j} = \tau_{ij}\frac{\partial \bar{c}_i}{\partial x_j} - \rho\epsilon + \frac{\partial}{\partial x_j}\left[\left(\mu + \frac{\mu_T}{\sigma_k}\right)\frac{\partial k}{\partial x_j}\right] \tag{2.31}$$

$$\frac{\partial(\rho \epsilon)}{\partial t} + \frac{\partial(\bar{c}_j \rho \epsilon)}{\partial x_j} = C_{\epsilon_1}\frac{\epsilon}{k}\tau_{ij}\frac{\partial \bar{c}_i}{\partial x_j} - C_{\epsilon_2}\rho\frac{\epsilon^2}{k} + \frac{\partial}{\partial x_j}\left[\left(\mu + \frac{\mu_T}{\sigma_\epsilon}\right)\frac{\partial \epsilon}{\partial x_j}\right] \tag{2.32}$$

The eddy viscosity is defined in the usual way with $\nu_T = C_\mu\ k^2/\epsilon$. The adopted constants in this case are $C_\mu = 0{,}09$, $C_{\epsilon_1} = 1{,}44$, $C_{\epsilon_2} = 1{,}92$, $\sigma_k = 1{,}0$ and $\sigma_\epsilon = 1{,}3$.

Through the solution of the k and ϵ transport equations, it is possible to calculate the turbulent dynamic viscosity, μ_T, which is substituted in the impulse equation for the determination of the effective dynamic viscosity μ_{eff}.

Due to its limitation to accurately predict the velocity profile in the near-wall region, the k-ϵ model is mostly employed in conjunction with wall functions in applications where the viscous sub-layer in the boundary layer is not determinant. The strength of the k-ϵ model consists in its ability to precisely reproduce the deffect layer in a variety of problems.

2.3.2 k-ϵ Low-Reynolds Model

In attached flows, the standard k-ϵ model can reasonably predict the boundary layer behaviour up to the logarithmic layer, but fails to reproduce it in the viscous sub-layer. If no wall function is used and the velocity profile is numerically solved up to the wall boundary, this turbulence model has to be modified to correctly match the flow characteristics at low Reynolds numbers. To achieve this effect, the closure coefficient C_μ and the production and dissipation terms in the ϵ equation are changed with the introduction of the damping functions f_μ, f_1 and f_2.

$$\frac{\partial(\rho k)}{\partial t} + \frac{\partial(\bar{c}_j \rho k)}{\partial x_j} = \tau_{ij}\frac{\partial \bar{c}_i}{\partial x_j} - \rho\epsilon + \frac{\partial}{\partial x_j}\left[\left(\mu + \frac{\mu_T}{\sigma_k}\right)\frac{\partial k}{\partial x_j}\right] \tag{2.33}$$

$$\frac{\partial(\rho \tilde{\epsilon})}{\partial t} + \frac{\partial(\bar{c}_j \rho \tilde{\epsilon})}{\partial x_j} = C_{\tilde{\epsilon}_1} f_1 \frac{\tilde{\epsilon}}{k}\tau_{ij}\frac{\partial \bar{c}_i}{\partial x_j} - C_{\tilde{\epsilon}_2} f_2 \rho\frac{\tilde{\epsilon}^2}{k} + E + \frac{\partial}{\partial x_j}\left[\left(\mu + \frac{\mu_T}{\sigma_k}\right)\frac{\partial \tilde{\epsilon}}{\partial x_j}\right] \tag{2.34}$$

An additional term, E, is included in the ϵ equation and the dissipation rate is substituted in the transport equations by the variable $\tilde{\epsilon}$, which involves the dissipation value at the wall, ϵ_0. Their relation is established by $\epsilon = \epsilon_0 + \tilde{\epsilon}$.

The damping function f_μ is present in the eddy viscosity expression:

$$\mu_T = C_\mu f_\mu \rho \frac{k^2}{\epsilon} \tag{2.35}$$

Jones and Launder [70], Launder and Sharma [79], Lam and Bremhorst [78] and Chien [26] give different expressions for the damping functions, which make use of the turbulence and near-wall Reynolds numbers, Re_T and Re_y, and the dimensionless sublayer-scaled distance, y^+.

2.3.3 *k-ω* Model

The k-ω model suggested by Wilcox [166] makes also use of the transport equation for the kinetic energy, but the second differential equation is the transport equation for the dissipation frequency ω, instead of the dissipation rate ϵ. One of its advantages is that it can be integrated up to the wall boundaries without the need for damping functions nor low Reynolds numbers corrections. According to Wilcox [167] this turbulence model can better reproduce separated flows than the k-ϵ based models. However, Menter [99] pointed out the excessive sensibility of this model to the boundary conditions, leading in some cases to erroneous solutions. The partial differential equations solved in the k-ω model are:

$$\frac{\partial(\rho k)}{\partial t} + \frac{\partial(\bar{c}_j \rho k)}{\partial x_j} = \tau_{ij}\frac{\partial \bar{c}_i}{\partial x_j} - \rho\beta^* k\omega + \frac{\partial}{\partial x_j}\left[(\mu + \sigma_k \mu_T)\frac{\partial k}{\partial x_j}\right] \tag{2.36}$$

$$\frac{\partial(\rho \omega)}{\partial t} + \frac{\partial(\bar{c}_j \rho \omega)}{\partial x_j} = \alpha\frac{\omega}{k}\tau_{ij}\frac{\partial \bar{c}_i}{\partial x_j} - \beta\rho\omega^2 + \frac{\partial}{\partial x_j}\left[(\mu + \sigma_\omega \mu_T)\frac{\partial \omega}{\partial x_j}\right] \tag{2.37}$$

The eddy viscosity is given by the relation $\nu_T = k/\omega$ and the constants chosen for the model are $\alpha = 5/9$, $\beta^* = 9/100$, $\beta = 3/40$, $\sigma_k = 1/2$ and $\sigma_\omega = 1/2$.

At wall boundaries, the turbulence kinetic energy is equal to zero, $k = 0$, leading to $\omega \to \infty$. In the numerical implementation of the turbulence model, limiter functions are introduced to overcome this indetermination. In spite of this numerical approximation, the k-ω model has proven in practical applications to be able to accurately determine the velocity profile in the near wall region of the boundary layer, even in problems with separation and reattachment. In the deffect layer, the k-ω model encounters difficulties to properly reproduce the boundary layer behaviour.

2.3.4 k-ϵ LCL Model and EASM

The k-ϵ LCL turbulence model comes from Lien, Chen and Leschziner [84] and relies on the non-linear eddy-viscosity approximation, with cubic terms. This higher order model should eliminate certain limitations of the Boussinesq approximation, in cases where the turbulence anisotropy is important, where sudden changes in the mean strain-rate occur or where the geometry contains strong curved surfaces. The advantage of using the LCL over the standard k-ϵ model must be evaluated in each case, since it requires more computational effort and, depending on the flow characteristics, may bring no improvement to the solution quality.

The explicit algebraic stress model (EASM), proposed by Rodi [125, 126] and Gatski and Speziale [51], also tries to eliminate the deficiencies of the Boussinesq approximation with the introduction of high-order terms (HOT) in the Reynolds stress expression. One of its main features is to count with the anisotropy tensor, b_{ij}. The EASM can present improved results, in comparison to other two-equation models, especially in problems with high streamline curvature and secondary flow, as noticed by Demuren [34]. When compared to Reynolds stress models (RSM), it has the advantage to require less computational resources, as long as it does not directly deal with the tensorial Reynolds stress transport equation. However, it cannot better predict sudden strain-rate changes or the return to isotropy.

2.3.5 k-ω SST

In order to overcome the excessive sensibility of the k-ω model to the boundary conditions, Menter [99] developed the k-ω SST model. It makes use of the blend functions F_1 and F_2 to achieve the blending from the standard k-ϵ and k-ω models. The purpose is to reproduce the k-ω behaviour in the viscous and logarithmic layers, where it can precisely describe the boundary layer dynamics, and to regain the k-ϵ characteristic in the defect layer, where it is less sensible to the boundary conditions. This approach combines both models to take the maximum advantage of their strengths in the distinct sub-layers of the boundary layer.

In the k-ω SST model, the kinetic energy, k, transport equation is the same as before, but the blending function is introduced in the turbulent dissipation frequency equation, as below:

$$\frac{\partial(\rho k)}{\partial t} + \frac{\partial(\bar{c}_j \rho k)}{\partial x_j} = \tau_{ij}\frac{\partial \bar{c}_i}{\partial x_j} - \beta^* \rho \omega k + \frac{\partial}{\partial x_j}\left[(\mu + \sigma_k \mu_T)\frac{\partial k}{\partial x_j}\right] \tag{2.38}$$

$$\begin{aligned}\frac{\partial(\rho\omega)}{\partial t} + \frac{\partial(\bar{c}_j \rho\omega)}{\partial x_j} = \frac{\gamma}{\nu_T}\tau_{ij}\frac{\partial \bar{c}_i}{\partial x_j} - \beta\rho\omega^2 + \frac{\partial}{\partial x_j}\left[(\mu + \sigma_\omega \mu_T)\frac{\partial \omega}{\partial x_j}\right] \\ + 2(1 - F_1)\rho\sigma_{\omega_2}\frac{1}{\omega}\frac{\partial k}{\partial x_j}\frac{\partial \omega}{\partial x_j}\end{aligned} \tag{2.39}$$

The last term in the last equation, which is not present in the original ω equation, comes from the transformation of the turbulent dissipation transport equation in the dissipation frequency transport equation. The factor $(1 - F_1)$ provides the blending from the k-ϵ with the k-ω model. Near to the wall boundaries, $F_1 \approx 1$ and $(1 - F_1) \approx 0$, reproducing the original k-ω model. From the defect layer and going in the opposite direction of the wall boundaries, $F_1 \approx 0$ and $(1 - F_1) \approx 1$, causing the equations to behave as the standard k-ϵ model.

The first blend function defined by MENTER [99] is:

$$F_1 = \tanh\left(arg_1^4\right), \quad arg_1 = \min\left[\max\left(\frac{\sqrt{k}}{0{,}09\omega y}; \frac{500\nu}{y^2\omega}\right); \frac{4\rho\sigma_{\omega_2}k}{CD_{k\omega}y^2}\right] \tag{2.40}$$

Where $CD_{k\omega}$ also include numerical limiters:

$$CD_{k\omega} = \max\left(2\rho\sigma_{\omega_2}\frac{1}{\omega}\frac{\partial k}{\partial x_j}\frac{\partial \omega}{\partial x_j}; 10^{-20}\right) \tag{2.41}$$

Additionally, in the k-ω SST model, MENTER [99] modified the turbulent dynamic viscosity, μ_T, with a numerical limiter, to improve the Boussinesq approximation and consider the shear stress transport.

$$\nu_T = \frac{a_1 k}{\max\left(a_1\omega; \Omega F_2\right)} \tag{2.42}$$

There appear the second blend function and its argument.

$$F_2 = \tanh\left(arg_2^2\right), \quad arg_2 = \max\left(2\frac{\sqrt{k}}{0{,}09\omega y}; \frac{500\nu}{y^2\omega}\right) \tag{2.43}$$

The constants ϕ in the k-ω SST model are calculated with the constants ϕ_1 and ϕ_2:

$$\phi = F_1\phi_1 + (1 - F_1)\,\phi_2 \tag{2.44}$$

The constants ϕ_1 in the first set are chosen as $\sigma_{k_1} = 0{,}85$, $\sigma_{\omega_1} = 0{,}5$, $\beta_1 = 0{,}0750$, $a_1 = 0{,}31$, $\beta^* = 0{,}09$, $\kappa = 0{,}41$ and $\gamma_1 = \beta_1/\beta^* - \sigma_{\omega_1}\kappa^2/\sqrt{\beta^*}$, while the constants ϕ_2 corresponding to the second set are given by $\sigma_{k_2} = 1{,}0$, $\sigma_{\omega_2} = 0{,}856$, $\beta_2 = 0{,}0828$, $\beta^* = 0{,}09$, $\kappa = 0{,}41$ and $\gamma_2 = \beta_2/\beta^* - \sigma_{\omega_2}\kappa^2/\sqrt{\beta^*}$.

The k-ω SST model encountered, among others, great application in the simulation field of free flows over aerofoils.

2.4 Wall Treatment

If appropriate turbulence models are used, like the k-ϵ low-Reynolds, the k-ω or the k-ω SST, the boundary layer can be numerically solved up the wall boundary. In this case, adequate boundary conditions have to be fixed at the wall boundary. The turbulence kinetic energy tends to zero as the wall is approached, $k \to 0$, as well as its derivative in the direction normal to the wall, $\partial k/\partial y \to 0$. According to its transport equation, $\epsilon = \nu\ \partial^2 k/\partial y^2$, which can be twice integrated, yielding $\epsilon \to 2\nu k/y^2$ at the wall. If the dissipation frequency is rather employed in the turbulence model, its limit at wall is $\omega \to \infty$ and its numerical implementation requires the use of a numerical limiter.

Nevertheless, the numerical resolution of the complete boundary layer requires very fine computational meshes near to the wall, with y^+ values around 1, incurring in high computational costs. If the solution of the boundary layer is not the main point of interest in the fluid flow problem being addressed, the wall function can be an alternative to the full numerical solution of the boundary layer. In many industrial applications, the wall function can be employed without negative effects on the simulated flow characteristics.

The wall function relies on the similitude law of the stable boundary layer for most part of the flows. If the dimensionless sublayer-scaled velocity, u^+, and distance, y^+, are used, the velocity distribution in the boundary layer describes a constant pattern, as shown in Figure 2.1.

The sublayer-scaled velocity and distance are defined as follows:

$$y^+ = \frac{y u_\tau}{\nu}, \quad u^+ = \frac{u_t}{u_\tau} \tag{2.45}$$

Where u_t is the velocity component in the direction tangent to the wall and the friction velocity, u_τ, is defined with the shear stress at the wall, τ_w.

$$u_\tau = \sqrt{\frac{\tau_w}{\rho}} \tag{2.46}$$

As seen in Figure 2.1, the boundary layer can be divided in the viscous sub-layer, the logarithmic layer and the defect layer. In the viscous sub-layer, the sublayer-scaled velocity is equal to the sublayer-scaled distance, $u^+ = y^+$. In the logarithmic region, they are related by the following law:

$$u^+ = \frac{1}{\kappa} \ln y^+ + C \tag{2.47}$$

The logarithmic layer goes typically from $y^+ = 30$ until $y = 0{,}1\delta$, where δ is the thickness of the boundary layer, according to Wilcox [167]. The von Kármán

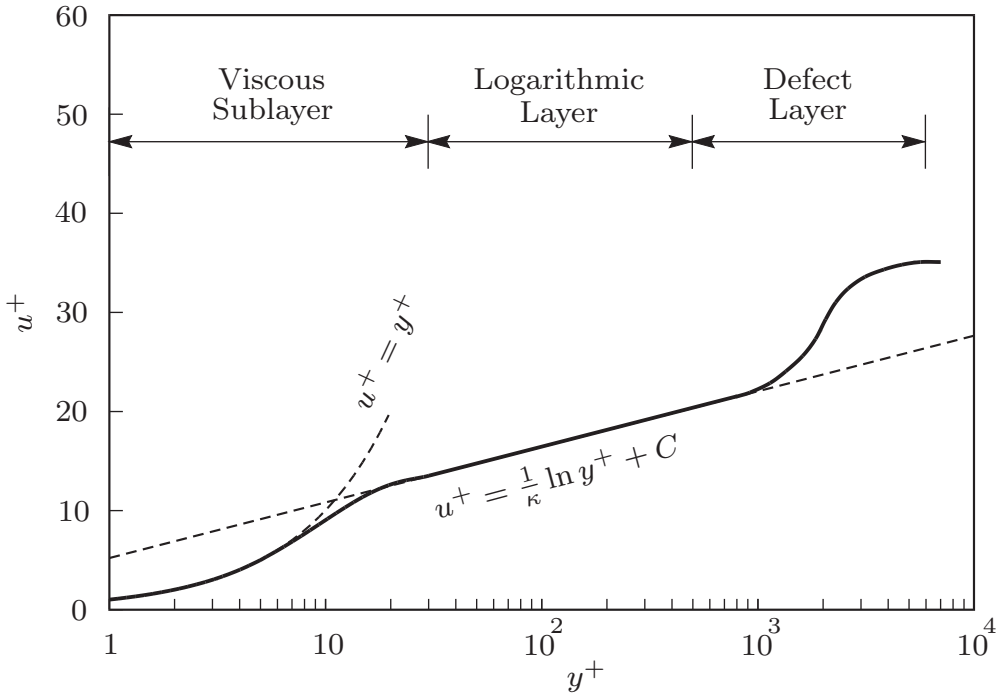

Figure 2.1: Typical velocity profile at the turbulent boundary layer.

constant is $\kappa = 0{,}41$. The constant C depends on the surface roughness and is $C = 5{,}2$ for smooth surfaces. When the wall function is employed, it is necessary that the distance between the first mesh point and the wall, y_2, produces y^+ values in the range mentioned above, where the logarithmic expression is valid.

The wall function can sometimes lead to difficulties in the prediction of highly unstable boundary layers or when massive separation is present. In these situations, the alternative would be the full numerical solution of the boundary layer up to the wall, in spite of the computational costs. In the other cases, the law of the wall should deliver satisfactory results, as in the case of hydraulic turbines.

2.5 Large Eddy Simulation and Hybrid Models

The unsteady Reynolds-Averaged Navier-Stokes equations (URANS), associated with k-ϵ or k-ω turbulence models and its variants, is not adequate for solving all dynamic fluid flow problems. There are classic simple test cases, in which URANS clearly fails to reproduce the dynamic flow pattern and to properly calculate the transient pressure and velocity values. Common examples are the flow around a circular cylinder or around a square cylinder, as shown by e.g. Spalart [145] and Bosch and Rodi [18] respectively, and vortex shedding in general, as commented by Fröhlich and Rodi [47]. Davidson [31] and also Wunderer [170] show that flow separation can be a problem as well. Other problematic cases are flow instabilities such as swirling flow in cones, treated by Ogor et al. [114], and

Kelvin-Helmholtz instabilities. In all these cases URANS cannot accurately predict the time dependent values of the pressure and velocity fields or even its oscillation amplitude.

In all these test cases and in most practical applications, the oscillating values are underestimated by URANS. Through the usage by URANS of traditional turbulence models, as k-ϵ, k-ω and its variants, excessive dissipation is introduced in the flow, causing the flow transient effects to be excessively damped. The reduction by URANS of the calculated oscillating effects is present in all flow regions, it means in the boundary layer, in the wake region and in the flow core, as respectively revealed by the sample cases with flow separation, vortex shedding and dynamic instabilities. This limitation in URANS is related to the averaging procedure and to the way in which the turbulence is modelled.

In URANS, no turbulent eddies are calculated. The motion of the eddies in all turbulent scales is ignored and their effect on the other flow structures tries to be included in the turbulence model alone, through the addiction of the turbulent eddy viscosity, μ_T, to the molecular viscosity, μ, resulting in the effective eddy viscosity, $\mu_{eff} = \mu + \mu_T$, in the Navier-Stokes equations. No matter how fine the computational grid and the time discretisation are, the turbulent eddies are not resolved by URANS and the extra dissipation term is added in all regions of the flow. This approach generates the excessive numerical damping and the underestimated transient results.

The other extreme to URANS, concerning turbulence, would be the direct numerical simulation (DNS), in which the eddies in all turbulent scales are simulated instead of modelled. Still DNS needs extremely refined grids and time steps to allow the simulation of the even smallest eddies. As pointed out by Spalart [145], with the current or in the near future available computer technology and computational costs, DNS constitutes no alternative for industrial applications.

The large eddy simulation (LES) appears as an alternative to URANS and DNS. In LES, not all turbulent eddies are simulated, but the eddies, which are larger than the grid resolution, have their motion calculated and are not modelled, similar to DNS. On the other hand, the smaller eddies, which cannot be resolved with the grid and time resolution available in the numerical model, have their interaction with the flow approximated by a turbulence model, as in URANS. Figure 2.2 illustrates this idea by qualitatively relating the modelled portions of the turbulent energy spectrum, $E(\kappa)$, to the turbulent wave length, $\lambda = 2\pi/\kappa$.

LES tries to eliminate the URANS limitations in the flow transient simulation, as well as the excessive damping and underestimation of the transient phenomena, with less computational resources than DNS. Though LES still requires finer meshes and time steps than URANS, in order to solve the larger turbulent eddies motion, incurring in computational cost, which might sometimes be high for the current industrial standards. Spalart [145] sees the introduction of LES in everyday industrial practice only in several years from now.

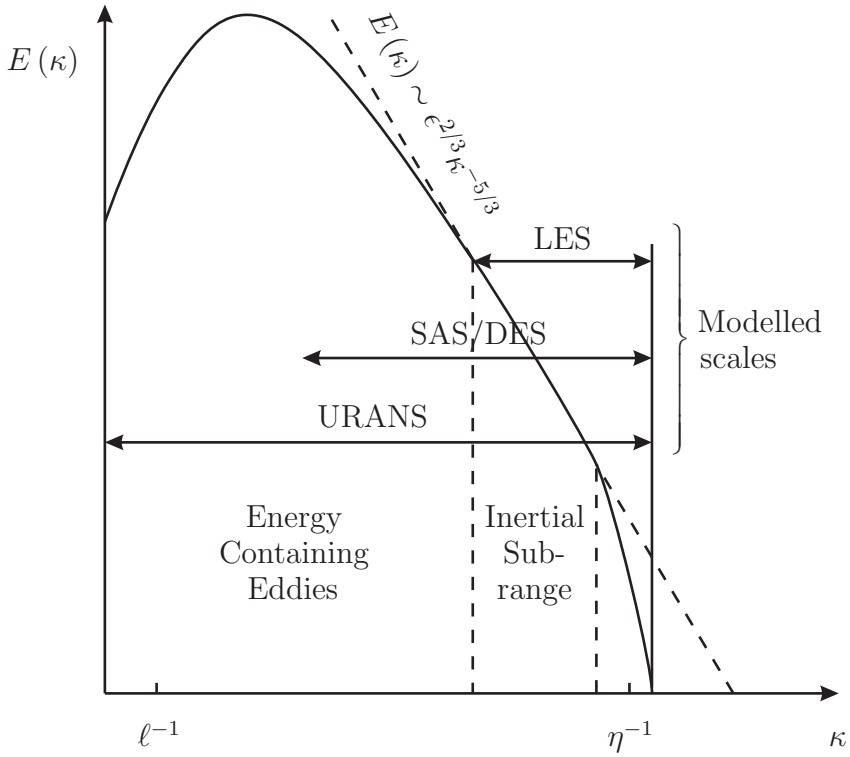

Figure 2.2: Qualitative representation of the modelled turbulent energy spectrum, $E(\kappa)$, as function of the turbulent wave number, $\kappa = 2\pi/\lambda$, for different approaches.

One solution to accurately simulate the transient flow in shorter times and with lower computational costs than with LES is the usage of hybrid turbulence models. They try to combine the speed and robust turbulence models of URANS with the precision of LES in simulating the dynamic flow details with no attenuation of the amplitude of transient variations. The central idea in the hybrid models is to behave like LES in regions of the flow, where the computational grid is fine enough to allow the solution of the eddies motion, and to switch to the URANS formulation, when the mesh does not attain this refinement requirement.

With this approach, it is possible to use less refined meshes than with LES in regions, which are not relevant to the overall flow dynamics and of no interest for the phenomena being studied. In such regions, the hybrid methods act with pure URANS behaviour, employing usual two-equation turbulence models that are more accurate than typical algebraic models used with LES and that can better deal with more complicated flows in case of coarse meshes. On the other hand, in parts of the computational domain with fine grids, the hybrid methods act like pure LES, solving the small turbulent structures with no artificial damping.

Currently, the detached eddy simulation (DES) introduced by Spalart et al.[148] and the scale adaptive simulation (SAS) developed by Menter and Egorov [100] enjoy the greatest popularity among the hybrid methods. Spalart [145] believes that it is nowadays possible to adopt the hybrid methods for industrial applications and design.

2.5.1 Large Eddy Simulation

The mathematical implementation of LES is based on a familiar idea: the separation of the velocity variables in two terms. However, the first one represents the resolved velocity scales, called resolvable-scale filtered velocity, and the second corresponds to the modelled scales, known as subgrid scale (SGS) velocity. The resolved velocity scales refer to the eddy motion, which can be simulated with the available grid and time step resolution, while the SGS velocity relates to the eddy motion occurring inside the grid cells and which needs to be modelled.

$$u_i = \bar{u}_i + u_i' \tag{2.48}$$

In the formal definition of LES, a mathematical filter is applied to the velocity components, allowing distinguishing and separating the resolved and unresolved scales. For example, the space discretisation process, i.e. the computational mesh, can be thought as an implicit filter, as long as velocity fluctuations occurring inside the cell volume cannot be captured and need to be modelled. In this example, the velocity fluctuations which can be resolved with the given mesh density correspond to the first term in equation (2.48) and the velocity fluctuations inside the cell volume are represented by the second term. Leonard [81] formulates a general filter expression as a convolution integral, where the filter function, G, is normalised and, Δ, is the filter width, based on the cell size.

$$\bar{u}_i(x_i, t) = \int_V G(x_i - \xi_i; \Delta)\, u_i(\xi_i, t)\, d\xi_i, \quad \Delta = (\Delta x \Delta y \Delta z)^{1/3} \tag{2.49}$$

Filters employed in LES include, among others, the volume-average box filter, used by Deardorff [32] and the more commonly used Gaussian filter, found, for example, in Ferziger [42]. The definition of such mathematical filters serves for the formal derivation of the motion equations, called in LES context resolvable-scale equations, and specially for developing the turbulence models, which attempt to take into account the SGS velocity. The filters do not explicitly appear in the resolvable-scale equations and need not to be directly implemented in numerical codes. Sagaut [134] recognises the theoretical character of filters: *"While the filters* [...] *are definable theoretically, they are almost never quantifiable in practice"*.

The derivation of the filtered mass and filtered moment conservation equations follows a similar procedure to the Reynolds averaging process: the filter function is applied to the complete mass conservation equations. Although the Reynolds averaged Navier-Stokes and the resolvable-scale equations have different physical meanings, they can assume exactly the same mathematical form, through the definition of the SGS stress.

$$\tau_{ij} = -\left(\overline{c_i c_j} - \bar{c}_i \bar{c}_j\right) \tag{2.50}$$

By the nature of the filter function, none of the terms in the first correlation $\overline{c_i c_j}$ is identically zero:

$$\overline{c_i c_j} = \overline{\bar{c}_i \bar{c}_j} + \overline{\bar{c}_i c'_j} + \overline{\bar{c}_j c'_i} + \overline{c'_i c'_j} \tag{2.51}$$

The SGS stress can be rewritten in terms of the Leonard stress, L_{ij}, the cross term, C_{ij}, and the SGS Reynolds stress, R_{ij}.

$$\tau_{ij} = -\left(L_{ij} + C_{ij} + R_{ij}\right) \tag{2.52}$$

$$L_{ij} = \overline{\bar{c}_i \bar{c}_j} - \bar{c}_i \bar{c}_j, \quad C_{ij} = \overline{\bar{c}_i c'_j} + \overline{\bar{c}_j c'_i}, \quad R_{ij} = \overline{c'_i c'_j} \tag{2.53}$$

The following step in the LES formulation is to satisfactorily model the SGS stress. This problem is very similar to the turbulence closure problem in RANS. Smagorinsky [143] proposed an estimation for the SGS stress similar to the Boussinesq approximation. In the case of incompressible fluids:

$$\tau_{ij} = 2\mu_T S_{ij} - \frac{2}{3}\rho k \delta_{ij} \tag{2.54}$$

The resolved strain-rate, S_{ij}, is computed with the resolvable-scale filtered velocity, $\bar{c}_i$, and ν_T represents the Smagorinsky eddy viscosity.

$$\nu_T = \left(C_S \Delta\right)^2 \sqrt{2 S_{ij} S_{ij}} \tag{2.55}$$

The filter width, Δ, in equation (2.55) is the evidence and consequence of the application of the mathematical filter for the derivation of the turbulence model. It is also the driving parameter to distinguish between the resolved and unresolved, i.e. modelled, velocity scales.

The closure equation (2.55) has the same form of the mixing length turbulence model, where the mixing length would be $\ell_{mix} = C_S \Delta$. The Smagorinsky approximation could be thought as the analogous to a simple zero-equation model, in the RANS closure problem. However, in the present model, the analogous to the mixing length is not constant, but proportional to the local cell size in the computational fluid domain. As seen in equation (2.55), the eddy viscosity decreases as the grid size is reduced, avoiding the introduction of excessive dissipation and the attenuation of the simulated fluid dynamic phenomena. The eddy viscosity is dependent on the local cell size. The model follows the logic that, if the grid is fine enough, i.e. if the cells are small enough to reproduce the eddy motion, no additional turbulent eddy viscosity, μ_T, is needed. Otherwise, the fluid motion would be excessively damped. The increased viscosity is needed only in regions, where the

computational mesh is not fine enough to resolve the eddies motion, resulting in unresolved velocity scales.

Similar to the mixing length turbulence model, the Smagorinsky coefficient, C_S, has no universal value and varies depending on the problem and on the flow type. Typical values are between 0,06 and 0,10. Moreover, near to wall boundaries, the Van Driest [159] damping function or the alternate damping function from Piomelli, Moin and Ferziger [119] must be used. Germano et al. [53] try to eliminate these deficiencies in the Smagorinsky model with the introduction of the dynamic SGS model. It express C_S as a function of further filtered values involving the Leonard stress, L_{ij}, and the resolved strain-rate, S_{ij}. Since it makes use of local flow properties for the determination of C_S, a parallel can be drawn to the algebraic zero-equation models applied in RANS.

The Smagorinksy and the dynamic SGS model are relative limited turbulence formulations, when compared to the sophisticated two-equation approach in RANS. Therefore, if the mesh refinement is inappropriate to capture the flow details, all eddies will be modelled with the SGS stress, and these models can eventually deliver poor predictions in complex flow regions. Besides the interest in simulating the small scale details of the transient flow, this is an additional reason, why LES requires refined meshes and time discretisation.

Moin [105] points out one numerical aspect in the application of LES, affirming that central difference schemes (CDS) are better suited for the simulation with LES than upwind difference schemes (UDS), because they are less susceptible to numerical dissipation.

2.5.2 Detached Eddy Simulation

The detached eddy simulation (DES) was first introduced by Spalart et al.[148] in the one-equation turbulence model proposed by Spalart and Allmaras [146]. In order to switch between the URANS formulation, where the turbulent eddies cannot be resolved, and the LES behaviour, where the grid density is adequate, the definition of the turbulent dissipation, ϵ, is modified, with a limiter for the turbulence length scale, L_T. Strelets [149] incorporates it in the k-ω SST model.

$$\epsilon = \frac{k^{3/2}}{L_T} F_{DES}, \quad F_{DES} = \max\left(\frac{L_T}{C_{DES}\Delta}; 1\right) \tag{2.56}$$

The representative mesh size is chosen to be the greatest cell edge, $\Delta = \max(\Delta_i)$. The constant multiplying it is part of the modelling and is defined as $C_{DES} = 0{,}61$.

In case that the predicted turbulence length scale is greater than the adjusted mesh size, $L_T > C_{DES}\Delta$, it implies that the grid refinement is enough to resolve the eddy

motion and the turbulent dissipation assumes the modified value $\epsilon = k^{3/2}/C_{DES}\Delta$, with the objective to imitate the LES formulation.

If the opposite occurs, i.e. if the turbulence length scale is smaller than the adjusted mesh size, $L_T < C_{DES}\Delta$, the turbulent motion cannot be explicitly solved and has to be modelled as in traditional URANS. The limiter yields the unit value and the dissipation assumes its original value $\epsilon = k^{3/2}/L_T$.

The modified version of the turbulent dissipation is used only in the turbulence kinetic energy transport equation and the turbulent dissipation transport equation remains unmodified.

Even though the DES approach was originally formulated with the dissipation rate, it can be employed with the dissipation frequency, due to their direct relation, $\epsilon = \beta^* k\omega$. The combination of the DES with the k-ω SST turbulence model results in the turbulent equations (2.57) and (2.58).

$$\frac{\partial(\rho k)}{\partial t} + \frac{\partial(\bar{c}_j \rho k)}{\partial x_j} = \tau_{ij}\frac{\partial \bar{c}_i}{\partial x_j} - \beta^* \rho\omega k F_{DES} + \frac{\partial}{\partial x_j}\left[(\mu + \sigma_k \mu_T)\frac{\partial k}{\partial x_j}\right] \tag{2.57}$$

$$\begin{aligned}\frac{\partial(\rho\omega)}{\partial t} + \frac{\partial(\bar{c}_j \rho\omega)}{\partial x_j} = {} & \frac{\gamma}{\nu_T}\tau_{ij}\frac{\partial \bar{c}_i}{\partial x_j} - \beta\rho\omega^2 + \frac{\partial}{\partial x_j}\left[(\mu + \sigma_\omega \mu_T)\frac{\partial \omega}{\partial x_j}\right] \\ & + 2(1 - F_1)\rho\sigma_{\omega_2}\frac{1}{\omega}\frac{\partial k}{\partial x_j}\frac{\partial \omega}{\partial x_j}\end{aligned} \tag{2.58}$$

Depending on the mesh and flow characteristics, there might be the undesired effect, pointed out by Menter and Kuntz [102], of inducing artificial flow separation in the numerical simulation, when the original DES limiter definition is used. They suggest eliminating this problem with the modification of the DES limiter, through the introduction of the SST blending function.

$$F_{DES} = \max\left[\frac{L_T}{C_{DES}\Delta}(1 - F_{SST})\,; 1\right] \tag{2.59}$$

The SST blending function can be chosen to have different definitions. If it is equal to zero, $F_{SST} = 0$, the limiter from Strelets is recovered. Otherwise, it can be equal to the first or the second SST blending functions, i.e. $F_{SST} = F_1$ or $F_{SST} = F_2$.

Spalart et al. [147] recognise this deficiency in their original model and define a new DES limiter, which takes into account not only the mesh characteristics, but also the flow properties. Again it was defined for the Spalart-Allmaras model, but Wunderer and Schilling [171] reformulated it into F_{DES}, for the application with two-equation models.

$$F_{DES} = \left[1 - (1 - F_d)\max\left(1 - \frac{C_{DES}\Delta}{L_T}; 0\right)\right]^{-1} \tag{2.60}$$

$$F_d = \tanh\left[(8r_d)^3\right], \quad r_d = \frac{\nu + \nu_T}{\sqrt{\frac{\partial \bar{c}_i}{\partial x_j}\frac{\partial \bar{c}_i}{\partial x_j}}\kappa^2 d^2} \tag{2.61}$$

After some mathematical manipulation, equation (2.60) can be written in a more familiar and meaningful form:

$$F_{DES} = \max\left[\frac{L_T}{(1 - F_d)\, C_{DES}\Delta + F_d L_T}; 1\right] \tag{2.62}$$

The F_d function is very similar in its form to the SST second blending function, F_2, and is designed to be zero, in LES mode, and one in URANS areas. Therefore, in pure LES, the modified DES limiter recovers the original limiter value, $F_{DES} = L_T/C_{DES}\Delta$, as well as in pure URANS areas, $F_{DES} = 1$. In mixed zones, the adjusted mesh size, $C_{DES}\Delta$, is substituted by its linear combination with the turbulence length scale, L_T, as seen in equation (2.62). This modification delays the switch to the LES mode, trying to avoid the artificial mesh induced fluid separation. Moreover, it causes a sharper transition from URANS to LES, when compared to the Menter and Kuntz [102] model.

As in LES, an additional aspect of the DES is the interpolation scheme adopted in the numerical solving method. In zones, where DES operates as LES, CDS has to be selected, whereas, in URANS dominated zones, high-order UDS is more suitable. This situation shows again the hybrid characteristic of DES. In order to switch between CDS, in LES regions, and high-order UDS, in URANS regions, the interpolation scheme is defined by Travin et al. [155] as a blend of both.

$$\Phi_e = \sigma\Phi_e^{UDS} + (1 - \sigma)\,\Phi_e^{CDS} \tag{2.63}$$

The blending function, σ, is itself defined with help of the function A.

$$\sigma = \sigma_{max}\tanh\left(A^{C_{H_1}}\right), \quad A = C_{H_2}\max\left(\frac{C_{DES}\Delta}{L_{turb}g} - 0{,}5; 0\right) \tag{2.64}$$

The blending function cannot present values greater than one and, for this reason, $\sigma_{max} = 1$. In the expression for the function A, L_{turb} represents a modified version of the turbulence length scale. Nevertheless, it can be approximated by the original turbulence length scale, $L_{turb} = L_T$. The parameter g serves to strength the dominance of high-order UDS in zones, where the flow is nearly irrotational and is defined by:

$$g = \tanh\left(B^4\right), \quad B = C_{H_3}\frac{\Omega \max\left(\Omega; S\right)}{\max\left(\frac{S^2+\Omega^2}{2}; 10^{-20}\right)} \tag{2.65}$$

The constants proposed by TRAVIN ET AL. [155] are chosen as $C_{H_1} = 3$, $C_{H_2} = 1$, and $C_{H_3} = 2$.

The MENTER AND KUNTZ [102] modification to avoid grid induced separation in DES includes one modification to the interpolation scheme blending function as well:

$$\sigma_{SST-DES} = \max\left(\sigma; F_{SST}\right) \tag{2.66}$$

Concerning the application of DES for turbomachines, WUNDERER [170] has successfully simulated one turbine channel, including the guide vane and the runner, at extreme part load, with the DES turbulence model.

2.5.3 Scale Adaptive Simulation

The scale adaptive simulation (SAS) is also a hybrid turbulence model, which can behave like LES or URANS, in order to accurately simulate the dynamic turbulent flow, without additional numeric damping and with a more robust turbulence modelling, in regions where the turbulent eddy motion cannot be solved. Contrary to DES, SAS tries to be mesh-independent and to switch from LES to URANS based on local flow characteristics, rather than on grid properties.

With the objective to develop such a model, MENTER, KUNTZ AND BENDER [101] first started following an idea similar to SPALART ET AL. [148], using a one-equation model for the eddy viscosity transport. They pointed out that the destruction term in the Spalart-Allmaras turbulence model is only significantly active near to the wall boundaries and that, in other regions, it does not avoid the build-up of excessive artificial dissipation. This modelling shortcoming can be avoided with the introduction of a destruction term based on the von Kármán length scale, L_{vK}, allowing the method to operate like LES, depending on the local value of L_{vK}. Although different and sometimes contradictory definitions for L_{vK} can be found, the form finally used for the SAS is:

$$L_{vK} = \kappa\frac{S}{\sqrt{\frac{\partial^2 \bar{c}_i}{\partial x_j^2}\frac{\partial^2 \bar{c}_i}{\partial x_j^2}}} \tag{2.67}$$

Later MENTER AND EGOROV [100] proposed to continue this approach with a formulation based on the k-ω SST model. In reality the von Kármán length scale,

L_{vK}, is first introduced into the k-kL model from ROTTA [129], whose equations can afterwards be transformed into the k-ω SST model. With an alternative modelling of the production terms in the k-kL model, a relation between L_{vK} and the length scale, L, can be found. This is how the von Kármán length scale is placed in the model and the reason to start the derivation with the k-kL model. The use of an alternative variable $\Phi = \sqrt{k}L$, is preferable for the transformation into the k-ω SST equations and the determination of the closure coefficients. The turbulent equations read:

$$\frac{\partial(\rho k)}{\partial t} + \frac{\partial(\bar{c}_j \rho k)}{\partial x_j} = P_k - C_\mu^{3/4}\rho\frac{k^2}{\Phi} + \frac{\partial}{\partial x_j}\left[\left(\mu + \frac{\mu_T}{\sigma_k}\right)\frac{\partial k}{\partial x_j}\right] \tag{2.68}$$

$$\begin{aligned}\frac{\partial(\rho\Phi)}{\partial t} + \frac{\partial(\bar{c}_j \rho\Phi)}{\partial x_j} &= \zeta_1\frac{\Phi}{k}P_k - \zeta_2\mu_T S\sqrt{\frac{\partial^2\bar{c}_i}{\partial x_j^2}\frac{\partial^2\bar{c}_i}{\partial x_j^2}}\frac{\Phi^2}{k^{3/2}} \\ &\quad - \zeta_3\rho k + \frac{\partial}{\partial x_j}\left[\left(\mu + \frac{\mu_T}{\sigma_\Phi}\right)\frac{\partial\Phi}{\partial x_j}\right]\end{aligned} \tag{2.69}$$

The eddy viscosity is determined from the relation between the length scale, the kinematic energy and the dissipation frequency. In this model, the length scale is defined with a modified constant:

$$L = \frac{\sqrt{k}}{C_\mu^{1/4}\omega} \tag{2.70}$$

Since $\Phi = \sqrt{k}L$ and $\nu_T = k/\omega$, the expression for the eddy viscosity can be directly found:

$$\nu_T = C_\mu^{1/4}\Phi \tag{2.71}$$

The ζ coefficients are calibrated with the logarithmic law of the wall and the σ coefficients with a viscid-inviscid interface, being defined as $C_\mu = 0{,}09$, $\kappa = 0{,}41$, $\sigma_k = \sigma_\Phi = 2/3$, $\zeta_1 = 0{,}8$, $\zeta_2 = 3{,}51$ and $\zeta_3 = 0{,}0326$.

In the Φ transport equation, the term containing the second partial derivatives is consequence of the more accurate Taylor expansion of the production term in the equations from ROTTA [129]. It represents a sink term in the Φ transport equation and it can be rewritten, to be explicitly expressed with the von Kármán length scale. Allowing only the independent variables to remain and using the definitions of L_{vK} and ν_T, the term in question becomes:

$$-\zeta_2\mu_T S\sqrt{\frac{\partial^2\bar{c}_i}{\partial x_j^2}\frac{\partial^2\bar{c}_i}{\partial x_j^2}}\frac{\Phi^2}{k^{3/2}} = -\zeta_2\rho C_\mu^{1/4}\kappa S^2\frac{\left(\Phi/\sqrt{k}\right)^3}{L_{vK}} \tag{2.72}$$

In the LES zones, the von Kármán length scale is reduced, causing the sink term to be increased, thus reducing the variable Φ, and, consequently, the eddy viscosity, ν_T. From the theoretical point of view, this approach seems to be effective to achieve the goal of reducing the excessive dissipation in the transient numerical simulations.

The transformation of the Φ into the ω transport equation is similar to the transformation of the ϵ into the ω equation, for obtaining the k-ω SST model, and begins with the substitution of the Φ variable and its first and second partial derivatives by their expressions as functions of k and ω. After some mathematical manipulation, the terms of the k equation can be identified in both sides of the new equation and cancel each other. After some modelling and the constants calibration, the final SAS equations are obtained.

$$\frac{\partial\left(\rho k\right)}{\partial t}+\frac{\partial\left(\bar{c}_j\rho k\right)}{\partial x_j}=\tau_{ij}\frac{\partial\bar{c}_i}{\partial x_j}-\beta^*\rho\omega k+\frac{\partial}{\partial x_j}\left[\left(\mu+\sigma_k\mu_T\right)\frac{\partial k}{\partial x_j}\right] \tag{2.73}$$

$$\begin{aligned}\frac{\partial\left(\rho\omega\right)}{\partial t}+\frac{\partial\left(\bar{c}_j\rho\omega\right)}{\partial x_j}=&\frac{\gamma}{\nu_T}\tau_{ij}\frac{\partial\bar{c}_i}{\partial x_j}-\beta\rho\omega^2+\frac{\partial}{\partial x_j}\left[\left(\mu+\sigma_\omega\mu_T\right)\frac{\partial\omega}{\partial x_j}\right]\\&+2\left(1-F_1\right)\rho\sigma_{\omega_2}\frac{1}{\omega}\frac{\partial k}{\partial x_j}\frac{\partial\omega}{\partial x_j}+F_{SST-SAS}\end{aligned} \tag{2.74}$$

The first four terms on the right-hand side of the dissipation frequency transport equation come from the transformation of the Φ equation. They have their coefficients adjusted to be identical to the k-ω SST model. The additional term, $F_{SST-SAS}$, shall control the switch between LES and URANS and includes L_{vK}.

$$F_{SST-SAS}=F_{SAS}\max\left(T_1-T_2;0\right) \tag{2.75}$$

The constant F_{SAS} is not obtained from the transformation and is introduced to adjust the SAS to the k-ω SST model. The limiter prevents the SAS term to become active in RANS regions. The functions T_1 and T_2 are defined as following:

$$T_1=\tilde{\zeta}_2\rho\kappa S^2\frac{L}{L_{vK}},\quad T_2=\frac{2\rho k}{\sigma_\Phi}\max\left(\frac{1}{\omega^2}\frac{\partial\omega}{\partial x_j}\frac{\partial\omega}{\partial x_j};\frac{1}{k^2}\frac{\partial k}{\partial x_j}\frac{\partial k}{\partial x_j}\right) \tag{2.76}$$

The term T_1 results directly from the transformation of the Φ equation, except for the calibrated constant, $\tilde{\zeta}_2$, and corresponds to the additional sink term in the Φ equation, which limits the eddy viscosity in URANS zones. The first term in the T_2 expression is also the direct result of the transformation, while the second one is an empirical included limiter.

In regions, where URANS should be active, T_1 and T_2 are approximately equal, cancel each other and the SAS model recovers the pure URANS formulation. In

fluid zones, where LES should be active, T_2 is much smaller than T_1, $T_2 \ll T_1$, and the term with the von Kármán length scale is largely dominating.

The last constants for the model closure are given by $F_{SAS} = 1{,}25$, $\tilde{\zeta}_2 = \zeta_2 C_{SAS}$ and $C_{SAS} = 0{,}5$.

The von Kármán term original multiplier, ζ_2, is modified by the constant C_{SAS}, with the objective to control the activation of the SAS term. Smaller values of C_{SAS} causes $F_{SST-SAS}$ to become 0 earlier, recovering the URANS mode, while larger values activate the LES mode earlier.

Finally, to prevent eventual additional numerical dissipations due to the discretisation scheme, the SAS model employs exactly the same approximation as DES for the discretisation of the convective fluxes.

The idea to make SAS grid independent shall be understood in the way that very particular mesh configurations do not adversely affect the numerical solution. After all, the computational grid must be fine enough to resolve the dynamic structures of interest or which might be affecting the flow, otherwise SAS will not alone bring more accuracy to the transient solution. Without problematic meshes, SAS is not necessarily more or less accurate than DES.

Regarding the usage and performance of SAS in practical applications, Benigni et al. [14] simulated a bulb turbine and achieved better results than with URANS, although the total number of computed time steps was excessively small. Wunderer [169] tested the SAS model in a turbine blade cascade with results similar to DES.

2.5.4 Very Large Eddy Simulation

Along the years, other hybrid turbulence models have been developed and sometimes they have been commonly designated very large eddy simulation (VLES). They achieved variable grade of success. However, with the popularisation of DES and SAS, their application is limited.

One of the VLES models, which deserves some attention in the simulation of hydraulic turbines was presented by Ruprecht et al. [130], as long as it was employed in the prediction of vortices in the turbine draft tube cone. The model in question makes use of the k-ϵ model from Chen and Kim [25], which has an additional production term in the dissipation transport equation. This VLES model introduces a limiter for the kinetic energy production term and for the eddy viscosity, which is, as in DES, based on the grid size and the turbulent length scale.

Although the calculated pressure pulsations were excessively damped downstream from the draft tube cone, the model prediction proved to be enough accurate in the cone region itself, when compared to experimental results. Due to its excessive

diffusion and no further development, this model was overran, as many others, by DES and SAS. Nevertheless, it is among the first applications of hybrid turbulence models to predict transient flows in hydraulic turbines.

2.6 Rotating Systems

One of the important characteristics of the fluid flow problem in turbomachines is the runner rotational motion. In an inertial reference system, the fluid flow through the runner always appears to be transient, even if the dynamic effects are neglected. This is due to the relative motion of the runner, which is reflected in the kinematic relations. However, in a non-inertial reference system attached to the runner centre and ignoring the dynamic phenomena, the flow through the runner is observed as stationary. This characteristic shall be used to avoid the appearance of additional transient terms in the basic equations*.

The runner movement is purely rotational, so that the absolute fluid velocity vector, in an inertial reference frame, $\mathbf{c}$, can be described by the sum of its relative velocity, in the runner reference frame, $\mathbf{w}$, and the frame transport velocity, $\mathbf{u}$, induced by the runner angular velocity vector, $\boldsymbol{\Omega}$.

$$\mathbf{c} = \mathbf{w} + \mathbf{u} = \mathbf{w} + \boldsymbol{\Omega} \times \mathbf{r} \tag{2.77}$$

The vector $\mathbf{r}$ corresponds to the fluid position in relation to the runner centre in the rotating reference frame. The angular velocity vector, $\boldsymbol{\Omega}$, is considered constant, leading to the following expression for the acceleration vector, $\mathbf{a}$:

$$\mathbf{a} = \mathbf{a}_{rel} + \mathbf{a}_c + \mathbf{a}_z, \quad \mathbf{a}_c = 2\boldsymbol{\Omega} \times \mathbf{w}, \quad \mathbf{a}_z = \boldsymbol{\Omega} \times (\boldsymbol{\Omega} \times \mathbf{r}) \tag{2.78}$$

The absolute acceleration, in the stationary reference frame, is compounded by the relative acceleration, in the rotating frame, $\mathbf{a}_{rel}$, the Coriolis acceleration, $\mathbf{a}_c$, and the centripetal acceleration, $\mathbf{a}_z$. In the runner non-inertial reference frame, $\mathbf{a}_c$ and $\mathbf{a}_z$ are responsible for the appearance of the inertial forces. If the fluid basic equations are written in terms of the relative velocity, w_i, the inertial forces must be considered in the source term of the moment equation, as done by Truckenbrodt [156].

$$\frac{\partial \rho}{\partial t} + \frac{\partial (\rho w_i)}{\partial x_i} = 0 \tag{2.79}$$

$$\frac{\partial (\rho w_i)}{\partial t} + \frac{\partial (w_j \rho w_i)}{\partial x_j} = -\frac{\partial p}{\partial x_i} + \frac{\partial}{\partial x_j} (t_{ij} + \tau_{ij}) + S_i^{rot} \tag{2.80}$$

* The Reynolds- and Favré-average overhead symbols, $\bar{}$ and $\tilde{}$, are omitted, since the equations are valid for both incompressible and compressible flows.

The additional source term, S_i^{rot}, coming from the runner rotational movement, presents the following expression:

$$\mathbf{S}^{rot} = \rho \begin{pmatrix} \Omega_x^2 & \Omega_y^2 & 0 \end{pmatrix}^{\mathbf{T}} + 2\rho \begin{pmatrix} \Omega w_y & -\Omega w_x & 0 \end{pmatrix}^{\mathbf{T}} \tag{2.81}$$

Even in the rotational reference frame, it is simpler to deal with the transport of the absolute velocity, c_i, instead of w_i, as observed by Kroll [76]. With this purpose, the half of the inertial force coming from the Coriolis acceleration and the complete inertial force arising from the centripetal acceleration are combined in the left side of the moment equation, resulting in:

$$\frac{\partial \rho}{\partial t} + \frac{\partial \left(\rho c_i\right)}{\partial x_i} = 0 \tag{2.82}$$

$$\frac{\partial \left(\rho c_i\right)}{\partial t} + \frac{\partial \left(w_j \rho c_i\right)}{\partial x_j} = -\frac{\partial p}{\partial x_i} + \frac{\partial}{\partial x_j}\left(t_{ij} + \tau_{ij}\right) + S_i^{mod} \tag{2.83}$$

Where the new source term, S_i^{mod}, is changed to adapt to the modifications on the left hand side of the equation.

$$\mathbf{S}^{mod} = \begin{pmatrix} \Omega c_y & -\Omega c_x & 0 \end{pmatrix}^{\mathbf{T}} \tag{2.84}$$

The advantage of this procedure is to maintain the absolute velocity, c_i, as unknown in the basic equations both in stationary or rotating grids, while only the equation coefficients have to be modified for the runner, during the numeric solution.

When the reference frame is changed, the energy reference is modified as well. Therefore, the energy conservation equation has also to be adjusted to consider the rotating reference system.

$$\begin{aligned} \frac{\partial \left(\rho e_t^{rel}\right)}{\partial t} + \frac{\partial \left(w_j \rho h_t^{rel}\right)}{\partial x_j} = & \frac{\partial}{\partial x_j}\left[\left(\frac{\mu}{Pr} + \frac{\mu_T}{Pr_T}\right)\frac{\partial h}{\partial x_j}\right] \\ & + \frac{\partial}{\partial x_j}\left[w_i\left(t_{ij} + \tau_{ij}\right)\right] \end{aligned} \tag{2.85}$$

The relative total specific energy and enthalpy, in the rotating frame, e_t^{rel} and h_t^{rel}, count with the additional term $u_i u_i$, which can be moved to the source term and explicitly handled during the numeric solution, in order to preserve the same unknowns in stationary and rotating meshes.

$$e_t^{rel} = e_t - u_i u_i, \quad h_t^{rel} = h_t - u_i u_i \tag{2.86}$$

Chapter 3

Finite Volume Method in Fluid Dynamics

The basic equations, which reproduce the fluid motion, have analytical solutions only for simple problems, with trivial geometry and limited practical application. Therefore, they must be discretised to allow their computational solution for arbitrary geometries and flow patterns. The currently most adopted method for fluid problems is the finite volume method (FVM). It has proven to be well adapted to the non-linearities of the basic equations and very efficient numerically.

In the FVM, the discretisation of the fluid domain in small volumes (cells) and the numerical approximation of the individual terms in the basic equations lead to a set of algebraic equations, where the velocity components, the pressure and the specific energy in each cell are the unknowns. The numerical advantages of this method are the existence of numerous algorithms, which can efficiently solve the matricial problem resulting from the algebraic equations set, and its simplicity to evaluate the matrix components, which have to be repeatedly calculated, due to the non-linear characteristic of the basic equations. From the theoretical point of view, the main advantage of this method is to be conservative in regard to the transport fluxes.

The CFD code NS3D developed by the FLM at the TUM employs the FVM, as well as the commercial codes ANSYS, Fluent and StarCD and the open source code OpenFOAM.

3.1 Finite Volume Discretisation

3.1.1 Integral form of the basic equations

For the mathematical formulation of the FVM, the transport equation is written in its general form, using the general variable Φ to represent the variable field to be

solved. For the mass conservation law, it assumes the unitary value, in the case of the momentum conservation law, it is substituted by the velocity, c_i, and for the energy conservation, it corresponds to the specific energy, e.

$$\frac{\partial(\rho\Phi)}{\partial t} + \frac{\partial(c_j\rho\Phi)}{\partial x_j} = \frac{\partial}{\partial x_j}\left(\Gamma\frac{\partial\Phi}{\partial x_j}\right) + q \tag{3.1}$$

The first term represents the variation in relation to time, the second is the convective transport term, the third the diffusive transport term and the last the source term. The complete equation can be integrated in the fluid volume and the Gauß theorem can be applied to the convective and to the diffusive terms to express them with area integrals.

$$\int_V \frac{\partial(\rho\Phi)}{\partial t}dV + \int_A c_j\rho\Phi n_j dA = \int_A \Gamma\frac{\partial\Phi}{\partial x_j}n_j dA + \int_V q dV \tag{3.2}$$

For the numerical development of the FVM, the terms must be discretised in space and time and the values of the variable Φ at each cell centre become the unknowns of the problem. The numerical schemes involved in the discretisations must confer acceptable precision to the method. The approximation employed for the discretisation of each term is explained separately.

3.1.2 Control volume

The physical domain, where the fluid flow takes place, e.g. blading channel, corresponds to the physical control volume, which is used for balancing and to represent the flow. Due to its numerical nature, the FVM requires the volume to be spatially discretised in small volume cells, which of them constitutes a single small control volume, where the conservation laws have to be respected. This leads to the conservative nature of the FVM.

The discretised volume cells can be represented by the control volume in Figure 3.1. The point P is located at the cell centre of the control volume being considered. In structured grids, the points W, E, N and S correspond to the centre points of the neighbouring cells and make reference to cardinal directions, i.e. west, east, north and south. For three dimensional geometries, there are two additional cells, denoted as bottom and top and whose centres are the points B and T. The control volume bounding faces are denoted by the small letters e, w, n, s, b and t and they are used for the balancing of the transported scalar and vectorial quantities. The vector $\mathbf{n}$ is the face normal vector and $\boldsymbol{\xi}$ represents the direction vector between the point P and one of its neighbouring points. In the case of structured meshes, the grid directions i, j and k are defined and are sufficient to locate any of the grid cells.

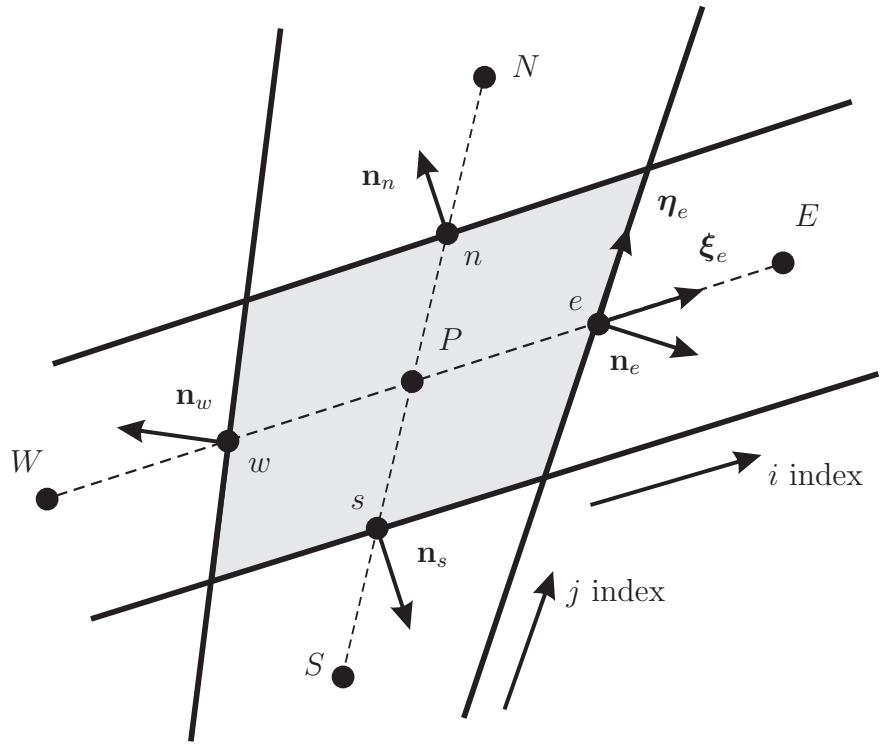

Figure 3.1: Typical control volume used in the FVM and its notation convention.

In the collocated variable system, the values of the quantity being transported, Φ, is calculated at the centre of each cell and they become the unknowns of the numerical problem. The variable values at the cell faces, for the determination of the transport flows, are obtained through interpolation and constitute an important topic in the discretisation of the basic equations, as it will be further seen.

3.1.3 Algebraic System

After the discretisation of the physical volume and of the transport equations, the algebraic equation below can be written for each cell.

$$A_P^{\Phi}\Phi_P + \sum_l A_l^{\Phi}\Phi_l = Q_P^{\Phi} \tag{3.3}$$

For structured grids, the variable value at each cell, Φ_P, is coupled only to its neighbours, Φ_l, in the algebraic equation system and results in a sparse banded matrix structure.

It must be observed, that the transport equations are non-linear and the mass flows depend on the velocity components, which are unknowns of the system as well. It means that the coefficients A_P and A_l, in the algebraic system, have to be updated

along the solution, with the values of the velocity components and density, in the case of compressible flows.

The solver iterations carried out with constant coefficients A_P and A_l are called inner iterations and the iterations, which update them are the outer iterations. The procedure used for solving the discretised equations will be commented in more detail further on.

3.1.4 Numerical Approximations

For the numerical calculation of the terms in the transport equation, the analytical integral relations have to be approximated by algebraic expressions. The mean value theorem for integrals states that a function value exists in the integration domain, which multiplied by the domain extension equals the exact integration result. This function value is in principle not known and is approximated in the FVM by the function value at the face centre, for area integrals. The expression for the area integral is:

$$F_e = \int_{A_e} f dA = \bar{f} A_e \approx f_e A_e \tag{3.4}$$

This approximation is also known as the midpoint rule and is second-order accurate. In the FVM with collocated variables, they are stored at the cell centre and its value at the face centre has to be calculated. To assure the second-order accuracy of the midpoint rule for the area integrals, the approximation used for determining the variables value at the face centre must also be second-order accurate.

The volume integral approximation is totally analogous to the area integral and the second-order precision is achieved by taking the function value at the cell centre. The volume integral is estimated by:

$$Q_P = \int_V q dV = \bar{q} \Delta V \approx q_P \Delta V \tag{3.5}$$

The source terms are explicitly handled and are directly calculated with this approximation. It means that, for the source term, the transported variable is not treated as unknown and its value is taken from the previous iteration. The explicit term is added to the independent vector in the matricial problem.

The gradients are also present in the transport equations and need to be numerically evaluated as well. Through the integration of the gradient in the cell volume and the application of the Gauß theorem, followed by the approximation of the integrals with the midpoint rule, the gradient at the cell centre, P, is estimated by:

$$\left(\frac{\partial \Phi}{\partial x_j}\right)_P \approx \frac{\sum_l \Phi_l n_{j,l} A_l}{\Delta V}, \quad l = w, e, s, n, b, t \tag{3.6}$$

3.1.5 Diffusive Flux Discretisation

The discretisation of the flux terms in the transport equation constitute an important element for the overall accuracy of the FVM and is not as trivial as it might appear. The second-order accuracy of the midpoint rule for the integrals evaluation depends on the precision of the flux terms discretisation.

The diffusive flux, in the east face, for example, is approximated with the use of the midpoint rule by:

$$F_e^d = \int_{A_e} \Gamma \frac{\partial \Phi}{\partial x_j} n_j dA \approx \Gamma_e \left(\frac{\partial \Phi}{\partial x_j}\right)_e n_{j,e} A_e \tag{3.7}$$

Using the derivative in relation to the face normal direction, the previous expression is equivalent to:

$$F_e^d = \Gamma_e \left(\frac{\partial \Phi}{\partial n}\right)_e A_e \tag{3.8}$$

In Cartesian grids, the normal face direction is aligned with one coordinate axis and the most evident approximation at the face centre is the central difference scheme (CDS). In this very particular case, it is no more than the linear interpolation from the cell centre values of the neighbouring cells. This interpolating scheme is second-order accurate and suitable for the diffusive fluxes, from the numerical point of view.

$$\left(\frac{\partial \Phi}{\partial n}\right)_e \approx \frac{\Phi_E - \Phi_P}{\Delta x} \tag{3.9}$$

In the general case, where arbitrary meshes are employed, the normal direction at the cell faces is not necessarily aligned with one coordinate axis and the normal derivative cannot be readily calculated with CDS. In this situation, the derivatives have to be determined from the gradient approximation in equation (3.6) and interpolated to the face centre.

Muzaferija [108] pointed out that this procedure can lead to oscillatory solution fields, possibly causing the solution convergence and precision to be severely deteriorated. His solution to eliminate the problem consists of a CDS estimation and a deferred correction involving the gradient approximation.

In opposition to the normal derivative in arbitrary meshes, the diffusive flux in the direction of the straight line connecting any two neighbour points, e.g. P and E, can be directly evaluated with CDS:

$$F_e^d = \Gamma_e \left(\frac{\partial \Phi}{\partial \xi}\right)_e A_e = \Gamma_e A_e \frac{\Phi_E - \Phi_P}{|\mathbf{x_E} - \mathbf{x_P}|} \tag{3.10}$$

The direction given by ξ is not the same from n, so the diffusive flux calculated in this manner is not the same as the one through the east face. The error introduced by the direction deviation is compensated with the deferred correction with the gradient approximation:

$$F_e^d = \Gamma_e A_e \left(\frac{\partial \Phi}{\partial \xi}\right)_e^n + \Gamma_e A_e \left[\overline{\left(\frac{\partial \Phi}{\partial n}\right)}_e - \overline{\left(\frac{\partial \Phi}{\partial \xi}\right)}_e\right]^{n-1} \tag{3.11}$$

The overline symbol in the previous equation denotes the calculation with the gradient approximation, in contrast to the normal CDS from equation (3.9). The superscript $n-1$ refers to the values from the previous iteration, which are treated explicitly. It can be verified that, when the convergence is achieved, the first and last terms cancel each other and the midpoint rule approximation for the diffusive flux, e.g. at the east face, is obtained.

When the grid is nearly orthogonal, the deferred correction is not significant, when compared to the implicit term and the convergence is not negatively impacted. The opposite effect can occur in high-skewed meshes. From this point of view, the mesh orthogonality is an important quality factor for arbitrary computational grids.

The diffusive term in the transport equation has a particularity in the case of the Navier-Stokes equations. The viscous stresses are proportional to the strain tensor, S_{ij} and in the turbulence models used here, the Reynolds stress tensor is modelled with the Boussinesq approximation, implying that this term is also a function of the strain tensor. The two terms of the strain tensor are separated in the evaluation of the integral:

$$F_e^d = \int_{A_e} \mu \frac{\partial c_i}{\partial x_j} n_j dA + \int_{A_e} \mu \frac{\partial c_j}{\partial x_i} n_j dA \tag{3.12}$$

The first term is treated implicitly, employing the diffusive flux discretisation, while the second term is calculated explicitly, as part of the source term, since it does not figure out as part of the diffusive flux in the general form of the transport equation.

3.1.6 Convective Flux Discretisation

The convective flux in the transport equation is calculated with the area integral approximation. For the east face, for example, the convective flux is numerically given by:

$$F_e^c = \int_{A_e} c_j \rho \Phi n_j dA \approx \dot{m}_e \Phi_e \tag{3.13}$$

The mass flux through the cell face, $\dot{m}$, is evaluated with the velocity components from the previous iteration, i.e. they are not treated as unknowns and this approach serves to linearise the equation system to a pure algebraic problem, so that it can be solved in the matricial form.

$$\dot{m}_e = (\rho c_j n_j A)_e \tag{3.14}$$

As long as the variable values are stored at the cell centre, an interpolation scheme is again needed to determine the values at the face centre. The most simple interpolation scheme for the convective flux is the upwind difference scheme (UDS). UDS guarantees the boundness of the solution and provides high stability to the solution convergence. Still, it is only first-order accurate and, as shown by Patankar [117], it creates excessive numerical diffusion, which sometimes might even be greater than the real diffusion. This significant lack of precision makes UDS unsuitable for most of the numerical simulations.

CDS could be a solution. However, CDS poses another problem for the convective fluxes. When the cell Peclet number is greater or equal to 2, $Pe = \rho u \Delta x / \Gamma \geq 2$, which is a common condition in practical applications, CDS might produce oscillatory solutions, affecting the solution convergence and accuracy.

To overcome the limitations from UDS and CDS, many interpolation methods have been developed. One of them is the quadratic upwind interpolation (QUICK) from Leonard [82], but which does not offer significant advantages over CDS. Other high-order upwind schemes have been developed and count with numerical limiters to avoid oscillations and poor convergence. Skoda [142] brings the summary of some of the popular high-order schemes like SMART, from Gaskell and Lau [50], MINMOD, from Harten [62] and OSHER, from Chakravarthy and Osher [23].

These high-order interpolation schemes involve more neighbour cells and, although they offer acceptable convergence, they are not as robust as UDS. To reduce the number of unknowns in the algebraic system and to improve the convergence behaviour, the deferred correction is used with the high-order schemes.

$$\Phi_e^n = \left(\Phi_e^{UDS}\right)^n + \gamma \left(\Phi_e^{HOS} - \Phi_e^{UDS}\right)^{n-1} \tag{3.15}$$

The high-order approximation is calculated from the previous iteration, $n-1$, while the coefficient matrix for the algebraic equation system has the same form as it would have with UDS. The solution process starts with small values for γ and, as convergence is approached, γ takes higher values. When $\gamma = 1$ and the convergence is reached, the UDS terms cancel each order and only the high-order approximation remains.

As already explained in the fluid theory, for the hybrid turbulence models employed here, i.e. DES and SAS, the convective flux is evaluated with the blend of CDS and high-order upwind schemes, in order to eliminate any possibility of numerical dissipation in LES mode.

$$\Phi_e = \sigma \Phi_e^{HOS} + (1 - \sigma)\, \Phi_e^{CDS} \tag{3.16}$$

Where the blending function, σ, comes from the turbulence modelling.

3.1.7 Instationary Terms Discretisation

The transient term in the transport equation needs to be discretised in relation to the time to allow its numerical computation as well. The second-order implicit Euler method was chosen to be used here. It is second-order accurate, as long as it takes information from the previous two time steps for the current time step discretisation. Considering a parabola in relation to the time, passing by the variable value in the current and previous two time steps, the volume integral of the instationary term can be approached with:

$$\int_V \frac{\partial (\rho\Phi)}{\partial t} dV \approx \frac{3 (\rho\Phi_P)^m - 4 (\rho\Phi_P)^{m-1} + (\rho\Phi_P)^{m-2}}{2\Delta t} \Delta V \tag{3.17}$$

The superscripts m, $m-1$ and $m-2$ correspond to the current and to the two previous time steps.

The method is fully implicit, since the values of the transport variable, used in all the other terms, i.e. convection, diffusion and source terms, is Φ^m and refers to the time step being currently solved. The terms in Φ^{m-1} and Φ^{m-2} are added to the independent vector in the matricial equation.

3.2 Boundary Conditions

For the solution of the mathematical system, boundary conditions have to be specified at the borders of the flow domain and they must reflect the physical

conditions at the boundaries. The boundary conditions can be set, imposing the values of the variables at the boundary faces, these are the so called Dirichlet boundary conditions. The boundary conditions can also be specified, fixing the gradients at the boundary faces, these are Neumann boundary conditions.

The types of boundary conditions in the FVM are, basically, inlet, outlet, walls, symmetry and periodicity. In a computational domain composed by several independent structured cell blocks, the boundary conditions at the interface faces between them are set, ensuring the conservation of the scalar and vectorial fluxes. There are different possible combinations for the boundary conditions, the most common and numerically stable set, which was also employed for the turbine simulations, is described below.

3.2.1 Inlet

The values of the velocity components, c_i, at the inlet faces are usually given. They can be derived from the total volumetric flow, Q, and the inlet flow direction, or from a known inlet velocity profile.

For incompressible flows, the gradients of the pressure, p, and of the pressure correction, p', are taken as constant at the domain inlet. For the FVM numerical implementation, it means that the values of the pressure and pressure correction are extrapolated from the interior of the fluid domain to the boundaries.

In the case of compressible subsonic flows, the pressure gradient is also imposed, while the pressure correction, as proposed by Ferziger and Perić [43], is given by $c'_{i,in} = c_{c_i} p'_{in}$. For supersonic flows, the pressure is specified at the inlet with Dirichlet instead of Neumann boundary conditions and, since its value is explicitly specified, the pressure correction becomes zero.

In the case of compressible flows, where the internal energy transport equation also has to be solved, the value of the temperature, T, at the inlet cell faces has to be given.

The value of the kinetic energy, k, is normally prescribed at the inlet face based on the turbulence intensity, Tu. Typical values for Tu are between 1% and 20%. They are known from experiments or, alternatively, its influence on the numerical simulation is tested. In flow simulations with long inlet sections or with turbulence triggering geometry, its effect is rather negligible.

$$k_{in} = \frac{3}{2} Tu^2 c_{in}^2 \tag{3.18}$$

The values of the turbulent dissipation, ϵ, are fixed, using an estimation based on the kinetic energy and on a characteristic length, $L_{char,\epsilon}$. This length is specific for

each flow and problem. As in the case of the kinetic energy, the value of $L_{char,\epsilon}$ must come from experiments or must be tested. Its effect on the numerical results is similar to the influence of k.

$$\epsilon_{in} = \frac{k_{in}^{3/2}}{L_{char,\epsilon}} \tag{3.19}$$

In the case of turbulence models derived from k-ω, the values from the turbulent dissipation frequency, ω, can be computed from ϵ, through the usual relation $\omega = \beta^* \epsilon / k$.

3.2.2 Outlet

The components of the velocity distribution at the fluid domain outlet make also part of the problem unknowns. Therefore, at the outlet a constant velocity gradient is imposed, leading to the extrapolation of the values in the domain interior to the boundaries.

$$c_{i,out} = c_{i,P} + \lambda_{out} \left(c_{i,P} - c_{i,Q} \right) \tag{3.20}$$

The index Q makes reference to the centre point of the cell neighbouring the boundary cell, whose centre is P. The parameter λ_{out} is the extrapolation factor and is derived from the distance between the cell centres and the boundary.

$$\lambda_{out} = \frac{|\mathbf{x_{pq}} - \mathbf{x_P}|}{|\mathbf{x_Q} - \mathbf{x_{pq}}| + |\mathbf{x_{pq}} - \mathbf{x_P}|} \tag{3.21}$$

For subsonic flows, the pressure at the outlet boundary is imposed constant and the pressure correction is set to zero, $p' = 0$. The pressure level in the individual boundary cells can be set equal to p_{const} or the pressure surface averaged at the outlet boundary, p_{PQ}, can be fixed. The blending of these both conditions is also possible, with the blending parameter α_P.

$$p_{out} = \alpha_P p_{PQ} + (1 - \alpha_P) \, p_{const} \tag{3.22}$$

In the case of supersonic flows, the pressure value at the outlet is also part of the solution and, therefore, is extrapolated from the domain interior values, corresponding once again to the constant gradient boundary condition.

In compressible flows, when the temperature is also calculated, the Neumann boundary condition is set for it at the outlet boundary. In the numerical implementation, the value extrapolation is used again.

At the outlet boundary, the gradients of the turbulence quantities, k and ϵ or ω, are constant. It means, their values are extrapolated from the domain interior.

3.2.3 Wall

In this study, only impermeable walls are considered. Therefore, there is no mass flow in the wall normal direction and the convective flux at the wall face disappears. Here, the diffusive flux assures the momentum conservation. The wall face of the cell is referred to as w.

Due to the no-slip condition at the wall, the velocity components are equal to the prescribed wall velocity, $c_i = c_{i,w}$. For the solution of the momentum equations at the wall cells, the diffusive flux is determined with the shear stress at the wall, τ_w, and its direction. The derivation of the diffusive flux makes use of the wall local coordinate system, (n, t, b), where n corresponds to the direction normal to the wall, t to the flow direction in the cell centre point, P, and b completes the orthogonal system, being normal to the n and t directions. The typical wall cell, as well as the coordinates and velocity components, can be seen in Figure 3.2.

The shear stress at the wall is calculated with the velocity partial derivatives. With the local coordinate system aligned to the flow direction, the shear stress components can be directly evaluated. It is different from zero only in the flow direction, t.

$$\tau_{nn} = 2\mu \frac{\partial c_n}{\partial n} = 0, \quad \tau_{nt} = \mu \frac{\partial c_t}{\partial n}, \quad \tau_{nb} = \mu \frac{\partial c_b}{\partial n} = 0 \tag{3.23}$$

The normal vector, n_i, is known from the problem geometry, while the tangential vector, t_i, is only determined by the flow. In the third vector direction, b_i, no flow takes places, $c_{b,P} = 0$. The normal velocity component, $c_{n,P}$, is calculated with the scalar product $c_{i,P}\ n_i$. The tangential velocity vector, $c_{i,t,P}$, is obtained from the difference between the velocity vector, $c_{i,P}$, and the normal velocity vector, $c_{i,n,P}$.

$$c_{i,t,P} = c_{i,P} - c_{i,n,P} = c_{i,P} - (c_{j,P}\ n_j)\, n_i \tag{3.24}$$

From the tangential velocity vector, $c_{i,t,P}$, the tangential direction vector, t_i, is readily evaluated by:

$$t_i = \frac{c_{i,t,P}}{|c_{i,t,P}|} \tag{3.25}$$

The diffusive flux at the wall face, $F^d_{i,w}$, is calculated with the shear stress in the flow direction and the integral is approximated, as usual, by the midpoint rule:

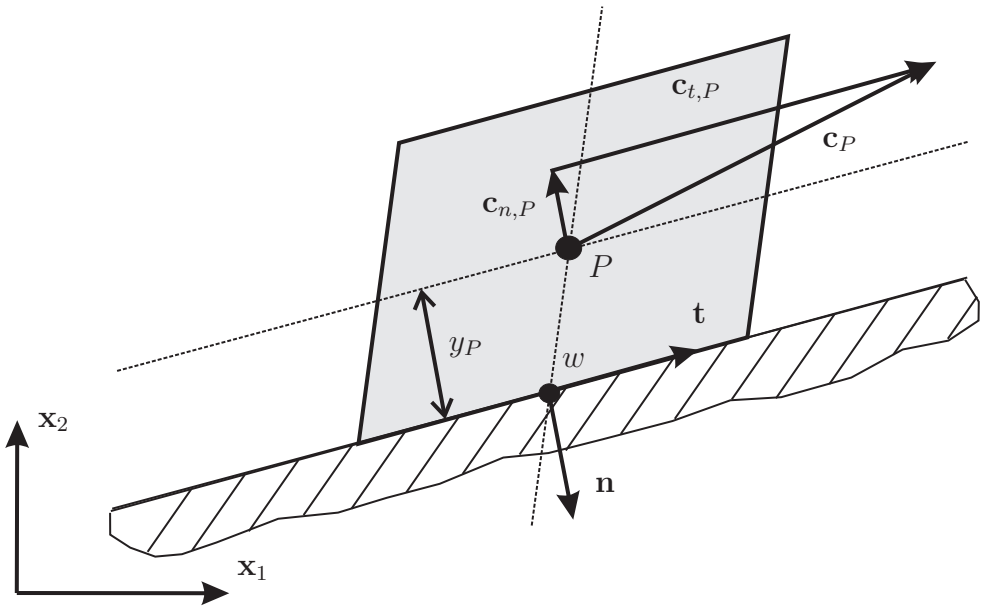

Figure 3.2: Typical control volume at a wall boundary.

$$F_{i,w}^d = \int_{A_w} \tau_{nt} t_i dA \approx \tau_{nt} t_i A_w \tag{3.26}$$

From the definition of the shear stress in the flow direction, involving the partial derivative $\partial c_t / \partial n$, its value, τ_{nt}, can be approximated with the cell centre velocity, $c_{i,P}$, the wall velocity, $c_{i,w}$, and the distance y_P between the point P and the wall.

$$\tau_{nt} \approx \mu \frac{(c_{i,P} - c_{i,w})\, t_i}{y_P} \tag{3.27}$$

In the numerical implementation of the FVM, the diffusive flux at the wall, $F_{i,w}^d$, is computed with a deferred correction, with the shear stress from the previous iteration, $n-1$, in order to keep the matrix diagonal coefficients $A_P^{c_i}$ the same for all cells. The deferred correction is added to the source term.

$$F_{i,w}^d \approx \left(c_i \frac{A_w}{y_P} \right)^n + \left[-c_i \frac{A_w}{y_P} + \mu \frac{(c_{j,P} - c_{j,w})\, t_j}{y_P} t_i A_w \right]^{n-1} \tag{3.28}$$

At the wall, Neumann boundary conditions are imposed for the pressure, as well as for the pressure correction term, leading to the extrapolation from the domain interior.

The wall temperature, T_w, can be fixed or the value of its derivative can be imposed, which is equivalent to specify the wall heat flux, $q_w = -\lambda \left(\partial T / \partial n \right)_w$.

At the wall, the turbulent kinetic energy as well as its derivative assume the zero value, leading to the Dirichlet, $k_w = 0$, and Neumann, $(\partial k/\partial n)_w = 0$, boundary conditions.

For turbulence models based on the k and ϵ transport equations, the value of the turbulent dissipations is fixed at the wall boundary, with the approximation suggested by Chapman and Kuhn [24].

$$\epsilon_w^{k-\epsilon} = \nu \frac{4k_P}{y_P^2} - \epsilon_P \tag{3.29}$$

In the case of turbulence models, which make use of the k and ω transport equations, the asymptotic behaviour of the relation $\omega = \beta^* \epsilon / k$ for $k_w = 0$ leads to $\omega_w \to \infty$. This boundary condition cannot be numerically implemented and, to overcome this issue, Menter [99] proposes the following limiter for the turbulent dissipation frequency at the wall boundary:

$$\omega_w = \alpha_{\omega_w} \frac{6\nu}{\beta y_P^2} \tag{3.30}$$

In this expression, Menter [99] recommends to choose $\alpha_{\omega_w} = 10$.

When the grid density near to wall is fine enough and adequate turbulence models are employed, the boundary layer can be numerically solved up to the wall. Nevertheless, due to the required mesh density to accurately and fully describe the boundary layer, the wall function is commonly used to model the turbulence in the cells adjacent to the wall boundary. This modelling is taken into account in the numerical computations, through the introduction of the dynamic viscosity at the wall face, μ_w, from the wall function.

From the numerical approximation of the shear stress at the wall, τ_{nt}, the dynamic viscosity can be expressed as:

$$\mu_w = \frac{y_P}{(c_{i,P} - c_{i,w})\, t_i} \tau_{nt} \tag{3.31}$$

In the cells at the wall boundary, the theoretical wall shear stress, τ_w, can be approximated by the numerical calculated shear stress, τ_{nt}, the tangential velocity, u_t, by $c_{t,P}$ and the wall distance, y, by y_P. With these approximations, substituting τ_{nt} by the definition $\tau_w = \rho u_\tau^2$ in the equation above and remembering the definitions of $u^+ = u_t/u_\tau$ and $y^+ = \rho u_\tau y/\mu$, the following expression for the numerical wall viscosity is obtained after some algebraic manipulation:

$$\mu_w = \mu \frac{y^+}{u^+} \tag{3.32}$$

In the logarithmic region of the boundary layer, the classical law of the wall can be used to evaluate the value of u^+ in the previous equation:

$$u^+ = \frac{1}{\kappa} \ln y^+ + C \tag{3.33}$$

Still, the value of y^+ needs to be calculated. However, it involves the friction velocity, u_τ, which is not explicitly known. FERZIGER AND PERIĆ [43] suggest approximating the friction velocity, in the numerical simulations using wall functions, by:

$$u_\tau = C_\mu^{1/4} k^{1/2} \tag{3.34}$$

With this approximation, y^+ can be evaluated, as well as u^+ with the law of the wall and, finally, the wall dynamic viscosity, μ_w, for the determination of the diffusive flux at the wall face in the momentum equations.

The application of the wall function to the wall cells, assumes that the first mesh point is inside the logarithmic region of the boundary layer, otherwise, the approximation is not valid. In some problems with turbulence scales of different magnitude and for which limited know-how about the flow is available, it might be difficult to achieve the requirements for the y^+ values. In such cases, it may be necessary to generate successive meshes, until the logarithmic condition is satisfied, or to employ modified versions of the wall function, as done e.g. by VIESER, ESCH AND MENTER [161], where the law of the wall is blended with the analytic expression of ω, near to the wall, for k-ω based turbulence models.

3.2.4 Free Slip Wall

The free slip wall is usually also referred to as Euler wall or symmetry boundary condition. It is impermeable, like the no-slip wall, but the flow can freely slip at its surface without any friction stress at the wall boundary. Again there is no mass flux across the wall and the diffusive flux accounts for the momentum conservation. Using the same coordinate system, as for the no-slip wall, the shear stresses can be derived:

$$\tau_{nn} = 2\mu \frac{\partial w_n}{\partial n}, \quad \tau_{nt} = \mu \frac{\partial w_t}{\partial n} = 0, \quad \tau_{nb} = \mu \frac{\partial w_b}{\partial n} = 0 \tag{3.35}$$

Proceeding in the same manner as before, as in the case of the no-slip wall, and again introducing the deferred correction, the diffusive flux at the free slip wall becomes:

$$F_{i,w}^d \approx \left(c_i \frac{A_w}{y_P} \right)^n + \left[-c_i \frac{A_w}{y_P} + 2\mu \frac{(c_{j,P} - c_{j,W})\, n_j}{y_P} n_i A_w \right]^{n-1} \tag{3.36}$$

The free slip wall normally constitutes a simplification of physical aspects of the fluid flow. Nevertheless, it can sometimes be useful to solve modelling difficulties, regarding the real problem.

3.2.5 Block Interface

When the problem being analysed involves the fluid flow through domains with different topology, through stationary and rotating components or through parts, for which different mesh strategies are desired, it might occur that the position of grid nodes at both sides of the block interfaces do not exactly match. This condition is also known as non-matching interfaces.

Taking the turbomachines as example, non-matching interfaces can take place at the interface between the spiral case and the stay vanes or between the runner and the draft tube, as long as different mesh strategies or grid densities are usually employed for each one of these components. Staying by the turbomachines, non-matching interfaces are also common at the interface between the guide vanes and the runner, because of their relative motion, different blocking, grid density and periodicity.

Figure 3.3 shows the typical example of non-matching interfaces between two structured grids. The numerical procedure, suggested by Lilek et al. [87] and implemented among others by Riedel [123], consists in dividing the interface faces into subfaces, defined by the intersection of the interface faces of one block with the edges of the other non-matching block, and calculating the fluxes conservation with these subfaces.

For example, taking the boundary cell of the left block, A, whose centre point is L, its west face is subdivided into the subfaces $l-1$, l and $l+1$, which are obtained from the intersection with the edges of the right block, B, boundary cells. The total flux through the west face is computed with the subfaces $l-1$, l and $l+1$. For higher order interpolating schemes, the interior cells, with point centres LL and RR, must also be taken into account for the computation of elements of the system matrix A.

3.2.6 Periodic Boundary Conditions

In several problems, there are geometrical patterns that are repeated in the computational domain. This characteristic is described as spatial periodicity. The classical example in turbomachines is the blading channel. Normally, all blade channels have the same geometry and they are rotational periodic. Mainly in stationary simulations, the numerical model counts with the simplification that the flow is also periodic, due to the recurring geometry, and only one single periodic part of the geometry is simulated. This simplification spares computational resources and, in the case of stationary and homogeneous flows, delivers quite acceptable results.

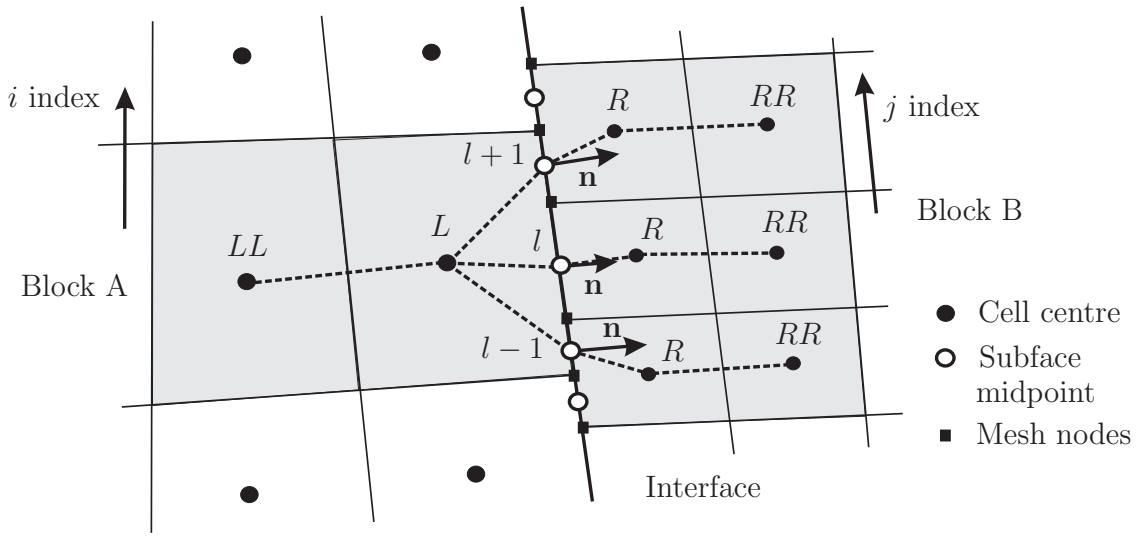

Figure 3.3: Typical block interface with non-matching nodes.

When the one single periodic geometry element is simulated, adequate boundary conditions have to set at the interface where the next periodic element would be. Due to the periodic condition imposed to the flow, the transported variables must assume the same value at the periodic interfaces. Taking the Figure 3.4 as example, the variable Φ has identical values at the interfaces A and B. This mathematical relation is imposed as boundary condition with the help of the so called shadow cells. The boundary cells at the interface B, with cell centres P and Q, are repeated next to the interface A, with cell centres P' and Q'.

In the case of translational periodicity, the boundary condition is simply imposed as $\Phi_P = \Phi_{P'}$, for all variables, also when they represent vector or tensor components. For rotational periodic geometries or general periodicity, the transformation matrix, T_{ij}, has to be used for vectorial and tensorial quantities, Φ_i and Φ_{ij}.

$$\Phi_{P'} = \Phi_P, \quad \Phi_{i,P'} = T_{ij}\Phi_{j,P}, \quad \Phi_{ij,P'} = T_{kl}\Phi_{ij,P}T_{lk} \tag{3.37}$$

In the case of translational periodicity, the transformation matrix is the identity matrix, $T_{ij} = \delta_{ij}$. For rotational periodicity, defined with by the angle γ, around the axial direction, as it is the normal case in turbomachines, the transformation matrix becomes the rotation matrix.

3.3 Solver

In the solution of the algebraic system $A_P^\Phi \Phi_P + \Sigma_l A_l^\Phi \Phi_l = Q_P^\Phi$, the matrix A contains the coefficients related to the variables, which are implicitly solved. On the other hand, the independent vector Q contains the source terms, the explicitly treated variables and the deferred corrections.

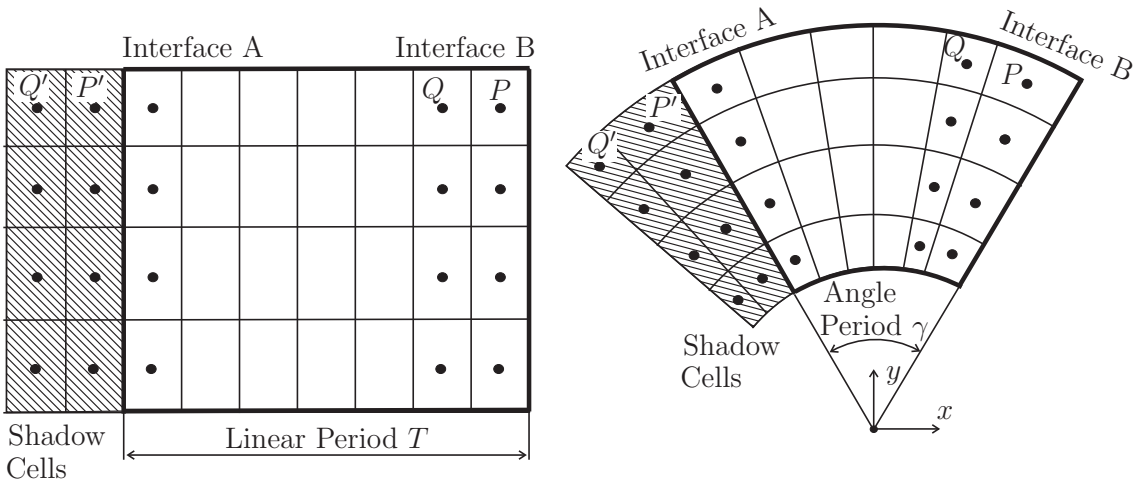

Figure 3.4: Translational and rotational periodic boundary conditions.

The matrix coefficients A_P and A_l depend on the velocity components, which themselves are at the same time unknowns of the problem. This is due to the non-linear property of the transport equations. Due to this characteristic, the solution procedure of the algebraic system can be divided in inner and outer iterations.

At a given outer iteration n, the matrix coefficients and the source terms are calculated with the values from the previous iteration, $n-1$. The inner iterations are then processed with constant values for A_P and A_l, during which the algebraic system is solved. After it, the matrix coefficients and source terms are update with the new values of velocity and density and a new outer iteration starts.

The algebraic system solution is solved iteratively, so that a convergence criterion is needed to decide when to stop the inner and outer loops. There are different criteria to define the convergence, the most common are based on the sum-norm, maximum-norm and RMS-norm of the residuum vector, R. Common convergence criteria are when the chosen residuum norm is smaller than a given value, ε, or when it is reduced by a given number of orders of magnitude in comparison to the initial residuum. The value of ε, or the reduction of how many orders of magnitude can differ between different computational codes and, in some cases, may be related to the nature of the physical problem being analysed.

As a general guideline, the inner iterations are solved with less accuracy than the outer loop, since they are repeatedly solved, for each new outer iteration. In stationary simulations, when some knowledge of the problem being solved is already previously available, the convergence might also be defined based on the asymptotic behaviour of important physical parameters of the flow.

Apart from the explicit treatment of some terms in the basic equations and the deferred corrections, which are both already included in the discretisation procedure, under-relaxation is also a common technique to increase the convergence stability. It

consists in updating the values of the unknown variables to just a certain amount of the current solved values, $\Phi^{n+1} = \Phi^n + \alpha_\Phi (\Phi - \Phi^n)$. Smaller values of α_Φ should, in theory, make the convergence behaviour more stable, to detriment of the convergence speed. The convergence stability can also be increased, by reinforcing the matrix diagonal dominance for the impulse equations, in the inner interactions.

3.3.1 Segregated Solver and Implicit Pressure Correction

In the discretisation of the impulse equations, the pressure term, $(-1/\rho)\ (\partial p/\partial x_i)$, is treated explicitly. This means that it is included in the source term and its value is taken from the previous solution iteration. Following this approach, the impulse equations deliver only the solution for the velocity components. The pressure field is solved, by coupling the pressure to the mass conservation, by means of the continuity equation. This procedure, known as pressure correction method, was first successfully adopted by Patankar [117] and further developed by Ferziger and Perić [43] for general geometry grids.

The SIMPLE algorithm, as introduced by Patankar [117], makes use of the staggered variable arrangement, instead of the collocated arrangement, as used here. The implicit pressure correction, in combination with the collocated arrangement, may lead, in several problems, to the numerical uncoupling between the velocity and the pressure fields. This situation can negatively affect the solution convergence and generate oscillating solutions. Rhie and Chow [122] propose a deferred correction, for the interpolated velocity at the cell faces, in order to eliminate this problem in collocated variable arrangements, assuring the coupling between velocity and pressure fields.

Demirdžić et al. [33] extend the SIMPLE algorithm for the application to compressible fluids, proposing an approximation for the pressure and density corrections. Further modifications are introduced by Van Doormal and Raithby [158] with the SIMPLEC algorithm or by Issa [68] in the PISO algorithm. The PISO algorithm is indicated for instationary problems, where large time steps are employed. In stationary problems, or when small time steps are used in transient simulations, the SIMPLE and SIMPLEC algorithms should be preferred.

3.3.2 Coupled Solver

The first FVM codes based themselves on segregated solvers for computing the numerical solution. Recently, some numerical codes employ coupled solvers as well or exclusively. The coupled solver makes no use of the implicit pressure correction method. It relies on the direct discretisation of the original mass conservation equation. The pressure variable is included in the unknowns vector, it is no more treated explicitly, but implicitly in the algebraic system, and it is solved simultaneously with the velocity components.

In general terms, the solution procedure is the same as for the segregated solver, with the exception that the pressure, velocity components and mass flows do not need to be corrected. As before, the mass and impulse conservation are first solved, after it the energy conservation equation, the turbulent transport equations and, eventually, any additional transport equation.

3.3.3 Linear Solvers

During the solution process, the algebraic system, $A\Phi = Q$, must be repeatedly solved and the computational performance of the FVM code is strongly influenced by the computational linear solver algorithm used for this task.

Direct elimination algorithms, e.g. the Gauß elimination or the LU Decomposition, are relative simple, but very computer expensive. Interactive solvers can provide much superior computational efficiency. The Incomplete LU Decomposition or the Strongly Implicit Decomposition (SIP) are examples of interactive methods.

However, other interactive methods, the conjugate gradient methods, like CGS (conjugate gradient squared) or BCGSTAB (biconjugate stabilised), are considerably faster and more stable, as commented e.g. by Ferziger and Perić [43].

Multigrid methods also deliver high performance for the solution of the linear system. This method consists in using meshes of different densities, originated from the coarsening of the original grid. The algebraic system is first solved in the coarsest mesh, whose solution is interpolated to the finer grids, where it is solved again. As explained by e.g. Brandt [20] or Hackbusch [59], there are different methods for coarsening the grid and for the interpolation procedure.

As commented by Ferziger and Perić [43] and also experienced in this study during the simulation of hydraulic turbines, the multigrid method might not bring any speed increase to the numerical simulations in the case of transient flows.

The computational speed can also be increased with help of parallelisation, where the solution of the algebraic system is distributed over several computers or computer cores forming a cluster. As explained by Skoda [142], for the parallelisation, the original computational mesh is divided, or partitioned, in several blocks, as if they were blocks with non-matching interfaces. The solution of each one of these blocks is assigned to one computer or core and the interface information, or interface fluxes, are exchanged between them. Mainly due to the data exchange between processing units, the performance increase is not a linear function of the number of processors or cores and is bound to a maximum.

Chapter 4

Structure Dynamics Theory

The basic concepts of structure dynamics are reviewed for the study of the turbine runner dynamic motion. The finite element method (FEM), used for the numerical evaluation of the runner transient displacements and stresses, is formulated with energy methods in structural mechanics. The elasticity theory is also involved in the derivation of the FEM and in the evaluation of the mechanical stresses in the Francis runner, while the fatigue theory is relevant for predicting its the fatigue life.

4.1 Elasticity Theory

The elasticity theory relates the displacements in a continuous elastic body to the mechanical strains and stresses acting on it. The mechanical stresses are important for the assessment of the structure strength, regarding static failure criteria and the fatigue theory. They are also required for deriving the equilibrium equations in structural mechanics, either using the equilibrium of forces of classical mechanics or energy methods of analytical mechanics. The mechanical strains can be related to the displacements, according to the following tensorial expression:

$$\epsilon_{ij} = \frac{1}{2}\left(\frac{\partial u_i}{\partial x_j} + \frac{\partial u_j}{\partial x_i}\right) \tag{4.1}$$

The strain tensor is given by ϵ_{ij}, while u_i is the structure displacement at the coordinate position x_i. One important property from ϵ_{ij} is that it is a symmetric tensor. The stress tensor, σ_{ij}, is also symmetric and can be obtained from the mechanical strains using the Hook law, as found in e.g. Timoshenko and Goodier [154].

$$\sigma_{ij} = C_{ijkl}\epsilon_{kl} \tag{4.2}$$

The elasticity tensor, C_{ijkl}, is symmetric as well and defined as follows:

$$C_{ijkl} = \frac{E}{2\,(1+\nu)}\,(\delta_{ik}\delta_{jl} + \delta_{il}\delta_{jk}) + \frac{E\nu}{(1+\nu)\,(1-2\nu)}\delta_{ij}\delta_{kl} \tag{4.3}$$

4.2 Dynamic Equilibrium

In systems with distributed mass and stiffness, it is practical to deal with the equations of motion in their infinitesimal form and to integrate them within the body boundaries. The fundamental law of motion, $F = m\,a$, can be written with differentials for an infinitesimal mass, $dm = \rho dV$, and using the tensorial notation, $\rho dV\ \ddot{u}_i = dF_{i_{ext}}$. The vector $F_{i_{ext}}$ represents the sum of the external forces acting on the body, m its mass and $\ddot{u}_i$ its acceleration. The local density is denoted by ρ and the volume is V.

In statics, the equilibrium condition for a body is given by $F_{i_{ext}} = 0$. Using the D'Alembert principle, the dynamic equation of motion can be expressed in a similar form:

$$dF_{i_{ext}} - \rho dV\ \ddot{u}_i = 0 \tag{4.4}$$

This expression characterises the dynamic equilibrium. The physical interpretation is that in the body inertial system, if the inertial forces are applied, it seems as if the structure were in static equilibrium in its own reference system. Even if this manipulation may seem trivial, it is useful to express the dynamic motion in this form, in regard to particular differential methods in analytical mechanics.

4.3 Equation of Motion for Elastic Bodies

When the dynamic of elastic bodies is analysed, its displacement, $u_i = u_i(x_i, t)$, velocity, $\dot{u}_i$, and acceleration, $\ddot{u}_i$, as well as the mechanical stresses, $\sigma_{ij} = \sigma_{ij}(x_i, t)$, are of interest.

With the energy method or with the force equilibrium method, the equation of motion for elastic bodies can be derived. The displacement, u_i, as function of the position coordinates and time is the unknown of the problem. Once it is solved, the stresses can be evaluated with the elasticity theory. The elastic properties of the body are not only important for the stress calculation, but they are also determinant for the deformed shape of the body, i.e. for the solution of u_i.

For the formulation of the motion equations, the forces acting on the body must be considered. Figure 4.1 shows the different kinds of forces applied to the body. The

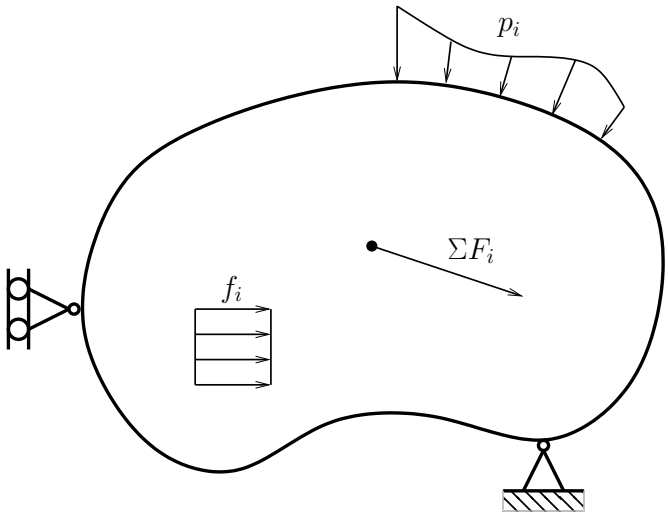

Figure 4.1: Nature of forces acting on the body.

total field force is obtained by integrating the specific field force, f_i, in the body volume, while the resulting total force from the surface loads, p_i, comes from the integration of p_i over the body surface, and the total punctual force is simply the summation of the imposed punctual forces, ΣF_i.

The equation of motion for elastic bodies is the starting point for the formulation of the FEM.

4.3.1 Energy Method

The energy method, combined with variational principles from analytical mechanics, offers a practical way to obtain the motion equations of the elastic body, in a suitable form for the derivation of the FEM.

The total energy potential in mechanical systems, Π, is given by the difference of the internal potential elastic energy, U, and the work of the external forces, W.

$$\Pi = U - W \tag{4.5}$$

The external loads, which contribute for the work, W, are the field forces, surface loads and punctual forces. In structure dynamics, the velocity, $\dot{u}_i$, and acceleration, $\ddot{u}_i$, must be considered. The D'Alembert principle can be employed here, to reach the dynamic equilibrium of the system. In this case, the inertial forces are treated as external forces and their work is included in W, in the expression of Π. The equation for the total energy potential can be expressed as:

$$\Pi = \left(\frac{1}{2}\int_V \sigma_{ij}\epsilon_{ij}dV\right) - \left[\left(\int_V f_i u_i dV + \int_A p_i u_i dA + F_i u_i\right) - \left(\int_V \rho\ddot{u}_i u_i dV\right)\right] \tag{4.6}$$

The dynamic equilibrium position of the elastic body, u_i is such that Π reaches its minimum value. In other words, the solution of the body motion, u_i, minimises the total energy potential. Using the variational principle, for any infinitesimal variation of the displacement, δu_i, Π is stationary:

$$\Pi\left(u_i\right) < \Pi\left(u_i + \delta u_i\right), \quad \forall\, \delta u_i < \varepsilon_i, \quad \varepsilon_i \to 0 \tag{4.7}$$

The stationarity of the total energy potential implies that its variation is equal to zero, when evaluated for the structure displacement solution, u_i.

$$\delta\Pi\left(u_i\right) = 0 \tag{4.8}$$

It follows immediately that, $\delta U - \delta W = 0$. It means that the variation of the work is equal to the variation of the potential energy, in conservative systems. Usually, δW is denoted as the virtual work of the external forces, while, in this formulation, δU could be seen as the virtual work of the internal forces.

The variational operator, δ, can be applied to the expression of Π, for elastic bodies. Considering that it is permutable with the integral and differential operators, in relation to the space coordinates, it can be moved inside the integrals.

$$\delta\Pi = \frac{1}{2}\int_V \delta\left(\sigma_{ij}\epsilon_{ij}\right) dV - \int_V \delta\left(f_i u_i\right) dV - \int_A \delta\left(p_i u_i\right) dA - \delta\left(F_i u_i\right) + \int_V \delta\left(\rho\ddot{u}_i u_i\right) dV \tag{4.9}$$

Remembering the relation, $\sigma_{ij} = C_{ijkl}\epsilon_{kl}$, the fact that the three tensors are symmetric, the product derivative rule and after some mathematical manipulation, the first integral becomes $\delta\left(\sigma_{ij}\epsilon_{ij}\right) = 2\sigma_{ij}\delta\epsilon_{ij}$.

In the integrals involving the applied loads, f_i, p_i and F_i are freely chosen, to match the characteristics of the physical problem being studied, and are completely independent from the variation. This means that in the second, third and fourth terms on the right hand side, the variational only applies to u_i.

The last term on the right hand side requires some more attention, as long as it involves the structure acceleration, which comes from the application of inertial forces in order to attain the dynamic equilibrium. The variation of the term to be integrated is $\delta\left(\rho\ddot{u}_i u_i\right) = \rho\delta\ddot{u}_i u_i + \rho\ddot{u}_i\delta u_i$. In analytical mechanics, the mathematically rigorous treatment of this term is done with the Laplacian functional or with the action principle. Here, it will only be mentioned that, in analytical mechanics, the displacement, u_i, and the velocity, $\dot{u}_i$, are treated as independent variables and the time dependence of $\dot{u}_i$ is considered only implicitly. In $\ddot{u}_i$, the time derivative should be explicitly taken, so that with the application of the variational operator, δ, the term is dropped way from the equation of motion.

With the previous considerations, the equilibrium equation for the elastic body motion becomes:

$$\int_V \rho \ddot{u}_i \delta u_i dV + \int_V \sigma_{ij} \delta \epsilon_{ij} dV = \int_V f_i \delta u_i dV + \int_A p_i \delta u_i dA + F_i \delta u_i \tag{4.10}$$

4.3.2 Force Equilibrium Method

This method starts with the forces equilibrium in an infinitesimal body volume, as in the classical mechanics theory. Nevertheless, the virtual displacement, which is itself a concept from analytical mechanics, is also used here. It is used to obtain the motion equations of the elastic body in a suitable form for the application of Rayleigh-Ritz solution methods in the derivation of the FEM.

Taking the infinitesimal volume, showed in Figure 4.2, in the interior of the body and considering the forces acting on it, related to the mechanical stresses, σ_{ij}, related to the external body forces, f_i, and related to the punctual forces, the law of motion can be expressed as:

$$\rho dV \ \ddot{u}_i = \left(\sigma_{ij} + \frac{\partial \sigma_{ij}}{\partial x_j} dx_j \right) dA_j - \sigma_{ij} dA_j + f_i dV + F_i \tag{4.11}$$

The terms in σ_{ij} cancel themselves mutually and the product $dx_j dA_j$ results in the infinitesimal volume, dV.

$$\rho \ddot{u}_i dV = \frac{\partial \sigma_{ij}}{\partial x_j} dV + f_i dV + F_i \tag{4.12}$$

At the body surface, boundary conditions are imposed. In this context, it corresponds to the surface loads applied to the body. At the boundaries, the stresses in the surface normal direction, n_j, assumes the value of the specific area load, p_i.

$$p_i = \sigma_{ij} n_j \tag{4.13}$$

Both sides of the force equilibrium equation, at the infinitesimal volume, can be multiplied by the virtual displacement, δu_i, which is completely arbitrary.

$$\rho \ddot{u}_i \delta u_i = \frac{\partial \sigma_{ij}}{\partial x_j} \delta u_i + f_i \delta u_i + F_i \delta u_i \tag{4.14}$$

Integrating equation 4.14 into the body volume, one obtains:

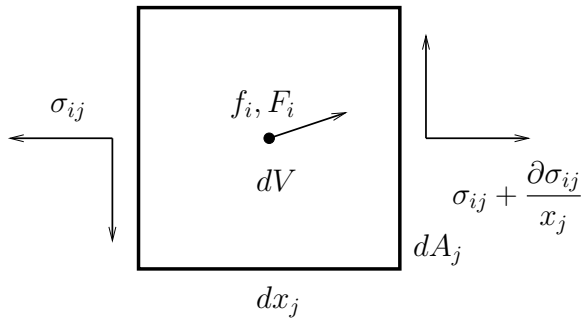

Figure 4.2: Forces acting on the infinitesimal body volume.

$$\int_V \rho \ddot{u}_i \delta u_i dV = \int_V \frac{\partial \sigma_{ij}}{\partial x_j} \delta u_i dV + \int_V f_i \delta u_i dV + F_i \delta u_i \tag{4.15}$$

The punctual force F_i is not integrated, but vectorial summed over the points of the body, where it is applied.

The stress quantity in the first integral on the right hand side, is one of the terms of the partial derivation of the product $\sigma_{ij}\delta u_i$:

$$\frac{\partial \left(\sigma_{ij}\delta u_i\right)}{\partial x_j} = \frac{\partial \sigma_{ij}}{\partial x_j}\delta u_i + \sigma_{ij}\frac{\partial \left(\delta u_i\right)}{\partial x_j} \tag{4.16}$$

Considering the invariability of the differential operator δ, regarding the partial derivatives in relation to the body coordinates, together with the product derivative above, the integral equation becomes:

$$\int_V \rho \ddot{u}_i \delta u_i dV = \int_V \frac{\partial \left(\sigma_{ij}\delta u_i\right)}{\partial x_j} dV - \int_V \sigma_{ij}\delta \frac{\partial u_i}{\partial x_j} dV + \int_V f_i \delta u_i dV + F_i \delta u_i \tag{4.17}$$

Applying the Gauß theorem to the second term on the right hand side and reminding of the definition of the strain tensor, ϵ_{ij}, as function of the displacement partial derivatives, and of the symmetry property of the stress tensor, one can write:

$$\int_V \rho \ddot{u}_i \delta u_i dV = \int_A \sigma_{ij}\delta u_i n_j dA - \int_V \sigma_{ij}\delta \epsilon_{ij} dV \int_V f_i \delta u_i dV + F_i \delta u_i \tag{4.18}$$

Finally, applying the boundary condition $p_i = \sigma_{ij} n_j$ and rearranging, the desired expression for the structure dynamic equilibrium is obtained.

$$\int_V \rho \ddot{u}_i \delta u_i dV + \int_V \sigma_{ij}\delta \epsilon_{ij} dV = \int_V f_i \delta u_i dV + \int_A p_i \delta u_i dA + F_i \delta u_i \tag{4.19}$$

4.4 Dissipation

In real problems, dissipation is always present in the motion of mechanical systems. It can be inherent to the body, as in the case of structural, i.e. hysteretic, damping or due to external forces, as when dampers are employed. The dissipative forces, also denoted as non-conservative forces, must be taken into account for the description and solution of the body motion. They need to be included in the equation of motion for elastic bodies.

Using the energy method, certain types of non-conservative forces can be derived from the Rayleigh dissipation function, $\mathscr{F}$. The virtual work of such forces, δW_{nc}, is given by:

$$\delta W_{nc} = -\frac{\partial \mathscr{F}}{\partial \dot{q}_i} \delta q_i \tag{4.20}$$

The virtual work of the non-conservative forces can be included in the virtual work of the external forces, δW. Invoking the stationarity of the total energy potential, $\delta \Pi = \delta U - \delta W = 0$, the dissipative forces can be considered in the equation of motion of the elastic body.

The definition of the non-conservative forces with the Rayleigh dissipation function is very restrictive. In analytical mechanics, the description of more general dissipative forces requires more elaborated concepts. On the other hand, with the force equilibrium method, any kind of non-conservative force can be considered in a much simpler manner.

Considering volume distributed dissipative forces, f_{nc}, they can be multiplied by the virtual displacement, δu_i, their product can be integrated in the volume domain and then added to the equation of motion, just like the other terms. If the non-conservatives forces are defined over body surfaces or at multiple points, after the multiplication by δu_i, they are integrated in the area, in one case, or summed over the points, in the other case, and added to the equation of motion.

The dissipative forces usually depend on the structure velocity, $\dot{u}_i$, as in the case of viscous damping, but they can also be function of e.g. u_i, as it occurs for hysteretic damping. Just as an example, considering the viscous damping and supposing that the damping distribution, $b = b\,(x, y, z)$, could be known, the motion equation would be:

$$\int_V \rho \ddot{u}_i \delta u_i dV + \int_V b \dot{u}_i \delta u_i dV + \int_V \sigma_{ij} \delta \epsilon_{ij} dV = \int_V f_i \delta u_i dV + \int_A p_i \delta u_i dA + F_i \delta u_i \tag{4.21}$$

In real cases, the damping distribution can seldom be determined, with exception of the cases where damping components, especially designed with this objective, are

used. In many problems, the damping is modelled as being proportional to mass and stiffness properties or modal damping factors are assumed.

4.5 Boundary Conditions

The boundary conditions, to which the elastic body is submitted, can be of various types. Usually, they are kinematic, restricting the displacement at given body points or regions. They might also couple the displacement of different points or regions. In the most common case, when the displacement is prescribed at given points, the boundary condition becomes $u_i\left(x_{c_i}\right) - c_i = 0$, where the displacement c_i is known and imposed.

In the general case, the displacement must obey one set of restrictions, i.e. functions defined by $C_i(u_i) = 0$, at the volume region, at the surfaces or at discrete points. Introducing the Laplace multiplier, λ_i, a new functional can be built:

In the general case, the displacement must obey one set of restrictions, i.e. functions defined by $C_i(u_i) = 0$. Introducing the Laplace multiplier, λ_i, the constrain can be expressed as $\lambda_i C_i(u_i) = 0$. The constrain can be defined at volume regions, surfaces or discrete points. In the first two cases, $\lambda_i C_i(u_i)$ must be integrated in the domain region. For the sake of simplicity, the mathematical derivation to follow will deal only with the punctual restrictions, as long as the volume and area restrictions are completely analogous, with exception of the integral operator.

The total energy potential, Π, can be modified to take into account the restrictions and a new functional, $\overline{\Pi}$ can be built:

$$\overline{\Pi} = \Pi + \lambda_i C_i \tag{4.22}$$

Similar to the unrestricted motion, treated before, the modified total energy potential, $\overline{\Pi}$, is minimised for the dynamic equilibrium position u_i, i.e. $\delta\overline{\Pi}\left(u_i\right) = 0$. Taking the variation of $\overline{\Pi}$ at u_i, the constrained equation of motion becomes:

$$\delta\overline{\Pi} = \delta\Pi + \delta\lambda_i C_i + \lambda_i \delta C_i = 0 \tag{4.23}$$

Even if the Laplace multiplier may first seem to be an artificial mathematical tool, it usually represents physical characteristics of the system. For example, when the set of constrains, C_i, refers to displacement restrictions at the body fixed supports, the Laplace multiplier, λ_i, corresponds to the reaction forces at them.

4.6 Initial Conditions

For the transient solution of the elastic body motion, initial conditions are needed. At the time instant t_0, the structure displacement, $u_i(x_i, t_0)$, and the velocity, $\dot{u}_i(x_i, t_0)$, must be given.

Normally, if no prior information is known, the displacement and velocity are usually set to zero, $u_i(x_i, t_0) = 0$ and $\dot{u}_i(x_i, t_0) = 0$. This corresponds to the case, where the structure is at rest and at the instant t_0, the load is applied and the motion begins.

Alternatively, the initial displacement can be prescribed as the structure static equilibrium position. This procedure is useful, if the initial transient motion is not of interest for the problem, and if just the steady-state condition is important. It avoids the mean portion of the dynamic load to be suddenly applied, suppressing its eventual impact load character.

4.7 Approximation Methods

The analytical solution of the equation of motion for elastic bodies is only practicable for simple problems, with simplified geometry, loads and boundary conditions. For general problems, approximation methods must be used. The approach from Rayleigh [150] and Ritz [124] offer approximate solutions for the equation of motion and it constitutes one of the underlying ideas in the FEM.

The vectorial notation is more suitable for the presentation of this approach. The structure displacement is represented by the vector $\mathbf{u} = \mathbf{u}(\mathbf{x}, t)$, where $\mathbf{x}$ is the coordinate vector.

The Rayleigh-Ritz method consists in representing the structure displacement in the complete structure domain, with help of trial functions, $\mathbf{N}_i$, and with the displacement of a limited number of coordinate points, $\mathbf{u}_i = \mathbf{u}(\mathbf{x}_i, t)$. The approximation becomes:

$$\mathbf{u} \approx \mathbf{N}_i \mathbf{u}_i \tag{4.24}$$

Normally, the functions $\mathbf{N}_i$ are polynomial functions. However, other differentiable functions could also be used. For the chosen trial functions, the problem is reduced to only solving the displacements $\mathbf{u}_i$ at the discrete points $\mathbf{x}_i$, instead of finding the functions $\mathbf{u}$, which are defined and satisfy the equation of motion in the complete domain at any coordinate $\mathbf{x}$. The original continuous problem is replaced by the discrete problem, where $\mathbf{u}_i$ are the unknowns.

If the approximated expression for $\mathbf{u}$ is introduced in the definition of the total energy potential, Π becomes a function of the discrete displacements, $\Pi = \Pi(\mathbf{u}_i)$. The stationarity condition, $\delta\Pi = 0$, becomes equivalent to:

$$\delta\Pi = \sum \frac{\partial \Pi}{\partial \mathbf{u}_i} \delta \mathbf{u}_i = 0 \tag{4.25}$$

Since the variations $\delta\mathbf{u}_i$ are arbitrary, the expression above leads to the vectorial relation:

$$\frac{\partial \Pi}{\partial \mathbf{u}_i} = 0 \tag{4.26}$$

Ordering the displacements $\mathbf{u}_i$ in the displacement vector $\mathbf{U}$, Zienkiewicz [177] argues that, for stationary systems, the above equation leads to a matricial expression of the form:

$$\mathbf{KU} = \mathbf{F} \tag{4.27}$$

Where $\mathbf{K}$ is the stiffness matrix and $\mathbf{F}$ is the load vector.

This is the familiar form of the matricial force equilibrium equation for stationary systems. This shows that the usage of trial functions, according to the Rayleigh-Ritz method, as in the FEM, leads to the desired matricial form of the equilibrium equations. The introduction of the $\mathbf{u}$ approximation in the equation of motion for elastic bodies produces the same matricial equilibrium equation, as it will be seen in the development of the FEM.

Zienkiewicz [177] shows that $\mathbf{K}$ is symmetric and that it is positive definite, since Π is minimised for the displacement solution.

In the instationary case, the trial functions yield the familiar discretised dynamic equilibrium expression, involving the mass matrix and damping matrices, $\mathbf{M}$ and $\mathbf{C}$, as well:

$$\mathbf{M}\ddot{\mathbf{U}} + \mathbf{C}\dot{\mathbf{U}} + \mathbf{KU} = \mathbf{F} \tag{4.28}$$

As described further on, in the FEM, the mass and stiffness matrices and the load vector are obtained by replacing the continuous displacement vector, $\mathbf{u}$, by its approximation in the equation of motion for elastic bodies. The damping matrix is often built with base on assumptions about the system dynamics.

4.8 Basic Concepts of Fatigue Theory

Mechanical structures submitted to dynamic loads are subjected to fatigue. The repeated alternating stresses, combined to the static stresses, may lead to the initiation and propagation of cracks. In this failure scenario, the cracks initiate after a given number of stress cycles and they may occur at dynamic and static stresses levels significantly below the material yield limit. The effect of the alternating stresses in opposite directions, repeated a large number of times, may bring the structure to fail, due to fatigue.

This text presents the current common procedures for fatigue evaluation, with the objective of estimating the turbine runner fatigue life and the fatigue damage caused by each one of the different analysed operating points.

The purpose of fatigue analysis in the design of mechanical components is to predict, how long they can operate, under determined load conditions, before a failure occurs. Alternatively, for a desired fatigue life, the admissible loads, or the security factors in relation to the actual loads, can be estimated. Fatigue failures are characterised by the initiation and propagation of cracks in structural components. The crack growth may even lead to fracture failure under determined conditions. How the presence of cracks is treated, depends on the problem and design philosophy. For most applications, as for example in the design and operation of hydraulic turbines, even minimal cracks are not tolerated.

4.8.1 Relevant Types of Stresses for Fatigue

Fatigue is essentially caused by alternating stresses, which arise from the dynamic structural loads. The alternating stress amplitude is represented by σ_a. The dynamic stresses can be any varying function of time. The mean stress, σ_m, also has an influence on the fatigue endurance limit. The mean stress is mainly due to the static mechanical loads, σ_s. Some manufacturing processes, such as welding and mechanical conformation, introduce residual stresses, σ_0, at the structural components. This effect must be taken into account as well, leading to the mean stress $\sigma_m = \sigma_s + \sigma_0$. Figure 4.3 illustrates, how the different types of stress compose the total stress.

The number of times, that the alternating stress is repeated, is represented by n and corresponds to the number of stress cycles.

4.8.2 Fatigue Life

The fatigue life is the number of stress cycles that a component can resist, before the initiation and propagation of cracks take place. It is sometimes referred to as service

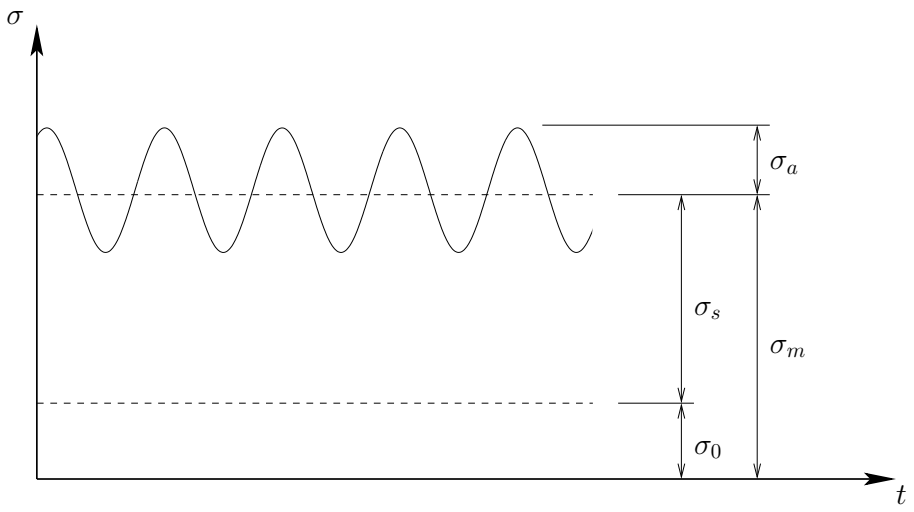

Figure 4.3: Relevant types of stress for the fatigue analysis as function of time.

life as well. The number of cycles that a component can support, depends mainly on the load intensity and on the material properties. However, other factors, such as the environment (e.g. water), surface finish, manufacturing processes or defects, also influence the fatigue life.

The fatigue resistance of the materials is obtained experimentally. Test specimens are submitted to different levels of alternating stress, until they are brought to failure. Normally, significant scattering is found in fatigue test data, so that the fatigue life for real applications is usually defined as the number of cycles, that high percentages of the total number of test specimens can support.

With the experimental data, fatigue life curves, the so called S-N curves or WÖHLER [168] curves, are derived. Figure 4.4 shows the typical Wöhler curve, where the amplitude of the alternating stress, σ_a, is related to the number of cycles before failure, N.

The curve in Figure 4.4 is typical for ferrous alloys. Below a given alternating stress level, σ_L, known as fatigue limit, the material is not subjected to fatigue failure.

The mean stress is an important parameter for the obtainment of the S-N curves, it influences significantly the material fatigue life. For each value of σ_m, different Wöhler curves are obtained. The multiple fatigue life curves can be combined in a single diagram, the so called HAIGH [60] diagram, which can be seen in Figure 4.5.

In the Haigh diagram, each curve corresponds to the admissible number of cycles for the mean and alternating stresses combinations, lying on this curve. Each pair of σ_m and σ_a defines a point in the Haigh diagram. The individual Wöhler curve, on which this point is found, gives the fatigue life for this point. Since only a limited number of Wöhler curves are available, it must be usually interpolated in the Haigh diagram, between the Wöhler curves, in order to obtain the fatigue life for the σ_m and σ_a combinations.

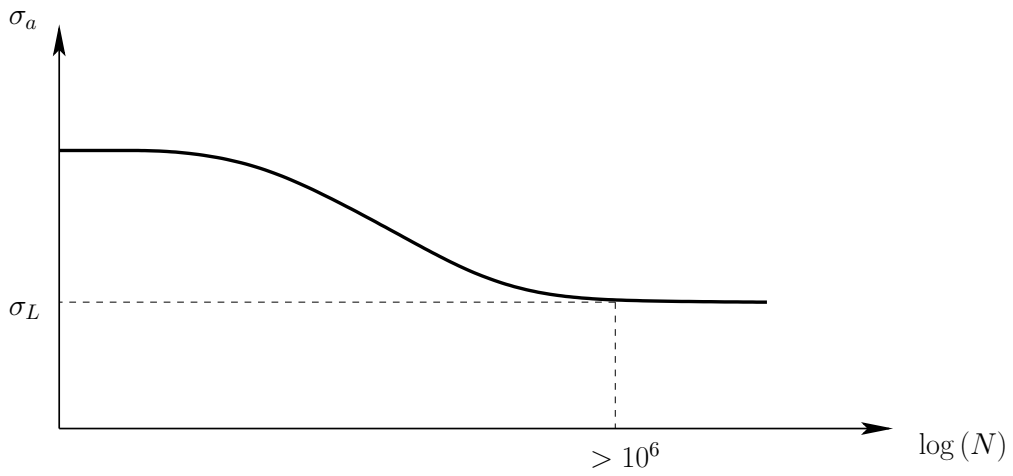

Figure 4.4: Typical Wöhler curve for ferrous alloys, relating the stress amplitude to the admissible number of cycles.

4.8.3 Cumulative Fatigue

Normally, the load history over the structures is composed by multiple combinations of static and alternating stresses, each of them occurring a different number of cycles. However, the Wöhler curves, associated to the fatigue life, are obtained under constant values of mean stress and stress amplitude. In order to find the fatigue life of structures submitted to multiple loads, PALMGREN [115] and MINER [104] developed the concept of fatigue damage accumulation.

Taking m combinations of mean and alternating stresses, σ_{m_i} and σ_{a_i}, occurring n_i number of cycles, each one of them causes to the structure a fatigue damage amount, $D_i = n_i/N_i$, where N_i is the fatigue life for the i-th stress combination. In this situation, the fatigue failure criterion, according to the Palmgren-Miner rule, is:

$$\sum_{i=1}^{m} \frac{n_i}{N_i} = C \tag{4.29}$$

The constant C may assume values between 0,3 and 3,0, depending on the material and manufacturing process. In most cases, $C = 1{,}0$. This means that, when the sum of the accumulated damage is smaller than the constant, $\Sigma D_i < C$, the structure can support the loads without the occurrence of fatigue. If the sum is larger than or equal to the constant, $\Sigma D_i \geq C$, fatigue failure will occur.

The Palmgren-Miner rule does not take into account the load history, i.e. how the dynamic stresses are applied in relation to the time. MILLER [103] shows that the order in which the loads are applied can influence the fatigue resistance. For example, low stress cycles followed by high stress cycles results in longer fatigue life as the opposite. However, in many practical applications, this effect is neglected.

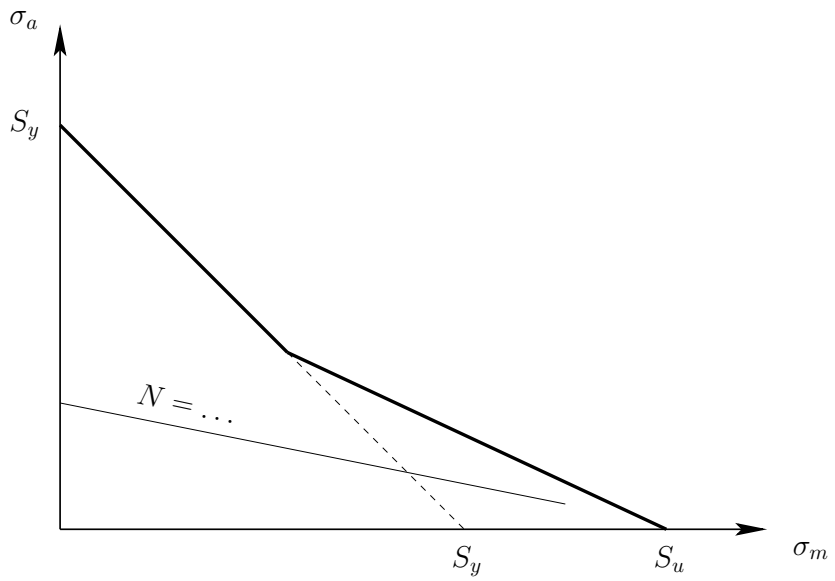

Figure 4.5: Typical Haigh diagram, relating the mean and alternating stresses combination to the admissible number of cycles.

4.8.4 Load History and Range Counting

For the correct application of the Palmgren-Miner rule, the number of cycle reversals for each load combination must be known. In other words, the load history actuating on the component has to be determined. This is one of the difficulties in the fatigue analysis, to accurately predict the operating conditions in which, for example, a machine will be operated. Even if the stresses are exactly known for each operating condition, sometimes is not clear how to estimate how often each of them will take place.

In addition, in practical applications, the stress history for the different load cases does not follow a simple sinusoidal variation in relation to the time. In numerous cases, the stresses variations in relation to the time may assume complicated forms, not described by analytical functions, and the cycle reversals and their amplitude cannot be promptly identified. For this situation, counting algorithms have to be employed to determine the number of cycles and their associated mean stress and alternating stress amplitude.

The rainflow counting technique, as described by Matsuishi and Endo [95], was originally developed for evaluating measured transient stress data for the fatigue analysis. It constitutes the current standard for dynamic stress assessment in fatigue analysis. The rainflow algorithm can also be used for counting the number of cycles, mean and alternating stresses, from complex design loads, obtained, for example, from instationary finite element simulations. The rainflow counting, divides the alternating stresses in classes and to each of these stress classes are associated n_i, σ_{m_i} and σ_{a_i}.

4.8.5 Elasto-Plastic Deformation

The fatigue mechanism described earlier, based on the mean and alternating stresses and on the Wöhler curves, is valid for total stresses below the yield limit of the material, S_y. This means that all deformations remain in the elastic regime. Under these conditions, the structure can support a high number of load cycles, before failing. This is classified as high cycle fatigue (HCF).

Depending on the manufacturing process, the residual stresses, σ_0, can be significantly high, near to or even exceed the material yield limit. In the same way, if σ_m, σ_a or both are much too high, the total stress may exceed the elastic limit as well. In these circumstances, the material works in plastic conditions. Under elasto-plastic deformation, the structure can support a much lower number of cycles than in the elastic regime. This condition is referred to as low cycle fatigue (LCF).

For elasto-plastic deformations, the elastic fatigue model has to be modified, in order to include the plastic effects. In the plastic region, small stress increments lead to large strain increments. For this reason, the strain is preferred for the elasto-plastic model. Morrow [107] proposes the following formulation, to relate the alternating strain amplitude, ϵ_a, to the fatigue life in the elasto-plastic regime, N_f:

$$\epsilon_a = \frac{\sigma'_f - \sigma_m}{E} (2N_f)^b + \epsilon'_f (2N_f)^c \tag{4.30}$$

The first term corresponds to the elastic deformation, ϵ^e_a, while the second one comes from the plastic deformation, ϵ^p_a. The elasticity modulus is represented by E as usual, σ'_f is the fatigue strength coefficient, b the fatigue strength exponent, ϵ'_f the fatigue ductility coefficient and c the fatigue ductility exponent. The parameters σ'_f, b, ϵ'_f and c are dependent from the material and are determined experimentally.

The effect of the mean stress, on the fatigue life is taken into account by the presence of σ_m in the previous expression. For each value of σ_m, the relation between the alternating strain amplitude, ϵ_a, and the elasto-plastic fatigue life, N_f, is modified.

The typical fatigue life curve, relating N_f to ϵ_a, obtained from the non-linear expression, can be observed in Figure 4.6.

With the alternating strain amplitude, the mean stress and the material fatigue parameters, the fatigue life can be derived from the relation from Morrow [107]. Some tested materials also count with extended Haigh diagrams for the plastic region.

The Morrow relation is valid only if the true alternating strain, $\epsilon_a = \epsilon^e_a + \epsilon^p_a$ is used. However, during the mechanical design of the components, the stresses are normally evaluated, based on linear stress-strain relationships. For the elasto-plastic fatigue analysis, the true alternating strain, ϵ_a is calculated from the elastic alternating stress and strain, σ^e_a and ϵ^e_a, with the Neuber [110] rule:

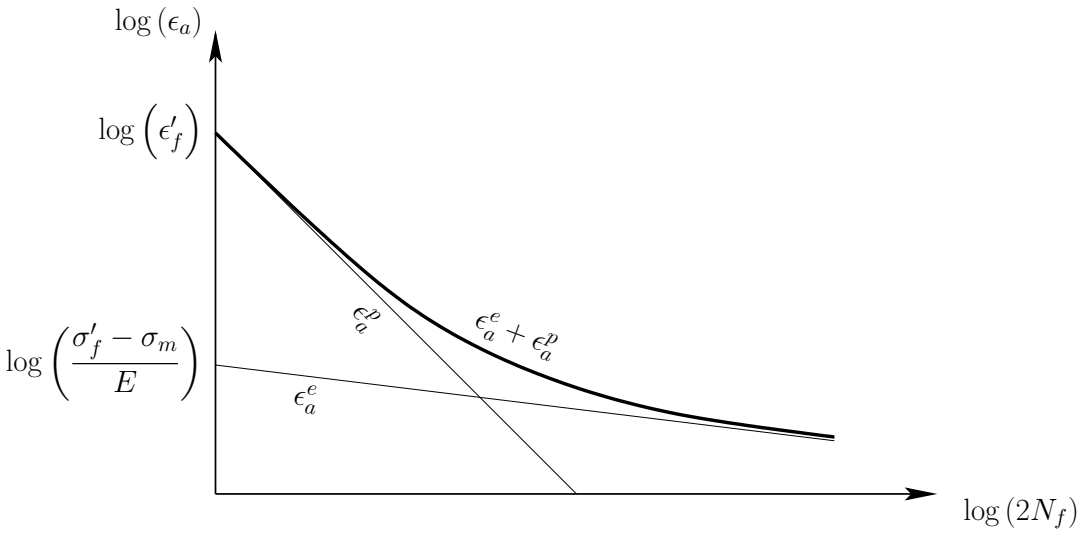

Figure 4.6: Typical fatigue life curve, for the non-linear fatigue model.

$$\sigma_a \epsilon_a = \sigma_a^e \epsilon_a^e \tag{4.31}$$

The formula above has two unknowns, σ_a and ϵ_a. To solve this indetermination, the equation is solved in conjunction with the hysteretic stress-strain relation:

$$\epsilon_a = \frac{\sigma_a}{E} + \frac{\sigma_a^{1/n'}}{K'} \tag{4.32}$$

The first term corresponds to the elastic alternating strain, ϵ_a^e and the second to the plastic alternating strain, ϵ_a^p. The cyclic strength coefficient, K', and the cyclic strain hardening exponent, n', are material constants. The typical hysteretic stress-strain relation is illustrated in Figure 4.7.

The ASME [3] recommends always applying the elasto-plastic fatigue approach, especially for welded structures. If the stresses remain at low values, in the elastic linear region, the traditional elastic approach, based on the Wöhler curves, is fully recovered by the non-linear formulation.

4.8.6 Multiaxial Fatigue

The experimental fatigue data normally refers to the uniaxial stress state. However, several mechanical components are subjected to multiaxial stresses, as in the case of hydraulic turbines. For the application of the fatigue data in general cases of multiaxial stress, the concepts valid for the uniaxial stress state have to be extended.

One of the extensions deals with the elasto-plastic deformation. Glinka and Buczynski [54] adapted the Neuber rule to the multiaxial stress state by the use

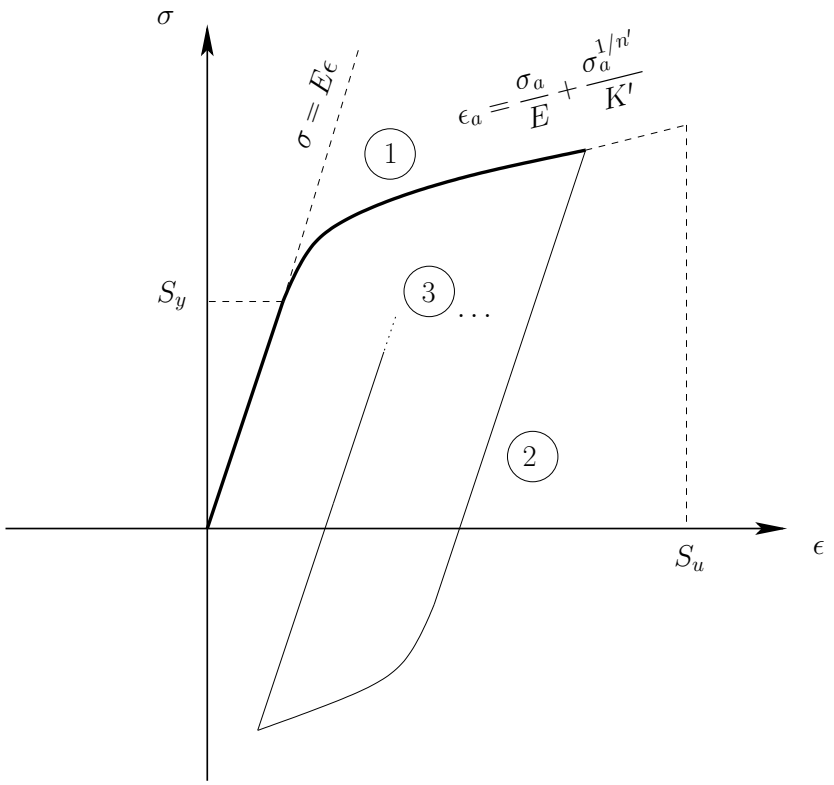

Figure 4.7: Non-linear stress-strain relation, hysteretic effect and load cycles example.

of tensorial stress and strain increments. This modification allows the derivation of the true strain with the adapted Neuber rule from linear multiaxial stress-strain analysis as performed for example with the finite element method (FEM).

As discussed by Arora et al. [9], depending on the transient load characteristics, the principal stress might be in phase or not. Papuga [116] and Ogarevic and Aldred [113] list several damage models, which can be employed for the general case where the load is non-proportional and the principal stresses are not in phase. For example, the Fatemi-Socie [40] model is based on the critical plane principle, while Wang and Brown [164] assume that the micro-crack direction is continuously changing.

The rainflow counting technique, used in cases where the stress time history is known, can also be extended to the multiaxial stress state. Wang and Brown [164] adapted the rainflow counting method to deal with multiaxial stress. For the definition of the turning point in the proposed method, the equivalent von Mises strain was used.

Chapter 5

Finite Element Analysis in Structure Dynamics

The structures of mechanical components often involve complicated geometry and loads. The most part of practical problems cannot be solved analytically for general cases. At present, numerical methods are commonly employed to solve the static structural problems as well as the dynamic motion of elastic mechanical bodies.

Today, the standard for such numerical calculations is the Finite Element Analysis (FEA). In this method, the body volume is discretised in small structural elements, as well as the motion equations. The discretised equations result in an algebraic system of equations, which can be numerically solved with efficient matricial algorithms.

Examples of commercial FEA programs, with the capability to solve mechanical structural problems, are ANSYS and NASTRAN. There also numerous codes developed by research institutes, as e.g. the FEM3D from the FLM of the TUM.

5.1 Discretisation

The finite element method employs the so called elements to discretise the volume of the structure in question. The volume of the mechanical body is divided in small components, which correspond to the finite elements. The elements may have different geometric forms, e.g. quadrilaterals or triangles in 2-D and tetrahedra or hexahedra in 3-D problems. The vertices of the finite elements are called nodes. Some types of finite elements present mid-nodes at their edges, allowing them to assume curved forms instead of configuring simply straight lines. Figure 5.1 shows a typical finite element, with the coordinate system and the element displacements.

For any finite element type or configuration, the displacements, $\mathbf{u^e} = \begin{pmatrix} u_x^e & u_y^e & u_z^e \end{pmatrix}^{\mathbf{T}}$, of any structure point, which is found inside this

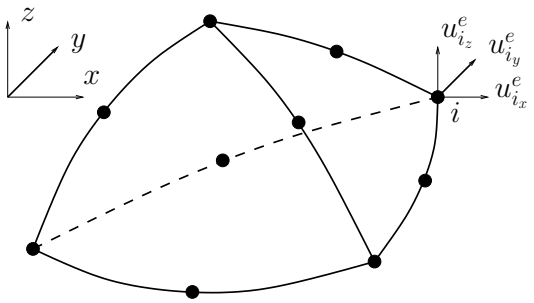

Figure 5.1: Typical finite element, coordinates and displacements.

element, at the element coordinates (x, y, z), are approximated based on the displacements of the element nodes, $\mathbf{u_i^e} = \begin{pmatrix} u^e_{i_x} & u^e_{i_y} & u^e_{i_z} \end{pmatrix}^{\mathbf{T}}$, with help of a chosen function N_i, called shape function.

$$\mathbf{u^e} = \sum_{i=1}^{N} N_i\,(x, y, z)\,\mathbf{u_i^e} \tag{5.1}$$

In the equation above, a finite element with N nodes was considered, the index i makes reference to the node number inside the element and the superscript $\mathbf{e}$ denotes one of the elements resulting from the structure discretisation.

With view to the numerical computations, the displacements of all element nodes in all directions can be ordered in a single element displacement vector, $\mathbf{U_e}$:

$$\mathbf{U_e} = \begin{pmatrix} u_{1_x} & u_{1_y} & u_{1_z} & \cdots & u_{N_x} & u_{N_y} & u_{N_z} \end{pmatrix}^{\mathbf{T}} \tag{5.2}$$

Using this representation, $\mathbf{U_e}$, for the displacements of the element nodes, the displacement at any point inside the element can be rewritten as:

$$\mathbf{u^e} = \mathbf{N}\,(x, y, z)\,\mathbf{U_e} \tag{5.3}$$

With this matricial formulation, $\mathbf{N}$ becomes the shape function matrix, whose elements are the individual shape functions:

$$\mathbf{N}\,(x, y, z) = \begin{pmatrix} N_1 & 0 & 0 & \cdots & N_N & 0 & 0 \\ 0 & N_1 & 0 & \cdots & 0 & N_N & 0 \\ 0 & 0 & N_1 & \cdots & 0 & 0 & N_N \end{pmatrix} \tag{5.4}$$

5.2 Shape Functions

The usage of shape functions to approximate the structure displacements in the finite element method is similar to the idea of representing the solution of the mechanical system with a given set of analytical functions, as in the case of the Rayleigh-Ritz method in analytical mechanics.

Complete polynomial functions offer simple mathematical handling and assure the convergence and boundness of the finite element solution. They can be constructed with Lagrange or serependity polynomials for quadrilateral and hexahedrical elements, as discussed by Ergatoudis, Irons and Zienkiewicz [37], and with area and volume coordinates for triangular and tetrahedrical elements, as described by Zienkiewicz [177].

The order of the polynomial functions, used to approximate the mathematical solution of the system motion, influences the accuracy of the numerical results. It is recommended to use second-order polynomials for the shape functions, so that the stresses and strains can better approximate the real solution. Moreover, quadratic polynomials offer better convergence than linear ones, being able to achieve far more accurate results with the same number of finite elements.

In the vicinity of mathematical singularities, as it is the case for the strain and stress fields near to concave sharp edges, the shape functions cannot properly approximate the theoretical solution. In such cases, the geometry must be improved to eliminate the singularity, e.g. with smooth chamfers or fillets, or cautious Engineering judgement must be adopted.

5.3 Stress and Strain Matrices

In structural analysis, it is usually desired not only to evaluate the structure displacements, but also to estimate the mechanical stresses, being often even the main goal. The components of the mechanical strain at any given point inside one element are ordered in the strain vector, $\boldsymbol{\epsilon} = \begin{pmatrix} \epsilon_{xx} & \epsilon_{yy} & \epsilon_{zz} & \gamma_{xy} & \gamma_{yz} & \gamma_{zx} \end{pmatrix}^{\mathbf{T}}$. The same is performed for the stress components, in the stress vector, $\boldsymbol{\sigma} = \begin{pmatrix} \sigma_{xx} & \sigma_{yy} & \sigma_{zz} & \tau_{xy} & \tau_{yz} & \tau_{zx} \end{pmatrix}^{\mathbf{T}}$.

The mechanical strains are obtained from the partial derivatives from the displacement components. Their relation can also be expressed with the matricial notation. For this purpose, the matrix $\mathbf{S}$ must be defined, which contains the partial derivative operators.

$$\boldsymbol{\epsilon} = \mathbf{S}\mathbf{u}^{\mathbf{e}}; \quad \mathbf{S} = \begin{pmatrix} \partial/\partial x & 0 & 0 & \partial/\partial y & 0 & \partial/\partial z \\ 0 & \partial/\partial y & 0 & \partial/\partial x & \partial/\partial z & 0 \\ 0 & 0 & \partial/\partial z & 0 & \partial/\partial y & \partial/\partial x \end{pmatrix}^{\mathbf{T}} \tag{5.5}$$

In the finite element method, the nodal displacements are the basic unknowns and they are obtained from the numerical solution of the problem. The structural strain of the discretised system is calculated with the solved nodal displacements, using the relation $\mathbf{u^e} = \mathbf{N}(x, y, z)\,\mathbf{U_e}$ and defining the strain-displacement matrix, $\mathbf{B}$, which contains the partial derivatives from the shape functions.

$$\boldsymbol{\epsilon} = \mathbf{B}(x, y, z)\,\mathbf{U_e}; \quad \mathbf{B} = \mathbf{SN}(x, y, z) \tag{5.6}$$

The elements of the matrix $\mathbf{B}$ can be calculated performing the multiplication between the matrix $\mathbf{S}$, containing the partial derivative operators, and the shape function matrix, $\mathbf{N}$.

From the relations between strain and displacement and strain and stress, $\sigma_{ij} = D_{ijkl}\epsilon_{kl}$, it is possible to calculate the stress from the nodal displacements, with the introduction of the stress-strain matrix, $\mathbf{D}$, whose elements are derived from the material-law tensor, C_{ijkl}.

$$\boldsymbol{\sigma} = \mathbf{D}\boldsymbol{\epsilon}; \quad \boldsymbol{\sigma} = \mathbf{DBU_e} \tag{5.7}$$

5.4 Element Matrices Calculation

After the discretisation of the structure with finite elements and the approximation of the structure displacements with the nodal displacements and shape functions, the motion equation for the continuous mechanical system must also be converted into a discrete approximation, in terms of the nodal displacements, which are the unknowns in the numerical problem. The approximate formulation of the motion equation, using the nodal displacements and shape functions, gives rise to the set of algebraic equations, which can be numerically solved, to find the values of the vector $\mathbf{U_e}$.

The dynamic equilibrium equation for the continuous system, written with the virtual displacements, δu_i, can be rearranged to gather the acceleration term and the elastic forces on the left hand side and the external body and surface loads in the right hand side.

$$\int_V \rho \ddot{u}_i \delta u_i dV + \int_V \sigma_{ij} \delta \epsilon_{ij} dV = \int_V f_i \delta u_i dV + \int_A p_i \delta u_i dA + \sum P_i \delta u_i \tag{5.8}$$

The material density is denoted by ρ, f_i represents the volume distributed body forces, p_i corresponds to the pressure loads at the surfaces and P_i relates to the punctual applied forces.

Since the objective is to come to a set of algebraic equations after the discretisation with finite elements, the motion equation can be expressed in its matricial form.

$$\int_V \rho \ddot{\mathbf{u}}^{\mathbf{e}^{\mathbf{T}}} \delta \mathbf{u}^{\mathbf{e}} dV + \int_V \boldsymbol{\sigma}^{\mathbf{T}} \delta \epsilon dV = \int_V \mathbf{f_e}^{\mathbf{T}} \delta \mathbf{u}^{\mathbf{e}} dV + \int_A \mathbf{p_e}^{\mathbf{T}} \delta \mathbf{u}^{\mathbf{e}} dA + \sum \mathbf{P_e}^{\mathbf{T}} \delta \mathbf{u}^{\mathbf{e}} \quad (5.9)$$

With the presence of the displacement vector $\mathbf{u^e}$, it is possible to proceed to the discretisation of the motion equations, through the introduction of the approximation, $\mathbf{u^e} = \mathbf{N}(x, y, z)\,\mathbf{U_e}$. Employing matricial relations, differential properties, after some algebraic manipulation and rearrangement, one comes to the discretised motion equation as a function of the nodal displacements, $\mathbf{U_e}$, and the load vectors, $\mathbf{f_e}$, $\mathbf{p_e}$ and $\mathbf{P_e}$.

$$\left(\int_V \rho \mathbf{N^T N} dV\right) \ddot{\mathbf{U}}_\mathbf{e} + \left(\int_V \mathbf{B^T D B} dV\right) \mathbf{U_e} = \int_V \mathbf{N^T f_e} dV + \int_A \mathbf{N^T p_e} dA + \sum \mathbf{N^T P_e} \quad (5.10)$$

At this point, the finite element properties can be clearly identified in the discretised equation of motion and it can be rewritten, with the definition of the finite element mass matrix, $\mathbf{M_e}$, stiffness matrix, $\mathbf{K_e}$, and load vector, $\mathbf{R_e}$.

$$\mathbf{M_e}\ddot{\mathbf{U}}_\mathbf{e} + \mathbf{K_e U_e} = \mathbf{R_e} \quad (5.11)$$

5.5 Mapped Elements

5.5.1 General Considerations

Mapped finite elements offer the possibility to transform the original real physical geometry into simple element shapes, called canonical elements. The first reason, for performing this transformation, is that any arbitrary element geometries can be considered. Moreover, with the simple definition of shape functions, at the canonical elements, elements of various orders and different properties can be easily defined. Even though the theoretical derivation of the mapped elements is relative sophisticated, the numerical evaluation of the element matrices and the numerical integrations become considerably uncomplicated. This method is also well suited for the modularisation of the computational code, allowing the element definitions to be separated from the main calculation procedures.

5.5.2 Coordinate Transformation

In very simple cases, the element shape functions can be directly written and integrated in the problem coordinates, most usually in Cartesian coordinates. However, in general tridimensional cases, with arbitrary elements and geometry, particular element coordinate systems are used, offering the possibility to handle the general cases with more ease. With this objective in mind, any given finite element, with arbitrary coordinates, shall be transformed into a canonical element. Figure 5.2 depicts the example of a generic quadratic three dimensional tetrahedral element and its corresponding canonical form. The coordinates used for the canonical elements are called natural coordinates and are also shown.

To pass from the real finite element geometry to its canonical form, a transformation function is needed, which associates the actual element coordinates to the natural coordinates, ξ, η and ζ. The transformation functions, $N_i' = N_i'(\xi, \eta, \zeta)$, can be defined in the same way as the shape functions:

$$\begin{pmatrix} x & y & z \end{pmatrix}^{\mathbf{T}} = \sum_{i=i}^{N} \begin{pmatrix} x_i & y_i & z_i \end{pmatrix}^{\mathbf{T}} N_i' \tag{5.12}$$

At the element nodes, (x_j, y_j, z_j) corresponds to (ξ_j, η_j, ζ_j) and the shape functions assume unitary values, $N_i' = \delta_{ij}$, where δ_{ij} is the Kronecker delta.

It is desirable that the transformation functions, N_i', and the shape functions, N_i, become identical. This condition can be enforced and, in this case, when $N_i = N_i'$, the finite element type can be classified as isoparametric. Such element types automatically follow the differentiability condition.

5.5.3 Jacobian Matrix

For the calculation of the element matrices, the expressions for $\mathbf{M_e}$, $\mathbf{K_e}$ and $\mathbf{R_e}$ must be integrated with respect to the Cartesian coordinates x, y and z. However, employing canonical elements, the shape functions are defined in terms of the natural coordinates ξ, η and ζ. This should pose no difficulty, since the coordinate transformation can also be taken into account in the integral, with the introduction of the Jacobian matrix, $\mathbf{J}$.

$$\int_V f(x, y, z)\, dV = \int_\Omega f(\xi, \eta, \zeta) \det \mathbf{J}(\xi, \eta, \zeta)\, d\Omega \tag{5.13}$$

Where the Jacobian matrix is defined as:

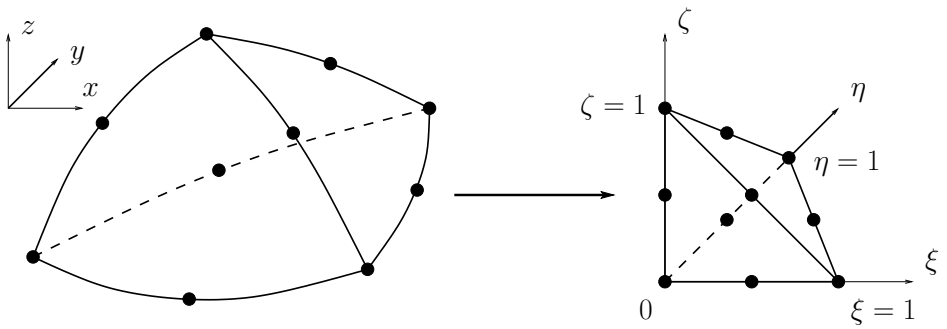

Figure 5.2: Example of a finite element with generic coordinates and its transformation into a canonical element.

$$\mathbf{J} = \begin{pmatrix} \partial x/\partial\xi & \partial y/\partial\xi & \partial z/\partial\xi \\ \partial x/\partial\eta & \partial y/\partial\eta & \partial z/\partial\eta \\ \partial x/\partial\zeta & \partial y/\partial\zeta & \partial z/\partial\zeta \end{pmatrix} \tag{5.14}$$

The problem resides now in the evaluation of the Jacobian matrix. Expressing the Cartesian coordinates x, y and z as functions of the natural coordinates ξ, η and ζ, with the help of the shape functions, N_i, the Jacobian matrix can be evaluated as:

$$\mathbf{J} = \begin{pmatrix} \partial N_1/\partial\xi & \cdots & \partial N_N/\partial\xi \\ \partial N_1/\partial\eta & \cdots & \partial N_N/\partial\eta \\ \partial N_1/\partial\zeta & \cdots & \partial N_N/\partial\zeta \end{pmatrix} \begin{pmatrix} x_1 & \cdots & x_N \\ y_1 & \cdots & y_N \\ z_1 & \cdots & z_N \end{pmatrix}^{\mathbf{T}} \tag{5.15}$$

In the expression above, the first matrix makes no reference to the Cartesian coordinates. It contains the partial derivatives of the shape functions in relation to the natural coordinates and can be readily evaluated, since the functions are defined in terms of these coordinates. The second matrix, $\mathbf{x}$, simply contains the physical coordinates of the element nodes. In this way the Jacobian matrix can be determined with no additional difficulty.

For the calculation of the element matrices, with the transformed coordinates, the partial derivatives in relation to the Cartesian coordinates, which appear e.g. in the strain-displacement matrix, $\mathbf{B}$, for the evaluation of the stiffness matrix, $\mathbf{K_e}$, must also be calculated in function of ξ, η and ζ. Applying the chain rule, the following relation can be established between the partial derivatives:

$$\begin{pmatrix} \dfrac{\partial}{\partial\xi} & \dfrac{\partial}{\partial\eta} & \dfrac{\partial}{\partial\zeta} \end{pmatrix}^{\mathbf{T}} = \mathbf{J} \begin{pmatrix} \dfrac{\partial}{\partial x} & \dfrac{\partial}{\partial y} & \dfrac{\partial}{\partial z} \end{pmatrix}^{\mathbf{T}} \tag{5.16}$$

If the Jacobian matrix is invertible, it follows that:

$$\left(\begin{array}{ccc} \frac{\partial}{\partial x} & \frac{\partial}{\partial y} & \frac{\partial}{\partial z} \end{array} \right)^{\mathbf{T}} = \mathbf{J}^{-1} \left(\begin{array}{ccc} \frac{\partial}{\partial \xi} & \frac{\partial}{\partial \eta} & \frac{\partial}{\partial \zeta} \end{array} \right)^{\mathbf{T}} \tag{5.17}$$

The analytical form of the inverse Jacobian matrix, $\mathbf{J}^{-1}$, is potentially complicated and could pose problems for the evaluation of the integrals. However, in practical finite elements methods, the analytical expression of the inverse Jacobian matrix is not derived, but numerically evaluated. This approach is suitable for the numerical integration of the element matrices.

5.5.4 Area and Volume Coordinates

In the case of quadrilaterals or hexahedrical elements, their canonical elements correspond to the unity-sided square and cube, in which the natural coordinates, ξ, η, ζ, are extremely practical for designating the position of any point. On the other hand, ξ, η and ζ do not form the best suited coordinate system, if triangles or tetrahedra are dealt with. For this kind of elements, the area and volume coordinates, the last defined by (L_1, L_2, L_3, L_4), offer more practicity than the natural coordinates, ξ, η, ζ.

The volume coordinates are depicted in Figure 5.3 for the quadratic tetrahedrical element and their physical meaning for the coordinates L_i is the volume ratio between the tetrahedron constructed substituting the i-th vertex node by an internal point P and the original tetrahedron. The coordinate system formed by the volume coordinates is redundant. The coordinates form a linear dependent set and at any point $\Sigma L_i = 1$.

There are significant advantages in using this coordinate system. The nodal coordinates and the shape functions can be defined in a simple manner, the derivatives can be simply calculated and the numerical integrations can be simplified too. Nevertheless, for the evaluation of the derivatives, for the strain-displacement matrix or for the Jacobian matrix, and the calculation of the integrals, for the element matrices, the natural coordinates still have to be used. Therefore, it is necessary to establish the relations between the volume coordinates, L_i, and the natural coordinates, ξ, η, ζ. The partial derivatives, in relation to the natural coordinates, can be obtained with the chain rule.

$$\left(\begin{array}{ccc} \frac{\partial N_i}{\partial \xi} & \frac{\partial N_i}{\partial \eta} & \frac{\partial N_i}{\partial \zeta} \end{array} \right)^{\mathbf{T}} = \sum_j \left(\begin{array}{ccc} \frac{\partial N_i}{\partial L_j}\frac{\partial L_j}{\partial \xi} & \frac{\partial N_i}{\partial L_j}\frac{\partial L_j}{\partial \eta} & \frac{\partial N_i}{\partial L_j}\frac{\partial L_j}{\partial \zeta} \end{array} \right)^{\mathbf{T}} \tag{5.18}$$

With these relations, the partial derivatives in relation to ξ, η and ζ can be calculated, allowing the evaluation of the Jacobian matrix too. With the Jacobian matrix, the derivatives in relation to the Cartesian coordinates can be obtained as before, while the element integrals need adjustments to the integration limits.

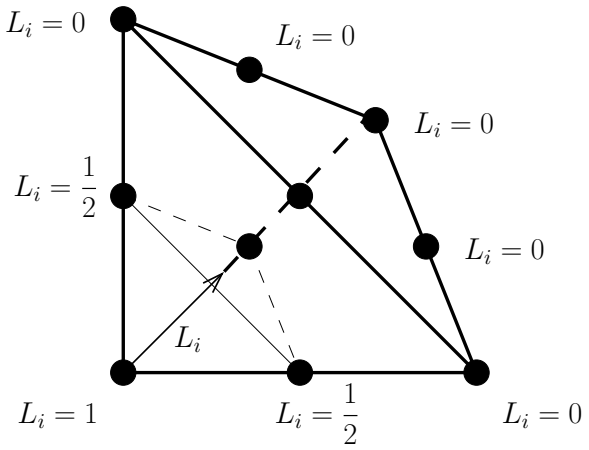

Figure 5.3: Example of a canonical finite element and its natural, or volume, coordinates.

5.6 Element Matrices Numerical Integration

Applying the finite element method to practical problems, with general geometry and elements, the element integrals are calculated with the help of numerical approximations. Most usually, the Gauß quadrature is employed. In this numerical procedure, the integral value is approximated by a weighted sum of the integrated function evaluated at selected points. These points are called integration points and their number, M, location, (ξ, η, ζ), and weight, w, define the precision of the numerical approximation. Denoting the integrand by the general function F, for notation simplicity, the value of the volume integral is approximated, in the Gaussian quadrature, by:

$$\int_{\Omega} F(\xi, \eta, \zeta)\, d\xi d\eta d\zeta \approx \sum_{i=1}^{M} w_i F(\xi_i, \eta_i, \zeta_i) \tag{5.19}$$

In the case of tetrahedra, the integrated function, F, is expressed in terms of the volume coordinates, $F = F(L_1, L_2, L_3, L_4)$ and calculated directly with them.

By the numeric integration with the Gaussian quadrature, one of the advantages of employing the canonical elements becomes clear. The integration points in the canonical elements are always the same, for any physical element. The actual geometry of the physical element needs only to be considered in the constant nodal coordinate vector, $\mathbf{x}$. This simplifies enormously the integration procedure itself and the calculation of the values of the integrated function, F, since, for a given element type, it is evaluated always at the same natural coordinates.

In the case of tetrahedra and triangles, the points location in volume or area coordinates and their weights, w_i, can be respectively found in Hammer, Marlowe and Stroud [61] and Cowper [29].

5.7 Damping

Most of the mechanical systems include some degree of damping, even if in some cases it can be very small. There are several kinds of damping, which may themselves have different mathematical formulations. Nevertheless, damping can be generally considered in the finite element discretisation, through the multiplication of the damping matrix, $\mathbf{C_e}$, by the velocity vector, $\dot{\mathbf{U}}_\mathbf{e}$. The new equation governing the system motion becomes:

$$\mathbf{M_e}\ddot{\mathbf{U}}_\mathbf{e}(t) + \mathbf{C_e}\dot{\mathbf{U}}_\mathbf{e}(t) + \mathbf{K_e}\mathbf{U_e}(t) = \mathbf{R_e}(t) \tag{5.20}$$

In theory, the damping matrix could be obtained through the integration in the element volume in the same way as the mass matrix, if the material specific damping factor, b, could be defined. However, this is seldom the case, configuring much more a mathematical abstraction than being applicable in the practice. Other formulations for the damping matrix have to be considered.

The structural damping, also referred to as hysteretic damping, is sometimes employed for mechanical structures, as exemplified by Meirovitch [98]. It assumes that the damping forces are proportional, with the factor γ, to the structure stiffness and that they present 90° phase shift in relation to the elastic forces, $\mathbf{C_e} = i\gamma\mathbf{K_e}$ with $i = \sqrt{-1}$.

As pointed out by Bathe [13], damping is usually proportional to frequency and damping ratios, ζ_i, at given frequencies, ω_i, are also often experimentally known for the system being analysed. In such cases the Rayleigh damping, or proportional damping, is commonly used, $\mathbf{C_e} = \alpha\mathbf{M_e} + \beta\mathbf{K_e}$.

5.8 Global Matrix Assembly

After the element equilibrium equations, the approximation for the displacements with element shape functions and the element matrices and load vector were formulated, the next step in the description of the finite element method focus on the assembly of the global matrices, $\mathbf{M}$, $\mathbf{K}$, and global vectors, $\mathbf{U}$, $\mathbf{R}$, which shall represent the complete mechanical system being studied.

The global displacement vector, $\mathbf{U}$, contains all the element displacement vectors, $\mathbf{U_e}$, in an ordered manner:

$$\mathbf{U} = \left(\mathbf{U}_{\mathbf{e}_1} \dots \mathbf{U}_{\mathbf{e}_N}\right)^\mathbf{T} \tag{5.21}$$

The individual element equilibrium equations enforce the equilibrium of each element node. In addition, any given node can be shared by more than one element, requiring

the addition of the force contribution of each element to this node. This leads to the summation of the element matrix components, which correspond to the same node. This process generates the global element matrices.

To allow the contribution of each element to the global matrices to be correctly summed, the components of the element matrices are rearranged in the matrices, $\mathbf{M}_i$, $\mathbf{K}_i$, which have the same dimension of the global matrices and where the position of their components agree with the position of the corresponding nodal displacements in the global displacement vector. The same is performed for the element load vector, providing the global load vector $\mathbf{R}_i$.

Finally, the rearranged matrices and vectors, $\mathbf{M}_i$, $\mathbf{K}_i$ and $\mathbf{R}_i$, can be added together, to obtain the global matrices and vector:

$$\mathbf{M} = \sum_i \mathbf{M}_i \,; \quad \mathbf{K} = \sum_i \mathbf{K}_i \,; \quad \mathbf{R} = \sum_i \mathbf{R}_i \tag{5.22}$$

With the global matrices and global load vector, the discretised matricial equation of motion for the complete structure can be written.

$$\mathbf{M}\ddot{\mathbf{U}}\,(t) + \mathbf{C}\dot{\mathbf{U}}\,(t) + \mathbf{K}\mathbf{U}\,(t) = \mathbf{R}\,(t) \tag{5.23}$$

The procedure of adding the matrix components of the individual elements might appear intuitive, although its formal mathematical derivation is not as evident as it might suggest. This development can be found in Zienkiewicz [177], where he deals with the concepts of internal equivalent nodal force and internal nodal force or, alternatively, with the integration over the complete structure domain.

5.9 Boundary Conditions

The structural motion is almost always restricted to some extent by mechanical constraints, like e.g. supports, couplings and bearings. These physical restrictions determine the boundary conditions of the mathematical problem. In mechanical systems, they reflect most of the time kinematic constraints. Common boundary conditions in finite element analysis are the displacement constraints, which configure Dirichlet boundary conditions. For example, at the connection between the turbine runner and shaft, some degrees of freedom of the runner coupling are restricted and their displacements are imposed equal to zero.

In the general case, the displacement vector can be rearranged as, $\mathbf{U} = \begin{pmatrix} \mathbf{U_1} & \mathbf{U_2} \end{pmatrix}^{\mathbf{T}}$, where the displacements are prescribed for the degrees of freedom grouped in the vector $\mathbf{U_2}$, and the degrees of freedom in the vector $\mathbf{U_1}$ remain unknown. Rearranging the coefficients in the mass, damping and stiffness

matrices and the forces in the load vector according to the reordered displacement vector, the equation of motion can be expressed as:

$$\begin{pmatrix} \mathbf{M_{11}} & \mathbf{M_{12}} \\ \mathbf{M_{21}} & \mathbf{M_{22}} \end{pmatrix} \begin{pmatrix} \ddot{\mathbf{U}}_\mathbf{1} \\ \ddot{\mathbf{U}}_\mathbf{2} \end{pmatrix} + \begin{pmatrix} \mathbf{C_{11}} & \mathbf{C_{12}} \\ \mathbf{C_{21}} & \mathbf{C_{22}} \end{pmatrix} \begin{pmatrix} \dot{\mathbf{U}}_\mathbf{1} \\ \dot{\mathbf{U}}_\mathbf{2} \end{pmatrix} + \begin{pmatrix} \mathbf{K_{11}} & \mathbf{K_{12}} \\ \mathbf{K_{21}} & \mathbf{K_{22}} \end{pmatrix} \begin{pmatrix} \mathbf{U_1} \\ \mathbf{U_2} \end{pmatrix} = \begin{pmatrix} \mathbf{R_1} \\ \mathbf{R_2} \end{pmatrix} \tag{5.24}$$

Expanding the matricial equation, the linear system to be solved for the unknown displacements, $\mathbf{U_1}$, becomes:

$$\mathbf{M_{11}}\ddot{\mathbf{U}}_\mathbf{1} + \mathbf{C_{11}}\dot{\mathbf{U}}_\mathbf{1} + \mathbf{K_{11}}\mathbf{U_1} = \mathbf{R_1} - \mathbf{M_{12}}\ddot{\mathbf{U}}_\mathbf{2} - \mathbf{C_{12}}\dot{\mathbf{U}}_\mathbf{2} - \mathbf{K_{12}}\mathbf{U_2} \tag{5.25}$$

All the terms on the right hand side are known and can be regarded as a generalised load vector. This equation preserves exactly the same structure as the general discretised equation of motion and can be solved in the same way as the original one.

After the linear system, is solved for the displacements $\mathbf{U_1}$, considering the imposed boundary conditions, the second matricial equation, resulting from the partition of the original equation of motion, can be used to evaluate the reaction forces at the nodes and directions defined by the prescribed displacement vector $\mathbf{U_2}$.

$$\mathbf{R_2} = \mathbf{M_{21}}\ddot{\mathbf{U}}_\mathbf{1} + \mathbf{M_{22}}\ddot{\mathbf{U}}_\mathbf{2} + \mathbf{C_{21}}\dot{\mathbf{U}}_\mathbf{1} + \mathbf{C_{22}}\dot{\mathbf{U}}_\mathbf{2} + \mathbf{K_{21}}\mathbf{U_1} + \mathbf{K_{22}}\mathbf{U_2} \tag{5.26}$$

General boundary conditions, relating for example one or more degrees of freedom, can also be imposed. This is the case, for example, when links between nodes or periodic boundary conditions between them are considered. Prior to the solution, the actual values of these nodal displacements are not known. Nevertheless, a relation between them is imposed.

This kind of kinematic relation can be expressed with algebraic equations and again grouped in one matricial equation: $\mathbf{T_c U} = \boldsymbol{\alpha}$. Taking the energy functional, for the structural problem, and adding the matricial constraint equation with help from Laplace multipliers, $\boldsymbol{\Lambda}$, the mathematical system to be solved becomes:

$$\begin{pmatrix} \mathbf{M} & \mathbf{0} \\ \mathbf{0} & \mathbf{0} \end{pmatrix} \begin{pmatrix} \ddot{\mathbf{U}} \\ \ddot{\boldsymbol{\Lambda}} \end{pmatrix} + \begin{pmatrix} \mathbf{C} & \mathbf{0} \\ \mathbf{0} & \mathbf{0} \end{pmatrix} \begin{pmatrix} \dot{\mathbf{U}} \\ \dot{\boldsymbol{\Lambda}} \end{pmatrix} + \begin{pmatrix} \mathbf{K} & \mathbf{T_c^T} \\ \mathbf{T_c} & \mathbf{0} \end{pmatrix} \begin{pmatrix} \mathbf{U} \\ \boldsymbol{\Lambda} \end{pmatrix} = \begin{pmatrix} \mathbf{R} \\ \boldsymbol{\alpha} \end{pmatrix} \tag{5.27}$$

Again the matricial equation to be solved has the same form of the original discretised equation of motion and can be solved by common numerical procedures.

5.10 Numeric Solver

The discretisation of the motion equations of the structural system with the finite element results in an algebraic set of linear equations, whose unknowns are the nodal displacements. This problem presents the general form $\mathbf{Ax} = \mathbf{b}$, and can be solved by a variety of numerical procedure such as, the Gauß-Seidel method, matrix factorisation or gradient methods. Here, the preferred tool for the solution of the discretised mechanical system is the preconditioned conjugate gradient (PCG) solver.

5.10.1 Static System

If the structural static problem is considered, all derivatives in relation to the time vanish, all displacements and forces are constant over the time and the equilibrium equation, describing the system becomes simply:

$$\mathbf{KU} = \mathbf{R} \tag{5.28}$$

This matricial equation, also considering the boundary conditions, is immediately identified as having the form $\mathbf{Ax} = \mathbf{b}$ and is solved, with no further complications, by one of the numerical methods already mentioned.

5.10.2 Direct Time Integration

In the case of unsteady motion of the mechanical system, the time derivatives of the structure displacements, $\mathbf{U}$, are present, in the form of the velocity and acceleration vectors, $\dot{\mathbf{U}}$ and $\ddot{\mathbf{U}}$. The displacements, velocities, acceleration and loads are functions of time. One alternative to solve this instationary problem with numerical methods, is the direct time integration. With this procedure, it is necessary to discretise the equations of motion also in relation to the time. The technique covered here is the Newmark [111] method.

At the original problem, with the equations of motion discretised in space with the finite elements, the displacement, velocity and acceleration vectors are not known. Applying the finite differences method in relation to time, the problem is reformulated in such a way, that the displacement vector becomes the only unknown. Supposing that the displacements, velocities and accelerations are known at the time step n, the displacement vector has to be solved for the following time step, $n + 1$.

$$\left(\frac{1}{\alpha\Delta t^2}\mathbf{M}+\frac{\delta}{\alpha\Delta t}\mathbf{C}+\mathbf{K}\right)\mathbf{U}_{n+1}=\mathbf{R}_{n+1} + \mathbf{M}\left[\frac{1}{\alpha\Delta t^2}\mathbf{U}_n+\frac{1}{\alpha\Delta t}\dot{\mathbf{U}}_n+\left(\frac{1}{2\alpha}-1\right)\ddot{\mathbf{U}}_n\right] + \mathbf{C}\left[\frac{\delta}{\alpha\Delta t}\mathbf{U}_n+\left(\frac{\delta}{\alpha}-1\right)\dot{\mathbf{U}}_n+\frac{\Delta t}{2}\left(\frac{\delta}{\alpha}-2\right)\ddot{\mathbf{U}}_n\right] \tag{5.29}$$

In this formula, the matrix on the left hand side can be calculated from the global element matrices and with the current time step size, Δt. The displacement vector, at the instant t_{n+1}, $\mathbf{U}_{n+1}$, is the only unknown and the vector on the right hand side is determined with the corresponding load vector, $\mathbf{R}_{n+1}$, the global element matrices and the known displacements, velocities and accelerations from the previous solved time step, $\mathbf{U}_n$, $\dot{\mathbf{U}}_n$, $\ddot{\mathbf{U}}_n$. Finally, this equation presents once again the traditional form, $\mathbf{Ax}=\mathbf{b}$, which can be solved as usual, at each time step.

In this approximation, α and δ are numerical constants and can be thought as relaxation parameters. Bathe [13] points out three requirements for these numerical parameters, so that the numerical stability and convergence in relation to the time are guaranteed.

$$\alpha\geq\frac{1}{4}\left(\frac{1}{2}+\delta\right)^2;\quad \delta\geq\frac{1}{2};\quad \frac{1}{2}+\delta+\alpha\geq 0 \tag{5.30}$$

The third condition is actually always fulfilled with the first two. Typical values for the numerical parameters, as originally proposed by Newmark [111], are $\alpha=1/4$ and $\delta=1/2$.

5.10.3 Modal Analysis

In the strict case of linear or explicitly linearised systems, the modal analysis delivers information about the dynamic behaviour of the structure, allowing the determination of the natural frequencies and mode shapes (i.e. eigenfrequencies and eigenmodes or natural modes).

Starting with the undamped motion, $\mathbf{M}\ddot{\mathbf{U}}+\mathbf{KU}=\mathbf{F}$, the Rayleigh coefficient can be calculated as function of the displacement, $\mathscr{R}=\mathbf{U^T KU}\,/\,\mathbf{U^T MU}$. When evaluated at the mode shapes, $\mathbf{\Phi}_i$, this functional assumes local minima, which are equal to the square of the corresponding natural frequencies, ω_{n_i}. If the structure has N degrees of freedom, there are N mode shapes and associated natural frequencies. Any dynamic displacement of the linear system can be exactly described by a linear combination of the mode shapes:

$$\mathbf{U} = \sum_{i=1}^{N} \mathbf{\Phi}_i q_i \; ; \quad \mathbf{U} = \mathbf{\Phi q} \tag{5.31}$$

The vector $\mathbf{q}$ contains the generalised coordinates of the system, q_i, and $\mathbf{\Phi}$ is the modal matrix, where the columns correspond to the mode shape vectors, $\mathbf{\Phi} = (\mathbf{\Phi}_1 \dots \mathbf{\Phi}_N)$.

Substituting $\mathbf{U}$ in the undamped equation of motion and premultiplying it by $\mathbf{\Phi^T}$, the mode shapes uncouple the linear system of equations:

$$\mathbf{\Phi^T M \Phi \ddot{q}} + \mathbf{\Phi^T K \Phi q} = \mathbf{\Phi^T F} \tag{5.32}$$

Each equation of the linear system becomes a forced ordinary second-order differential equation in q_i. Using the relation $\omega_{n_i}^2 = \mathbf{\Phi}_i^\mathbf{T} \mathbf{K} \mathbf{\Phi}_i / \mathbf{\Phi}_i^\mathbf{T} \mathbf{M} \mathbf{\Phi}_i$, the uncoupled individual equations can be rewritten as:

$$\ddot{q}_i + \omega_{n_i}^2 q_i = \omega_{n_i}^2 \frac{\mathbf{\Phi}_i^\mathbf{T} \mathbf{F}}{\mathbf{\Phi}_i^\mathbf{T} \mathbf{K} \mathbf{\Phi}_i} \tag{5.33}$$

In the uncoupled equations, it can be observed that the effect of the external forces on the system dynamic response does not depend only on the excitation frequency, but also on how the shape of the external loads matches with the mode shapes. The product $\mathbf{\Phi}_i^\mathbf{T} \mathbf{F}$ can be interpreted as the projection of the load vector on the natural mode.

For harmonic excitations with forced frequency ω_f, the generalised coordinates assume the classical sinusoidal solution form. If the external forces vary arbitrarily in relation to the time, they can be decomposed in Fourier series. Alternatively, the uncoupled equations of motion, in generalised coordinates, can be solved numerically in the time domain, as it is normally done in the FEM.

Premultiplying the free undamped equation of motion, $\mathbf{M\ddot{U}} + \mathbf{KU} = \mathbf{0}$, by $\mathbf{M}^{-1}$, remembering that, in this special case, $\ddot{\mathbf{q}}_i = -\omega_{n_i}^2 \mathbf{q}_i$, and after some mathematical manipulation, it can be shown that the mode shapes and natural frequencies correspond to the eigenvectors and eigenvalues of the following eigenproblem:

$$\left(\mathbf{M}^{-1}\mathbf{K}\right) \mathbf{\Phi}_i = \left(\omega_{n_i}^2\right) \mathbf{\Phi}_i \tag{5.34}$$

As solution of the eigenproblem, the mode shapes are orthogonal between them and form a vectorial base. This explains why they uncouple the equation system and why they can describe any dynamic displacement of the structure. In the FEM the natural frequencies and natural modes of the system are commonly extracted with the block Lanczos method, as described by Grimes, Lewis and Simon [55].

Normally, in the numerical solution of the natural frequencies and natural modes with the FEM, not all mode shapes are extracted. Usually a limited number M of frequencies and modes are calculated, with $M < N$. Therefore, the structure displacement is actually approximated by:

$$\mathbf{U} \approx \sum_{i=1}^{M} \mathbf{\Phi}_i q_i \tag{5.35}$$

When the FEM is applied, it must be assured, that the number of extracted modes is sufficient to properly simulate the structure motion and that they are significant for the load geometry being applied, as long as the force vector is projected on the mode shapes: $\mathbf{\Phi}_i^{\mathbf{T}}\mathbf{F}$.

If damping is considered, i.e. $\mathbf{M}\ddot{\mathbf{U}} + \mathbf{C}\dot{\mathbf{U}} + \mathbf{K}\mathbf{U} = \mathbf{F}$, the linear system can only be uncoupled in the same manner as before, if $\mathbf{\Phi}^{\mathbf{T}}\mathbf{C}\mathbf{\Phi}$ results in a diagonal matrix. In this special case, $\mathbf{\Phi}_i^{\mathbf{T}}\mathbf{C}\mathbf{\Phi}_i / \mathbf{\Phi}_i^{\mathbf{T}}\mathbf{M}\mathbf{\Phi}_i = 2\zeta_i\omega_{n_i}$, where ζ_i is the damping factor, or modal damping, associated to the i-th mode shape. The uncoupled equations, in generalised coordinates, become:

$$\ddot{q}_i + 2\zeta\omega_{n_i}\dot{q}_i + \omega_{n_i}^2 q_i = \omega_{n_i}^2 \frac{\mathbf{\Phi}_i^{\mathbf{T}}\mathbf{F}}{\mathbf{\Phi}_i^{\mathbf{T}}\mathbf{K}\mathbf{\Phi}_i} \tag{5.36}$$

For harmonic excitations, the solution of this forced damped ordinary second-order differential equation has the usual damped sinusoidal form. As for undamped motion, the external forces can be expanded in Fourier series or the uncoupled equations of motion can be numerically solved for general excitation forces.

In the general case, where the double product of the damping and mode shape matrices does not result in a diagonal matrix, as e.g. when the gyroscopic effect is considered as formulated by Geradin and Kill [52] and Guo, Chu and Zheng [58], the eigenproblem must be treated with state-space coordinates. This means that the velocity becomes an additional unknown of the problem. On the other hand, the relation between the displacement, $\mathbf{U}$, and velocity, $\mathbf{V}$, is included as an additional matricial equation, $\dot{\mathbf{U}} = \mathbf{V}$. This equation can be combined with the equation of motion in a new matricial expression, which represents the eigenproblem to be solved in the damped case:

$$\begin{pmatrix} \mathbf{C} & \mathbf{M} \\ \mathbf{M} & \mathbf{0} \end{pmatrix} \begin{pmatrix} \dot{\mathbf{U}} \\ \dot{\mathbf{V}} \end{pmatrix} + \begin{pmatrix} \mathbf{K} & \mathbf{0} \\ \mathbf{0} & -\mathbf{M} \end{pmatrix} \begin{pmatrix} \mathbf{U} \\ \mathbf{V} \end{pmatrix} = \begin{pmatrix} \mathbf{F} \\ \mathbf{0} \end{pmatrix} \tag{5.37}$$

The eigenproblem counts now with $2N$ eigenvalues and eigenvectors, significantly increasing the computation times. The problem takes the form $\mathbf{A}\mathbf{z} = \lambda\mathbf{z}$, where the mode shapes $\mathbf{z}$ are complex numbers vectors. In physical terms, this means that the structural displacements are not necessarily synchronous for a given mode shape, they might be phase delayed.

5.10.4 Harmonic Analysis

When limited information about the excitation forces is available, or when it is desired to deliberately simplify the problem, for computational reasons for example, the dynamic external loads may be supposed to vary harmonically in relation to the time.

Under this assumption and making use of the complex numbers notation, the load vector is modelled by $\mathbf{F} = \mathbf{F_0} e^{i\omega_f t}$.

Considering this approximation, the displacements also vary sinusoidally, with the exciting frequency, ω_f, and with a phase delay φ. In the steady state, the displacements vary according to $\mathbf{U} = \mathbf{U}_0 e^{i\omega_f t}$, where $\mathbf{U}_0$ is a complex valued vector, whose module and argument correspond to the vibration amplitude and phase delay.

Substituting $\mathbf{U}$ and $\mathbf{F}$ in the damped equation of motion and using the fact that, for harmonic vibrations, $\ddot{\mathbf{U}} = -\omega_f^2 \mathbf{U}$ and $\dot{\mathbf{U}} = i\omega_f \mathbf{U}$, the matricial equation of motion can be transformed into:

$$\left(-\omega_f^2 \mathbf{M} + i\omega_f \mathbf{C} + \mathbf{K}\right) \mathbf{U}_0 = \mathbf{F_0} \tag{5.38}$$

This expression has the same form as the static equilibrium equation, $\mathbf{KU} = \mathbf{F}$, except for the fact that it involves complex numbers. Employing the complex number arithmetic, the harmonic problem can be solved with the same solver algorithm as static problems.

When more information is available, on how the dynamic loads vary in relation to the time, and when the computational resources are not scarce, no simplification has to be made. In this situation, the equations of motion can be directly solved in the time domain, instead of making use of the harmonic procedure. This is the case, for example, when the force time history is known for each time step of the numerical simulation.

5.11 Initial Conditions

For the solution of the unsteady equations of motion, it is necessary to impose the initial conditions for the system. Values have to be defined for the displacements, velocities and accelerations at the starting time step, t_0. These are $\mathbf{U}_0$, $\dot{\mathbf{U}}_0$, $\ddot{\mathbf{U}}_0$. The initial conditions may assume any physical value, which is compatible with the motion of the system. However, as long as the motion is normally not known before the simulation, the velocities and accelerations are usually set as zero.

The displacements can also be taken as zero or be obtained from the solution of the corresponding static system submitted to the initial load, $\mathbf{F}_0 = \mathbf{F}(t_0)$. The latter

is the chosen approach here, since it should reduce the amplitude and duration of initial free vibrations of the system, which would be consequence of a sudden applied step load at the initial time step, t_0. These initial conditions can be formulated as:

$$\mathbf{K}\mathbf{U}_0 = \mathbf{F}_0; \quad \dot{\mathbf{U}}_0 = \mathbf{0}; \quad \ddot{\mathbf{U}}_0 = \mathbf{0} \tag{5.39}$$

5.12 Fluid-Structure Interaction

The fluid-structure interaction (FSI) belongs to the class of so-called multi-field problems, where phenomena of distinct physical nature take place simultaneously and interact to eventually modify the system response. The fluid-structure interaction (FSI) can be bidirectional or unidirectional, i.e. two-way or one-way interaction, depending on with which intensity the fluid flow modifies the structural behaviour or the opposite way around.

5.12.1 Bidirectional Coupling

The bidirectional coupling is from the theoretical point of view the most accurate procedure for solving fluid-structure problems. With the two-way interaction, the forces originated from the fluid flow are transferred to the structure surfaces, displacing and deforming it. On the other hand, the structure motion modifies the fluid flow domain geometry as well as the fluid flow impulse.

In the bidirectional coupling the computational grids representing the fluid domain and the structure have to be updated at every simulated time step. The force transfer from the fluid to the structure is obtained with the application of the fluid pressure at the walls as surface load at the structure. The structure displacements are calculated by the finite element algorithm and used for updating the structural mesh and the fluid wall boundaries. The wall displacements are used for adapting the fluid domain grid and cause the variation of the fluid flow momentum.

The monolithic approach in the solution of the fluid-structure interaction is seldom applicable for problems of practical interest. The monolithic procedure solves the fluid and structure motion equations simultaneously. It requires matching meshes at the fluid-structure interface, which is rarely feasible for complex arbitrary geometries. The simultaneous solution procedure of all physical fields increases the stiffness of the resulting solution matrix and decreases the solver stability.

Practical fluid-structure interaction (FSI) problems are normally solved with the sequential method, as done by Einzinger [36]. As described by Flurl [45], the fluid flow and the structure motion are calculated separately, sequentially, the meshes are updated, the data is interpolated for the distinct interface grids and transferred between the finite volume (FV) model and the finite element (FE) model.

From the point of view of the numerical solver, the two-way coupling may be weak or strong. In the weak coupling, the data is transmitted between both fields only at the end of each time step calculation. In the strong coupling, the data is transferred several times for a single time step and the fluid flow and structural displacements are solved, until the defined convergence criterion is reached.

5.12.2 Unidirectional Coupling

In several practical problems, the fluid-structure interaction is dominated by only one of the physical fields. In such cases, the dominating field clearly influences the behaviour of the second one, but suffers negligible influence from it. For example, a thin flexible structure with small displacements and low oscillating velocities, as in the case of Francis runners, suffers the influence of fluid flow pressure distribution but cannot significantly affect the fluid flow dynamics. On the other hand, an enough rigid structure may modify and control the flow without being displaced or deformed.

In case of unidirectional coupling, the dominating field can be simulated without considering the second physical field. Continuing with the previous example, the transient fluid flow through the Francis turbine could be simulated without considering the structural motion and without meaningful loss of accuracy. The results from the numerical simulation of the dominating field can be used as input for the numerical evaluation of the second one. For Francis turbines, the transient pressure distribution from the CFD analysis can be used as surface load for the structure dynamic analysis, as done e.g. by Magnoli [88], Seidel et al. [141] and Guillaume et al. [56].

5.12.3 Acoustic Coupling

In the unidirectional coupling, several authors, between them Seidel et Grosse [140], Keck et al. [72], Monette, Coutu and Velagandula [106] and Guillaume et al. [56], extend the effect of the fluid on the structure with acoustic fluid finite elements. Among other authors, Rodriguez et al. [128] claim the utility of this method with experimental results, but which were not obtained under real physical boundary conditions of an operating Francis turbine runner.

For the derivation of the acoustic finite elements, massive simplifications and assumptions are applied to the Navier-Stokes equations, limiting the validity of the acoustic approach in several applications. Kinsler [73] limit the acoustic problem to fluid mediums with no viscosity, no primary flow, no variation of the mean pressure and no variation of the mean density. With such assumptions, the fluid flow momentum conservation is reduced to:

$$\frac{\partial\left(\rho c_i\right)}{\partial t} = -\frac{\partial p}{\partial x_i} \tag{5.40}$$

Considering the acoustic flow as adiabatic and small variations in pressure and density, they can be related by $\partial p/\partial\rho = a^2$, where a is the sound velocity in the fluid for the reference density, ρ_0. Linearising the dependency between pressure and density around a reference pressure, p_0, and density, ρ_0, the partial time derivative can be written as:

$$\frac{\partial\rho}{\partial t} = \frac{1}{a^2}\frac{\partial p}{\partial t} \tag{5.41}$$

Taking the gradient of the simplified momentum equation, the time derivative of the mass conservation equation and combining them together, using the pressure and density time derivative relation, the acoustic wave pressure equation is obtained.

$$\frac{1}{a^2}\frac{\partial^2 p}{\partial t^2} + \frac{\partial^2 p}{\partial x_i^2} = 0 \tag{5.42}$$

Introducing the virtual work of the pressure, δp, integrating the acoustic wave pressure equation in the volume and with some mathematical manipulation, Zienkiewicz [178] obtained the following integral expression in matricial form:

$$\int_V \frac{1}{a^2}\delta p\frac{\partial^2 p}{\partial t^2}dV + \int_V \left(\frac{\partial}{\partial \mathbf{x}}^{\mathbf{T}}\delta p\right)\left(\frac{\partial}{\partial \mathbf{x}}p\right)dV = \int_A \mathbf{n}^{\mathbf{T}}\delta p\left(\frac{\partial}{\partial \mathbf{x}}p\right)dA \tag{5.43}$$

At the interfaces between the fluid and structure domains, the normal flow velocity at the wall is equal to the normal velocity of the structure surface, $c_i n_i = \partial u_i/\partial t\; n_i$. At the interface, the simplified fluid flow momentum conservation can be rewritten in matricial form with the structural displacement derivatives, $\rho_0\,\mathbf{n}^{\mathbf{T}}\partial^2\mathbf{u}/\partial t^2 = -\mathbf{n}^{\mathbf{T}}\partial/\partial\mathbf{x}\,p$. The acoustic wave pressure integral equation becomes:

$$\int_V \frac{1}{a^2}\delta p\frac{\partial^2 p}{\partial t^2}dV + \int_V \left(\frac{\partial}{\partial \mathbf{x}}^{\mathbf{T}}\delta p\right)\left(\frac{\partial}{\partial \mathbf{x}}p\right)dV = \int_A \rho_0\,\delta p\,\mathbf{n}^{\mathbf{T}}\frac{\partial^2\mathbf{u}}{\partial t^2}dA \tag{5.44}$$

The acoustic elements are allowed to count with different shape function for the pressure distribution, N_i', in relation to the displacement shape function, N_i. In the same way as the virtual displacements, the virtual pressure, δp, is arbitrary and can be eliminated from the acoustic wave pressure equation for the individual finite elements.

$$\left(\frac{1}{a^2}\int_V \mathbf{N}'\mathbf{N}'^{\mathbf{T}}dV\right)\ddot{\mathbf{P}}_\mathbf{e} + \left(\int_V \mathbf{B}'^{\mathbf{T}}\mathbf{B}'dV\right)\mathbf{P}_\mathbf{e} + \left(\rho_0\int_A \mathbf{N}'\mathbf{n}^{\mathbf{T}}\mathbf{N}^{\mathbf{T}}dA\right)\ddot{\mathbf{U}}_\mathbf{e} = \mathbf{0} \tag{5.45}$$

The matrix $\mathbf{B}'$ combines the matricial differential operator and the pressure shape function, $\mathbf{B}' = \partial/\partial\mathbf{x}\ \mathbf{N}'^{\mathbf{T}}$. The acoustic wave pressure can be written in a compact form with the acoustic fluid mass matrix, $\mathbf{M}_\mathbf{e}^\mathbf{P}$, acoustic fluid stiffness, $\mathbf{K}_\mathbf{e}^\mathbf{P}$, and acoustic coupling matrix, $\mathbf{R}_\mathbf{e}^\mathbf{P}$.

$$\mathbf{M}_\mathbf{e}^\mathbf{P}\ddot{\mathbf{P}}_\mathbf{e} + \mathbf{K}_\mathbf{e}^\mathbf{P}\mathbf{P}_\mathbf{e} + \rho_0\mathbf{R}_\mathbf{e}^{\mathbf{P}\,\mathbf{T}}\ddot{\mathbf{U}}_\mathbf{e} = \mathbf{0} \tag{5.46}$$

If dissipation of the acoustic pressure wave is present, the term $\mathbf{C}_\mathbf{e}^\mathbf{P}\dot{\mathbf{P}}_\mathbf{e}$, where $\mathbf{C}_\mathbf{e}^\mathbf{P}$ is the acoustic fluid dissipation matrix, can be added to the left hand side of the discretised acoustic pressure wave equation.

The acoustic coupling from the structure to the fluid was achieved with the kinematic condition at the wall interface. From the fluid to the structure, this is done with the application of the area integrated acoustic pressure as surface load to the structure. The discretised structural element dynamic equilibrium equation is modified to:

$$\mathbf{M}_\mathbf{e}\ddot{\mathbf{U}}_\mathbf{e} + \mathbf{C}_\mathbf{e}\dot{\mathbf{U}}_\mathbf{e} + \mathbf{K}_\mathbf{e}\mathbf{U}_\mathbf{e} = \mathbf{R}_\mathbf{e} + \left(\int_A \mathbf{N}\mathbf{N}'^{\mathbf{T}}\mathbf{n}dA\right)\mathbf{P}_\mathbf{e} \tag{5.47}$$

The last term, related to the acoustic pressure surface load, results in $\mathbf{R}_\mathbf{e}^\mathbf{P}\mathbf{P}_\mathbf{e}$. The discretised equations for the structural dynamic equilibrium and for the acoustic pressure wave can be combined, resulting in the single matricial system to be solved.

$$\begin{pmatrix} \mathbf{M}_\mathbf{e} & \mathbf{0} \\ \rho_0\mathbf{R}_\mathbf{e}^{\mathbf{P}\,\mathbf{T}} & \mathbf{M}_\mathbf{e}^\mathbf{P} \end{pmatrix}\begin{pmatrix} \ddot{\mathbf{U}}_\mathbf{e} \\ \ddot{\mathbf{P}}_\mathbf{e} \end{pmatrix} + \begin{pmatrix} \mathbf{C}_\mathbf{e} & \mathbf{0} \\ \mathbf{0} & \mathbf{C}_\mathbf{e}^\mathbf{P} \end{pmatrix}\begin{pmatrix} \dot{\mathbf{U}}_\mathbf{e} \\ \dot{\mathbf{P}}_\mathbf{e} \end{pmatrix} + \begin{pmatrix} \mathbf{K}_\mathbf{e} & -\mathbf{R}_\mathbf{e}^\mathbf{P} \\ \mathbf{0} & \mathbf{K}_\mathbf{e}^\mathbf{P} \end{pmatrix}\begin{pmatrix} \mathbf{U}_\mathbf{e} \\ \mathbf{P}_\mathbf{e} \end{pmatrix} = \begin{pmatrix} \mathbf{R}_\mathbf{e} \\ \mathbf{0} \end{pmatrix} \tag{5.48}$$

The usage of acoustic elements for the structural simulation of Francis runners is controversial. None of the four simplifications introduced by Kinsler [73] and used in the derivation of the acoustic elements are valid for hydraulic turbines. Actually, they represent serious deviations from the real physic governing the dynamic fluid flow in hydraulic turbines. Moreover, the relative motion of the stationary components in relation to the runner cannot be covered by the acoustic elements. For these reasons, it is recommended caution in the analysis of the results obtained with the acoustic coupling in the simulation of hydraulic runners. Possible solutions would be the one-way fluid-structure interaction (FSI) or the coupled numerical calculation of the variable fields associated to the fluid and to the structure over the time.

Chapter 6

Concepts of Hydraulic Turbines

This chapter brings some basic concepts about hydraulic turbines, which are important for the better understanding of the numerical simulation results. The two main topics here are the basic working principle of hydraulic turbines as well as the essentials of the dynamic effects found especially in Francis turbines.

6.1 Machine Components

The Francis turbine is composed by the hydraulic machine, which converts most of the water total pressure difference, Δp_t, in mechanical torque at the runner, and by the generator, which converts the shaft mechanical power into electrical current. The hydraulic and electrical machines can be visualised in Figure 6.1.

The hydraulic part of the Francis turbine is composed by the spiral case, stay vanes, guide vanes, runner and draft tube, as observed in Figure 6.1. The spiral case provides the nearly homogeneous pressure and velocity distribution around the blading channels, as well as the inlet swirl. The stay vanes and guide vanes have the function to guide the flow and provide the ideal flow inlet angle for the runner. The guide vanes opening can be adjusted, so that they can determine the volume flow through the machine and optimise the flow inlet angle at the runner. The turbine runner converts the water total pressure difference, Δp_t in mechanical torque at the machine shaft. The draft tube decelerates the flow, reducing the friction losses after the runner and reducing the pressure level at the runner outlet.

For interest, other machine components, which are not direct related to the turbine hydraulic parts can also be seen in Figure 6.1.

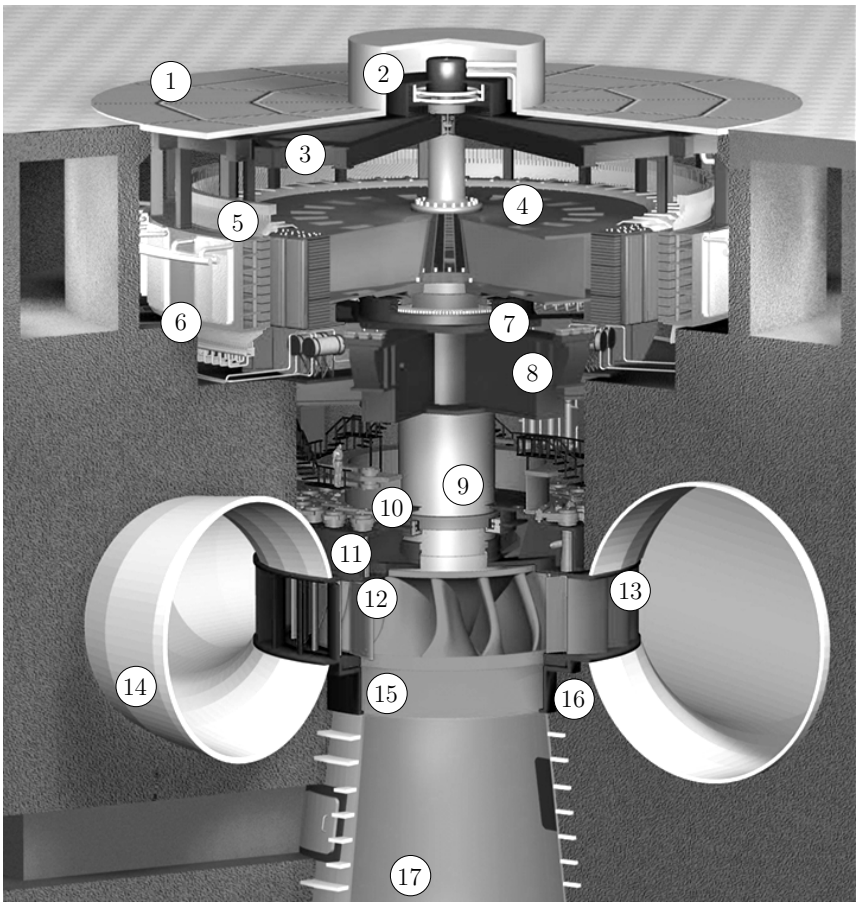

(1) Generator cover
(2) Slip ring
(3) Upper bracket
(4) Generator rotor
(5) Stator
(6) Cooling
(7) Brake
(8) Lower bracket
(9) Shaft
(10) Operating ring
(11) Head cover
(12) Guide vanes
(13) Stay vanes
(14) Spiral case
(15) Turbine runner
(16) Bottom ring
(17) Draft tube

Figure 6.1: Components in a typical Francis turbine. Adapted from Voith Hydro [162].

6.2 Coordinates and Geometric Transformations

6.2.1 Blade Coordinates

The turbine blades present elaborated tridimensional shapes, with variable inlet angle, outlet angle, wrap, camber and thickness distribution. For design purposes, these are some of the parameters, which describe the blade geometry. For the objectives of this study, especially to present the results from the numerical simulation, it suffices to locate the points on the blade surface. This is achieved with the usage of the u and v coordinates, as shown in Figure 6.2.

The u and v coordinates parameterise the blade surface and they are normalised, varying from 0 to 1. With the pair of coordinates u and v, all points can be uniquely located on the blade surface.

The u parameter runs along the blade length, from the blade trailing edge on the pressure side (TE-PS), to the blade trailing edge on the suction side (TE-SS), passing by the blade leading edge (LE). At the blade trailing edge on the pressure side

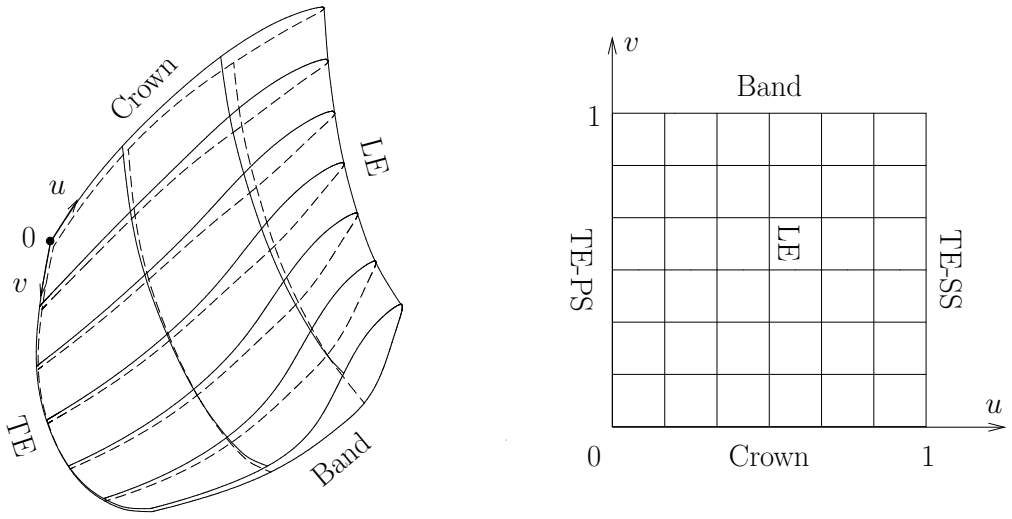

Figure 6.2: Typical coordinates from a Francis blade.

$u = 0{,}0$, at the leading edge $u \approx 0{,}5$ and at the blade trailing edge on the suction side $u = 1{,}0$. The v parameter runs over the blade, going from the crown to the band. At the crown $v = 0{,}0$ and at the band $v = 1{,}0$.

An important part of the numerical results is presented based on the u and v coordinates.

6.2.2 Meridian Plane

The cross-section of turbomachines is usually represented at the meridian plane. The machine outline, at the meridian plane, is referred to as meridian contour. For Francis turbines, the stay vanes, guide vanes, runner and draft tube cone are depicted in the meridian plane, as for example in Figure 6.3.

The meridian contour makes use of the fact that the stay vane, guide vane and runner blade geometry is always the same for every channel. In other words, the meridian contour uses the periodic symmetry property of these components and shows only the stay vanes, guide vanes and runner inlet and outlet edges and the crown, band and draft tube cone contours.

Normally, on one side of the meridian plane, the pressure side of the hydraulic components is represented, while, on the other side, the suction side can be found.

The meridian contour is obtained by the coordinate transformation $(x, y, z) \rightarrow (r, z)$. The first two Cartesian coordinates x and y are replaced by the distance to the machine rotation axis, i.e. by the radius, r, and the axial coordinate, z, is preserved.

The meridian contour contains all necessary information about the cross-section of the water passages. The meridian representation is also practical to show analytical, numerical or experimental results at hydraulic surfaces.

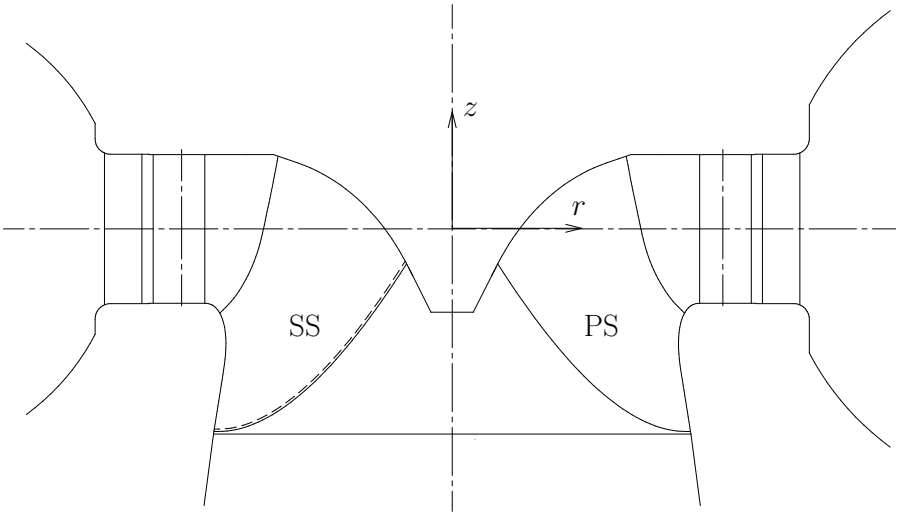

Figure 6.3: Typical meridian contour from a Francis turbine.

6.2.3 Potential Streamlines

The potential streamlines are obtained from the solution of the two-dimensional potential flow through the meridian contour. For the runner, it means the two-dimensional potential flow between crown and band, without the blade influence. Due to this simplified problem formulation, the determination of the potential streamlines becomes simply the solution of a Poisson differential equation.

The potential streamlines are presented in an example in Figure 6.4.

The coordinate m runs along each individual streamline and it is also the measure of the developed length along the streamline. The coordinate ξ is normal to the streamlines and is enough to identify them.

With the current CFD methods, the potential streamlines do not offer much relevant information about the fluid flow. However, they are needed for the application of the conformal transformation, which is often used for the design of the blade profiles.

6.2.4 Conformal Planes

For the project of turbomachines, the conformal transformation is usually employed. It offers the advantage to preserve the geometrical angles in the transformed geometry in relation to the original one. For this reason, the conformal mapping is normally used in the design of blade profiles. Still, it can also be useful for the presentation of analytical, numerical and experimental results in the blading passages, as done here. An example of conformal transformation can be visualised in Figure 6.5.

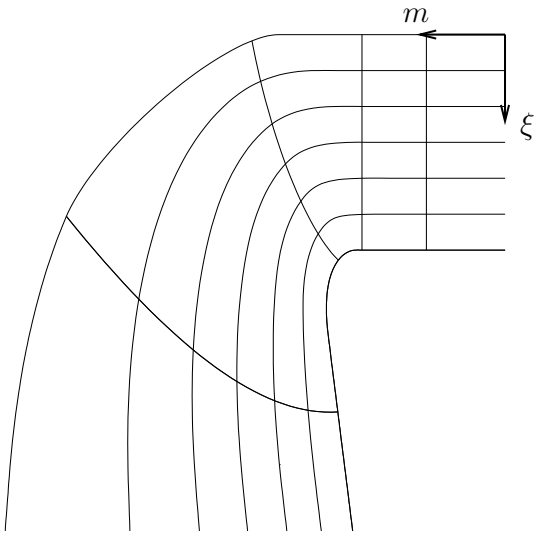

Figure 6.4: Example of potential streamlines through the meridian contour from a Francis turbine.

As exemplified in Figure 6.5, the conformal mapping, used for turbomachines, transforms the revolution surface, obtained from a given potential streamline at the meridian plane and defined by the coordinate set (r, θ, z), into a planar geometry described by the coordinate pair (χ, ℓ). Taking the constant reference radius, R, and the constant reference meridional parameter, M, the conformal coordinates are given by:

$$\chi = R\theta \ , \quad \ell = R \int_M^m \frac{dm}{r} \tag{6.1}$$

The blade angle, β_S, which is defined by $\tan \beta_S = -dm/\left(rd\theta\right)$, can be obtained from the conformal transformation by $\tan \beta_S = -d\ell/\left(Rd\theta\right)$.

6.3 Energy Conversion in the Turbine

The hydraulic turbine converts the most part of the hydraulic energy associated to the fluid total pressure difference between the head water and tail water sections, Δp_t, into mechanical power at the turbine shaft, $P_m = T\omega$. The shaft torque and rotation are given by T and ω. The total pressure difference, Δp_t, is calculated with the mass averaged quadratic flow velocity, $\tilde{c}^2$, pressure, $\tilde{p}$ and elevation, $\tilde{z}$, and with the water density, ρ, and local gravity acceleration, g.

$$\Delta p_t = \rho \frac{\Delta \tilde{c}^2}{2} + \Delta \tilde{p} + \rho g \Delta \tilde{z} \tag{6.2}$$

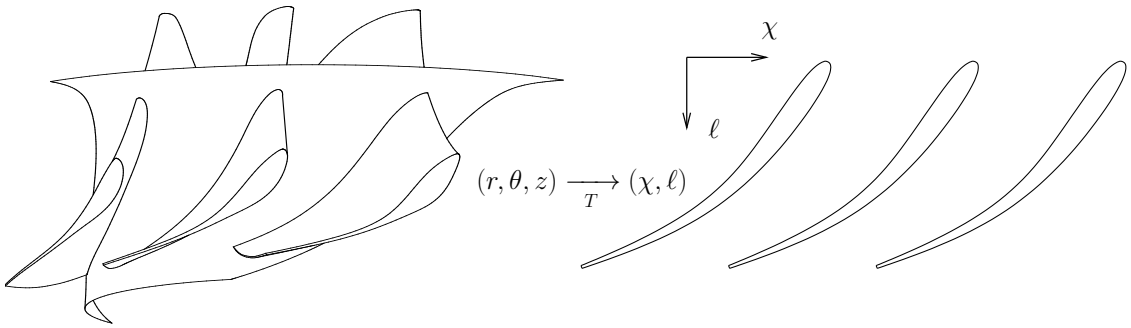

Figure 6.5: Typical conformal transformation from Francis blades.

The total pressure difference in the turbine can also be simply expressed in terms of water net head by $H = \Delta p_t / (\rho g)$, between the sections 1-1 and 2-2 in Figure 6.6. The net head is usually easily obtained by the elevation difference between head water and tail water levels, $z_{HWL} - z_{TWL}$, minus the head losses at the inlet and outlet circuits, ΔH_{inlet} and ΔH_{outlet}, before and after the turbine measuring planes 1-1 and 2-2. Figure 6.6 illustrates the water levels, hydraulic circuits and measuring planes, in relation to the turbine.

6.3.1 Power, Efficiency and Losses

The hydraulic power available for the turbine depends on the net head, H, and on the volume flow, Q. The total available power for the hydraulic turbine is $P = \rho g H Q$. However, the turbine cannot convert all the total hydraulic energy in mechanical power and the delivered power is calculated with the turbine efficiency, η:

$$P_m = \eta \rho g H Q \tag{6.3}$$

Typical peak efficiency values, η_{opt}, for high quality new Francis turbines are above 94%, for the model machine. With the non-scalable viscosity effects, there are prototype machines, which achieve almost 97% efficiency at optimum.

The head losses, ΔH, associated to the hydraulic energy conversion in the machine, can be divided among the turbine hydraulic components, i.e. spiral case, stay vanes, guide vanes, runner, runner seals, runner disc, draft tube cone and draft tube. The head losses in the different components, can also be expressed as efficiency losses through $\Delta\eta = \Delta H / H$. The relation between the efficiency losses and the turbine efficiency is simply $\eta = 1 - \Sigma\, \Delta\eta$.

6.3.2 Euler Head

According to the theory, the fluid angular momentum variation in the runner control volume between the blade inlet and outlet surfaces, respectively sections 1 and 2,

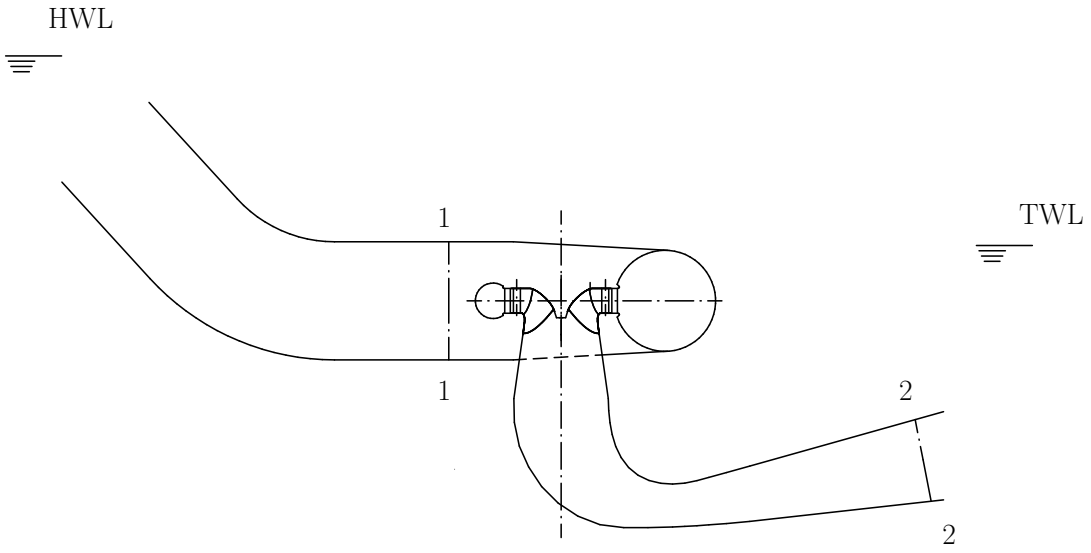

Figure 6.6: Example of Francis turbine, showing the water levels, simplified hydraulic circuits and measuring planes.

is responsible for the blade torque. Considering no transient effects neither fluid viscosity and assuming homogeneuous flow distribution at inlet and outlet for the theoretical approximation, the net head, H, can be related to the product of the radius, r, and absolute velocity tangential component, c_u.

$$\eta H = \frac{\omega}{g} \left(r_1 c_{u_1} - r_2 c_{u_2} \right) \tag{6.4}$$

The term ηH can be interpreted as the net head amount that the turbine can convert into mechanical power. With the potential fluid theory, this equation can be interpreted as the relation between the runner power and the fluid vectorial velocity variation caused by the blades geometry.

The term $(\omega/g)\, r c_u$ is defined as the local Euler head, e.g. H_{E_1} and H_{E_2} at the blades inlet and outlet. It follows immediately the expression for the Euler head, given by its variation in the runner, $H_E = H_{E_1} - H_{E_2}$ or by the effective head, $H_E = \eta H$.

In spite of the simplifications in the derivation of the Euler head, it is often used as design parameter in the development of modern Francis turbines.

The classical turbine theory, based on the potential flow, assumes homogeneous velocity distributions across the streamlines. This is reflected by the derivation of the Euler head for each streamline. Nevertheless, the Euler head or local Euler head can also be defined for arbitrary velocity distributions, through the mass flow average. This kind of averaging is useful, when the local Euler head are desired as design parameter in the evaluation of CFD simulations.

6.3.3 Velocity Triangle

The velocity components in the runner are important for the design of hydraulic turbines due to the relation between the angular momentum variation and the Euler head. The velocity triangle offers the possibility to relate the velocity coordinates in absolute and relative system to the runner rotational motion and blade angles.

Figure 6.7 shows an arbitrary conformal plane, with a typical example of the velocity triangle in the runner. The absolute velocity is represented by $\mathbf{c}$, with the tangential and meridional components, c_u and c_m. In the potential flow theory, there is no flow in the conformal plane normal direction. The meridional velocity component, c_m, is determined by the turbine volume flow and remains the same in the stationary and rotating coordinate systems. The tangential velocity component in the absolute system is c_u. The relative velocity in the runner rotating coordinate system is $\mathbf{w}$ and the peripheral velocity, associated to the runner rotational motion, is given by $U = r\omega$. The angle α is measured in the stationary coordinate system and is formed by the vectors $\mathbf{U}$ and $\mathbf{c}$. The angle between the vectors $\mathbf{U}$ and $\mathbf{w}$ refers to the rotating coordinate system and is represented by β.

Classical turbine texts, as e.g. the one from PFLEIDERER [118], assume α_1 equal to the guide vane outlet angle and β_2 equal to the runner blade outlet angle, β_{2_S}. They normally also sustain that the optimal runner blade inlet angle, β_{1_S} is the same as β_1.

Actually, the real fluid flow is more complicated than described in the potential theory. For example, α_1 is strongly influenced by the guide vane opening. However, it is not equal to the guide vane outlet angle. SCHILLING ET AL. [138] experimentally showed that the optimum runner blade inlet angle, β_{1_S}, deviates from β_1, by $\delta_i = \beta_1 - \beta_{1_S}$ different from zero. They observed that the flow outlet angle β_2 also deviates from the runner blade outlet angle β_{2_S}, with $\delta_d = \beta_2 - \beta_{2_S}$.

The relations between the vectors shown in Figure 6.7 can be analytically obtained by vectorial sum, vectorial scalar product and angular relations. The vectors can also be constructed graphically, as in Figure 6.7.

In the classical analysis of turbine blades, the flow inlet angle α_1 is derived from the guide vane opening and with the known value of c_{m_1}, $\mathbf{c}_1$ is calculated. From $\mathbf{c}_1$ and $\mathbf{U}_1$, the relative velocity vector, $\mathbf{w}_1$ can be determined. At the outlet, β_2 is derived from the blade outlet angle and, with the value of c_{m_2}, $\mathbf{w}_2$ is calculated. With known $\mathbf{w}_2$ and $\mathbf{U}_2$, the absolute velocity vector, $\mathbf{c}_2$ can be obtained.

The current modern hydraulic design process of Francis runners starts with the prescription of the Euler head at the blade outlet, H_{E_2}. Experience shows that the optimum values for H_{E_2} are function of the n_q value. From H_{E_2} and c_{m_2}, the blade outlet contour, which is function of r_2, and the blade outlet angle, β_{2_S}, are chosen. Taking the Euler head difference, for a given head, and assuming a turbine efficiency value, H_{E_1} can be calculated by $\eta H = H_{E_1} - H_{E_2}$. Experience also shows that there

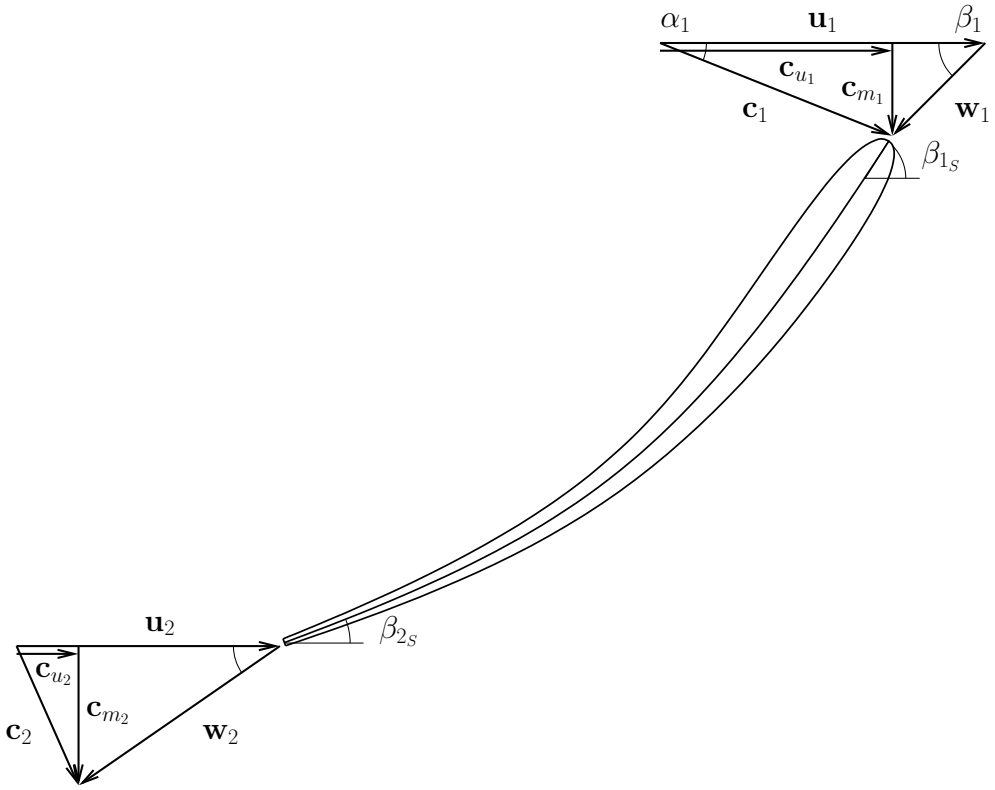

Figure 6.7: Typical velocity triangle for Francis runners.

is a range of blade inlet angles, β_{1_S}, which optimise the design. In conjunction with the required Euler head at the inlet, H_{E_1}, and c_{m_1}, the guide vane position and the blade inlet contour are determined.

The runner design is supported by CFD simulations to predict the real viscous and turbulent fluid flow and to allow the further geometric optimisation. This is an iterative design process, as long as there are several parameter combinations, which satisfy the above mentioned conditions. Moreover, there are other parameters, which influence the blade geometry, as e.g. wrap, rake angle, curvature and thickness distribution, among others. The runner blade design must not only satisfy the head requirements, but also optimise the efficiency, guarantee reasonable cavitation safety margins and provide safe mechanical design.

6.4 Hydraulic Similarity

At design phase, new turbine designs are usually tested in the laboratory or calculated at the model scale, in order to optimise and predict the prototype behaviour. The experimental or simulation results, obtained for the model machine, need to be transposed to the prototype conditions. This is only possible, if the hydraulic similarity laws are respected. In general, the geometric similarity and given sets of dimensionless numbers must be considered.

6.4.1 Dimensionless Numbers

The complete hill chart can be fully determined with two coordinates, usually the machine head, H, and flow, Q. To allow the transposition from the model to the prototype, the unit speed, n'_1, and the unit flow, Q'_1, are used to locate the points on the model hill chart.

$$n'_1 = \frac{nD}{\sqrt{H}} \ , \quad Q'_1 = \frac{Q}{D^2\sqrt{H}} \tag{6.5}$$

The machine rotation is given by n and the characteristic diameter, D, is usually chosen as D_{1_a} or D_{2_a}. The unit speed, n'_1, can be thought as an indirect measure of the head, H, while the unit flow, Q'_1, is normally associated to the machine flow, Q.

At hydraulic similar operating conditions, the model and the prototype have the same values of n'_1 and Q'_1, apart from the local gravity acceleration correction, $n'_{1_M}/n'_{1_P} = \sqrt{g_M}/\sqrt{g_P}$ and $Q'_{1_M}/Q'_{1_P} = \sqrt{g_M}/\sqrt{g_P}$. The subscripts M and P denote the model and prototype values, respectively. The prototype head or flow, for example, can be determined from the model n'_1 and Q'_1 values.

Dimensionless numbers are also defined for the unit power, P'_1, related to the turbine mechanical power, P, and for the unit torque, T'_1, associated to the turbine shaft torque, T.

$$P'_1 = \frac{P}{D^2H^{3/2}} \ , \quad T'_1 = \frac{T}{D^3H} \tag{6.6}$$

Not all dimensionless numbers are equal at the model and prototype. This is the case, for example, of the Reynolds number, Re. Such non-similarities are taken into account with corrections formulae. To remain with the example of the Reynolds number, the higher ratio between inertial and viscous forces, at the prototype, causes lower viscous losses and the model efficiency is increased, when transposed to the prototype. Other dimensionless numbers are seldom identical at the model and prototype, as for example the Froude number, Fr.

Some defined dimensionless numbers, as the specific speed, n_q, and the specific load, K, are not needed for the transposition from model to prototype conditions, but they provide information about the machine characteristic.

$$n_q = \frac{n\sqrt{Q}}{H^{3/4}} \ , \quad K = n_q\sqrt{H} \tag{6.7}$$

Hydraulic turbines are commonly classified according to the specific speed value at the best efficiency point. Typical specific speed values for Francis turbines are found between $n_{q_{opt}} = 20$ min^{-1} and $n_{q_{opt}} = 100$ min^{-1}. At low n_q values the runner flow

is predominantly radial, while at high n_q values the runner flow becomes more axial. From the dynamic point of view, Francis machines with low n_q are more affected by rotor-stator interaction (RSI) rather than by draft tube instabilities (DTI), with the opposite occurring at high n_q values, as reported by SEGOUFIN ET AL. [139].

The specific load, K, is related to the power density. It also constitutes an approximate reference number to indicate, how large the mechanical loads are. With the current technology, values of specific load around $K = 500$ denote conservative designs, while values approximating $K = 900$ are associated to aggressive designs.

6.5 Model Test

Most of the hydraulic characteristics of the turbine cannot be measured in the prototype with enough accuracy. Moreover, some hydraulic parameters, as the net head or suction head, cannot be freely imposed at the power plant. The model test offers the possibility to measure the turbine characteristic at the laboratory, with high precision. It is also used for the turbine optimisation, during the design phase, as well as to proof contractual guarantees.

For the model test, the hydraulic machine is constructed homologously to the prototype geometry at reduced scale. The model machine is mounted at the laboratory between high pressure and low pressure vessels that allow the arbitrary variation of the net and suction heads. Hydraulic pumps are responsible for regulating the head and flow.

During the model test, the hydraulic turbine can be tested at every desired operating point. Normally the efficiency, cavitation characteristics, runaway speed, hydraulic thrust, guide vane torque and pressure oscillations are measured at the model test. The measured model data is expressed in terms of dimensionless numbers, which allow the transposition to the prototype. The experimental data is often expressed as function of the dimensionless numbers n'_1 and Q'_1 and graphically represented as model hill chart, as in Figure 6.8.

Standards for the conduction of the model test, evaluation of the experimental results and transposition to the prototype can be found in the IEC STANDARD 60193 [67].

6.6 Cavitation

Cavitation might be present in hydraulic turbines under certain operating conditions. The flow acceleration, caused by smaller cross-sections or flow direction changes, can reduce the water static pressure level, p, at some regions to values below its vapour pressure, p_{va}. When this condition occurs, cavitation takes place. There are different types of cavitation patterns, depending on the machine component and

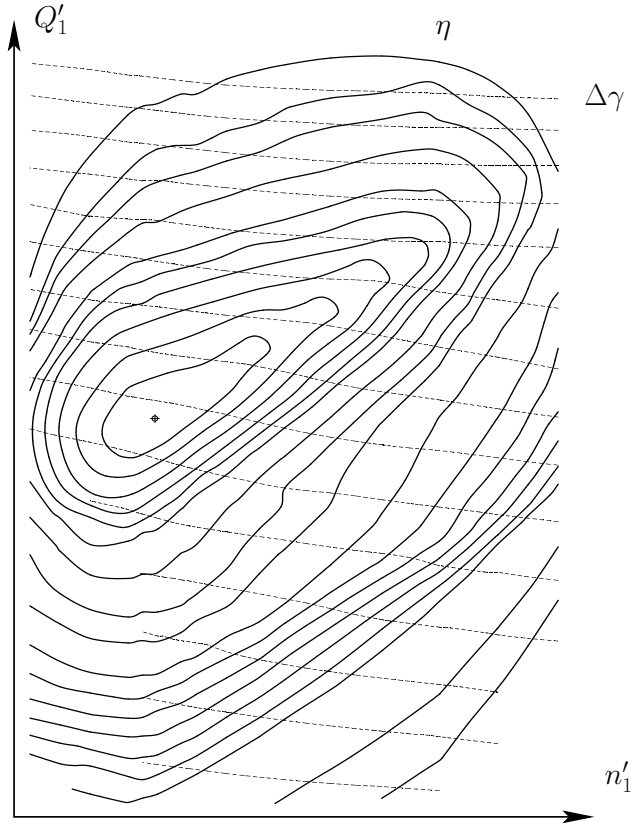

Figure 6.8: Example of model hill chart, showing efficiency and guide vane opening isocurves.

operating condition. The Thoma number, σ, defined below, is used as parameter for the cavitation phenomenon.

$$\sigma = \frac{(h_{amb} - h_{va} - H_s)}{H} \tag{6.8}$$

The ambient, i.e. barometric pressure, h_{amb}, and the water vapour pressure, h_{va}, are dependent from environment conditions and are expressed here in water column meters. The net head and the machine submergence are expressed by H and H_s.

If the highest Thoma number value at the runner blades, σ_i, becomes higher than the plant Thoma number, σ_{pl}, cavitating bubbles develop at the blades surface, configurating areal cavitation. In theory this condition can occur at any operating point. However, this is more typical at full load operation. Still, the current design of large Francis machines does not tolerate areal cavitation at real prototype conditions.

At full load and part load, an intense vortex can be found in the draft tube cone. Its swirl velocities reduce the local static pressure and brings the vortex core to cavitate. The resulting cavitating region can be well observed during the model test and allows the visualisation of the draft tube vortex. This cavitating phenomenon experiences moderate influence from the Thoma number.

When the net head exceeds the turbine operating range, considered during the design phase, leading edge cavitation might appear. At these extreme head conditions, the inflow angle at the runner deviates significantly from the one of the blades inlet and the flow separates at the runner leading edge. The separated flow develops into vortices, whose core cavitates. This kind of cavitation is connected to the separation and experiences low influence from σ_{pl}.

The channel vortex can also be observed through the cavitation phenomenon. As in the case of the leading edge cavitation, the channel vortex comes from the flow separation. At some operating conditions, the channel vortex is even related to the leading edge separation. The channel vortex experiences moderate influence from the Thoma number.

For some runner blade geometries and at given operating conditions, more typically at full load and overload, VON KÁRMÁN [163] vortex streets may develop at the trailing edges. Depending on the intensity of the vortex shedding and on σ_{pl}, the vortices might cavitate.

Although the numerical simulation of cavitation is not considered in this study, the cavitation phenomenon offers an interesting possibility to compare experimental observations with numerical results. Since the cavitating regions can be visualised during the model test, it is an indication that the pressure in this region is below the vapour pressure. When analysing the numerical simulation results, the isobarometric surfaces, with the value p_{va}, allow the qualitative comparison with the experiments.

The cavitation limits are usually marked in the hill chart, as exemplified in Figure 6.9. Detailed information about the cavitation phenomenon in hydraulic turbines can be found, among others, in FRANC ET AL. [46] and in AVELLAN [11]. Basic knowledge about the cavitation phenomenon is brought by e.g. YOUNG [175].

6.7 Operating Range and Operating Points

The turbine operating range defines a closed region of the model hill chart, where the turbine can be continuously operated. Inside the operating range, operating points are defined. These are points, at which the machine is often operated, points with special requirements or points, which are chosen for the machine design or performance evaluation. The turbine design has to guarantee in the whole operating range and especially at the operating points the agreed efficiency level, cavitation safety, pressure oscillation amplitude, hydraulic forces limit, runaway limit and structural safety, among others.

The model hill chart region, associated to the operating range, is commonly defined by curves corresponding to constant maximum head, H_{max}, constant minimum head, H_{min}, constant maximum power, P_{max}, constant maximum guide vane opening, $\Delta\gamma_{max}$, and minimum power, P_{min}, as function of the maximum power at each head.

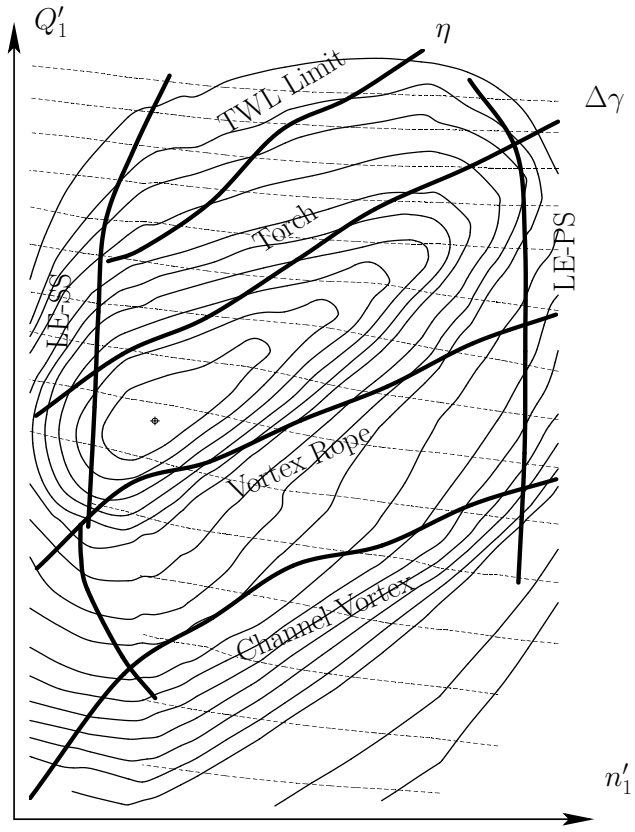

Figure 6.9: Example of cavitation limits on the model hill chart.

Figure 6.10 shows an example of operating range, defined in this way. Instead of constant guide vane opening, the higher flows may also be limited by the cavitation limit as function of the tail water level.

The maximum and minimum head limits are imposed to avoid the flow separation at the runner blades leading edge. The maximum turbine power is limited by the generator capacity. The maximum guide vane opening is imposed by mechanical limits or by the cavitation safety at the point with the highest volume flow, Q_{max}. The minimum power is often defined as a fraction of the maximum power, with the objective to limit the pressure oscillation amplitudes in the turbine and, consequently, to keep the structural loads within reasonable limits.

Some of the important points inside the operating range are associated to maximum and minimum head and maximum and minimum power. High static mechanical loads in Francis turbines are often related to the point with maximum head and maximum power, (H_{max}, P_{max}), to the point with minimum head and maximum power, (H_{min}, P_{max}), and to the point with maximum flow, Q_{max}. Normally, the two last points also present the lowest cavitation safety margin.

The part load operating points are relevant for the dynamic mechanical loads due to the pressure oscillations in the turbine. Therefore, the point with minimum head and minimum power, (H_{min}, P_{min}), and the point with maximum head and minimum power, (H_{max}, P_{min}), should be considered in the design of Francis turbines.

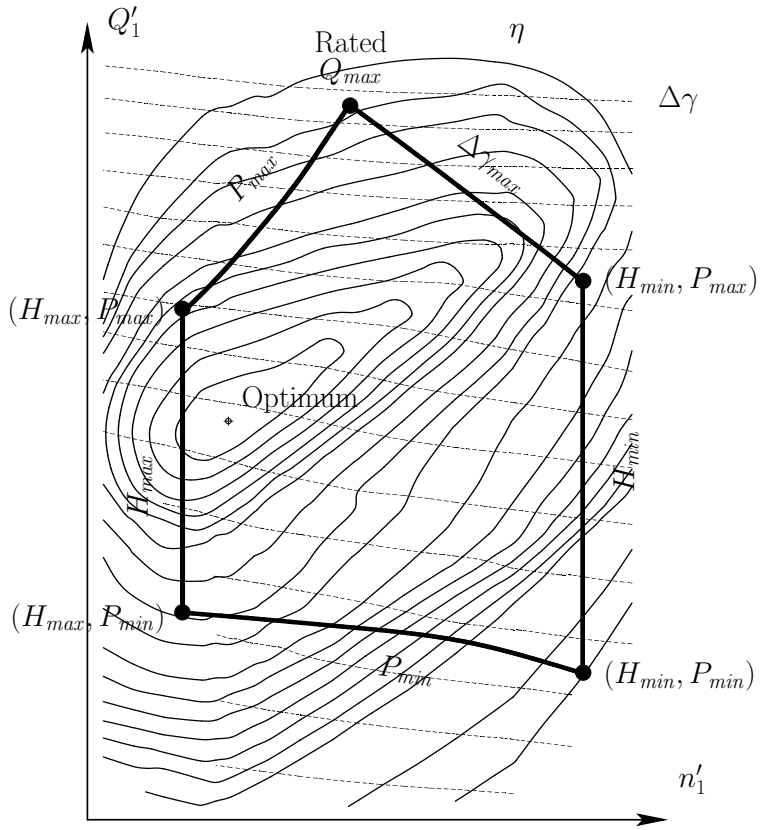

Figure 6.10: Example of prototype operating range.

The rated point definition may depend on the customer or manufacturer philosophy, often presenting more informative character rather than design meaning. The rated point is commonly defined as the point with maximum power, P_{max}, maximum flow, Q_{max}, and maximum guide vane opening, $\Delta\gamma_{max}$.

The optimum clearly corresponds to the point with the best efficiency, η_{opt}, in the overall model hill chart. Especially for machines with high specific speed, the optimum may lie beyond the leading edge cavitation limit at the blade suction side, thus, beyond the maximum head limit, outside the prototype operating range.

6.8 Instationary Effects

The operation of hydraulic turbines involves numerous dynamic aspects, concerning, among others, the fluid flow and the structure vibrations. Depending on the machine characteristics and on the operating conditions, dynamic phenomena, as rotor-stator interaction, flow instabilities, separation and vortex shedding, can take place. The runner structure is excited by these effects, leading to its dynamic motion.

In the past, hydraulic turbines counted with very massive constructions, when compared with current designs. Ulith [157] argues that, for this reason, the

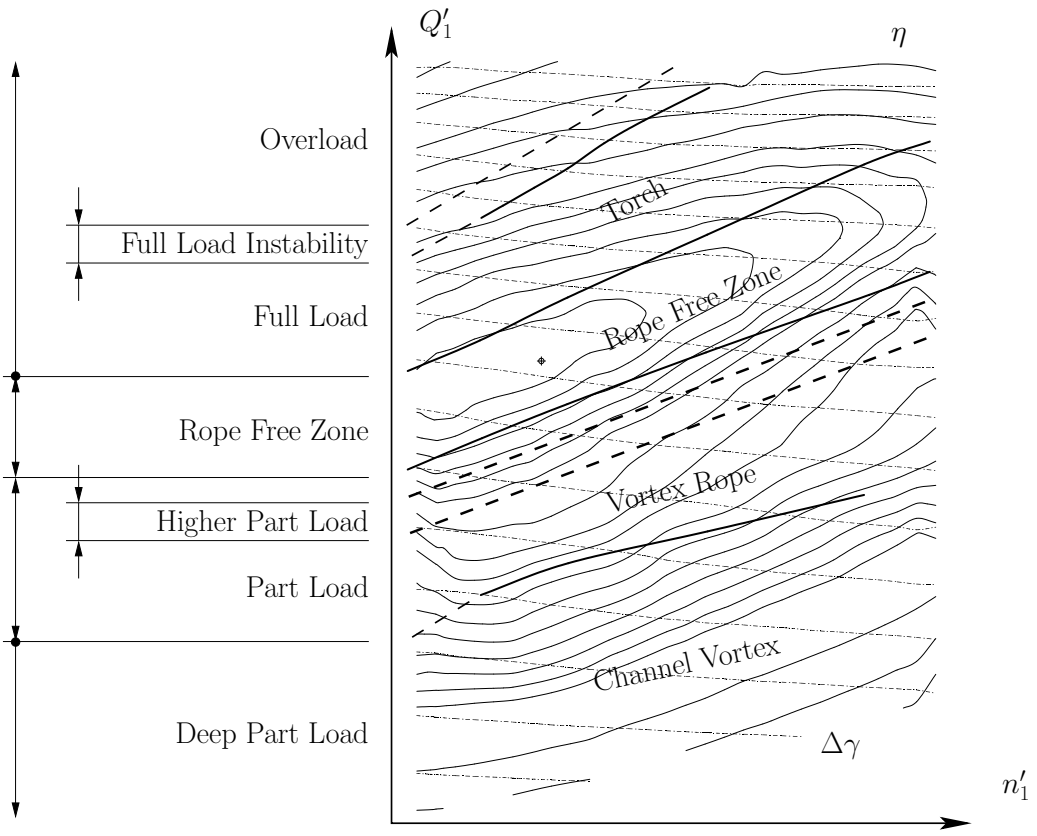

Figure 6.11: Regions related to dynamic effects in the turbine hill chart.

dynamic effects could seldom be observed in old machine constructions and that, in recent years, they became an important issue in the design of hydraulic machines.

The dynamic effects in hydraulic turbines are associated with the location of the operating points in the model hill chart. Four major regions can be identified, as seen in Figures 6.11 and 6.12. Figure 6.11 shows the different regions at the model hill chart, while Figure 6.12 qualitatively illustrates these regions over a cross section of the model hill chart. According to the dynamic effects, the different regions can be identified as the rope free zone, the full load and overload zone, the part load zone and the deep part load zone. Inside the full load and overload region, the full load instability zone may exist for particular machines. Inside the part load region, the higher part load zone might be present. The definition of these regions, their description and the theoretical discussion about the dynamic phenomena taking place in each of them are presented in the sequence. Figure 6.13 summarises the typical flow patterns observed at the model test according to the different regions.

6.8.1 Rope Free Zone

The rope free zone is usually located around the best efficiency point (BEP), i.e. around the optimum, or close to it, as depicted in Figure 6.11. In this region, the swirl at the turbine outlet is close to zero and the velocity profile at the draft tube

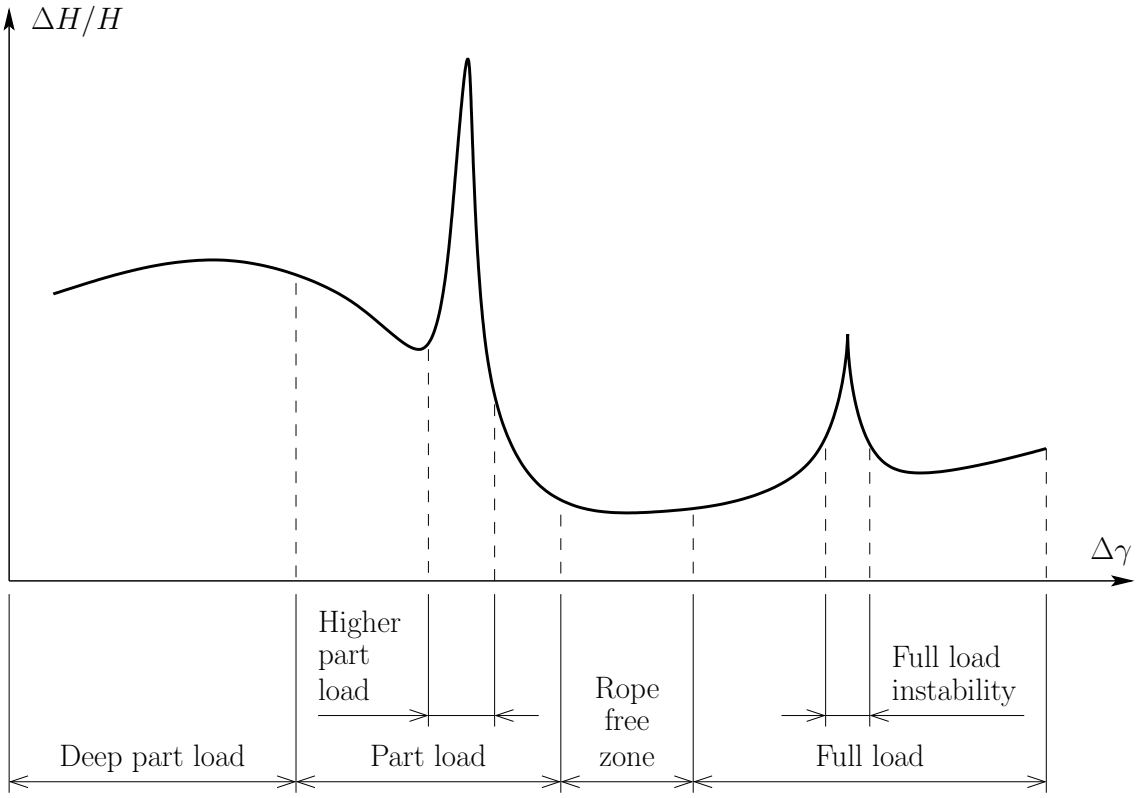

Figure 6.12: Regions related to dynamic effects at the turbine hill chart cross section.

inlet is extremely homogeneous. In the rope free zone, the pressure in the draft tube cone is high enough to prevent the flow from cavitating. Under these conditions, no important fluid flow instabilities take place in the draft tube cone and no vortex rope or torch can be observed during the turbine model test, as exemplified in Figure 6.14. Due to these favourable flow conditions, the pressure pulsations in the draft tube are considerably low.

In the rope free zone, the dynamic phenomenon, which becomes more important is the rotor-stator interaction (RSI). This effect comes from the interaction between the turbine runner, which is rotating, the guide vanes, which are stationary, and the inhomogeneous pressure distribution along the spiral case. With the relative motion between runner and guide vanes, the inflow velocity vector at the runner varies and leads to pressure pulsations. Each time that a blade leading edge passes behind the trailing edge of a guide vane, a pressure pulse is originated, being responsible for the pressure oscillations. The inhomogeneous pressure distribution at the spiral case is seen by the runner as a dynamic load, because of its rotational motion. In the rotating reference frame, the spiral case pressure distribution rotates around the runner.

The runner excitation through the spiral case pressure distribution has the same frequency as the machine rotation, f_n. The excitation through the guide vanes passage occurs with the frequency $z_0\, f_n$, where z_0 is the number of guide vanes.

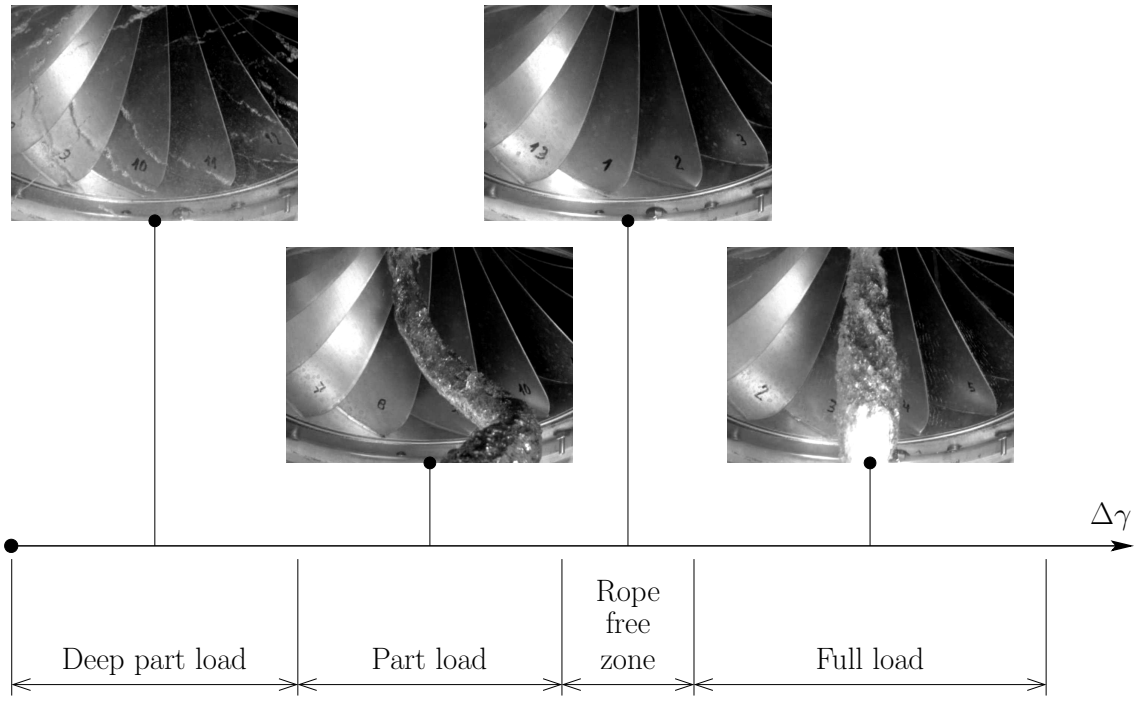

Figure 6.13: Flow patterns associated to dynamic effects in the different hill chart regions.

The rotor-stator interaction (RSI) is present in all the operating range of the machine. Its intensity mostly depends on the distance between the runner leading edge and the guide vane trailing edge, as well as on the shape of the runner leading edge. High head Francis turbines, with low n_q values, are more subjected to strong rotor-stator interaction (RSI), due to the small gap between runner and the guide vanes, while low head Francis machines, with high n_q, are not so concerned by this dynamic effect, as observed by Brekke [22].

At high head machines, with low n_q values, the distance between the runner blade inlet edge and the guide vane outlet edge is considerably small and it may lead, in some cases, to the propagation of pressure waves in the guide vanes channels, in the stay vanes channels and even in the spiral case. The pressure waves are associated to the water compressibility. This effect has already been observed in some prototype machines, as reported by Liess [85] and Dörfler [35], and it could be simulated in a Francis pump-turbine considering the water compressibility by Yan et al. [173].

6.8.2 Full Load and Overload

The full load and overload regions are situated above the rope free zone, as seen in Figure 6.11, and are characterised by the set-in of the torch vortex in the draft tube cone. Full load and overload have essentially the same characteristic and their distinction is just a matter of definition in particular projects. At full load and overload, the pressure in the draft tube cone becomes lower and brings the vortex

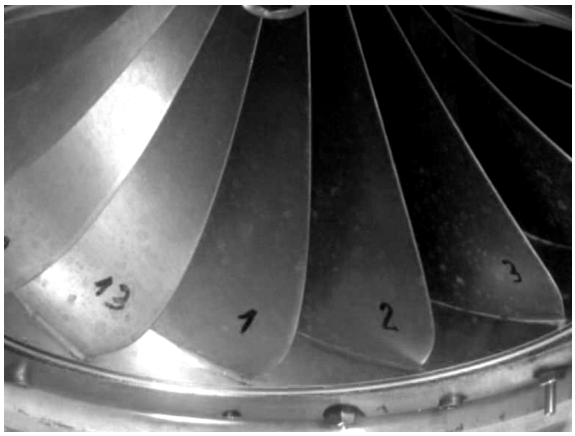

Figure 6.14: Example of the free rope zone observation during the model test.

core to cavitate, making it visible, as seen in Figure 6.15. At this operating condition, the swirl at the turbine outlet is in many cases negative and the vortex is stable, assuming a pattern similar to a torch. The pressure pulsations coming from the vortex at this operating condition are typically very low.

At full load and overload, the rotor-stator interaction (RSI) is present and is, commonly, the principal dynamic effect, being responsible for the pressure oscillations. The rotor-stator interaction (RSI) was covered in the turbine simulations performed during this study.

Most typically at full load and overload, von Kármán vortex streets may be observed at the runner trailing edge of some Francis turbines. The vortex shedding can reach high excitation frequencies and in cases, where the runner trailing edge geometry is not optimise with chamfers to reduce the amplitude of the von Kármán vortices, this effect might even lead to structural damages.

6.8.3 Full Load Instability

Few machines can experience a rare, but severe phenomenon, called full load instability, as investigated by Alligné et al. [2]. When present in the turbine, this effect is restricted to a very thin range of guide vane openings, at high opening angles, usually beyond the machine operating range. The portion of the turbine hill chart, where the full load instability may appear is located inside the full load and overload region, as shown in Figure 6.11.

The full load instability is characterised by the pulsation of the torch vortex, as described by Koutnik, Faigle and Moser [74]. Through the variation of the vortex radius, the cavitating fluid volume also changes and induce strong pressure pulsations. The symmetrical shape of the pulsating vortex produces a symmetrical pressure oscillation field in the draft tube, leading to possibly high head and torque variations in the runner. The head variations and the associated synchronous

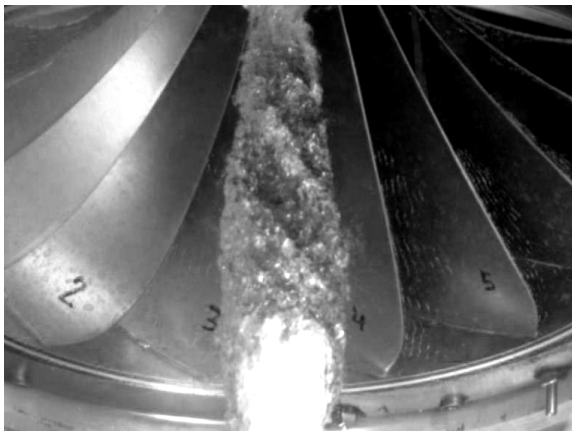

Figure 6.15: Example of the full load torch observation during the model test.

pressure pulsations might propagate through the complete machine. At the full load instability region, the torch vortex has the same appearance as in full load and overload, with the exception of its larger radius.

The occurrence and magnitude of the full load instability is highly dependent on the runner deflector geometry and on the Thoma number, σ. According to Ulith [157], in the cases where this phenomenon takes place, the volume flow is greater than 1,35 Q_{opt} and its oscillating frequency is found between $0{,}10 f_n$ and $0{,}25 f_n$. The study of this two-phase fluid flow effect is beyond the scope of this text.

6.8.4 Part Load

The part load zone is found below the rope free zone, as identified in Figure 6.11, and begins with the set-in of the rotating vortex rope in the draft tube cone. Rheingans [121] was one of the first to identify this phenomenon in hydraulic turbines. He was also able to determine the characteristic frequency of this effect, which is normally between $0{,}25 f_n$ and $0{,}35 f_n$. The vortex rope assumes a spiral shape, as observed in Figure 6.16.

The flow pattern in the draft tube is primary dependent from the volume flow and from the runner outlet swirl. At part load, the volume flow is lower than at the rope free zone and the swirl assumes increasing positive values. At these flow conditions, dynamic instabilities arise in the draft tube cone and the vortex rope is the result of the vortex breakdown, as explained by Sarpkaya [136].

The pressure pulsations at part load may assume great amplitude, being higher for machines with high n_q and being lower at low n_q values, as confirmed by Brekke [22]. The pressure oscillation under this condition is often spread through all the hydraulic passage and might be noticed even at the spiral case. The Thoma number has often limited influence on the pressure pulsations in the draft tube cone at normal part load.

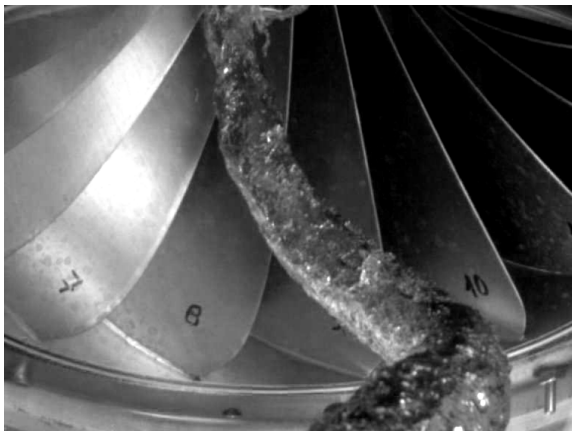

Figure 6.16: Example of the part load vortex rope observation during the model test.

Due to the important participation of part load in the pressure pulsations taking place in the machine, the investigation of this operating condition, of the associated draft tube instabilities (DTI) and of the rotating vortex rope constitutes an important part of this study.

6.8.5 Higher Part Load

The higher part load (HPL) region is located inside the part load zone, as represented in Figure 6.11, and it is limited to an extremely narrow range of guide vane openings. This phenomenon is not always present in the turbine and it strongly depends on the runner deflector geometry and on the Thoma number. The higher part load is characterised by high pressure oscillation amplitudes, normally the highest over the complete hill chart.

This phenomenon has first been identified in Francis turbines in the last decades and its essential nature is still not completely revealed. Due to the recent identification of the higher part load effect, extremely few research material is available on this topic. In one of the few publications about this subject, Koutnik et al. [75] observed that the vortex rope, at higher part load, rotates about itself, that it assumes an elliptic shape and that its frequency is typically between $2{,}5f_n$ and $5{,}0f_n$. Nicolet et al. [112] have performed the same observations as well.

To the author knowledge, until present in no published work there has been the attempt to numerically simulate the higher part load phenomenon. The very first successful numerical simulation of this effect in Francis turbines has been reported by Magnoli and Schilling [92], as part of this research work. The choice of the machine and of the operating points allowed the quite accurate numerically prediction of the higher part load phenomenon. The calculation results and the comparison with experimental data is available within the simulation results contained in this study.

6.8.6 Deep Part Load

Below the part load region, one can find the deep part load zone. It begins with the set-in of the channel vortex, as marked in Figure 6.11. The theoretical and numerical studies about the deep part load are still very limited.

The channel vortex comes from the flow separation in the runner. The separation takes place normally at the blade leading edge, but it may also occur at the crown. An example of channel vortex is found in Figure 6.17.

At moderate deep part load, the vortex rope continues influencing the pressure pulsations and the Rheingans frequency can still be found. As the turbine flow is reduced, the inlet flow angle at the runner deviates more and more from the design values and the separated flow region becomes larger. The flow becomes progressively more chaotic, up to the point that no characteristic frequency can be identified. Xingqi et al. [172] empirically identified high pressure pulsation values associated to the flow separation at deep part load.

The channel vortex is also characterised by the cavitation of the separated flow. This cavitation phenomenon might explain the strong influence of the Thoma number on the pressure pulsations at deep part load and why different machine components, e.g. spiral case and draft tube, are diversely affected by the σ values.

Because of the strong effect of the cavitation phenomenon at low volume flow values, this study was limited to the analysis of deep part load operating points close to the set-in of the channel vortex.

6.8.7 Start-Stop Operating Conditions

Some transient conditions in the turbine operation are related to the start and stop of the machine. The normal start and stop are controlled procedures, which should assure the smooth operation of the turbine. Nevertheless, malfunctions at the electric or hydraulic machine may lead to the sudden shut-off of the turbine or to the runaway condition.

Start-Stop

When the machine is started, the guide vanes are progressively opened and the turbine goes from the origin of the hill chart, $n'_1 = 0$ and $Q'_1 = 0$, to a point of small guide vane opening, where the torque is just enough to accelerate the shaft to the synchronous speed and to overcome the mechanical losses. At this condition, known as speed-no-load, the generator is synchronised with the electrical circuit and the turbine is operating in a condition similar to runaway, but at small and controlled

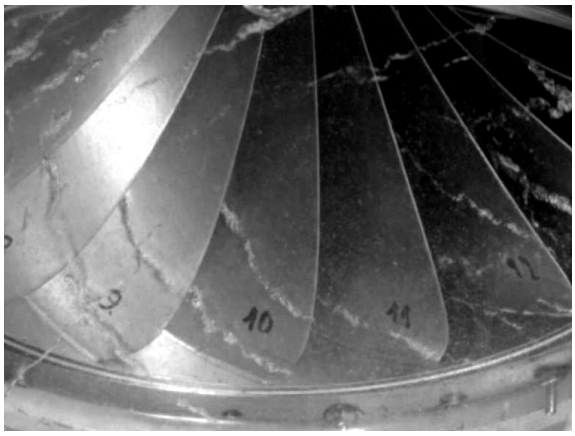

Figure 6.17: Example of the channel vortex observation during the model test.

guide vane opening. From this moment on, the machine can progressively take power load, until the desired operating point is reached.

At the normal machine stop, the power load is smoothly removed from the machine and the guide vanes are progressively closed, until the generator is disconnected from the electrical circuit. The guide vanes are completely closed and the turbine is stopped by the actuation of the generator mechanical breaks.

Speed-no-Load

When operating at speed-no-load, the machine runs at the synchronous speed and the generator is synchronised with the electric circuit, so that the machine is able to take power load at any moment. At this condition, the turbine required torque is just enough to equilibrate the mechanical losses and it operates with small guide vane openings. At speed-no-load, the machine is actually running in a condition similar to runaway, with $n'_1 = n'_{1_D}$, but at synchronous speed. Depending on the operating philosophy, some turbines might operate several hours at speed-no-load, with the objective to provide immediate power reserve to the overall electrical grid.

Load Rejection

There are exception cases, in which the machine is operating at normal power load and the generator has to be suddenly disconnected from the electrical grid. At the load rejection condition, the turbine torque is no longer equilibrated by the resistive electromagnetic moment and the machine accelerates, until the guide vanes are rapidly closed. The turbine overspeed reaches, typically, values between 15% and 40%. The fast closure of the distributor leads to a water hammer in the hydraulic circuit upstream from the guide vanes. In the runner and draft tube, the pressure assumes low values and oscillates, as consequence of the fast machine

shut-off. Typical overpressure values, caused by the water hammer, are between 15% and 50% at Francis machines.

Runaway

At the runaway condition, the generator from the hydraulic turbine is unexpectedly and suddenly disconnected from the electrical grid and the guide vanes cannot be closed, for any kind of malfunction. In this situation, the resistive electromagnetic torque at the generator disappears and does not equilibrate the turbine torque any more. The turbine accelerates up to the runaway speed, which can reach, depending on the machine design, 1,5 up to 3,0 of the nominal rotational speed, n. The dimensionless runaway speed, n'_{1_D}, can be measured during the turbine model test.

Ulith [157] explains that, at the runaway, the defective inflow angle at the runner causes the massive flow separation at almost the whole blade extension. The shaft moment becomes lower and lower, up to the point that just a thin healthy flow near to the band is responsible for the turbine torque, which is just as large as the mechanical losses.

6.8.8 Transposition to Prototype

The pressure oscillation amplitude is normally simply scaled from the model to the prototype through the head similarity, as recommended by the IEC Standard 60193 [67].

$$\frac{\Delta H_P}{\Delta H_M} = \frac{g_M}{g_P}\left(\frac{n_P}{n_M}\frac{D_P}{D_M}\right)^2 \tag{6.9}$$

In most of the cases, this approximation is enough accurate. Nevertheless, depending on the specific machine design and power plant conditions, the transposition is not completely correct. This may occur because of the non-similarities between the model and the prototype, which can be geometric or related to dimensionless numbers, as e.g. to the Froude number, Fr. In the cases of discrepancy between the model and the prototype, the influence and interaction with the power plant hydraulic circuit constitute the most probable reasons.

6.8.9 Loads for Fatigue Analysis

At the design phase, the load history definition for the runner fatigue analysis can be assumed based on the machine dynamic characteristics and on the expected operating range. For the fatigue assessment, it is necessary to know, what the

desired fatigue life is, how many hours the machine will operate at each operating condition per year, how many starts and stops are expected per day and what is the probability per year that the turbine goes into the runaway condition.

The fatigue life is defined according to the turbine manufacturer quality standards and safety factors or on customer requirements. The operating hours at each operating condition are sometimes precisely defined by the customer, otherwise, they have to be estimated from the given turbine operating points and their weights. If not defined by the customer, the number of starts and stops per day and the probability of runaway have to be assumed during the turbine design based on the experience.

At continuous operating conditions such as full load, part load, deep part load and speed-no-load, the static and alternating mechanical stresses are derived from the structural analysis, performed with the instationary fluid simulation output. The normal start and stop operating conditions are simply approximated by a dynamic mechanical load, starting from $\sigma = 0$ and whose amplitude is equal to the static mechanical load at the reached operating point, $\sigma_a = \sigma_s$ and $\sigma_m = \sigma_a/2$. Among others, this calculation procedure is suggested by Huth [66]. The same procedure is adopted for the runaway condition, but assuming that the stresses go from the normal level from continuous operating conditions to the runaway stress level.

Chapter 7

Turbine Fluid Flow Simulation

One of the main goals of this study was to apply the previously discussed mathematical and numerical methods to investigate the dynamic behaviour of real hydraulic turbines, concerning the fluid flow, the structural strength and their interaction. The precise simulation of the machine allowed achieving the additional goal of predicting the runner fatigue life and fatigue strength, leading to the objective of optimising the turbine design and avoiding structural failures.

In this context, this chapter shall explain how to apply the mathematical and numerical methods to the turbine calculation. The developed numerical model of the machine and the chosen numerical parameters are described and proofed with experimental data. The calculated results are presented and allow the deeper understanding of the hydraulic turbines dynamic behaviour and the prediction of important parameters, relevant for the machine design and operation.

7.1 Turbine Characteristics

The turbine model took as example for the investigations was a Francis vertical machine, with specific speed $n_{q_{opt}} = 80{,}3\ \text{min}^{-1}$, with recent hydraulic design and which was already used for numerous prototypes in operation today. This machine is identified here by FT 80. The model counted with $z_0 = 24$ guide vanes and $z_2 = 13$ runner blades. This turbine model was chosen, because, as stated by Farhat et al. [39], experience showed that Francis machines with high specific speeds are more susceptible to most types of instationary fluid flow phenomena, which might damage the runner in some cases. Therefore, this application example allowed drawing practical conclusions about the general dynamic behaviour of Francis turbines and, at the same time, configured a challenging case from the point of view of the numerical simulation.

7.1.1 Experimental Data

Model test results were available for the FT 80 and offered the possibility to proof part of the computational calculated values with the reality. Figure 7.1 presents the machine configuration during the model test and the measuring points. Four pressure transducers were used at the spiral case inlet and another eight, four at each draft tube outlet side, to measure the net head, H. The flowmeter for the determination of the total volume flow, Q, and the electrical devices for measuring the shaft torque, T, and rotation, n, are not shown. Four additional pressure transducers were located at the draft tube cone, with the only objective to watch the pressure fluctuations.

The measured values in the model test are expressed, through the similarity law, in terms of dimensionless parameters: the unit speed n'_1, unit flow Q'_1, unit power P'_1 and unit torque T'_1. They can be thought as indirect measures of the head, flow, power and torque.

Other values were also measured, which are themselves already dimensionless: the model efficiency η, the cavitation coefficient or Thoma number σ and the distributor or guide vane opening $\Delta\gamma$.

Considering P'_1, T'_1 and η, just one of them is necessary to fully characterise one operating point, since $P'_1 = \eta\rho g Q'_1$ and $P'_1 = 2\pi/60\ T'_1 n'_1$.

To make the results more general, they are all presented in terms of normalised variables in relation to the values at the optimum or best efficiency point (BEP). Figures 7.2 and 7.3 show the experimentally determined model hill chart. The normalised efficiency, η/η_{opt}, guide vane opening, $\Delta\gamma/\Delta\gamma_{opt}$, and unit power, $P'_1/P'_{1_{opt}}$, are plotted in Figure 7.2 as function of the normalised unit speed, $n'_1/n'_{1_{opt}}$, and unit flow, $Q'_1/Q'_{1_{opt}}$. Figure 7.3 contains the normalised opening, the Thoma number, σ, the cavitation fixed limits for the leading edge at the pressure and suction sides and the set-in of the channel vortex at deep part load. Both figures count with the graphical representation of the machine operating range and selected operating points.

Additional model hill charts are presented in Figure 7.4, where the amplitude of the pressure fluctuations, ΔP, at the four draft tube measuring points can be seen.

The pressure pulsation values contained in the experimental results were considered in relation to the time domain, i.e. they refer to the pressure signal variation along the time:

$$\Delta p\,(t) = p - \overline{p} \tag{7.1}$$

The pressure is a function of time and varies from point to point, $p = p\,(x, y, z, t)$. The same applies to the pressure oscillation, $\Delta p = \Delta p\,(x, y, z, t)$. The time-averaged

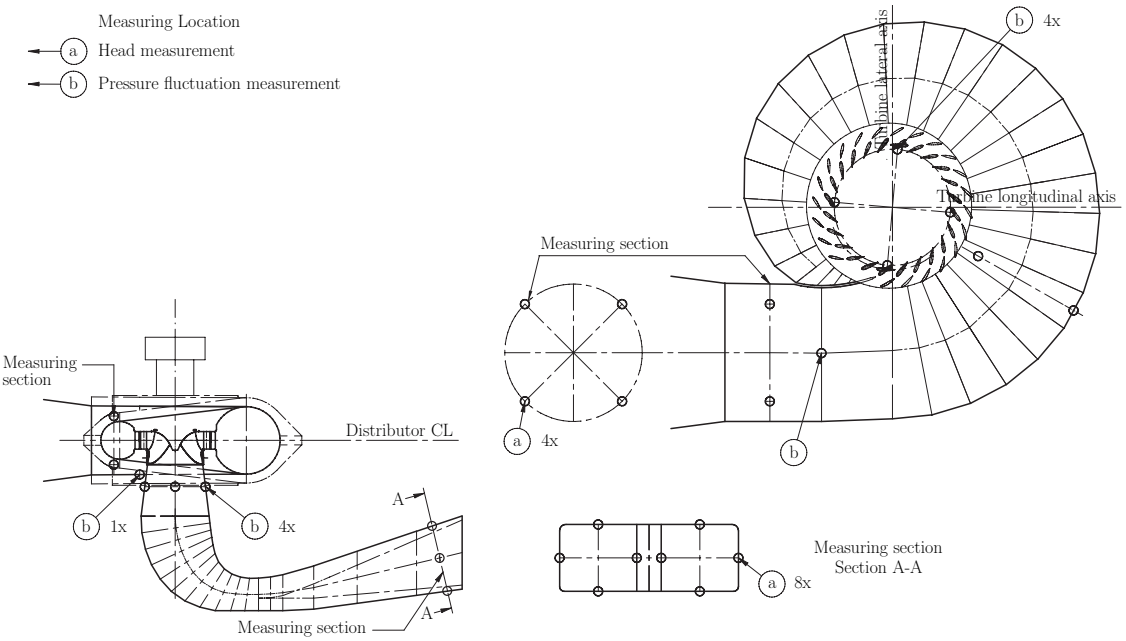

Figure 7.1: Turbine model and measuring points used in the model test.

pressure, $\overline{p} = \overline{p}\,(x, y, z)$ is approximated over the time period $t_2 - t_1$, which is chosen considerably long in relation to the phenomenon of interest.

$$\overline{p} = \frac{1}{t_2 - t_1} \int_{t_1}^{t_2} p \, dt \tag{7.2}$$

The experimental data presented here brings the pressure pulsation characteristic amplitude, as defined and recommended by the IEC Standard 60193 [67]. The characteristic amplitude is similar to the simple signal amplitude, with the difference of applying statistical methods to eliminate spurious maxima and minima, induced by the measurement error and interactions with the test rig.

As long as there were no external factors, which could perturb the numerical simulations, as it might be the case for experimental values, the pure signal amplitude was considered for the computational results.

$$\Delta P = \frac{1}{2} \left[\max p\,(t) - \min p\,(t) \right], \quad \Delta P = \frac{1}{2} \left[\max \Delta p\,(t) - \min \Delta p\,(t) \right] \tag{7.3}$$

The amplitude defined here follows the mathematical definition and is the half peak-to-peak value. Numerous studies bring the peak-to-peak value and several experiments use the expression peak-to-peak characteristic amplitude. If the comparison from the results here with other references is desired, it might be necessary, in some cases, to multiply the values here by two.

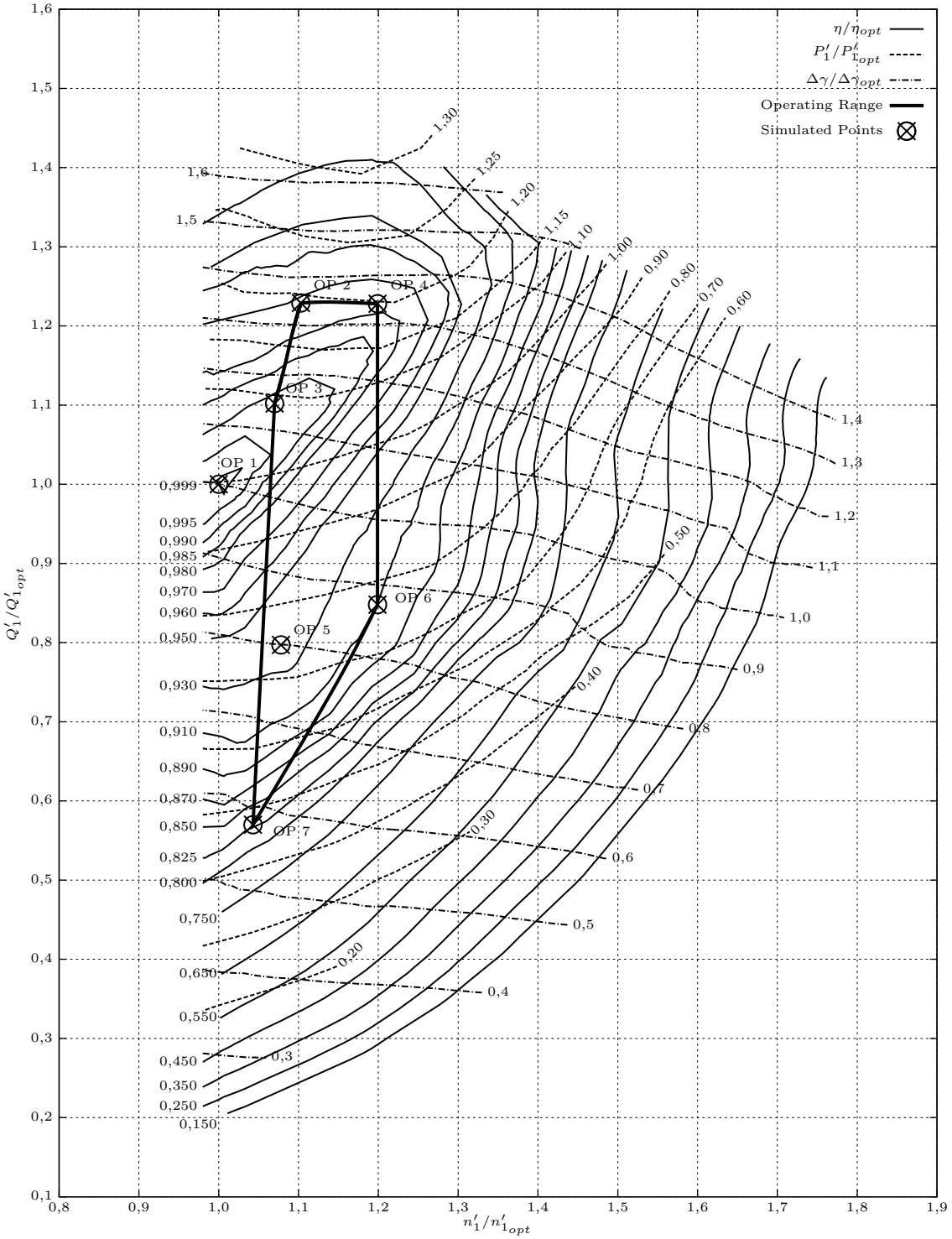

Figure 7.2: Turbine model hill chart, showing efficiency, guide vane opening, power and the simulated points.

The pressure pulsation measurements were performed at stationary points at the wall of the draft tube cone. Assuming the non-slip condition, the fluid velocity at the wall was constantly equal to zero, $c = 0$. The location of the measuring points did not change, resulting in no elevation variation, $\Delta z = 0$. Considering the

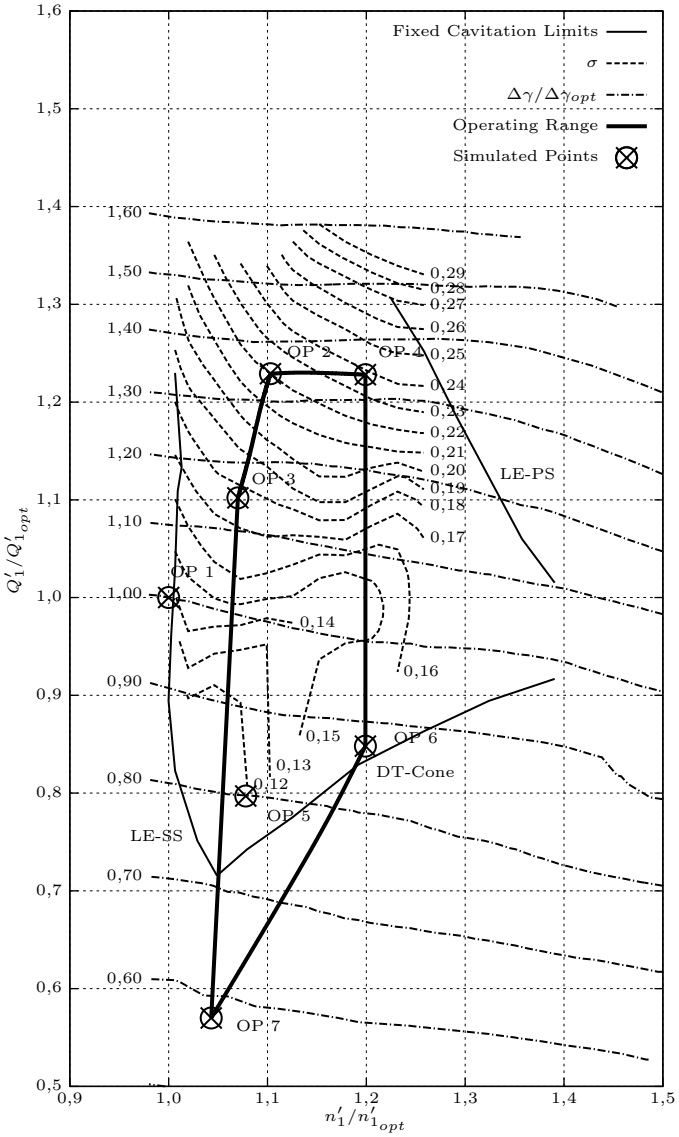

Figure 7.3: Turbine model hill chart, showing cavitation fixed limits, Thoma number, guide vane opening and the simulated points.

stationary local head at a fixed point at the wall, $h = c^2/(2g) + p/(\rho g) + z$, the head oscillation amplitude, ΔH, could be directly related to the pressure oscillation amplitude, ΔP.

$$\Delta H = \frac{\Delta P}{\rho g}, \quad \frac{\Delta H}{H} = \frac{\Delta P}{\rho g H} \tag{7.4}$$

Because of the direct relation between ΔH and $\Delta P/(\rho g)$, the pressure oscillation amplitude is often denoted by ΔH and expressed in per cent of the turbine net head as $\Delta H/H$. Nevertheless, the notation $\Delta P/(\rho g H)$ was preferred here.

At the pressure pulsation hill charts, in Figure 7.4, it can be observed that there is no experimental data available for high guide vane openings and Q'_1 values. If full

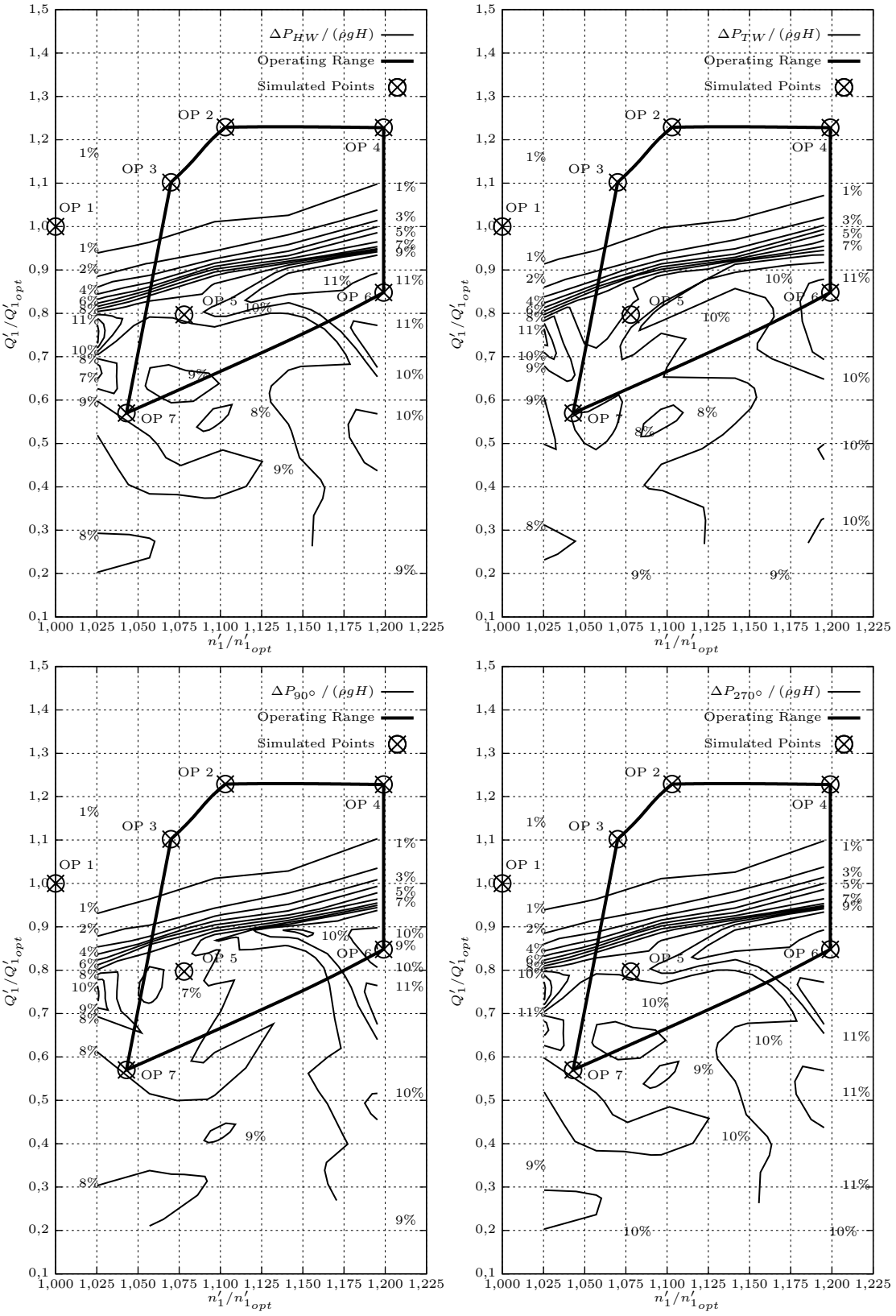

Figure 7.4: Turbine model hill chart, showing pressure pulsation amplitude and the simulated points

load instabilities were to be present in this machine, they would have been missing in the model experimental data. Since the simulation of the full load instabilities was not in the focus of this study, this limitation regarding the experimental data was not relevant here.

7.1.2 Operating Points

The operating points chosen for the numerical simulations presented most of the typical dynamic flow phenomena, which take place in Francis turbines, e.g. rotor-stator interaction (RSI), draft tube instabilities (DTI) and runner channel vortex (RCV). For all simulated points, there were experimental measurements of head, flow, efficiency and pressure pulsations. The selected operating points are presented in Table 7.1, with their normalised values for n'_1, Q'_1, T'_1 and η, as well as the pressure oscillation amplitude and frequency at the measuring points in the draft tube cone. The position of the operating points in the hill chart is plotted in Figures 7.2, 7.3 and 7.4.

The optimum is the best efficiency point, denoted by OP 1. At this point, no significant dynamic effects were to be expected, as long as the flow incidence at the runner blades and the runner outlet velocity profile are designed to be optimal, resulting in the smallest efficiency losses. This point should only pose difficulties for the numerical simulation in what concerns the rotor-stator interaction (RSI) between the spiral case, stay vanes, guide vanes and runner.

The rated operating point corresponds, in the case of the FT 80, to the prototype maximum guide vane opening, maximum power and maximum flow, identified by OP 2. Again, no important instabilities in the draft tube cone were to be expected. However, due to the high power and flow, high static structural loads were expected. From the numerical point of view, it should pose the same difficulties as the optimum point.

The operating point OP 3 is found between the optimum and rated and corresponds to the maximum prototype head at full load. Its flow characteristics should be

Table 7.1: Operating points chosen for the numerical simulations.

Operating Point	$\frac{n'_1}{n'_{1_{opt}}}$ (-)	$\frac{Q'_1}{Q'_{1_{opt}}}$ (-)	$\frac{T'_1}{T'_{1_{opt}}}$ (-)	$\frac{\eta}{\eta_{opt}}$ (-)	$\Delta P/(\rho g H)$ HW (%)	90° (%)	TW (%)	270° (%)	$\frac{f}{f_n}$ (-)
OP 1 Optimum	1,000	1,000	1,000	1,000	0,41	0,38	0,39	0,49	0,220
OP 2 Rated	1,103	1,229	1,083	0,972	0,36	0,39	0,38	0,40	0,165
OP 3 Full load high head	1,070	1,102	1,022	0,993	0,29	0,32	0,33	0,33	0,610
OP 4 Full load low head	1,199	1,228	1,000	0,977	0,32	0,35	0,39	0,39	1,740
OP 5 Part load high head	1,078	0,797	0,693	0,938	4,70	3,65	4,28	5,25	0,302
OP 6 Part load low head	1,199	0,848	0,644	0,910	5,29	4,51	5,71	6,78	0,282
OP 7 Deep part load	1,043	0,570	0,452	0,828	4,54	4,00	4,29	4,95	0,299

similar to the optimum and rated points. From the structural point of view, this point should be responsible for high stresses, because of the high head and load. The rated and the full load and high head operating points could also serve as test cases for the vortex shedding prediction at the runner trailing edges, since these vortical structures could be observed at the model test.

One additional point, OP 4, is located at the minimum head, i.e. maximum n'_1 for the plant, and maximum guide vane opening. This point is also located at the full load portion of the hill chart and was chosen because it lays at one of the limits of the machine operating range. From the numerical point of view, its simulation is similar to the three preceding points.

The remaining simulated operating points are found at part load. This flow regime is characterised by strong flow instabilities in the draft tube cone, as reported by Ciocan, Mombelli and Avellan [27]. The part load simulation constituted one interesting challenge for the numerical model. Moreover, the highest pressure pulsation amplitudes in the machine take place at part load operating conditions.

One of the simulated points is part load at high head, OP 5. At this typical part load operating point, the flow magnitude in comparison to the optimum is $Q'_1/Q'_{1_{opt}} = 0{,}797$ and its position in the model hill chart is found inside the region of high pressure pulsation amplitudes.

At part load and low head, the simulated operating point, OP 6, with $Q'_1/Q'_{1_{opt}} = 0{,}848$, is located in the narrow portion of the hill chart, where the higher part load phenomenon takes place. The pressure pulsation amplitude is even higher than at normal part load, caused by the elliptical shape and self-rotation of the vortex rope in the draft tube cone. This operating condition is very challenging for the computational model and was first numerically simulated by Magnoli and Schilling [92].

The last part load operating point, OP 7, can be found at the deep part load portion of the hill chart. This point corresponds to the lowest prototype power and flow, $Q'_1/Q'_{1_{opt}} = 0{,}569$, in its whole operating range. At this condition, the flow presents one more dynamic aspect, as long as the channel vortex is well developed inside the runner blades channel, as depicted in Figure 7.3. In several prototypes, this point would be outside of the operating range, as well as the hill chart region below the part load operating points OP 5 and OP 6. For the prototype in question here, the portion of the operating range corresponding to deep part load corresponded to approximately 10% of the operating hours.

The rated operating point, OP 2, was taken for the computational tests and validation of the numerical parameters for the stationary flow simulation.

The optimum, rated, full load at high head, part load at high head and part load at low head operating points, OP 1, OP 2, OP 3, OP 5 and OP 6, were employed for the comparison with the experimental data, regarding head, flow and efficiency.

The part load operating points OP 5 and OP 6 were also used for the verification of the instationary fluid flow simulation parameters and turbulence modelling in transient flow conditions.

At the full load operating points, OP 2, OP 3 and OP 4, the dynamic flow effect was essentially the rotor-stator interaction (RSI). The part load operating points, OP 5, OP 6 and OP 7, were dominated by the draft tube instabilities (DTI). At deep part load, OP 7, the runner channel vortex could also be observed.

The operating points OP 2, OP 3, OP 4, OP 6 and OP 7 correspond to the limits of the prototype operating range, which can be observed in Figures 7.2, 7.3 and 7.4. Together, they combine most of the dynamic fluid phenomena, which can take place in Francis turbines. These points shall also be responsible for the most extreme continuous operating conditions in the prototype machine, being of interest for the structural simulation and fatigue assessment as well.

7.2 Fluid Simulation Numerical Setup

7.2.1 General Settings

The numerical model shall reproduce as accurately as possible the model machine behaviour at the test rig. Therefore, numerous numerical schemes and parameters were tested and verified with the available experimental results. The model accuracy was assessed on terms of its agreement with the measured head, flow, torque and efficiency. To test the numerical model accuracy, 5 from the 7 different operating points in the machine hill chart were chosen. They correspond to optimum (OP 1), rated (OP 2), normal operation (OP 3), partial load at high head (OP 5) and at low head (OP 6).

The validation step is considered to be absolutely necessary, in order to achieve reliable numerical results for the intended pressure pulsations simulation. The tests and the final simulations were carried out both with the NS3D code, developed by the Institute of Fluid Mechanics (FLM) from the Munich University of Technology (TUM), and with the commercial code CFX [4] from ANSYS.

Geometry

The numerical model geometry reproduced exactly the geometry of the water passages of the spiral case, stay vanes, guide vanes, runner and draft tube. In other words, the geometry presented no deviations between the model machine and the numerical model. This statement applies to the trailing edge geometry of the runner blades as well. In the original model test, the blades trailing edges were blunt. The numerical model counted with geometric extensions at the inlet, before

the spiral case, and at the outlet, after the draft tube. The purpose was to avoid any undesirable influence of the numerical boundary conditions on the region of interest for the fluid flow.

The only simplification in the machine was the suppression of the runner seals and runner side chambers. They are respectively responsible for the seal leakage and disc friction at the runner. In Francis turbines with high specific speed, as in the case here, these secondary flows are negligible for the runner fluid dynamics. According to Liess et al. [86], Viano [160] and Schilling [137], the leakage and friction losses can be determined algebraically with empirical factors and, for the machine studied here, they represented no more than 0,22% and 0,21%, respectively.

All the simulations were performed at the model scale, allowing the direct comparison with the available experimental model test data. This approach assured the same conditions for the model test and for the numerical model, including the Reynolds, Re, and Froude, Fr, numbers similarity.

Keeping in mind the machine dimensions, another advantage was the proportionally thicker boundary layer in the model machine as in the prototype, which allowed the resolution of the boundary flow with moderate number of cells. Typical values at the model machine are $Re \approx 10^7$, while in the prototype they are typically $Re \approx 10^8$. The transposition of the model results to the prototype was carried out with the hydraulic similarity laws.

Pressure, Head, Flow, Torque, and Losses Evaluation

The net head, H, in the numerical model was evaluated in the same manner as in the model machine, following the IEC Standard 60193 [67].

$$H = \frac{\Delta p_t}{\rho g}, \quad \Delta p_t = \rho \frac{\Delta \overline{c}^2}{2} + \Delta \overline{p} + \rho g \Delta \overline{z} \tag{7.5}$$

As specified in the standard, the average of the square velocity, $\overline{c}^2$, is calculated with the area averaged velocity value, given by Q/A, where A is the cross-sectional area of the measuring section. The average pressure, $\overline{p}$, is given by the mean value of the pressure transducers measurements. The average elevation $\overline{z}$ is the mean elevation of the pressure transducers position, at each measuring section.

According to the theory, the total pressure, Δp_t, should be determined with the mass-averaged values of the square velocity, $\tilde{c}^2$, of the pressure, $\tilde{p}$, and elevation, $\tilde{z}$. However, the IEC Standard 60193 [67] specifies the head determination during the model tests as described above for practical reasons and experimental limitations. The net head calculated with the numerical model could have been evaluated with mass-averaged values, but for the consistency in the comparison with the experimental values, it followed the method specified by the IEC Standard

60193 [67]. Nonetheless, the numerical simulation results showed that the deviation in the head values computed with the experimental model test method and with the mass-averaged values was below 0,1% for the chosen simulation points.

As long as the water was assumed as incompressible, the flow in the numerical simulations, Q, was calculated by the area integration of the normal velocity at the outlet of the computational domain.

$$Q = \int c_i n_i dA \tag{7.6}$$

At the numerical model inlet and outlet, monitor points located at the same position as the pressure transducers in the model machine were responsible for the numerical pressure measurement. The elevation, z, where the numerical measurements were performed, was the same as in the model test, due to the identical geometry of the numerical and experimental models.

The numerical torque on the runner water passage was determined by the area integration of the moment caused by the pressure on the hydraulic surfaces:

$$T_k = \int r_i p_j n_j \epsilon_{ijk} dA \tag{7.7}$$

The hydraulic head losses, ΔH, at the spiral case, pre-distributor, distributor and draft tube were evaluated by the mass-averaged total pressure difference between their inlet and outlet. At the inlet and outlet of each component, control surfaces were defined and the mass-averaged total pressure was calculated at them. The efficiency loss at each component was directly calculated by $\Delta\eta = \Delta H/H$.

The head losses at the turbine runner could not be calculated only by the mass averaged total pressure difference between its inlet and outlet, because the most part of the hydraulic energy is converted in rotational work. From the total pressure difference between runner inlet and outlet, the amount, which was used for producing the runner torque, had to be subtracted, in order to obtain the runner head losses:

$$\Delta H_{ru} = \frac{\tilde{p}_{t_{ru,in}} - \tilde{p}_{t_{ru,out}}}{\rho g} - \frac{T\omega}{\rho g Q}, \quad \Delta\eta_{ru} = \frac{\Delta H_{ru}}{H} \tag{7.8}$$

The head losses at the runner seals and runner side chambers were estimated, based on the works from Liess et al. [86], Viano [160] and Schilling [137]. The head losses associated to these effects were considered in the computation of the numerically predicted turbine efficiency. For the analysed operating points, the estimated losses at the best efficiency point coming from the seals and disc friction did not exceed 0,22% and 0,21%, respectively.

The simulated total head loss in the turbine was simply the sum of the head losses in the different components. Alternatively, the total efficiency loss could be obtained by the sum of the individual efficiency losses. The turbine efficiency could be directly derived by $\eta = 1 - \Sigma\ \Delta\eta$ or $\eta = 1 - \Sigma\ \Delta H/H$.

The numerical simulated pressure pulsations were obtained directly from the time history of the calculated pressure at the monitor points in the numerical model.

Mesh Generation

The first step in the numerical model preparation was the mesh generation. As long as an important part of the pressure oscillations arises from the interaction between the stationary and rotating components, the complete machine was simulated and the computational grid considered all the machine components: spiral case, stay vanes, guide vanes, runner and draft tube.

The single components were separately meshed, using their own appropriate mesh strategy and using exclusively structured hexahedral grids. They were coupled together for the numerical simulation with non-matching interfaces. The grid for the complete machine simulation contains slightly more than 6 million cells. The stay vanes, guide vanes and runner were meshed using the IDS software, developed by the FLM, while the spiral case and the draft tube made use of the commercial code ICEM [6] from ANSYS. The turbine blading, i.e. stay vanes, guide vanes and runner, counts with the multiblock mesh strategy and with H-grids next to the blading profiles. The spiral case and the draft tube were meshed with O-grids.

Figures 7.5 and 7.6 show the finite volume grid used for the numerical simulations. At Figure 7.5, on the left, the meshing at the spiral case wall, at the stay vanes, at the guide vanes, at the runner crown and at the pier nose can be observed. On the right, the stay vanes, guide vanes, runner band and part of the draft tube can be visualised. At Figure 7.6, on the left, the spiral case and draft tube meshes can be easily identified. On the right, the O-grid at the spiral case sections and at the inlet of the draft tube can be observed, as well as the runner, guide vanes and stay vanes surface meshes.

On the left side of Figure 7.7, the multiblock strategy and the H-grid around the stay vanes, guide vanes and runner blades are showed in more detail. The grid is presented making use of the conformal transformation and corresponds to the conformal plane $v = 0{,}50$. On the right, the grid is displayed at the meridian plane.

Mesh Density

The mesh parameters were optimised to keep the grid in a reasonable size, without prejudice to the simulation accuracy. Default parameters for current automatic grid

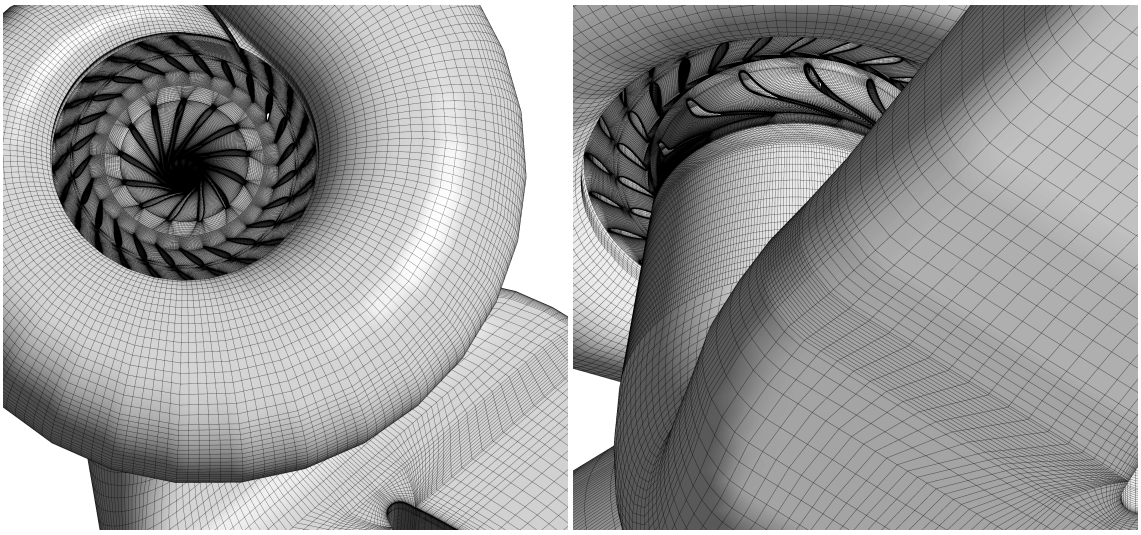

Figure 7.5: Finite volume mesh for the complete machine simulation.

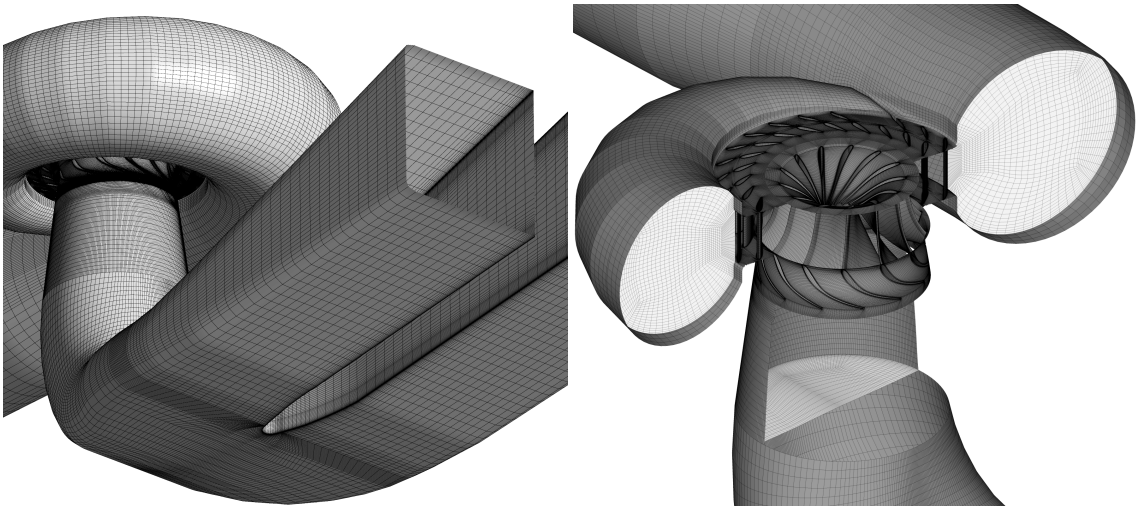

Figure 7.6: Surface and cross-section mesh for the complete machine simulation.

generators or tetrahedral meshes could have resulted in about 2 to 6 million cells just for one blading passage. The number of cells achieved here, slightly more than 6 million cells for the complete machine, is similar to other current studies, which concentrate on numerical transient simulations of the fluid flow in hydraulic turbines, as found in Yan et al. [174] and Alligné et al. [2].

The mesh resolution in the boundary layer is an important parameter, which can influence the overall grid size in the case of hexahedral meshes. Since the phenomena of interest here, rotor-stator interaction, draft tube instabilities and channel vortex, occur mainly in the core of the fluid flow, distant from the solid boundaries, wall functions were used to represent the boundary-layer behaviour. This allowed to optimise the mesh density near to the walls, with the objective to achieve y^+ values between 30 and 100 for all turbine components. It should be noticed that, due to the flow velocity in the different machine components, the distance of the first cell

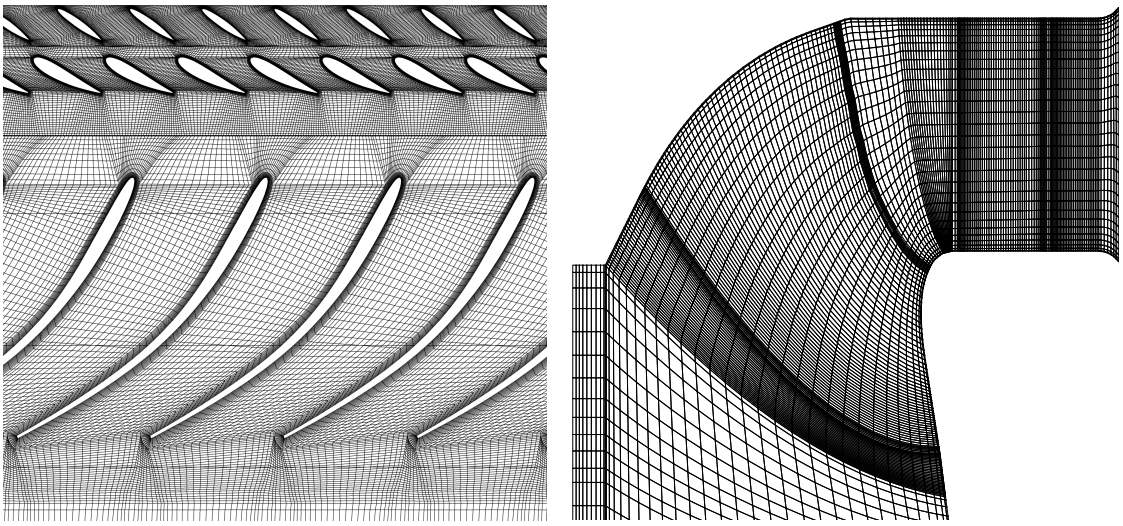

Figure 7.7: Mesh at the conformal plane $v = 0{,}50$ and at the meridian plane for the stay vanes, guide vanes and runner.

centre to the wall, y_2, can be significantly different e.g. in the runner blades and in the draft tube.

The numerical parameters were tested with the individual components and then used for the complete machine simulation. The mesh density was varied until grid independent results and y^+ values in the logarithmic region, between 30 and 100, were obtained. For the spiral case, the mesh refinement went from approximately 500 thousand to 800 thousand cells. For one blading passage, i.e. stay vane, guide vane and runner, the number of cells went from 80 thousand to 300 thousand. For the draft tube, the cell number varied from 270 thousand to 550 thousand. The maximum deviation with the finest grid, taking into account all simulated points and all measured values, was 1,6%, as seen in Table 7.2 for the rated point, whereas the maximum deviation with the coarsest mesh was 3,4%.

The deviations $\delta n'_1$ and $\delta Q'_1$ presented identical values, indicating that it came from the head estimation and not from the volumetric flow determination, as long as $n'_1 = nD/\sqrt{H}$ and $Q'_1 = Q/(D^2\sqrt{H})$, resulting in $\delta Q \approx 0$.

Table 7.2: Mesh density effect on results. Rated point.

	Simulation				Deviation			
Number of Cells	$n'_1/n'_{1_{opt}}$ (%)	$Q'_1/Q'_{1_{opt}}$ (%)	$T'_1/T'_{1_{opt}}$ (%)	η/η_{opt} (%)	$\delta n'_1$ (%)	$\delta Q'_1$ (%)	$\delta T'_1$ (%)	$\delta\eta$ (%)
$3{,}6 \cdot 10^6$	1,065	1,187	1,060	0,951	−3,4	−3,4	−2,2	−2,2
$5{,}0 \cdot 10^6$	1,079	1,203	1,070	0,960	−2,1	−2,2	−1,2	−1,2
$6{,}0 \cdot 10^6$	1,096	1,222	1,100	0,987	−0,6	−0,6	1,6	1,5
Model Test	$n'_1/n'_{1_{opt}} = 1{,}103$		$Q'_1/Q'_{1_{opt}} = 1{,}229$		$T'_1/T'_{1_{opt}} = 1{,}083$		$\eta/\eta_{opt} = 0{,}972$	

Interpolation Schemes

Distinct interpolation schemes were also evaluated. Common interpolation schemes as found, for example, in Ferziger [43] were tested. As expected, UDS and CDS resulted in inaccurate velocity and pressure distribution fields, as well as deviations in the integral measured values, as e.g. in the efficiency values, with deviations up to 5,1%. The second-order schemes MINMOD, from Harten [62], and QUICK delivered the most accurate results for all measured quantities, as seen in Table 7.3. However, MINMOD showed superior convergence behaviour, when compared to QUICK and was used for the machine simulations.

Table 7.3: Interpolation scheme effect on results. Rated point.

	Simulation				Deviation			
Interpolation Scheme	$n'_1/n'_{1_{opt}}$ (-)	$Q'_1/Q'_{1_{opt}}$ (-)	$T'_1/T'_{1_{opt}}$ (-)	η/η_{opt} (-)	$\delta n'_1$ (%)	$\delta Q'_1$ (%)	$\delta T'_1$ (%)	$\delta\eta$ (%)
UDS	1,069	1,192	1,028	0,926	−3,0	−3,0	−5,1	−4,7
CDS	1,069	1,192	1,028	0,926	−3,1	−3,1	−5,1	−4,7
QUICK	1,093	1,219	1,102	0,993	−0,9	−0,9	1,8	2,2
MINMOD	1,096	1,222	1,100	0,987	−0,6	−0,6	1,6	1,5
Model Test	$n'_1/n'_{1_{opt}} = 1{,}103$		$Q'_1/Q'_{1_{opt}} = 1{,}229$		$T'_1/T'_{1_{opt}} = 1{,}083$		$\eta/\eta_{opt} = 0{,}972$	

Turbulence Models for Stationary Simulations

The standard k-ϵ, k-ϵ LCL and k-ω turbulence models, described e.g. in Wilcox [167], as well as the k-ω SST turbulence model developed by Menter [99] were considered for the steady-state simulations. The models based on the eddy-dissipation equation provided the best results and the fastest convergence rate. Due to the non-linear formulation of the k-ϵ LCL turbulence model, the computations using it were more than 30% slower than with the standard k-ϵ model, with no noticeable accuracy improvement. Although the k-ω models produced acceptable results, with maximum deviation of 3,0%, its numerical stability and convergence were poorer. The results from the test are shown in Table 7.4.

Table 7.4: Turbulence model effect on results. Rated point.

	Simulation				Deviation			
Turbulence Model	$n'_1/n'_{1_{opt}}$ (-)	$Q'_1/Q'_{1_{opt}}$ (-)	$T'_1/T'_{1_{opt}}$ (-)	η/η_{opt} (-)	$\delta n'_1$ (%)	$\delta Q'_1$ (%)	$\delta T'_1$ (%)	$\delta\eta$ (%)
k-ϵ	1,096	1,222	1,100	0,987	−0,6	−0,6	1,6	1,5
k-ϵ LCL	1,103	1,230	1,115	0,987	0,0	0,0	3,0	1,6
k-ω	1,080	1,204	1,076	0,952	−2,1	−2,1	−0,6	−2,0
Model Test	$n'_1/n'_{1_{opt}} = 1{,}103$		$Q'_1/Q'_{1_{opt}} = 1{,}229$		$T'_1/T'_{1_{opt}} = 1{,}083$		$\eta/\eta_{opt} = 0{,}972$	

Turbulence Content

Since the inlet turbulence content is of difficult experimental determination, the prescribed inlet turbulence intensity was varied in the numerical tests from 1% up to 10%. Nevertheless, it yielded negligible variations on the calculated values. Reasons for it were possibly the long inlet pipe, about 2,5 times the spiral case inlet diameter, and the significant turbulence production in the turbine. Table 7.5 brings the simulation results.

Table 7.5: Turbulence content effect on results. Rated point.

	Simulation				Deviation			
Turbulence Intensity	$n'_1/n'_{1_{opt}}$ (-)	$Q'_1/Q'_{1_{opt}}$ (-)	$T'_1/T'_{1_{opt}}$ (-)	η/η_{opt} (-)	$\delta n'_1$ (%)	$\delta Q'_1$ (%)	$\delta T'_1$ (%)	$\delta\eta$ (%)
1%	1,103	1,230	1,116	0,987	0,1	0,1	3,0	1,6
2%	1,096	1,222	1,100	0,987	−0,6	−0,6	1,6	1,5
5%	1,102	1,228	1,104	0,977	−0,1	−0,1	1,9	0,6
10%	1,099	1,225	1,090	0,964	−0,3	−0,3	0,6	−0,8
Model Test	$n'_1/n'_{1_{opt}} = 1{,}103$		$Q'_1/Q'_{1_{opt}} = 1{,}229$		$T'_1/T'_{1_{opt}} = 1{,}083$		$\eta/\eta_{opt} = 0{,}972$	

Inlet and Outlet Boundary Conditions

In addition to the prescribed turbulence intensity, the total volume flow completed the boundary conditions set at the spiral case inlet section. At the outlet, the computational domain extension was varied, in order to avoid boundary effects and inaccuracies at the draft tube end, where the velocity and pressure fields are still of interest. As studied by Mauri [96], a rectangular extension of the outlet section was employed, with an extent of one third of the draft tube longitudinal length. The pressure was fixed to a constant reference level at the outlet section.

Numerical Solver

To represent the evaluation of the computational codes, the pressure coefficient distribution, C_p, at the rated operating condition, calculated with NS3D and CFX, was plotted in Figure 7.8 over the normalised blade surface length, s, at three conformal planes. The deviations between the two codes were minimal.

Numerical Results and Experimental Data

Table 7.6 shows the stationary simulation results, obtained with the more accurate numerical model and parameters, i.e. with the finer grid density, the MINMOD

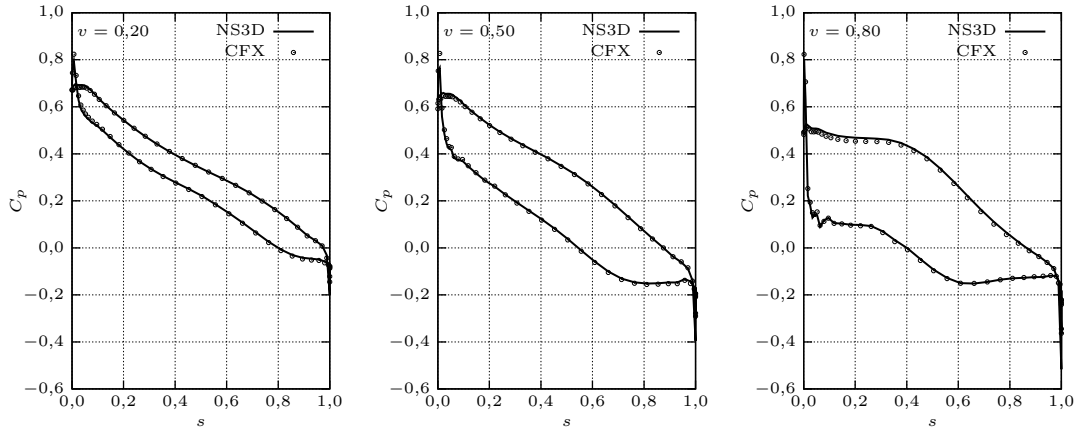

Figure 7.8: Pressure coefficient distribution, along the runner blade, at the rated point, simulated with NS3D and CFX.

interpolation scheme, the k-ϵ turbulence model, 5% turbulence intensity at inlet and the extended draft tube outlet. The computed head, flow, torque and efficiency were compared to the experimental values, measured at the test rig, in terms of dimensionless parameters, using the normalised unit speed, $n'_1/n'_{1_{opt}}$, unit flow, $Q'_1/Q'_{1_{opt}}$, unit torque, $T'_1/T'_{1_{opt}}$ and efficiency, η/η_{opt}. Considering all the simulated operating points, the deviations in the numerical results in relation to the measured model test data was considerably low, mostly not exceeding 1,0% and with a maximum computed value of 1,6%. Based on these results, the numerical model was judged to be enough accurate for the further simulation steps, which dealt with pressure pulsations, rotor-stator interaction and flow instabilities.

Figures 7.9 and 7.10 bring examples of the simulation results. The flow streamlines through the complete machine at full load can be seen in Figure 7.9. In the runner, the displayed streamlines were derived from the relative velocity in the runner rotating reference frame, instead of being obtained from the absolute velocity. At the left of Figure 7.10, the streamlines through the runner are presented together with the piezometric pressure contours. On the right, streamlines starting from the spiral case and entering into the pre-distributor and distributor can be observed.

Table 7.6: Experimental results obtained at the model test and numerically simulated results.

Operating Point	Model Test				Simulation				Deviation			
	$\frac{n'_1}{n'_{1_{opt}}}$ (-)	$\frac{Q'_1}{Q'_{1_{opt}}}$ (-)	$\frac{T'_1}{T'_{1_{opt}}}$ (-)	$\frac{\eta}{\eta_{opt}}$ (-)	$\frac{n'_1}{n'_{1_{opt}}}$ (-)	$\frac{Q'_1}{Q'_{1_{opt}}}$ (-)	$\frac{T'_1}{T'_{1_{opt}}}$ (-)	$\frac{\eta}{\eta_{opt}}$ (-)	$\delta n'_1$ (%)	$\delta Q'_1$ (%)	$\delta T'_1$ (%)	$\delta\eta$ (%)
Optimum	1,000	1,000	1,000	1,000	0,994	1,000	1,003	1,002	−0,6	−0,6	0,3	0,2
Rated	1,103	1,229	1,083	0,972	1,096	1,222	1,100	0,987	−0,6	−0,6	1,6	1,5
Normal	1,070	1,102	1,022	0,993	1,060	1,092	1,024	0,994	−1,0	−1,0	0,2	0,1
High Head	1,078	0,797	0,693	0,938	1,067	0,789	0,693	0,938	−1,0	−1,0	0,0	0,0
Low Head	1,199	0,848	0,644	0,910	1,190	0,842	0,651	0,919	−0,7	−0,7	1,0	1,0

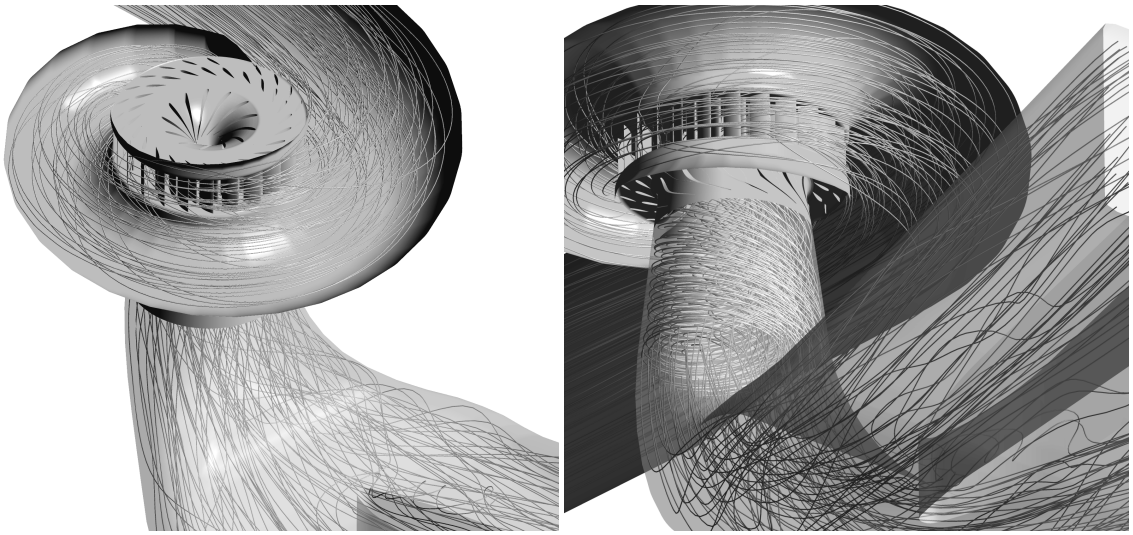

Figure 7.9: Time-averaged streamlines at full load, obtained from the complete machine simulation.

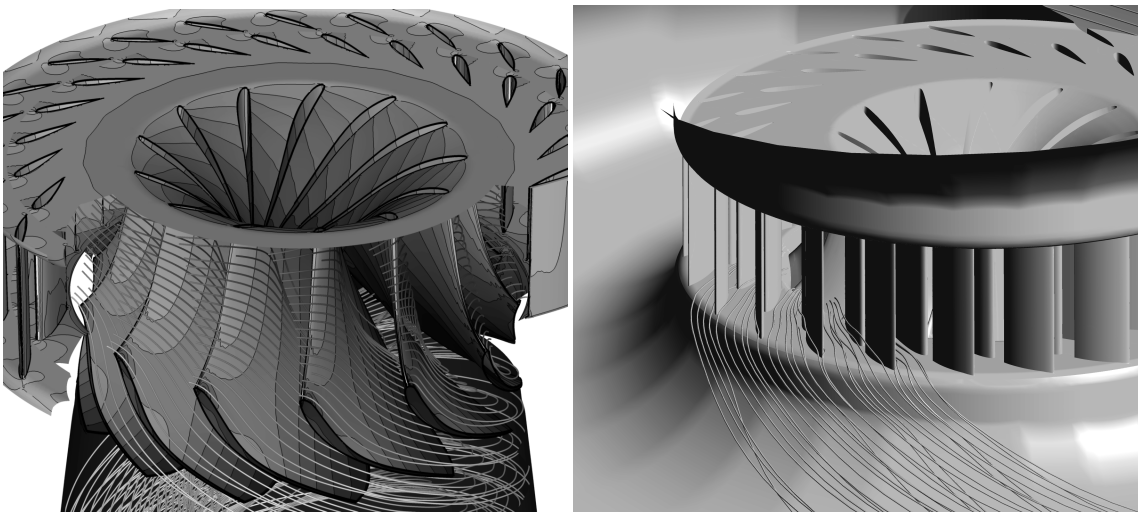

Figure 7.10: Time-averaged streamlines in the runner and in the spiral case at full load, obtained from the complete machine simulation.

7.2.2 Transient Simulation Settings

Time Step

For the transient simulations of the complete machine, several time step sizes, Δt, were considered. The sensitivity of the results to different values of Δt was checked to assure the accuracy of the numerical calculations. The time step size was also varied to optimise the computational speed, but without introducing any loss of precision at the numerical results.

Table 7.7: Size of the time steps tested for the transient simulations.

$\Delta t/T$	θ	N	N/z_2	N/z_0	Time Steps per Period			Turbulence Model
					DTI[(1)]	HPL[(1)]	VSE[(2)]	
(-)	(°)	(-)	(-)	(-)	(-)	(-)	(-)	
$8{,}50 \cdot 10^{-3}$	3,06	117,6	9,0	4,9	417,0	34,9	0,8	URANS, DES, SAS
$2{,}55 \cdot 10^{-3}$	0,918	392,2	30,2	16,3	1 391	116,3	2,5	URANS, DES, SAS
$1{,}70 \cdot 10^{-4}$	0,0612	5 882	452,5	245,1	20 858	1 744	38,2	LES

Operating point: [(1)] Part load and low head (OP 6), [(2)] Rated (OP 2).

The time step size had also to be adequate to the phenomena being studied. It had to be able to capture the dynamic effects and also to offer enough resolution to describe the relevant pressure and velocity variations along the time.

Table 7.7 brings the tested time step sizes, Δt, normalised to the machine rotation period, T. The corresponding runner rotation per time step, θ, can be read in the table as well. The number of time steps per machine revolution, N, is shown, as well as the number of time steps per guide vane and runner passage, respectively N/z_0 and N/z_2, which are important for the rotor-stator interaction (RSI). The number of time steps for one oscillation period of other fluid dynamic phenomena, i.e. draft tube instabilities (DTI), higher part load (HPL) and vortex shedding (VSE), is presented in Table 7.7. The tested turbulence models with each time step size can be found in the table.

With 117,6 time steps per machine revolution and the appropriate turbulence model, it was possible to reproduce the overall flow behaviour in the draft tube, among others the draft tube instabilities (DTI). However, at this condition, the rotor-stator interaction could not be represented in detail. To obtain adequate time resolution for the description of the interaction between the guide vanes and the runner, 392,2 time steps per machine revolution were used. It corresponded to 0,918° per time step. This resulted in 30,2 time steps per runner blade passage and 16,3 time steps per guide vane passage. This was the time step chosen for obtaining the transient results.

The number of time steps per runner and guide vane channel and per oscillation period did not correspond to an integer number, in order to avoid meeting the oscillatory pressure pulsation signal always at the same point. With the non-integer numbers of time steps for a complete oscillation period, the periodic time signal was met at different points at each cycle. This simple procedure reduced the chances of systematically missing maxima and minima of the pressure oscillation curve.

The time step size had a direct impact on the total elapsed time for the numerical computations. On one hand, the reduced time step size implied in a larger number of time discretisation points for a machine rotation. On the other hand, with smaller time steps, fewer iterations were needed to achieve convergence within a given time step. Using 392,2 time steps per machine revolution was about 8 times

faster than using 5 882 and about twice slower than using 117,6. As a reference for the computation speed, 1,7 machine rotations with 392,2 time steps per revolution could be computed within 24 hours in a Linux cluster with 8 Intel Q6600 processors, each with 4 kernels, 2,4 GHz and 2 GB memory.

The transient simulation was initialised with the stationary solution corresponding to the operating point being simulated. The main flow through all turbine components, i.e. from the spiral case inlet until the draft tube exit, was only stabilised after all the initial fluid volume had left the machine, passing the outlet section of the computational finite volume model. In the case of the FT 80 turbine, it corresponded to approximately 34 machine revolutions, at the rated operating point, OP 2. This initial simulation period did not bring physical information about the machine behaviour. Nevertheless, it was absolutely necessary to guarantee the correctness of the numerical results simulated afterwards. Waiting for the initial fluid volume to let the machine was essential for the validity of the numerical simulations.

To speed up the solution process, the first revolutions, which were computed until the initial fluid volume had left the machine and which were discarded for the analysis, were simulated with 196,1 time steps per turbine rotation. The time step size was progressively reduced until 392,2 time steps per rotation were reached. After the initial fluid volume let the machine, 30 runner rotations were computed for each simulated operating point for the evaluation of the turbine dynamic behaviour.

The time step sizes were tested with different turbulence models. They had influence on the stability of the numerical solution. With URANS, SAS and DES, the numerical convergence could be reached already with 117,6 time steps per runner revolution. On the other hand, the LES simulation diverged even with 392,2 time steps per machine revolution. With $N = 5\,882$, it could be carried out.

With the finest time resolution and LES, it was even possible to numerically reproduce the von Kármán vortex streets at the trailing edge of the runner blades. However, the resulting vortex shedding phenomenon should be analysed with caution. In opposition to the rotor-stator interaction (RSI), draft tube instabilities (DTI) and runner channel vortex (RCV), where the structure vibrational motion exercises no noticeable influence on the fluid flow, the vortex shedding effect can be strongly affected by it.

At the rated operating point, the volume flow and the velocities were higher than at the other calculated operating points. At this condition, the Courant number, *CFL*, resulting from the LES simulation with 5 882 time steps per machine revolution is reproduced in Figure 7.11. The Courant number distribution at the stay vanes, guide vanes and runner is shown at three different conformal planes, near to crown, at the middle of the blades and near to band. The resulting values were always smaller than one and in most regions even smaller than 0,5. It respected the recommendations for LES simulations, as suggested by Wunderer [170] for example.

The URANS, SAS and DES simulations employed time steps 15 times larger and consequently resulted in corresponding Courant number values 15 times larger as

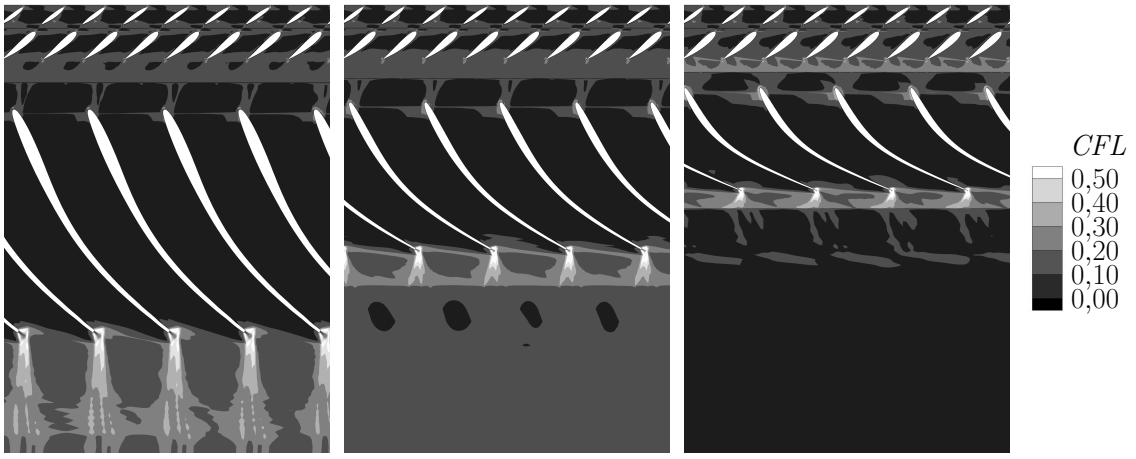

$v = 0{,}20$ $v = 0{,}50$ $v = 0{,}80$

Figure 7.11: Courant number, *CFL*, for the LES simulation of the rated point, at different conformal planes and $\Delta t/T = 1{,}70 \cdot 10^{-4}$.

well. As seen in the results from the transient flow simulation through the hydraulic turbine, which are presented further on, the SAS and DES simulations could produce as accurate results as LES, even with greater values for *CFL*.

Besides the recommendation of $CFL \leq 1{,}0$ for LES simulations, the time step size for LES was limited in this problem, as discussed before, by the numerical convergence. In the calculations performed for the turbine, LES was unable to reach convergence with the time step size employed with SAS and DES. For this reason, the hybrid models SAS and DES could offer significant smaller computational times, when compared to LES, with no deterioration of the simulation accuracy.

Solver

The numerical procedure for solving the transient time steps was tested. As stated by Ferziger, Perić [43], multigrid methods brought no acceleration to the numerical solution of the transient fluid flow equations. The BCGSTAB solution method was as fast as the multigrid method, with the additional advantage of introducing no artificial numerical oscillations in the computed transient pressure signals. Its better numerical stability was possibly related to the very different turbulent scales present in the complete machine simulation, as for example in the runner channels in contrast to the draft tube.

The last test related to the solution of the transient fluid motion equations dealt with the use of double or single computational precision. No deviation could be identified in the results obtained with single or double precision. Therefore, the simulations were carried out with single precision, with the advantage of running twice as fast as with double precision.

Turbulence Modelling and Experimental Data

In order to properly reproduce the flow transient effects, adequate turbulence models were essential. They should allow the dynamic flow structures to develop, without the introduction of excessive dissipation and artificial damping. The turbulence modelling constituted an essential part of the transient numerical model and was determinant for the success of the numerical calculations.

The URANS, SAS, DES and LES turbulence models were tested, with focus mainly on the draft tube instabilities. To verify the accuracy and suitability of the different turbulence models for the simulation of the transient flow in hydraulic turbines, the numerical calculated results were compared with the available model test data.

The part load at high head and part load at low head operating points, OP 5 and OP 6, were chosen for the evaluation of the turbulence models. These points were chosen, firstly because they were responsible for causing the highest pressure pulsation amplitudes in the draft tube cone, as seen in the model hill chart, and secondly because of the numerical difficulty to qualitatively and quantitatively reproduce the rotating vortex rope in the draft tube cone. Therefore, these points could offer meaningful and challenging test conditions for the turbulence modelling.

The pressure pulsation values measured in the draft tube cone during the model test were compared with the simulated values calculated with each one of the tested turbulence models. The comparison of the amplitude values could indicate, if they were enough accurate and which of them were more accurate for the problem being solved here. Moreover, the comparison of the simulated vortex rope shape with the observed one could also give one more indication of the precision of the turbulence modelling.

Tables 7.8 and 7.9 present the pressure oscillation amplitudes at the four measuring points at the draft tube cone and the vortex rope rotation frequency. Table 7.8 brings the results for part load at high head, OP 5, and Table 7.9 for part load at low head, OP 6. The experimental results from the model test and the calculated values with URANS, SAS, DES and LES can be found in both tables.

The tables show that URANS was absolutely unable to reproduce the dynamic flow effects in the draft tube, resulting in unacceptable deviation values for the pressure oscillation amplitude and frequency. The weak performance of URANS was due to its introduction of excessive damping in the numerical simulations. This characteristic of URANS at transient problems had already been observed by e.g. Fröhlich and Rodi, among many others, for much simpler problems.

On the other hand SAS, DES and LES delivered nearby similar results and all three showed up to be able to properly reproduce the flow dynamic behaviour in the Francis turbine. The comparison of the numerical and experimental results points it out. At part load and high head, OP 5, the maximum deviations between the experimental values and the ones calculated with SAS, DES and LES were

Table 7.8: Experimental results obtained at the model test and numerically simulated results, at part load and high head.

Turbulence Model	Results $\Delta P/(\rho g H)$ HW (%)	90° (%)	TW (%)	270° (%)	$\frac{f}{f_n}$ (-)	Deviation $\delta\Delta P$ HW (%)	90° (%)	TW (%)	270° (%)	δf (%)
URANS	0,07	0,08	0,07	0,06	20,82	−98,5	−97,8	−98,4	−98,9	6794
SAS	4,31	3,23	3,85	4,52	0,298	−8,3	−11,5	−10,0	−13,9	−1,3
DES	4,18	3,02	3,84	4,59	0,301	−11,1	−17,3	−10,3	−12,6	−0,3
LES	5,02	3,52	4,31	5,02	0,309	6,8	−3,6	0,7	−4,4	2,3
Model Test	$\frac{\Delta P}{\rho g H} = 4{,}70\%_{(HW)}$		$\frac{\Delta P}{\rho g H} = 3{,}65\%_{(90°)}$		$\frac{\Delta P}{\rho g H} = 4{,}28\%_{(TW)}$		$\frac{\Delta P}{\rho g H} = 5{,}25\%_{(270°)}$		$\frac{f}{f_n} = 0{,}302$	

Table 7.9: Experimental results obtained at the model test and numerically simulated results, at part load and low head.

Turbulence Model	Results $\Delta P/(\rho g H)$ HW (%)	90° (%)	TW (%)	270° (%)	$\frac{f}{f_n}$ (-)	Deviation $\delta\Delta P$ HW (%)	90° (%)	TW (%)	270° (%)	δf (%)
URANS	0,07	0,11	0,11	0,09	0,069	−98,6	−97,5	−98,1	−98,6	−75,8
SAS	5,04	4,44	5,94	6,40	0,315	−4,7	−1,6	4,0	−5,6	11,7
DES	5,47	4,13	5,41	6,24	0,295	3,4	−8,4	−5,3	−8,0	4,6
LES	5,30	4,41	5,77	6,70	0,294	0,4	−2,3	1,1	−1,3	3,8
Model Test	$\frac{\Delta P}{\rho g H} = 5{,}29\%_{(HW)}$		$\frac{\Delta P}{\rho g H} = 4{,}51\%_{(90°)}$		$\frac{\Delta P}{\rho g H} = 5{,}71\%_{(TW)}$		$\frac{\Delta P}{\rho g H} = 6{,}78\%_{(270°)}$		$\frac{f}{f_n} = 0{,}282$	

respectively −13,9%, −17,3% and 6,8%, as seen in Table 7.8. At part load and low head, OP 6, the maximum calculated deviations for the pressure pulsation amplitude were −5,6%, −8,4% and −2,3%, with SAS, DES and LES respectively, as observed in Table 7.9.

Menter and Kuntz [102] modified the DES limiter in relation to the original turbulence model from Spalart et al. [148]. The purpose of this modification was to avoid artificial grid induced separations. This effect should not be relevant for the draft tube instabilities. However, since this modification could affect the DES limiter, its influence on the turbine transient simulation was evaluated during the present study.

The DES limiter was modified with the SST blending functions, $F_{SST} = F_1$ or $F_{SST} = F_2$. When $F_{SST} = 0$, it corresponded to the traditional DES model. The numerical results for the pressure pulsation amplitudes at part load and low head, OP 6, calculated with the different limiter functions, are presented in Table 7.10. No significant difference, caused by the modified limiters, could be observed at the draft tube instabilities. The SST blending function F_1 presented the larger deviation with

Table 7.10: Influence of the blend function on the DES results, at part load and low head.

Turbulence Model	Results					Deviation				
	$\Delta P/(\rho g H)$				$\frac{f}{f_n}$	$\delta\Delta P$				δf
	HW (%)	90° (%)	TW (%)	270° (%)	(-)	HW (%)	90° (%)	TW (%)	270° (%)	(%)
$F_{SST} = 0$	5,25	4,35	5,88	6,18	0,313	−0,8	−3,5	3,0	−8,8	11,0
$F_{SST} = F_1$	5,06	5,17	6,23	6,30	0,314	−4,3	14,6	9,1	−7,1	11,3
$F_{SST} = F_2$	5,47	4,13	5,41	6,24	0,295	3,4	−8,4	−5,3	−8,0	4,6
Model Test	$\frac{\Delta P}{\rho g H} = 5{,}29\%_{(HW)}$		$\frac{\Delta P}{\rho g H} = 4{,}51\%_{(90°)}$		$\frac{\Delta P}{\rho g H} = 5{,}71\%_{(TW)}$	$\frac{\Delta P}{\rho g H} = 6{,}78\%_{(270°)}$		$\frac{f}{f_n} = 0{,}282$		

14,6%, while the traditional DES model and the one modified with F_2 showed similar maximum deviations of −8,8% and −8,4%. The modification with F_2 brought the benefit of better predicting the vortex rope rotating frequency.

The SAS turbulence model from Menter and Egorov [100] counts with the closure coefficient $C_{SAS} = 0{,}50$, which is responsible for switching between the URANS and LES behaviour in the calculation domain. Higher values of C_{SAS} lead to larger portions of the fluid domain to assume the LES behaviour, while lower values favour the URANS approach. To verify the influence of this closure coefficient on the turbine dynamic flow simulation, the simulation of the part load and low head operating point, OP 6, was repeated with $C_{SAS} = 0{,}75$. No noticeable effect on the pressure pulsation results could be observed going from $C_{SAS} = 0{,}50$ to $C_{SAS} = 0{,}75$.

Figures 7.12, 7.13 and 7.14 offer one more possibility to verify the instationary simulation results. They present the simulated vortex shape confronted to the model test observation. The three visually compared operating points were the rated, OP 2, part load at high head, OP 5, and part load at low head, OP 6. The vortical structures observed during the model tests were due to the cavitating water volume. The vortex surfaces extracted from the numerical simulations corresponded to isobars at the water vapour pressure, i.e. the pressure level where the water volume should begin to cavitate, p_{va}. The numerical results in Figures 7.12, 7.13 and 7.14 were obtained with the hybrid turbulence models SAS and DES, with no significant difference between them.

When observed during the model test, the rated operating point was visually characterised by the vortex torch under the runner cone and by the vortex shedding at the blades trailing edges. Figure 7.12 suggests that the simulated torch was slightly smaller than the actual one, possibly because of the one-phase numerical modelling of water. Nonetheless, the numerical calculations could fairly well reproduce the torch shape at the rated point and even the von Kármán vortex streets at the blades trailing edge.

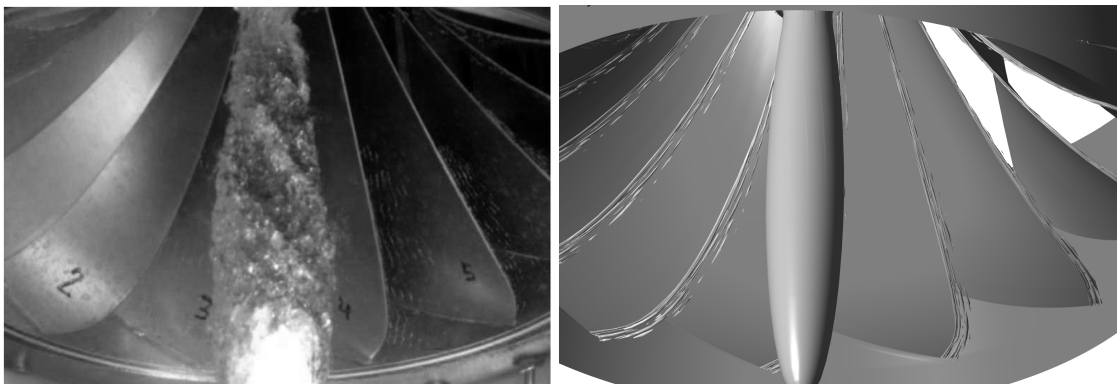

Figure 7.12: Comparison of the von Kármán vortex streets observed at the model test and numerically simulated at the rated point.

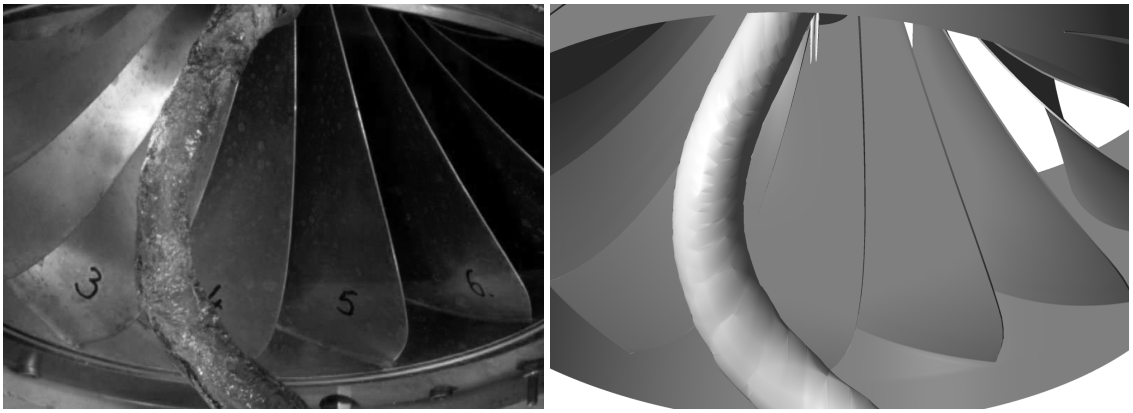

Figure 7.13: Comparison of the vortex rope shape observed at the model test and numerically simulated at part load and high head.

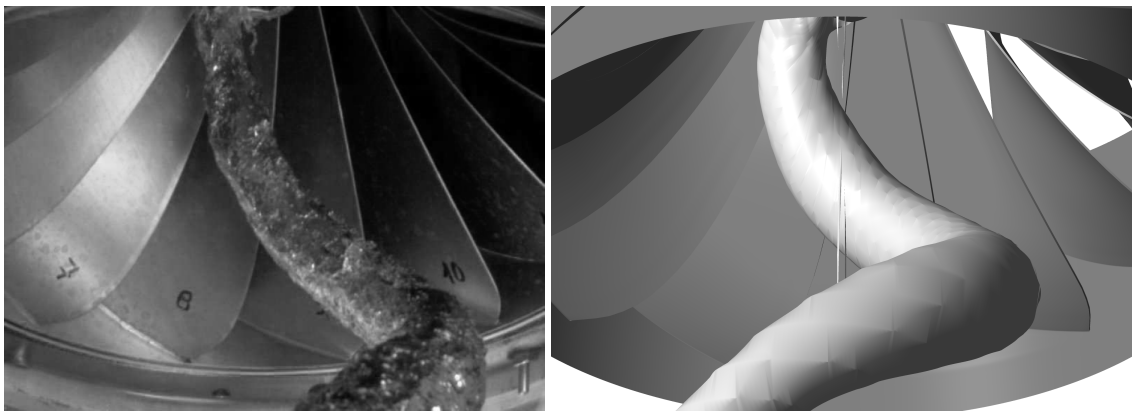

Figure 7.14: Comparison of the vortex rope shape observed at the model test and numerically simulated at part load and low head.

At part load and high head and at part load and low head, the comparison of the experimental observations with the numerical results, in Figures 7.13 and 7.14, shows that the simulations with SAS and DES could extremely accurately reproduce the shape of the rotating vortex rope in the draft tube cone. This also constituted an

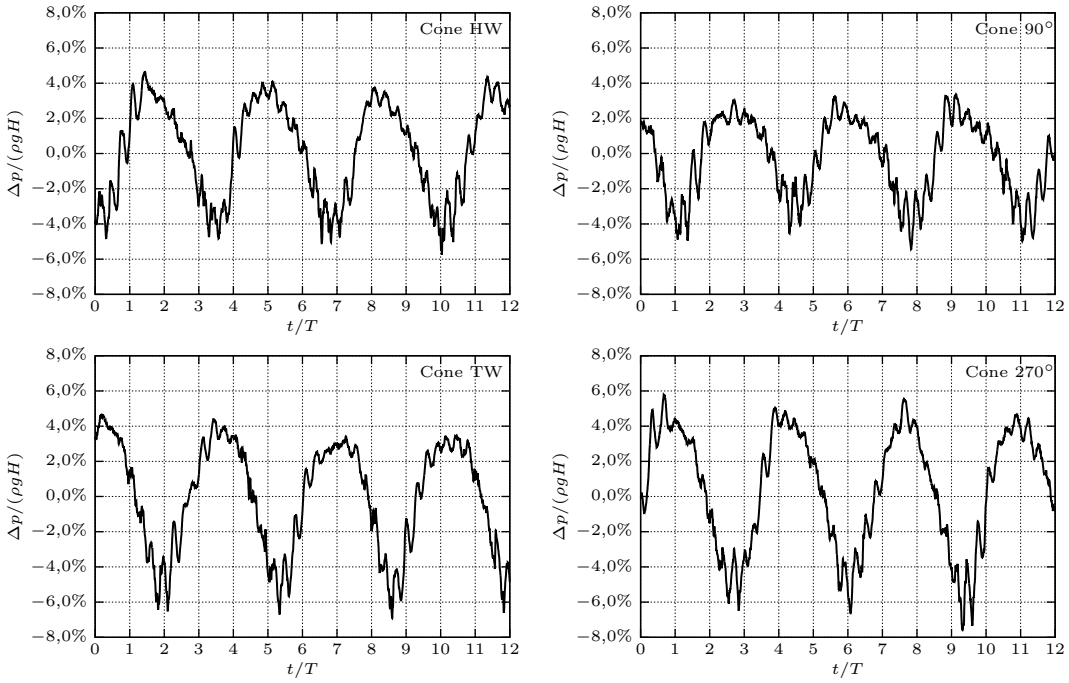

Figure 7.15: Pressure oscillation time history at the draft tube at part load and low head.

indication that the dynamic pressure field predicted by the numerical model could precisely match the real one.

The similarity between the calculated and the experimentally observed vortex shapes, at the rated operating point and, especially, at part load, also showed that the hybrid turbulence models, associated to the chosen numerical parameters for the finite volume model and to the mesh topology and density, were appropriate for the transient simulation of the turbine fluid flow. In contrast to the SAS, DES and LES calculations, the simulations carried out with URANS were unable to generate the draft tube instabilities and to generate the shape of the vortex rope.

The pressure time history at part load and low head, OP 6, calculated in the points corresponding to the four draft tube measuring transducers, can be seen in Figure 7.15, while its Fourier transform is represented in Figure 7.16. This last figure shows that the characteristic Rheingans [121] frequency, typical from the vortex rope rotation, could be identified in the calculated frequency spectrum. This could again confirm the precision achieved with the usage of the hybrid turbulence models in the simulation of the transient fluid flow through the turbine.

The complex form of the pressure variation, in relation to the time, resulted in a frequency spectrum, where the signal intensity was spread along a wide frequency range. Therefore, the maximum value read from the Fourier transform did not represent the real pressure fluctuation amplitude. The pressure oscillation amplitude should be read from the pressure time history in Figure 7.15 and the characteristic frequencies from the Fourier transform in Figure 7.16.

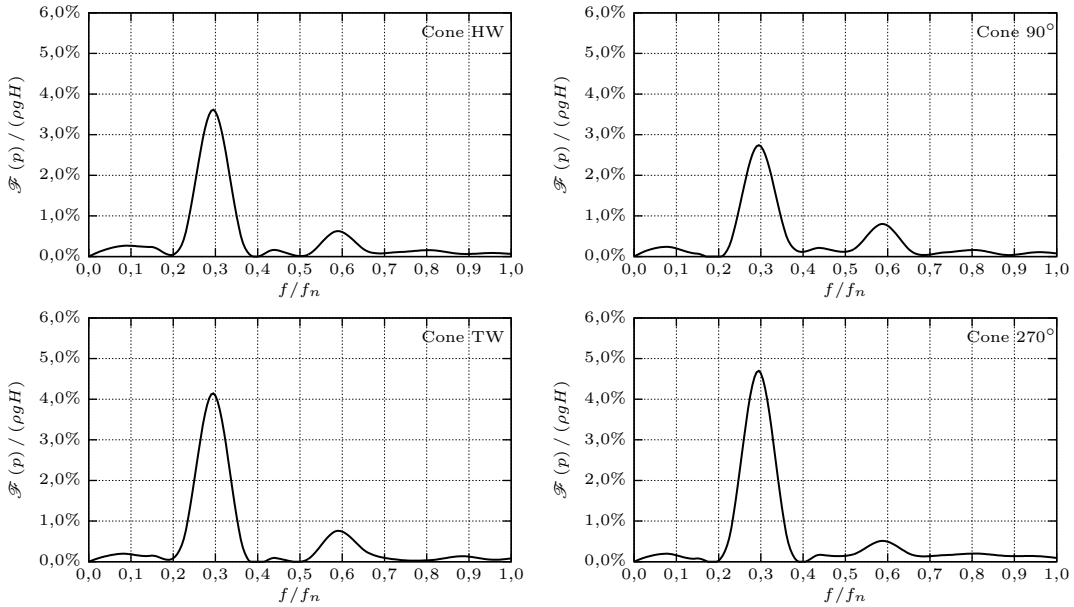

Figure 7.16: Pressure oscillation Fourier transform at the draft tube at part load and low head.

Considering the deviations achieved in the calculation of the pressure pulsation amplitude, seen in Tables 7.8 and 7.9, SAS, DES and LES would all be suitable to accurately simulate the fluid flow dynamic behaviour through the turbine. Although LES proved to be the most exact of the three methods, it required the finest time discretisation tested, 5 882 time steps per machine revolution, in order to maintain numerical stability and convergence. SAS and DES achieved fast as accurate results as LES, but with considerably larger time steps per turbine rotation. SAS and DES required just 392,2 time steps per machine revolution to assure the proper numerical convergence during the computational calculations. This resulted in much shorter durations for the simulations using SAS or DES in comparison to the ones using LES. In relation to URANS, the SAS and DES simulation were slightly slower. From the point of view of numerical convergence, computational costs and model preparation effort, but also considering the deviations, SAS and DES were the most attractive alternatives for the simulation of the fluid flow in hydraulic turbines in industrial applications.

7.3 Fluid Simulation Results

The objective in the development and verification of the numerical model for the simulation of the transient fluid flow through the turbine was to allow the precise simulation of the pressure fluctuations in the hydraulic machine, especially at the turbine runner. After the extensive verification of the numerical model with experimental data, during the numerical setup, the model accuracy was considered adequate for the extraction of dynamic results related to the transient fluid flow.

The extension of dynamic measurements in the model machine or in the prototype is very limited at present. Therefore, the numerical model developed here was used to obtain more quantitative information about the dynamic behaviour of Francis turbines, with the main purpose to predict how the pressure fluctuations might affect the runner fatigue life. They are responsible for the dynamic structural load at the runner and required for the accurate calculation of the dynamic structural stresses. The CFD model allowed the numerical computation of the fluid flow transient effects, providing the pressure dynamic distribution in the complete machine, including the turbine runner.

The simulation results for which experimental data was available, i.e. efficiency, head, volume flow, torque and punctual pressure pulsations at the draft tube cone, were employed in the validation of the numerical model. Other calculated integral quantities and calculated scalar and vectorial fields, which could not be extracted from the experiments, e.g. the transient pressure distribution at the runner, are presented here as results of the numerical simulation. Since the most important dynamic phenomena in the turbine flow were associated with well determined regions of the model hill chart, the main dynamic effects are studied at the chosen operating points. The rotor-stator interaction (RSI) is discussed based on the full load operation at the rated point, OP 2. The discussion on the draft tube instabilities (DTI) relies on the part load operating points at high and low head, OP 5 and OP 6. The higher part load (HPL) could be simulated at part load and low head, OP 6, and is also discussed. The runner channel vortex (RCV), typical, for example, at deep part load, OP 7, is presented as well. At the operating point chosen at deep part load, draft tube instabilities were also typical.

As long as the numerical setup showed the determinant influence of the turbulence modelling on the accurate prediction of the pressure oscillations, comparisons between URANS, SAS and DES calculations make also part of the numerical simulations results.

7.3.1 Rotor-Stator Interaction at Full Load

At full load, the main dynamic effect in the Francis machine was the rotor-stator interaction (RSI). This phenomenon arose from the relative motion between the inlet stationary parts, i.e. spiral case, stay vanes and guide vanes, and the rotating runner.

When the runner blades move along the stay vanes and guide vanes channels, they constitute an obstacle to the flow, causing pressure oscillations in relation to the stationary pressure field. The pressure pulsation amplitude caused by this interaction depends on the radial distance between the guide vanes trailing edges and the runner blades inlet edges and on the number of stay vanes, guide vanes and runner blades, z_T, z_0 and z_2, as discussed by Nennemann, Vu and Farhat [109].

In the runner reference frame, it appears as if the stay vanes and guide vanes were rotating. They constitute the periodic restriction to the flow and, together with the guide vanes wake, they cause the pressure variations. With the same number of stay vanes and guide vanes, the theoretical oscillating frequency of this phenomenon in the runner reference frame is $z_0\, f_n$, where f_n is the machine rotating frequency.

In the runner rotating frame, the slightly inhomogeneous pressure distribution along the spiral case in the rotational direction is also a source for rotor-stator interaction. For the turbine runner, this inhomogeneous pressure distribution is transformed in a dynamic load, because of the machine rotation. In the runner reference frame, the theoretical oscillating frequency of the pressure variation induced by the spiral case pressure distribution should be f_n.

The rotor-stator interaction can also generate pressure waves, which can be reflected inside the hydraulic machine, as shown by YAN ET AL. [173] with a compressible CFD simulation. Due to constructive characteristics, especially the distance between guide vanes and runner and their shape, this aspect of the rotor-stator interaction should only be significant for Francis turbines, pump-turbines or pumps with very low specific speed. As long as the calculated machine, the FT 80, counted with $n_{q_{opt}} = 80{,}3$ min^{-1}, the compressibility of water was not considered.

For the simulated machine, the chosen operating point in the full load region of the hill chart was the rated point, OP 2, $n'_1/n'_{1_{opt}} = 1{,}103$, $Q'_1/Q'_{1_{opt}} = 1{,}229$. This point should be representative for the rotor-stator interaction and the numerical simulations confirmed this assumption. Figure 7.17 shows the normalised pressure oscillations, $\Delta p/\left(\rho g H\right)$, in the runner as a function of time, for the rated point. In the figure, three selected conformal surfaces can be seen at different time instants. The conformal surface in the first column was located in the runner near to the crown, at $v = 0{,}20$. The conformal surface in the second column was taken at the middle of the runner channel, at $v = 0{,}50$, and the one on the last column could be find near to the band, at $v = 0{,}80$. Each row corresponds to successive time steps, allowing to observe how the pressure oscillation evoluted at these three representative conformal surfaces. The time span from the first to the last picture was the time required by the blades to move one runner channel pitch, T/z_2, where T is the rotating period. At the pictures, the grey scale was limited to $\pm 3{,}0\%$, to improve the visualisation.

As seen in Figure 7.17, the pressure oscillations at the runner at full load were dominated by the rotor-stator interaction. The influence of the non-axisymmetric pressure distribution in the spiral case can be observed at the conformal surfaces near to the crown and at the middle of the runner channel. At the conformal surface near to the band, where the distance between the guide vanes and the runner was smaller, the effect of the guide vanes passage on the pressure oscillations at the runner was significantly more pronounced. Also the effect of the runner blade passage could be identified at the stationary components.

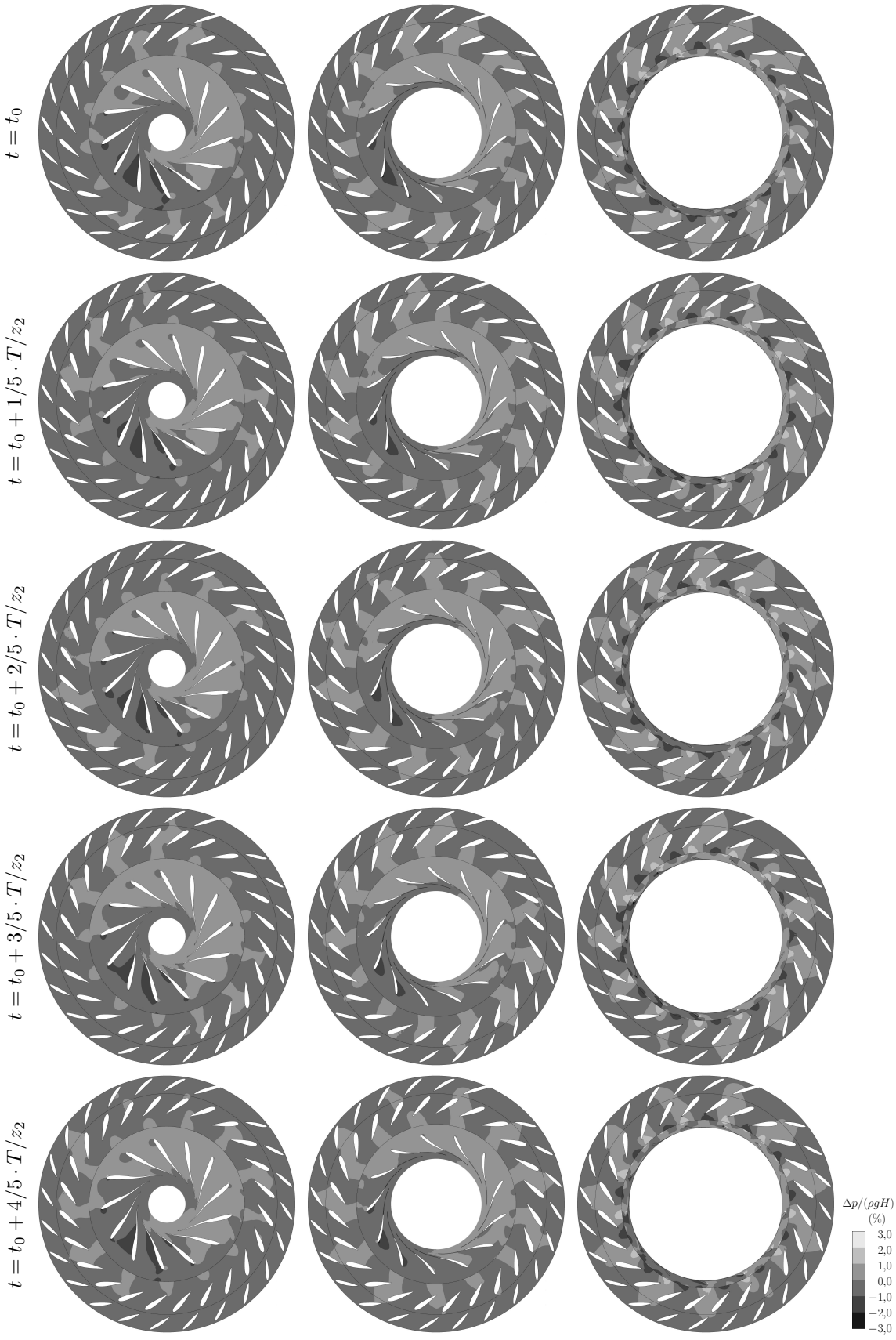

Figure 7.17: Pressure oscillations over one runner channel pitch rotation at the rated operating point at conformal planes $v = 0{,}20$, $v = 0{,}50$, $v = 0{,}80$.

The pressure oscillation originated from the rotor-stator interaction (RSI) could be observed in more detail by plotting the pressure time history for individual points taken at the runner blade surface. The pressure oscillation time history for the selected points is found in Figure 7.18. The points were chosen at the blade leading edge, $u = 0{,}50$, near to the middle of the blade pressure side, $u = 0{,}25$ and near to the middle of the blade suction side, $u = 0{,}75$, starting near to the crown, $v = 0{,}05$, going along the blade, $v = 0{,}25$, $v = 0{,}50$, $v = 0{,}75$, and arriving near to the band, $v = 0{,}95$. The points on the blade leading edge were chosen because they were the points, at each conformal surface, where the distance to the guide vanes was minimal. The other points were chosen on the blade pressure and suction sides with the objective to identify the effect of the rotor-stator interaction on the blade body. The point distribution from the crown up to the band was performed to evaluate the effect of the radial distance between guide vanes and runner on the rotor-stator interaction.

The analysis of the pressure oscillation time history, $\Delta p\,(t)\,/\,(\rho g H)$, in Figure 7.18, confirms that the distance to the guide vanes trailing edge is an important parameter for the intensity of the pressure oscillations. As expected, the pressure variations were much higher at the runner blades inlet edges than at the rest of their bodies. At all conformal planes, i.e. at constant v coordinates, the pressure oscillations decayed considerably from the blade inlet edge to the middle of the blade.

Analysing in the other blade coordinate direction, u, i.e. from the crown in direction to the band, the effect of the radial gap size, between runner and guide vanes, could again be observed. The pressure pulsations were significantly higher near to the band than near to the crown, due to the fact that the radial distance between runner and guide vanes was much smaller at the band, $0{,}035 D_{1_a}$, than at the crown, $0{,}136 D_{1_a}$. At the crown, where the distance was larger, the fast oscillations, related to the guide vanes passing frequency, was not as much pronounced as at the band. At the crown, the slower oscillations, caused by the inhomogeneous pressure distribution at the spiral case, dominated.

The Fourier transform of the pressure time history, seen in Figure 7.19, confirmed the theoretical considerations about the oscillating frequency of the rotor-stator interaction phenomenon. The plots show that the dominating frequencies were $f/f_n = 1{,}0$ and $f/f_n = 24$, corresponding exactly to the machine rotating frequency and to the number of guide vanes, $z_0 = 24$. As already discussed and verified with the frequency plots, the low frequent oscillation was originated by the non-axisymmetric pressure distribution at the spiral case, while the high frequent oscillation came from the interaction with the guide vanes. The Fourier transforms also pointed out the influence of the distance between runner and guide vanes on the rotor-stator interaction. Near to the crown and in the middle of the blade, the frequency spectrum was dominated by the effect coming from the spiral case pressure distribution. Near to the band, at the leading edge, the peak in the Fourier transform, corresponding to the guide vanes passing frequency, became much more pronounced. The amplitudes presented in the frequency domain were smaller than

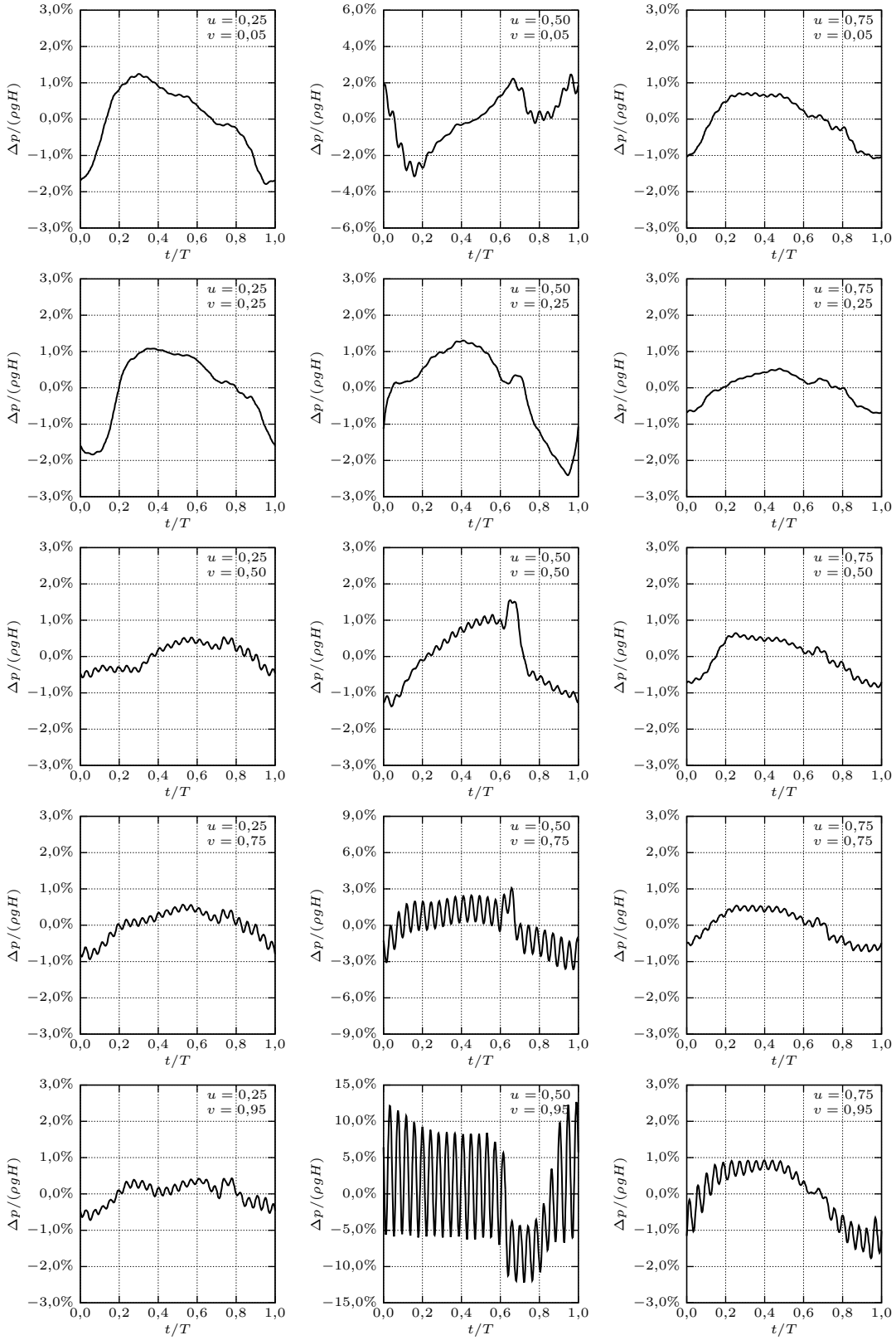

Figure 7.18: Pressure oscillation time history at selected points at the rated operating point.

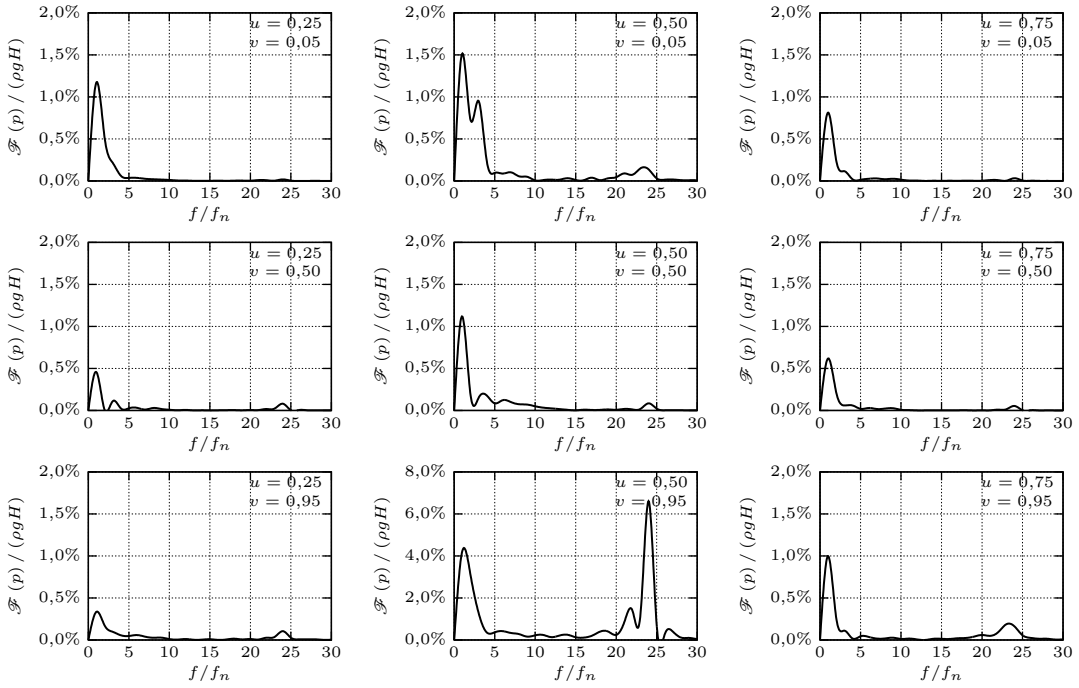

Figure 7.19: Pressure oscillation Fourier transform at selected points at the rated operating point.

in the time domain, because of the intensity distribution over a frequency range, in opposition to a pure sinusoidal curve.

The pressure fluctuation amplitude at the runner blade surface, obtained from the pressure time history, can be found in Figure 7.20. The results generated with three different turbulence models, URANS, SAS and DES can be encountered in the figure. Seven conformal planes were used for representing the pressure oscillation amplitude, $\Delta P/(\rho g H)$, at the runner blades. They were again placed near to the crown, $v = 0{,}025$, at the middle of the channel, $v = 0{,}500$, near to the band $v = 0{,}0975$, and at intermediate positions, $v = 0{,}125$, $v = 0{,}325$, $v = 0{,}725$ and $v = 0{,}875$. For each conformal plane, the values of $\Delta P/(\rho g H)$ were plotted along the blade extension, along the u coordinate, starting from the trailing edge at the pressure side, $u = 0{,}00$, passing by the leading edge, $u = 0{,}50$, and arriving at the trailing edge at the suction side, $u = 1{,}00$.

Once again, it can be identified in Figure 7.20 that the pressure pulsations arising from the rotor-stator interaction were more pronounced around the blade leading edge, $u = 0{,}50$, and near to the band. The other interesting information brought by Figure 7.20 was the comparison between the turbulence models. The results obtained with SAS and DES were extremely close to each other. The $\Delta P/(\rho g H)$ values predicted with SAS could reach 13,7% at the blade leading edge, while it did not exceed 2,7% at the rest of the blade. These values were comparable to the measurements from Avellan et al. [12], Farhat, Avellan and Seidel [38] and Nennemann, Vu and Farhat [109] in similar machines.

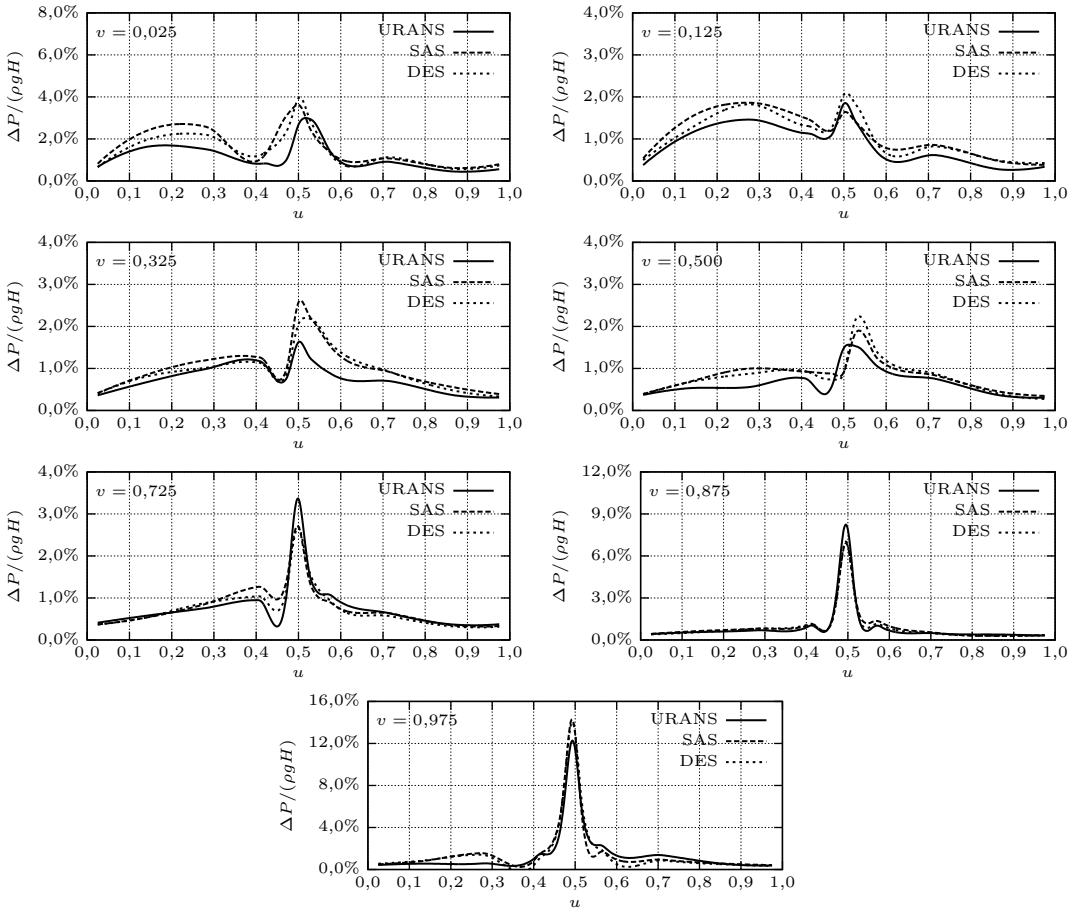

Figure 7.20: Pressure oscillation amplitude at selected conformal planes at the rated operating point.

The URANS turbulence model could almost reach the pressure pulsation level achieved with SAS and DES, but with less accuracy, especially at the blade body. The URANS simulations predicted 12,4% for the maximum pressure fluctuation amplitude at the leading edge and no more than 2,1% at the blade body. As long as the rotor-stator interaction phenomenon was mainly driven by the kinematic interaction between the runner and the stationary parts, the URANS inaccuracy was not as much pronounced as during the simulations of the draft tube instabilities.

Figure 7.21 brings the pressure fluctuation amplitudes, $\Delta P/(\rho g H)$, as contour plot at the pressure and suction sides of the runner blades and guide vanes. This representation allows the more intuitive visualisation of the dynamic pressure distribution over the runner blades. The hydraulic surfaces were transformed to the meridian view. The right side of the figure corresponds to the pressure side and the left to the suction side. The colour scale was limited to 3,0% to improve the visualisation. The high pressure fluctuation amplitude can be seen at the blade leading edge and a second smaller local peak region was found at the pressure side, near to the crown.

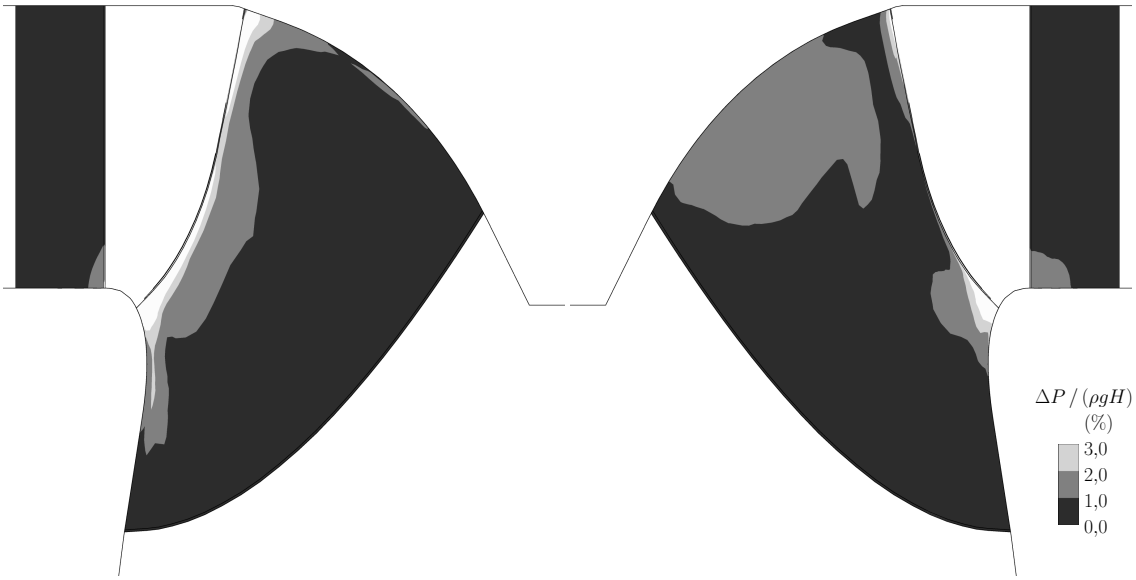

Figure 7.21: Pressure oscillation amplitude at the rated operating point, meridian view.

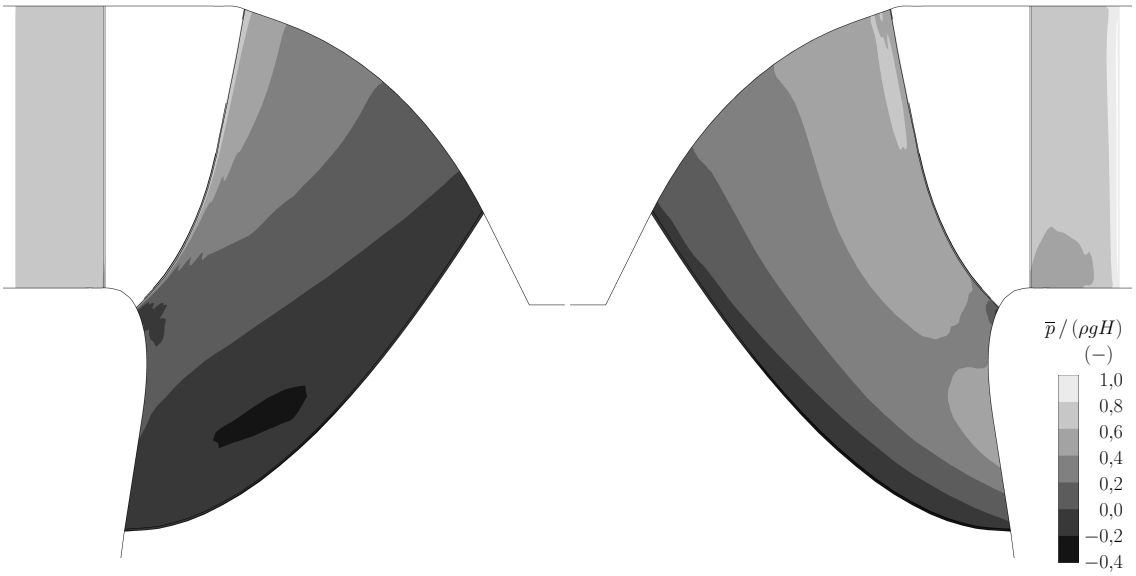

Figure 7.22: Time-averaged pressure at the rated operating point, meridian view.

For the structural simulations of the turbine runner, not only the dynamic pressure field was needed, but also the static pressure distribution on the runner blades. The calculated static pressure at the runner, normalised to the turbine net head, $\overline{p}/(\rho g H)$ can be found in Figure 7.22. The contour plot made use of the meridian transformation to show the runner and guide vanes pressure and suction sides. The runner blade pressure side is found at the right and the suction side at left. The pressure reference level for the static pressure at the outlet of the finite volume model was set to be equal to the relative pressure at the downstream tank at the model test.

7.3.2 Draft Tube Instabilities at Part Load

At part load, draft tube instabilities (DTI), associated to the vortex breakdown phenomenon studied by SARPKAYA [136], usually take place under the runner cone and in the draft tube cone of Francis turbines. With the reduced turbine volume flow, the rotating vortex rope dominates the flow at the runner outlet and in the draft tube cone. In hydraulic turbines, the vortex rope rotates at the RHEINGANS [121] frequency, typically between $0{,}25 f_n$ and $0{,}35 f_n$, observed at the stationary reference frame and where f_n is the machine rotating frequency. The high pressure pulsation amplitudes at part load are related to the rotational motion of the vortex rope.

The principal interest in studying the part load operating condition came from the high structural loads in the turbine runner induced by the draft tube instabilities. Due to the highly instationary character of this phenomenon, the appropriate choice of the turbulence modelling for the CFD analysis played a determinant role in the accurate prediction of the pressure pulsations at part load. For the simulated Francis turbine, FT 80, the chosen operating point for studying the draft tube instabilities was located at part load and high head, OP 5, $n'_1/n'_{1_{opt}} = 1{,}078$, $Q'_1/Q'_{1_{opt}} = 0{,}797$.

Figure 7.23 shows the variation of the dynamic pressure field at the runner blades and the motion of the vortex rope under the turbine runner. The pictures in each row correspond to successive time instants. The complete time span was equal to the rotating period of the vortex rope, T_{Rh}. In the first column of Figure 7.23, the runner bottom view is presented. The blades were coloured according to the instantaneous dynamic pressure value, $\Delta p/(\rho g H)$ and the vortex rope was omitted. In the second column, besides the dynamic pressure contour plots, the vortex rope was also shown. The vortex rope surface was the isobar at the pressure level at which the water volume should begin to cavitate, p_{va}. The third column brings a tridimensional view of the runner and vortex rope, very similar to the angle at which it is normally observed at the model test.

In Figure 7.23, it can be observed that the vortex rope took place immediately below the runner cone, extending up to the draft tube cone. The dynamic pressure field rotated together with the vortex rope. The dynamic pressure distribution at the bottom of the runner, at the blades suction side, presented a spiral form. These aspects indicated the relation between the rotating vortex rope in the draft tube cone and the pressure pulsations at the runner at part load.

The success in reproducing the real shape and motion of the vortex rope relied on suitable turbulence models, associated to adequate computational grids. This might possibly be the reason for the difficulty encountered by other authors to accurately simulate the pressure oscillations in hydraulic turbines at part load.

Considering the pronounced dynamic characteristic of the flow at part load, the appropriate choice of the turbulence model was fundamental for the accurate simulation of the pressure oscillations. As already mentioned before, during the discussion of the transient simulation settings, the flow instabilities at part load

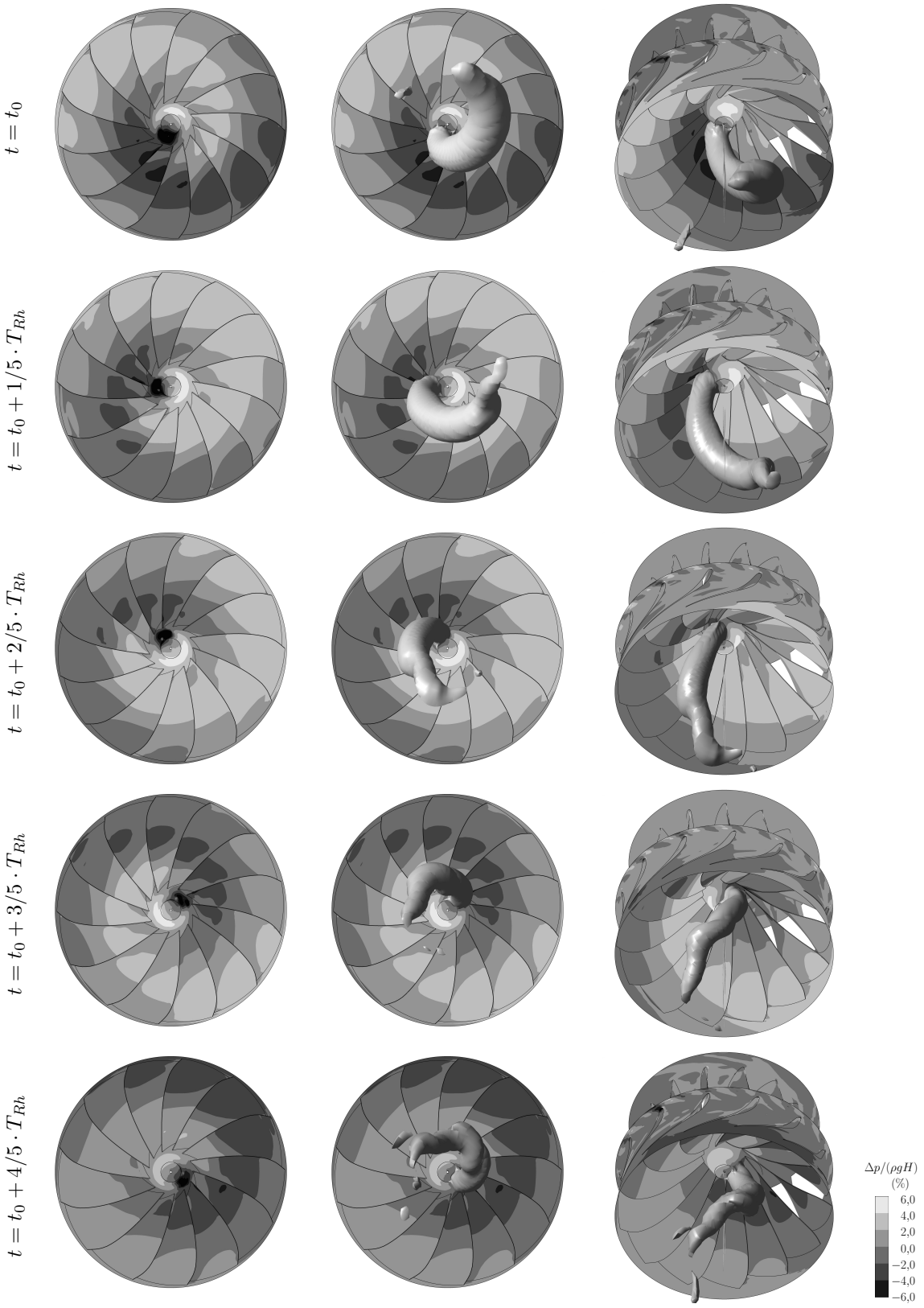

Figure 7.23: Pressure oscillations over one vortex rope rotation period at part load and high head viewed from the draft tube.

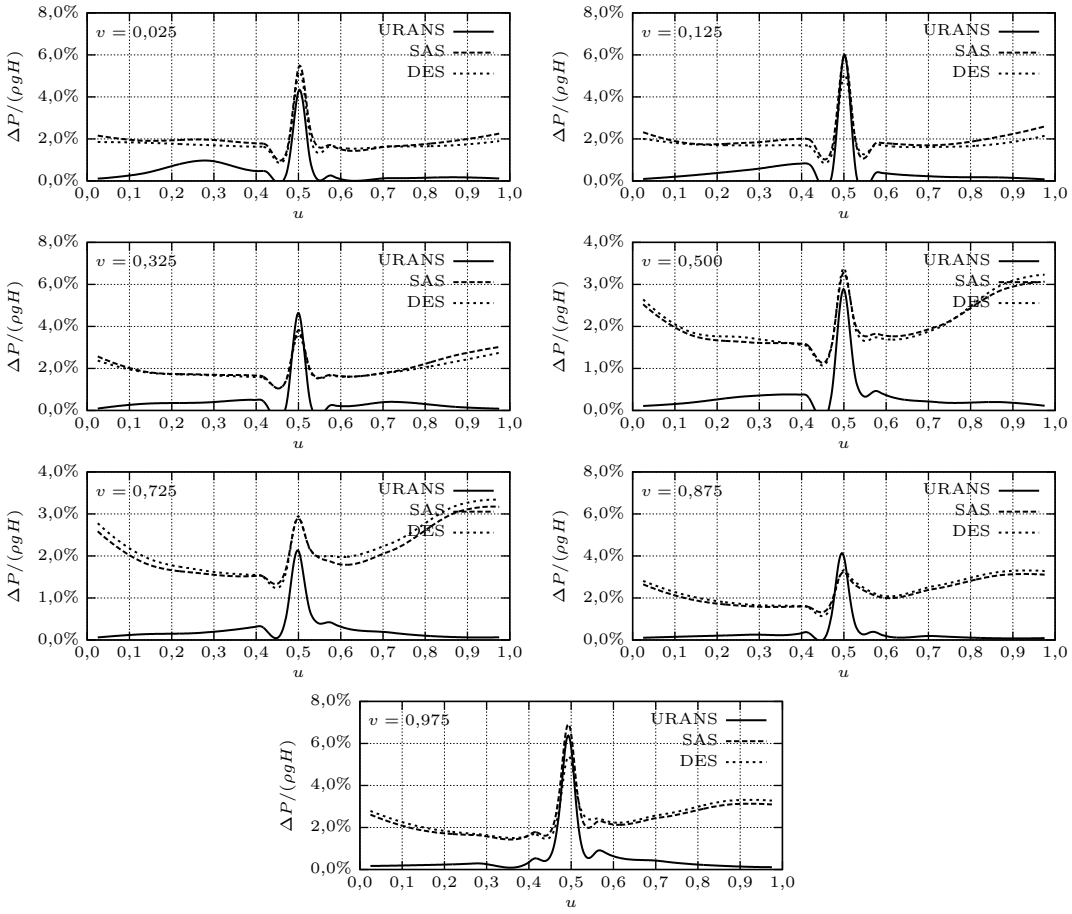

Figure 7.24: Pressure oscillation amplitude at selected conformal planes at partial load and high head.

could only be captured by SAS, DES and LES. URANS was unable to reproduce this effect. The adequate accuracy of the hybrid turbulence models and the limitation from URANS was clearly demonstrated by the comparison of the measured and the simulated pressure oscillation amplitudes in the draft tube cone.

Here, the pressure oscillation amplitude, $\Delta P/(\rho g H)$, at the runner blades, calculated with URANS, SAS and DES are compared in Figure 7.24. As already explained for the rotor-stator interaction results, seven conformal planes were used for representing the pressure fluctuation amplitude, each of them at constant v coordinates, going from the vicinity of the crown up to the vicinity of the band. The u coordinate went from the trailing edge at the pressure side, $u = 0{,}00$, passing by the leading edge, $u = 0{,}50$, and arriving at the trailing edge at the suction side, $u = 1{,}00$.

As seen in Figure 7.24, the values calculated with SAS and DES for the pressure oscillation amplitude at the runner blades were extremely close to each other along the complete blade surface. The maximum reached pressure oscillation amplitude at the blade body, predicted with SAS, was 3,1% and at the blade leading edge 6,6%. Farhat, Avellan and Seidel [38] measured similar values for a similar Francis

turbine. Differently from the rotor-stator interaction, the high pressure oscillation values at the blade body were distributed along the most part of the blade and not only at limited regions.

The maximum pressure pulsation amplitudes predicted by URANS were 6,0% at the blade leading edge and 0,9% at the blade body. At the leading edge, because of the rotor-stator interaction, the values predicted by URANS were not significantly below the ones obtained with SAS and DES. On the other hand, at the complete extension of the blade body, where the pressure variations were dominated by the rotating vortex rope, the $\Delta P/(\rho g H)$ values simulated with URANS were considerably below the results obtained with SAS and DES. The low values predicted by URANS were the consequence of its incapacity to capture the draft tube instabilities and to reproduce the vortex rope in the draft tube cone. This limitation of URANS was already expected, because of the excessive dissipation introduced in the transient simulations, avoiding the normal development of the dynamic effects.

The capacity of SAS and DES to correctly reproduce the dynamic flow behaviour in the draft tube lies on their hybrid characteristic, combining LES and URANS. In the regions, where the mesh resolution is fine enough to allow the simulation of the full transient flow characteristics, the SAS and DES models switch to the LES behaviour. In other regions, where the mesh does not allow the resolution of the larger eddies, SAS and DES assume the URANS character. As explained in the theory chapter, the change between the LES and URANS behaviour is controlled by the local mesh density, by the local fluid flow and by the blending function, which is characteristic of each hybrid turbulence model. When the blend function tends to 0, SAS and DES approach the pure LES-like behaviour and, when it tends to 1, it recovers the pure URANS characteristic. The combination of appropriate turbulence modelling and adequate mesh density allows the simulation of the dynamic fluid flow phenomena, without the addition of artificial and excessive dissipation.

The blending function presents different formulations in the SAS and DES turbulence models. Nonetheless, they have the same function and for similar numerical results, they should present similar values. In Figures 7.25 and 7.26, the distribution of the DES blending function, F_{DES}, in the simulated Francis turbine, FT 80, can be encountered. Figure 7.25 brings the longitudinal cross-section of the Francis turbine, starting from the spiral case and going up to the beginning of the draft tube pier, while in Figure 7.26 the corresponding transversal cross-section is depicted. In both figures, the stay vanes, guide vanes and runner blade surfaces were transformed to the meridian view. The instant position of the rotating vortex rope, at an arbitrary chosen time step, was also marked at the figures.

Figures 7.25 and 7.26 show that, behind the runner blades, under the runner cone and in the interior of the draft tube cone and elbow, the blending function assumed small values, tending to zero. In these regions, the low values of the blending function caused the hybrid turbulence models to switch to pure LES mode. The vortex rope could be predicted at these regions, with low blending function values, at the location and with the shape, which were expected. The LES behaviour of the

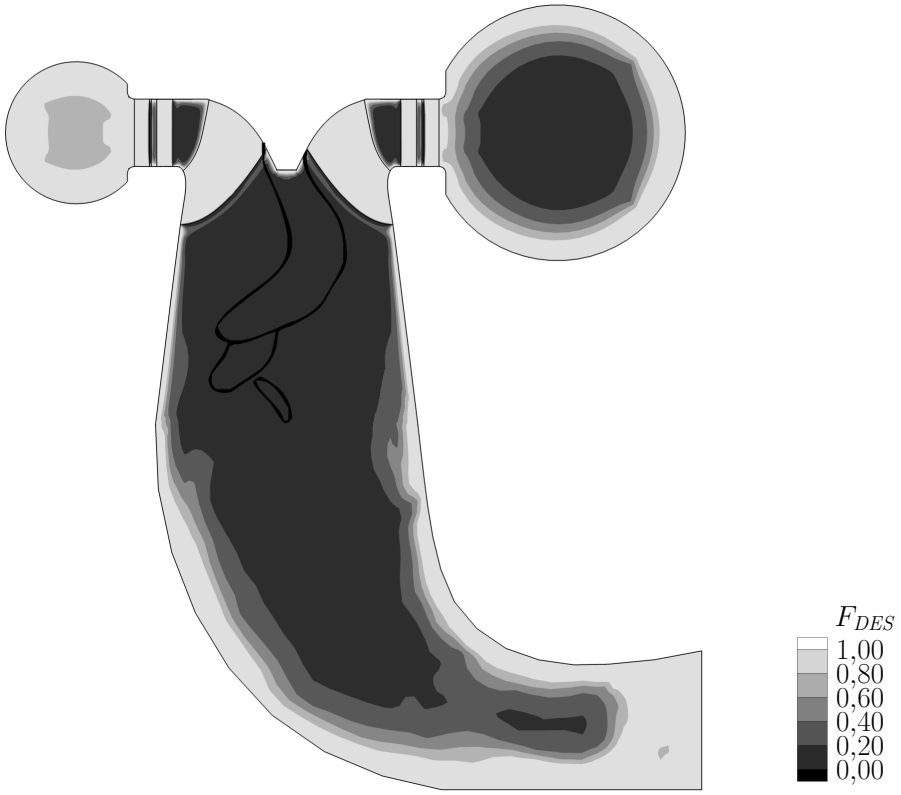

Figure 7.25: Limiter for the DES model, F_{DES}, at the longitudinal plane cut.

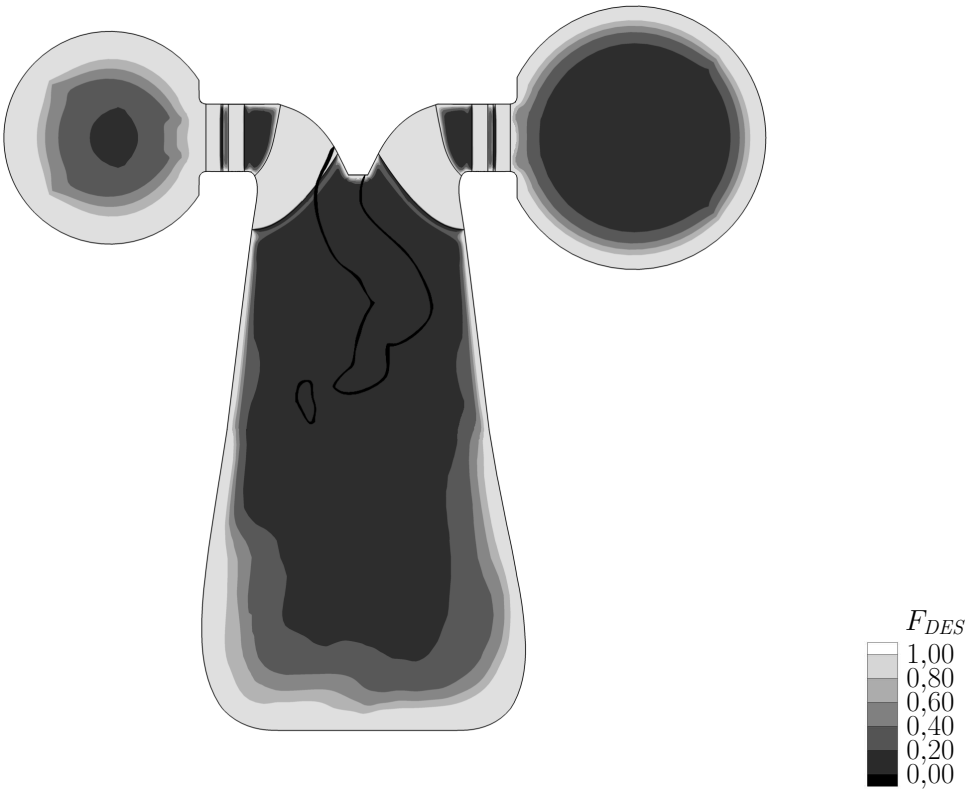

Figure 7.26: Limiter for the DES model, F_{DES}, at the transversal plane cut.

hybrid turbulence models behind the runner blades, under the runner cone and in the interior of the draft tube cone and elbow, avoiding the introduction of artificial numerical damping, allowed the draft tube instabilities to develop their real dynamic character in the numerical simulations.

Other LES regions could be identified at the interior of the larger spiral case sections and at the vaneless space between the stay vanes and guide vanes and between the guide vanes and the runner. The low values of the blending function at the vaneless space, between the guide vanes and the runner, could explain why the rotor-stator interaction results from URANS could not reach the level predicted by SAS and DES.

Near to the wall boundaries in the computational simulation domain, i.e. near to the turbine hydraulic surfaces, the blending function tended to 1. This caused the hybrid turbulence models to switch to the URANS behaviour near to the walls of the spiral case, stay vanes, guide vanes, runner and draft tube. As long as the important flow dynamic effects in Francis turbines occur in the main stream regions, the computational grid used for the numerical simulations intentionally did not offer the mesh resolution for solving the boundary layer with the LES approach. Therefore, in the wall vicinity, the hybrid turbulence models switched to URANS, in this case to k-ω SST, which was able to properly model the fluid flow in the boundary layer.

The application of the SAS and DES to the transient turbine flow simulation offered the advantage to allow the simulation of the draft tube instabilities with the LES approach without the need to solve the boundary layer with LES. This allowed avoiding excessive grid refinement in the wall regions as well as excessively small time steps, thus keeping the computational costs in reasonable current industrial standards for research and development.

The local mesh density is a parameter in the calculation of the local values of the blending function. The blending function distribution in the turbine finite volume mesh, in Figures 7.25 and 7.26, with low values in the vortex rope region, confirmed that the employed grid density was adequate for the problem. At the same time, it shows that the knowledge about the phenomenon being studied and about the machine is required for the mesh generation and numerical setup of the problem. However, in the case of the Francis turbines, the chosen mesh density was in accordance to current industrial practices, which means that the simulation with SAS or DES should be possible in current industrial applications without significant additional effort.

The turbulent dynamic viscosity, μ_T, at selected cross-sections of the draft tube cone, calculated according to the different turbulence models, can be found in Figure 7.27. The cross-section planes A-A, B-B and C-C were respectively located near to the draft tube cone inlet, at $z/D_{1_a} = -0{,}49$, close to the middle, at $z/D_{1_a} = -0{,}93$, and near to the cone outlet, at $z/D_{1_a} = -1{,}38$, with the z coordinate measured from the

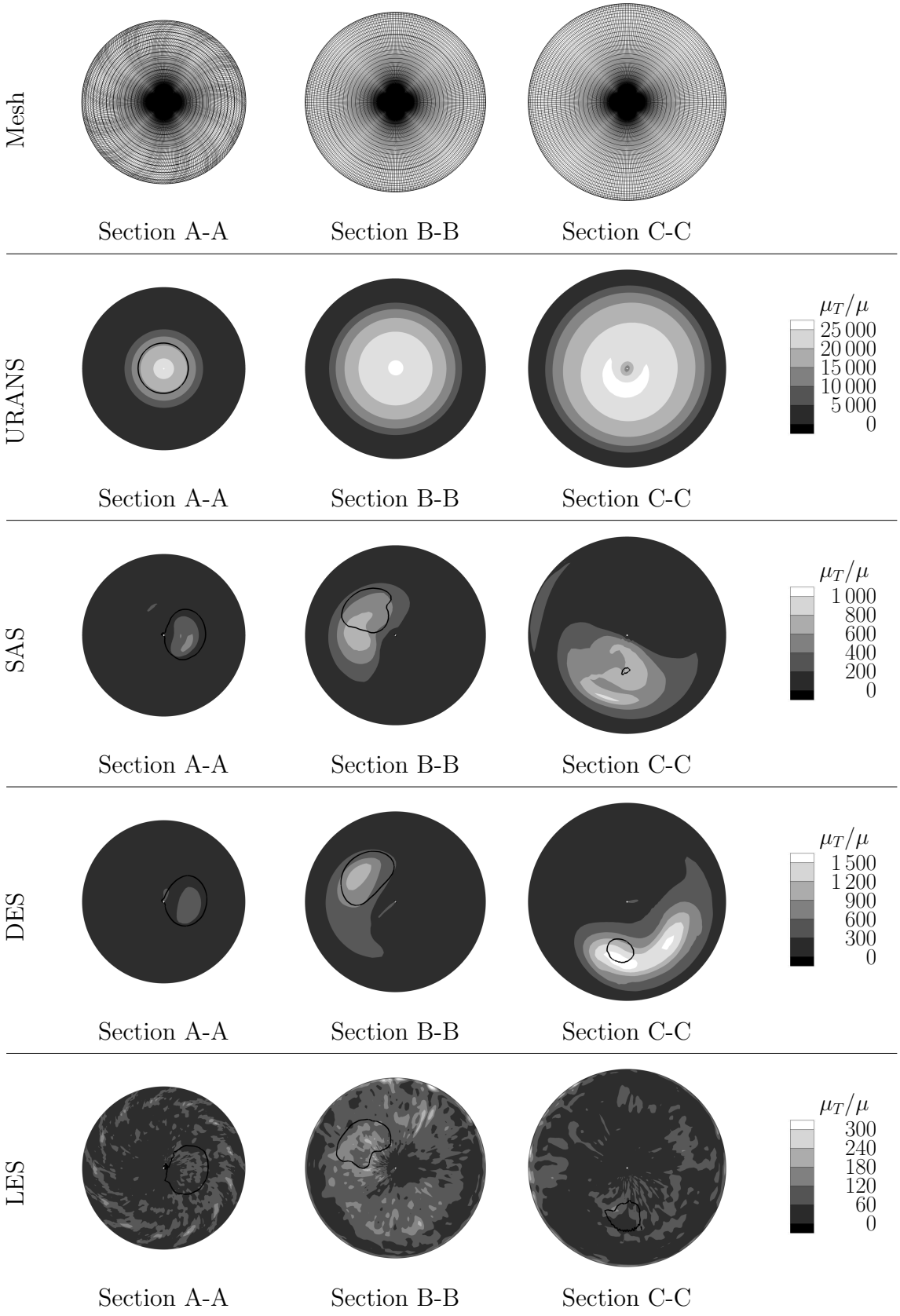

Figure 7.27: Dimensionless dynamic turbulent viscosity, μ_T/μ, calculated with different turbulence models, at selected draft tube cone sections.

distributor centreline. The cross-sections of the vortex rope, simulated with each different turbulence model were also indicated.

As discussed in the theory section of this work, when turbulence models are employed, the effective turbulent dynamic viscosity, $\mu_{\text{eff}} = \mu + \mu_T$, replaces the molecular dynamic viscosity, μ, in the Navier-Stokes equations. The diffusive transport term becomes larger and induces more dissipation in the fluid flow. Figure 7.27 helps to explain how this effect affect the simulation of the draft tube instabilities.

Next to regions, where the vortex rope was located, the turbulent dynamic viscosity increased. The values calculated with LES were of the same order of magnitude as the experimental values obtained by Algifri, Bhardwaj and Rao [1], in spite of their simpler flow and geometry.

Taking the LES results as reference, the ratio of the turbulent to the molecular dynamic viscosity, μ_T/μ, did not exceed 300. On the other hand, the μ_T/μ values simulated with URANS reached almost 25 000, two orders of magnitude higher than the calculation results obtained with LES. The high values for the turbulent dynamic viscosity at large portions of the draft tube cone were in great part the reason for the inability of URANS to properly reproduce the vortex rope and for its inaccuracy in predicting the transient pressure variations.

The hybrid turbulence models, SAS and DES, thanks to their ability to switch to the LES behaviour in the draft tube cone, led to values significantly lower than calculated with URANS. The maximum μ_T/μ values computed with SAS and DES were around 1 000 and 1 500, respectively, and were limited to small regions of the draft tube cone. The accuracy of the pressure pulsation results calculated with SAS and DES confirmed that these values of μ_T/μ and their distribution were acceptable for the successful simulation of the turbine part load operation.

Focusing again on the pressure pulsation results themselves, their amplitudes, $\Delta P/(\rho g H)$, can be seen in Figure 7.28. The guide vanes and runner blades are presented at their meridian view. The right side of the figure corresponds to the pressure side and the left to the suction side. In opposition to the rated operating point, at part load and high head, the higher pressure pulsation amplitudes were distribute at the blade body as well and not only at the leading edge. The pressure pulsation amplitudes at the blade body were higher at the suction than at the pressure side, because of the vortex rope position under the runner.

The static pressure distribution, normalised to the turbine net head, $\overline{p}/(\rho g H)$, is presented in Figure 7.29. This load was necessary for the determination of the static stresses in the structural analysis. Similar to the results at full load, the contour plot employed the meridian transformation for the runner and guide vanes. At the right side, the runner blade pressure side can be found and, at the left side, the runner blade suction side. The pressure reference level for the static pressure at the

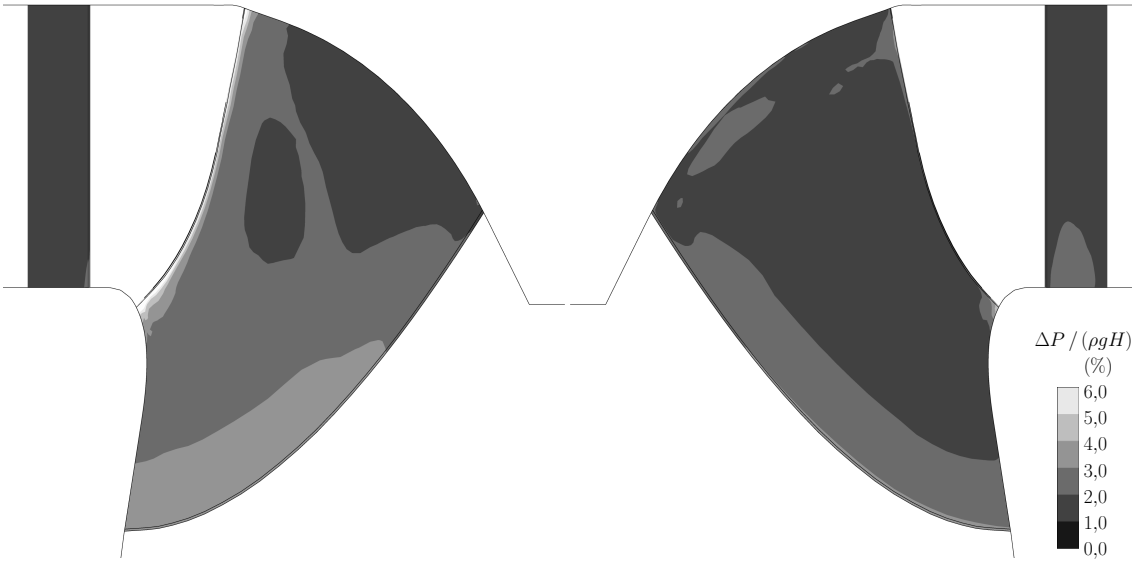

Figure 7.28: Pressure oscillation amplitude at part load and high head, meridian view.

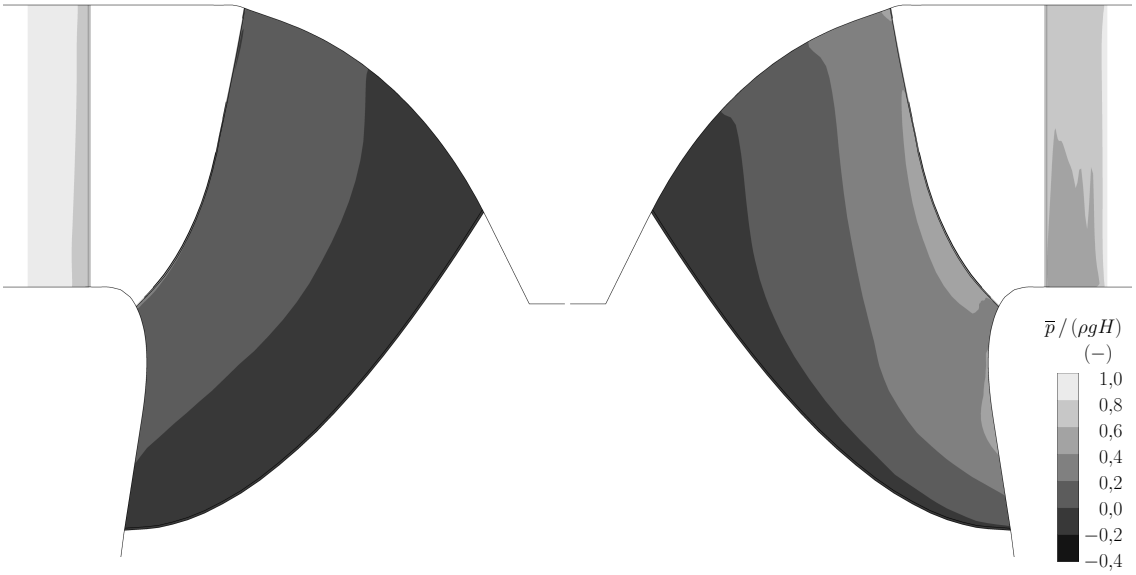

Figure 7.29: Time-averaged pressure at part load and low head, meridian view.

outlet of the finite volume model was set to be equal to the relative pressure at the downstream tank at the model test.

7.3.3 Draft Tube Instabilities and Higher Part Load

Inside the part load region of the turbine hill chart, there might exist a thin region, where higher part load takes place. At higher part load, the pressure pulsation amplitudes in the draft tube cone are higher than at normal part load. The

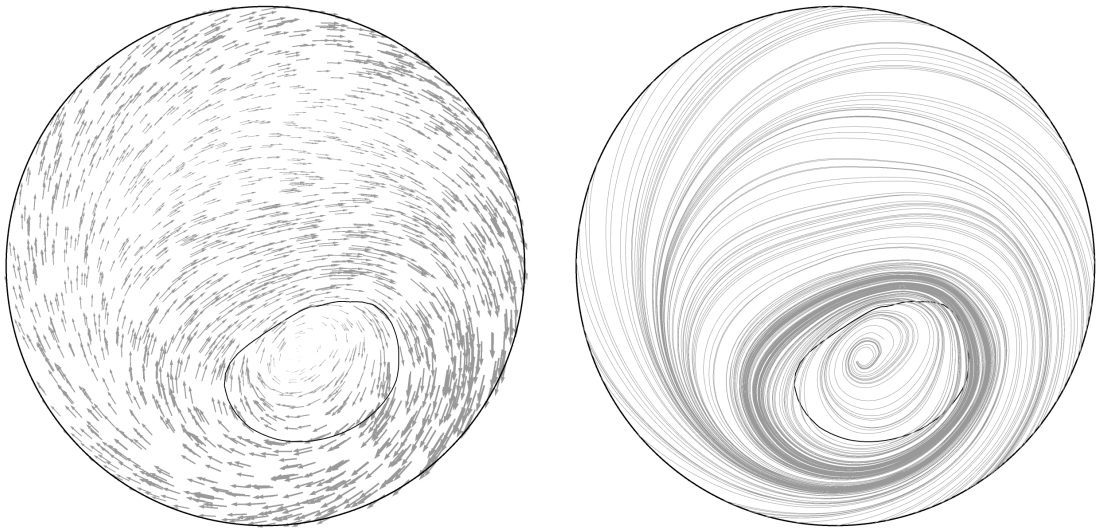

Figure 7.30: Vector plots, streamlines and isobarometric contour in the draft tube cone at higher part load.

experimental results and the numerical simulations indicated that the machine took as example in this study, the FT 80, presented the higher part load phenomenon.

At part load, the vortex rope in the draft tube rotates not only around the machine vertical axis, but also around itself. Due to the near cylindrical shape of the vortex cross-section at normal part load, the rotation around itself, i.e. the spin, can be hardly observed. As described by KOUTNIK ET AL. [75] and experimentally observed by NICOLET ET AL. [112], at higher part load, the vortex rope cross-section assumes an elliptical shape. This shape is related to the pressure distribution. The elliptical shape, associated to the vortex rope spin, causes the further increase of the pressure oscillation in the draft tube cone. According to KOUTNIK ET AL. [75], the spin occurs at frequencies higher than the Rheingans frequency, typically between $2{,}5f_n$ and $5{,}0f_n$.

The part load and low head point, OP 6, $n'_1/n'_{1_{opt}} = 1{,}199$, $Q'_1/Q'_{1_{opt}} = 0{,}848$, was initially chosen for the interest in studying the operating points with the highest pressure oscillation amplitudes, because of the subsequent structural analysis. The part load and low head operating point was not only located at the part load region of the turbine hill chart, but also at the higher part load region, so it offered the possibility to numerically investigate the higher part load phenomenon as well.

Figure 7.30 brings the axial projection of the simulated velocity vectors at the draft tube cone section located at $z/D_{1_a} = -0{,}93$, as well as the associated streamlines and the vortex rope cross-section. As seen from the vector distribution and from the flow path described by the streamlines, the numerical model was able to reproduce the vortex rope spinning movement as well as the rotation movement around the machine axis. The vortex rope elliptical shape at higher part load could also be reproduced by the numerical calculations, as illustrated in Figure 7.30.

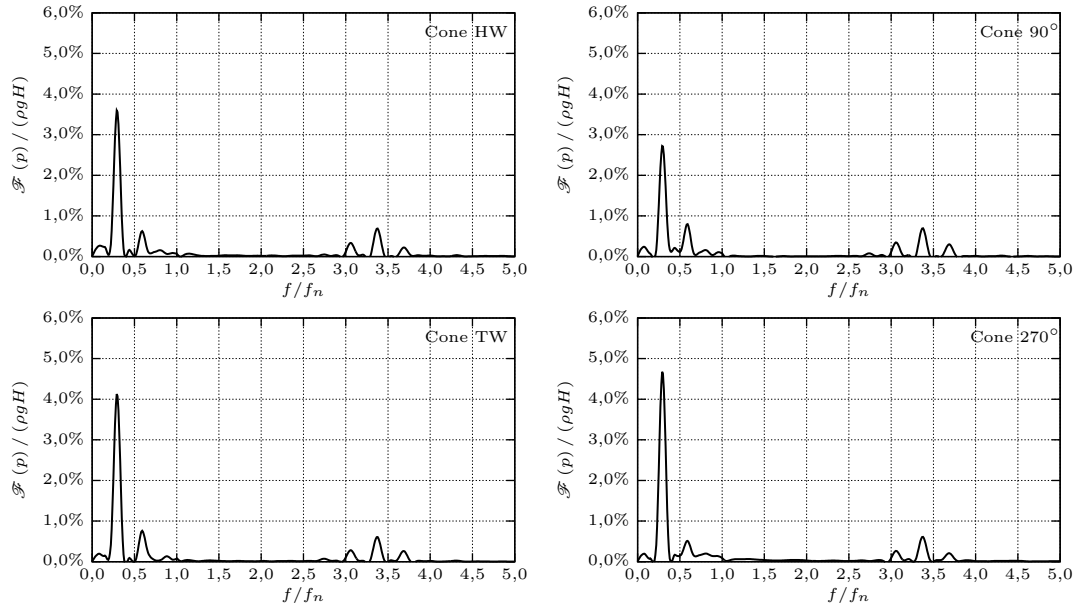

Figure 7.31: Pressure oscillation Fourier transform at the draft tube at higher part load.

The higher frequency, associated to the higher part load phenomenon and coming from the vortex rope spin, can be identified in Figure 7.31. The diagrams show the Fourier transform of the simulated pressure time history at the four measuring points in the draft tube cone. At the calculated frequency spectrum, the second amplitude peak, located at $f/f_n = 3{,}37$, was clearly captured.

From Figures 7.30 and 7.31 and their analysis, it could be verified that the numerical model employed for the simulation of the Francis machine was capable to properly simulate the higher part load phenomenon and its main characteristics, i.e. the vortex rope spin, its elliptical shape and the higher frequency.

To the author knowledge, the numerical results presented here and by Magnoli and Schilling [92, 93, 94] constituted the first successful numerical simulation of the higher part load phenomenon, which was published up to now.

Considering the pressure pulsation amplitudes at the runner at part load and low head, OP 6, they were qualitatively similar to the ones calculated for part load and high head, OP 5. Nevertheless, they presented higher amplitudes at OP 6 than at OP 5. The pressure pulsation amplitudes at part load and low head, at selected conformal planes, can be encountered in Figure 7.32. Once again, as for the previously presented operating points, the pressure oscillation amplitude, $\Delta P / (\rho g H)$, at the runner blades were extracted for seven conformal planes. The conformal planes were located at the coordinates, $v = 0{,}025$, $v = 0{,}125$, $v = 0{,}325$, $v = 0{,}500$, $v = 0{,}725$, $v = 0{,}875$, $v = 0{,}975$, going from the crown vicinity up to the band vicinity. The u coordinate started at the trailing edge at the pressure side, $u = 0{,}00$, passed through the leading edge, $u = 0{,}50$, and arrived at the trailing edge at the suction side, $u = 1{,}00$.

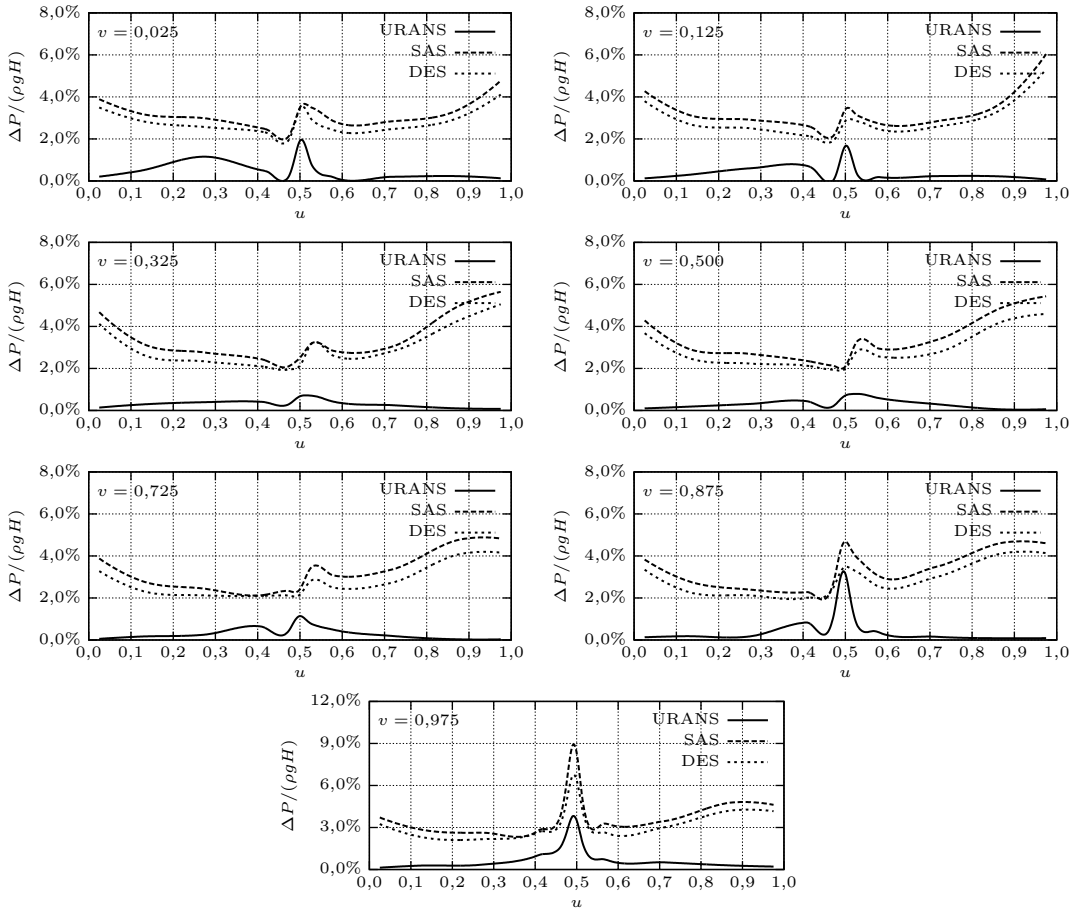

Figure 7.32: Pressure oscillation amplitude at selected conformal planes at partial load and low head.

In the diagrams in Figure 7.32, the results of the numerical simulations obtained with URANS, SAS and DES are compared. Again the $\Delta P/(\rho g H)$ values calculated with SAS and DES were close to each other, while URANS was inaccurate and could not even approach the amplitudes predicted by the hybrid turbulence models. This was the same behaviour already observed at the simulation of the part load and high head operating point, OP 5. Due to the similarity of the two operating points, the performance of the turbulence models at part load and low head was already expected. The reasons for the accurate predictions of SAS and DES and for the limitations of URANS were the same as discussed before.

From the diagrams in Figure 7.32, the numerically predicted values for the pressure pulsation amplitudes with the hybrid turbulence models at part load and low head were respectively 8,6% and 6,0% at the blade leading edge and at the blade body. As seen in the plots, the values of $\Delta P/(\rho g H)$ at the blade body were higher at part load and low head, OP 5, in comparison to the other operating points previously analysed. Moreover, the regions with higher pressure oscillation amplitudes, caused by the rotating vortex rope under the runner, covered larger portions of the blade surface, especially at its suction side.

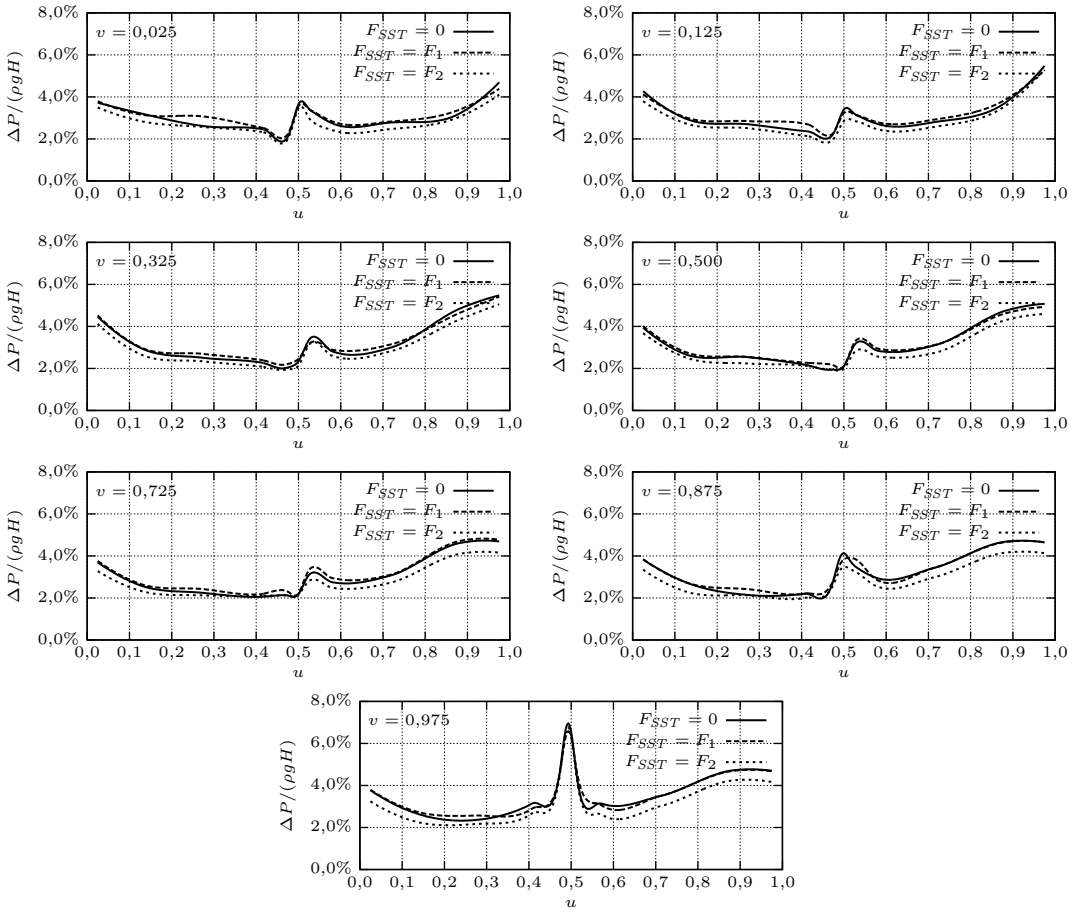

Figure 7.33: Effect of the DES blend function on the pressure oscillation amplitude at selected conformal planes at partial load and low head.

At part load and low head, one additional test was performed, concerning the DES limiter modification introduced by Menter and Kuntz [102]. The DES simulations were repeated with F_{SST} equal to zero, F_1 and F_2. The results for the pressure pulsation amplitude at the runner can be seen in Figure 7.33. As observed in the figure, the usage of the different blending functions did not significantly influence the level of the calculated pressure pulsation amplitudes. The only systematic effect, which could be determined, was the slightly smaller values predicted by using the blending function F_2, instead of the zero function or F_1. The reason for it was that the blending function F_2, suggested by Menter and Kuntz [102] to avoid non-physical flow separations induced by the computational grid, caused the DES model to switch slightly later to the LES mode. As long as no grid-induced separation was observed and $F_{\mathrm{SST}} = 0$ and $F_{\mathrm{SST}} = F_1$ produced similar results, the values considered for further analysis made use of $F_{\mathrm{SST}} = 0$.

The distribution of the pressure oscillation amplitude, $\Delta P/(\rho g H)$, at the runner blades can be viewed in Figure 7.34. The contour plot is shown with help of the meridian transform of the runner blades and guide vanes. The blade pressure side is found at the right side of the figure and the blade suction side at the left side. The contour plot also indicated that, at this operating point, the higher amplitudes

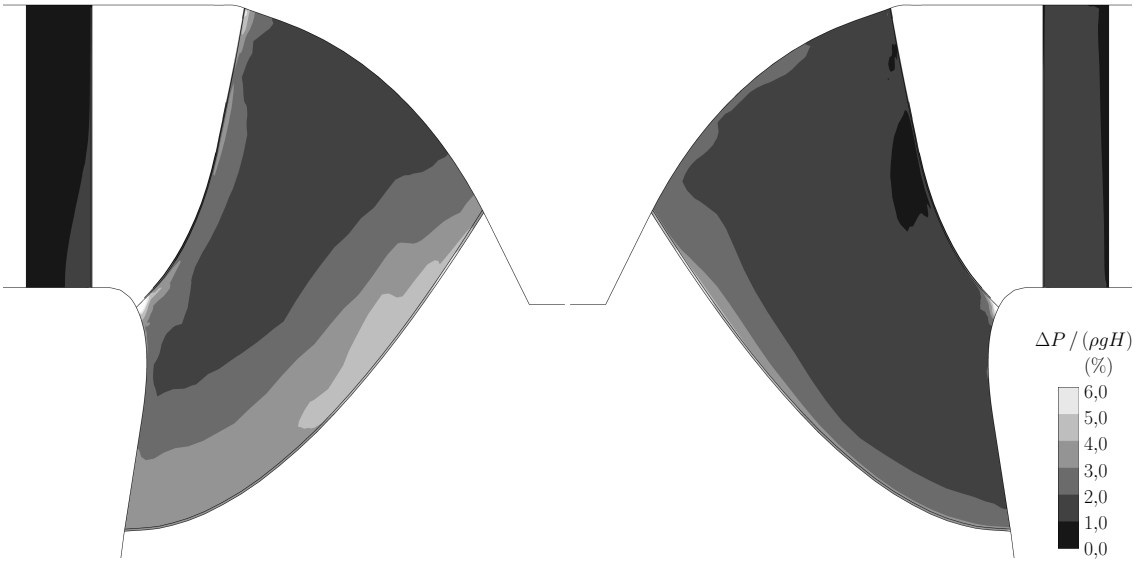

Figure 7.34: Pressure oscillation amplitude at part load and low head, meridian view.

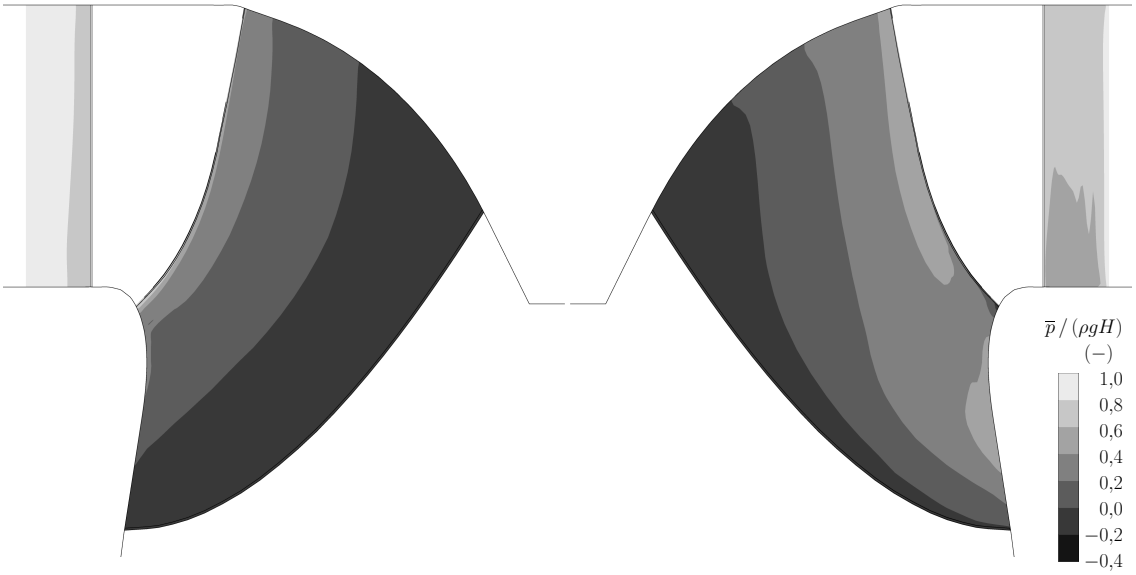

Figure 7.35: Time-averaged pressure at part load and low head, meridian view.

extended over large regions of the blade body, especially at its suction side, caused by the proximity to the vortex rope.

Repeating the procedure for the previously calculated operating points, the time-averaged pressure field was determined for the part load and low head operating point, OP 6. Figure 7.35 depicts the static pressure distribution at the runner and guide vanes, normalised to the net head, $\overline{p}/\left(\rho g H\right)$. The contour plot is shown at the meridian transform of the hydraulic surfaces. The pressure and suction sides can be respectively found at right and left side of the picture. The experimental level of the downstream tank during the model test was used as reference level for the static pressure.

7.3.4 Channel Vortex, Draft Tube Instabilities and Deep Part Load

The deep part load region of the turbine hill chart is characterised by the set-in of the channel vortex between the runner blades and by low volume flows. At this operating condition, diverse transient phenomena take place in the Francis machine. Naturally, the channel vortex in the runner, which defines the begin of the deep part load region, belongs to them. The second dynamic phenomenon, present at deep part load, is the flow separation at the runner blade leading edge. At moderate part load, the rotating vortex rope under the runner cone and in the draft tube diffusor, typical from part load, is still present. For very reduced volume flows, backflow and recirculation occur in the turbine runner, up to the point that speed-no-load is reached. At the lower portion of the deep part load region of the hill chart, cavitation phenomena can also strongly influence the flow dynamics.

Up to now, there has been extremely limited research on the dynamic phenomena taking place at deep part load. The possible reason for it is the complexity to model the dynamic flow effects and cavitation, which might become important at very reduced flows. Nonetheless, the presence of the highly transient flow phenomena makes the deep part load an interesting operating condition for the dynamic behaviour of Francis turbines. Experience in prototypes confirms that deep part load constitutes a demanding operating condition for the runner structure.

For the importance of this operating condition, the deep part load operating point, OP 7, $n'_1/n'_{1_{opt}} = 1{,}043$, $Q'_1/Q'_{1_{opt}} = 0{,}570$, was included in the numerical simulations for this study. This point was located at moderate deep part load, i.e. near to the hill chart curve corresponding to the set-in of the vortex channel. This operating point was frequent for the real prototype operation and, due to its moderate characteristics, the cavitation effects were not significant, as experimentally observed in the model test.

After the analysis of the influence of the turbulence models on the previously computed operating points and the accuracy obtained with the hybrid models, it was judged to be sufficient to calculate the deep part load point with just one method. The transient numerical simulations at deep part load were carried out exclusively with the DES turbulence model.

Figure 7.36 shows the calculated pressure pulsation amplitude, $\Delta P/(\rho g H)$, at the runner blades at seven conformal planes. As before, the conformal planes were located at the coordinates $v = 0{,}025$, $v = 0{,}125$, $v = 0{,}325$, $v = 0{,}500$, $v = 0{,}725$, $v = 0{,}875$ and $v = 0{,}975$, starting from the crown in direction to the band. The u coordinate assumed the values $u = 0{,}00$, $u = 0{,}50$ and $u = 1{,}00$ respectively at the trailing edge at the pressure side, at the leading edge and at the trailing edge at the suction side.

From the plots in Figure 7.36, it could be identified that the pressure pulsation amplitudes at the blade body were considerably high in comparison to the previously

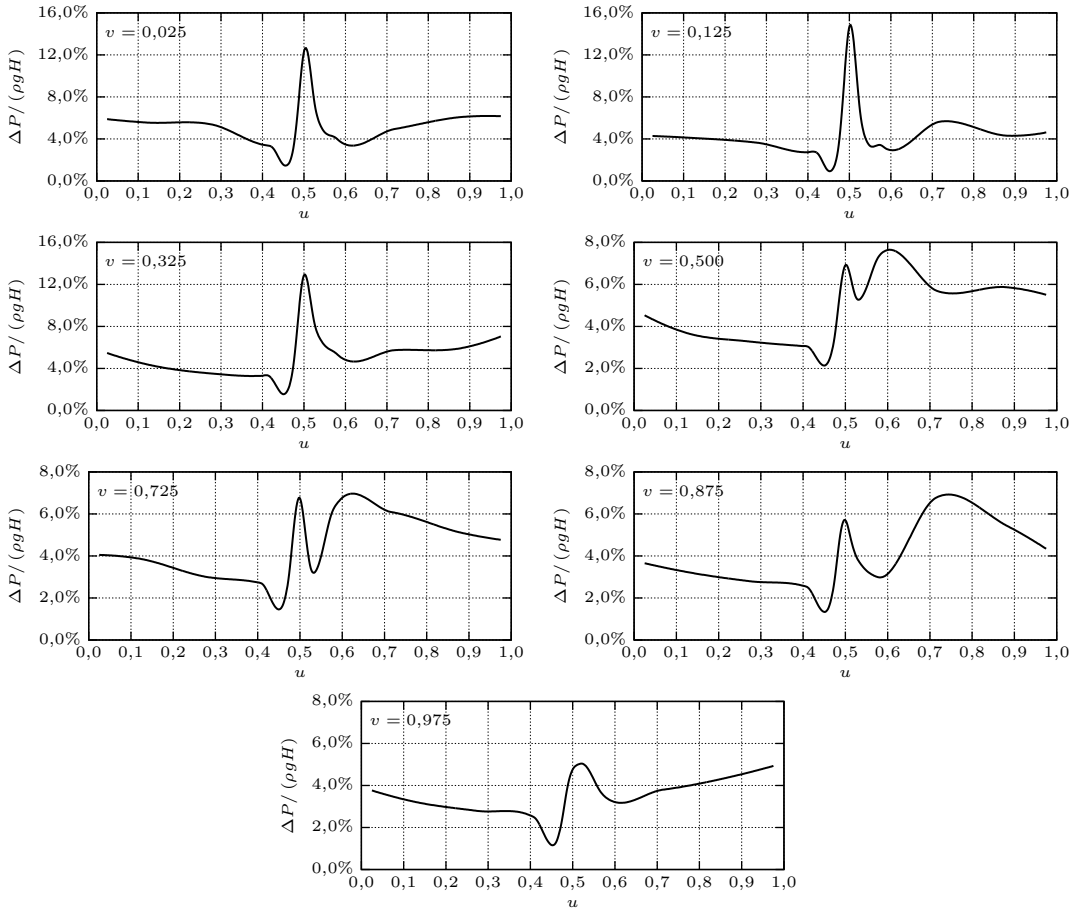

Figure 7.36: Pressure oscillation amplitude at selected conformal planes at deep part load.

operating points, especially at the blade suction side. The maximum values for $\Delta P/(\rho g H)$ were 14,7% at the blade leading edge and 7,6% at the blade body. These high values, when compared to the previously simulated operating points, were reached at deep part load because of the rotor-stator interaction (RSI), flow separation, channel vortex and vortex rope.

The pressure oscillations at the blade leading edge were in part due to the rotor-stator interaction (RSI). In addition to it, at deep part load, the flow separation at the blade inlet edge and the associated vortex contributed to the high values of $\Delta P/(\rho g H)$ at the inlet edge.

Figure 7.37 shows the time-averaged streamlines at three conformal planes at the runner, near to the crown, $v = 0{,}20$, at the middle of the runner channel, $v = 0{,}50$ and near to the band $v = 0{,}80$. The streamlines at the stay vanes and guide vanes were in the absolute reference system, while the ones at the runner were at its rotational reference system. At operating conditions distant from the optimum, the runner flow shape differed considerably from the conformal surfaces, so that the streamlines did not appear parallel to the surfaces at this representation.

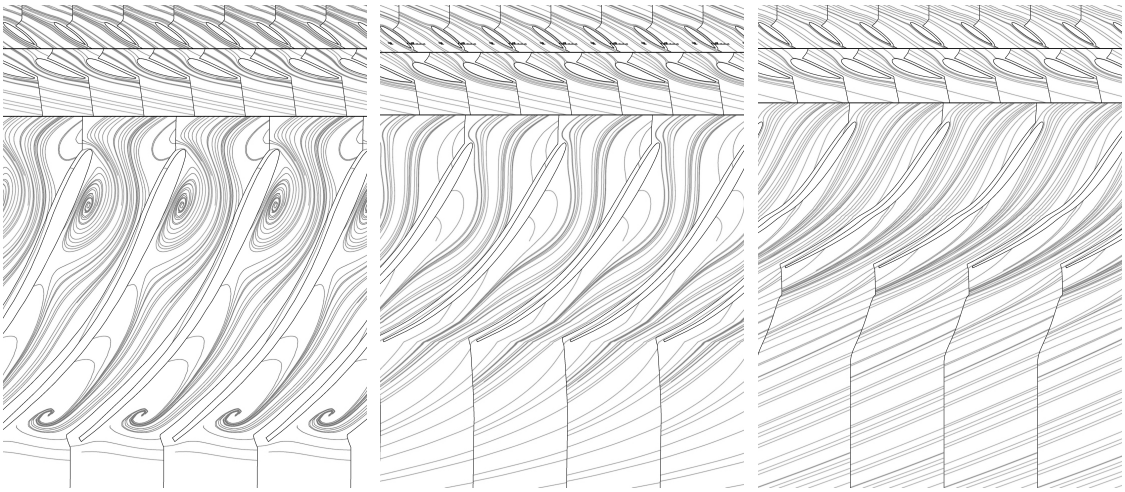

Figure 7.37: Time-averaged streamlines at the runner at deep part load, at the conformal planes $v = 0{,}20$, $v = 0{,}50$, $v = 0{,}80$.

Due to the high head, $n'_1/n'_{1_{opt}} = 1{,}043$, and to the reduced volume flow, $Q'_1/Q'_{1_{opt}} = 0{,}570$, the required guide vane opening resulted in small opening angles, as seen in Figure 7.37. The consequently small flow inlet angle at the runner caused the fluid separation at the blade leading edge at the suction side near to the crown. The resulting separation vortex contributed for increasing the pressure oscillations in the runner.

As before, the pressure pulsations at the blade body experienced the effect of the vortex rope in the draft tube cone. At deep part load, they were also influenced by the additional effect of the runner channel vortex. Figure 7.38 shows the time-averaged streamlines and vortical structures in the runner channel. Different visualisations are presented. On the left side of Figure 7.38, three channels and three blades can be observed and, on the right side, one channel and one blade from another angle. The streamlines were extracted in the runner rotating reference frame. The vortical structures, represented by isosurfaces, were extracted with the λ_2 method proposed by Jeong and Hussain [69].

The helical path of the streamlines around the channel vortex indicated its rotational movement between the runner blades. This motion, associated to the instationary character of the channel vortex, was responsible for the increase of the pressure pulsations in the runner at deep part load. As seen in Figure 7.38, the channel vortex started at the crown, near to the blade suction side, and developed along the blade length, in direction to the band and to the blade outlet.

The channel vortex obtained from the instationary numerical simulations could also be identified by the cavitating surfaces. Using the same method employed for the previous operating points, the isobarometric surfaces at the vapour pressure, p_{va}, are shown in Figure 7.39. On the left side of Figure 7.39, the runner is viewed from the top, showing how the channel vortex initiated near to and along the blade inlet edge on the suction side. On the right side of Figure 7.39, the runner is viewed from

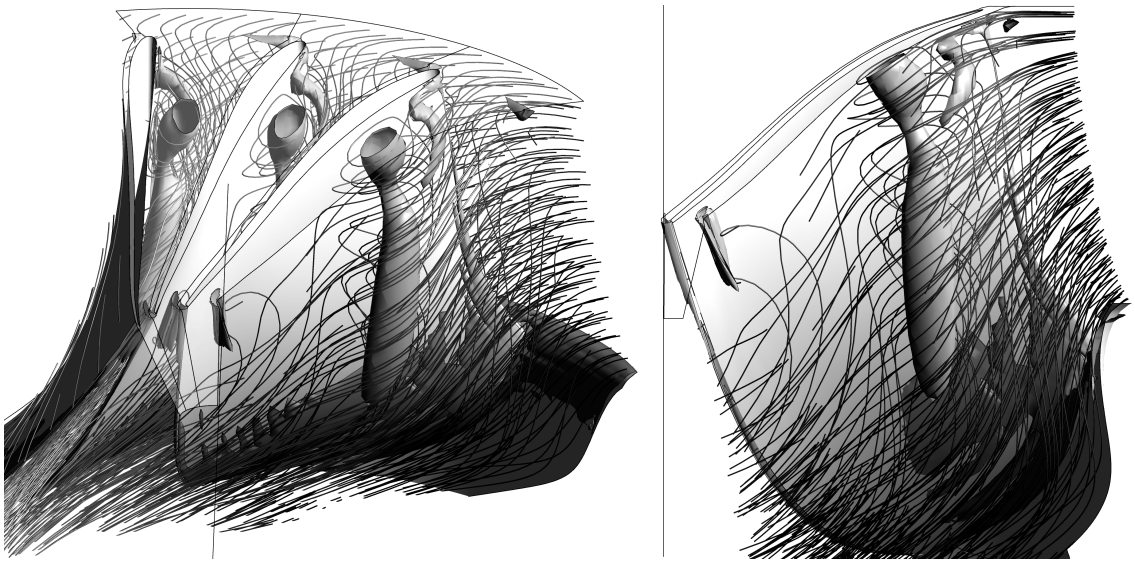

Figure 7.38: Time-averaged channel vortex at the runner blades suction side at deep part load.

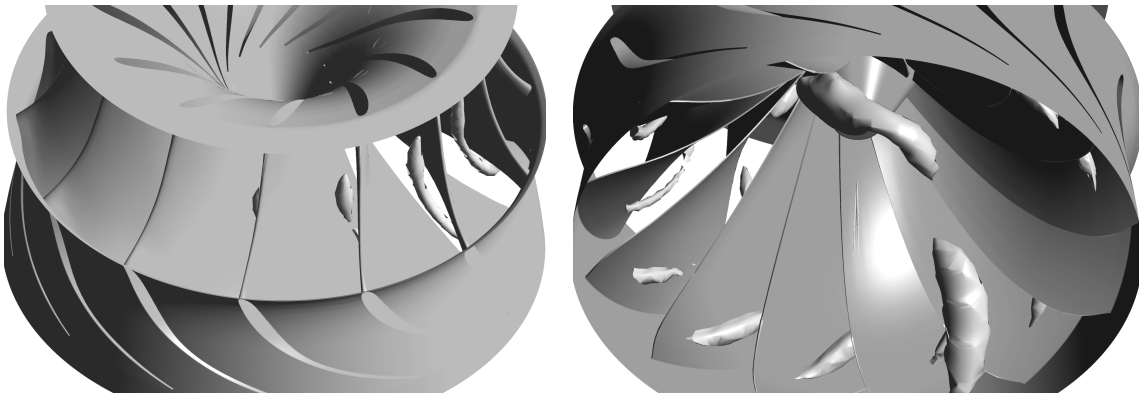

Figure 7.39: Cavitating channel vortex at the runner at deep part load.

the bottom, allowing to see how the channel vortex extended from the inlet to the outlet of the runner channel. The numerically calculated channel vortex resulted in the typical shape observed during model tests.

Figure 7.40 brings the contour plot with the distribution of the pressure oscillation amplitude at the runner. The meridian transform of the blades pressure side and of the guide vanes can be found on the right side, while the suction side transform is on the left side. As already discussed, the high pressure oscillation amplitudes and its complex distribution were caused by the numerous dynamic effects at moderate deep part load, i.e. rotor-stator interaction (RSI), leading edge separation, runner channel vortex (RCV) and draft tube instabilities (DTI).

For the upcoming numerical simulation of the static runner stresses at deep part load, the time-averaged pressure distribution on the runner blades was evaluated. Figure 7.41 shows the contour plot for the static pressure, $\overline{p}/\left(\rho g H\right)$, at the meridian transform of the runner blades and guide vanes. The blade pressure side can be

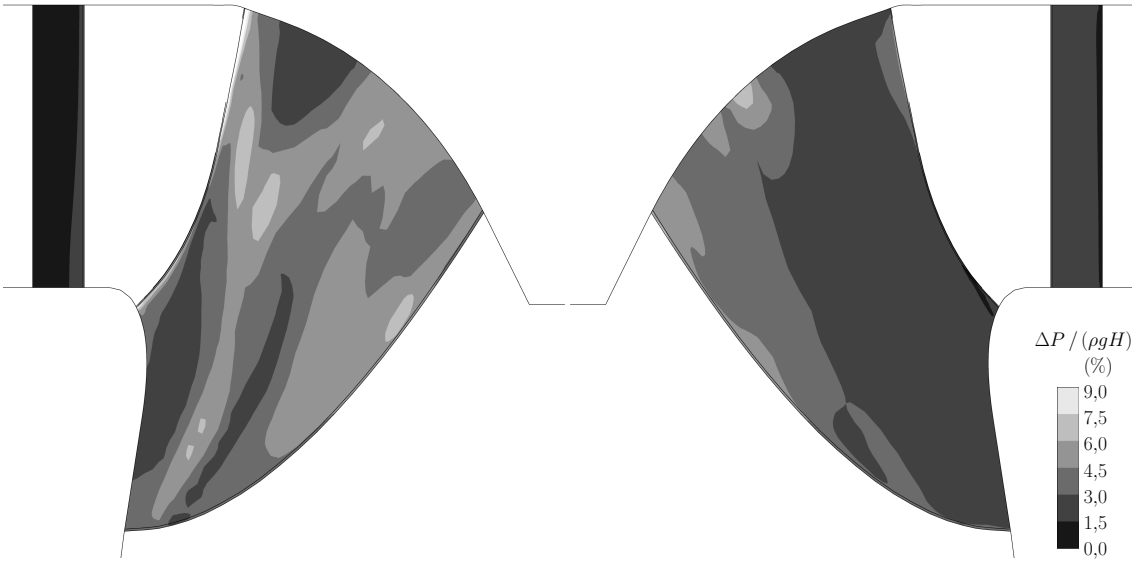

Figure 7.40: Pressure oscillation amplitude at deep part load, meridian view.

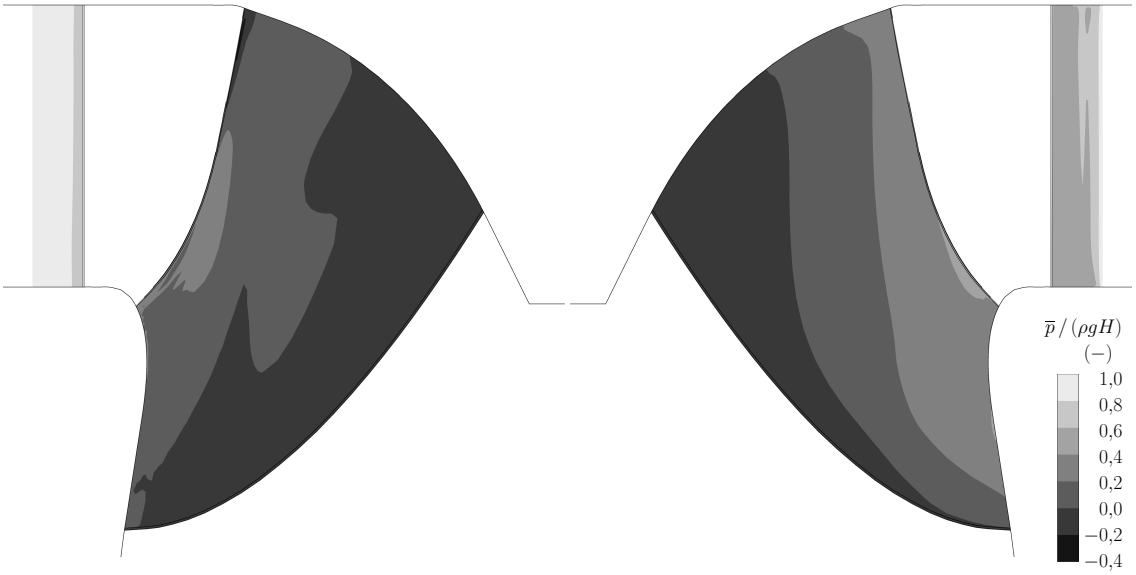

Figure 7.41: Time-averaged pressure at deep part load, meridian view.

found on the right and the suction side on the left. The pressure reference level at the outlet of the computational domain was set to match the relative pressure at the downstream tank during the model test.

7.3.5 Vortex Shedding Effects

Depending on the trailing edge geometry of the runner blades and on the operating conditions, vortex shedding may take place in Francis runners. The runner blade constitutes a blunt body and, behind it, VON KÁRMÁN [163] vortex streets may appear at different intensities.

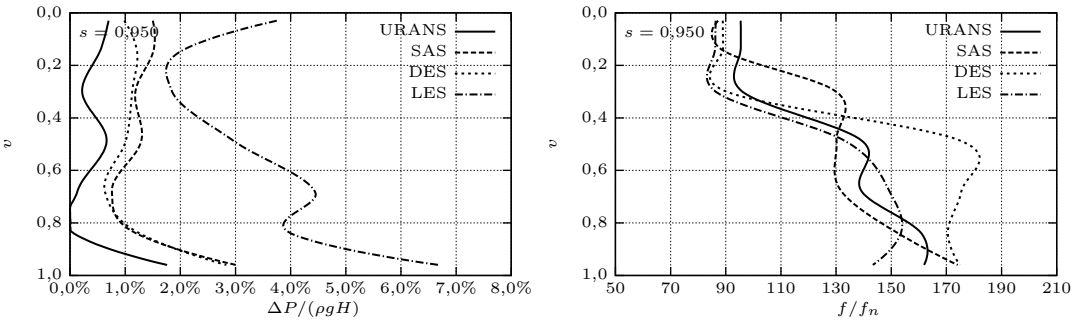

Figure 7.42: Vortex shedding differential pressure oscillation amplitude and oscillating frequency at the trailing edge at the rated operating point.

In modern designs, the trailing edge of the Francis blades is chamfered and brought to extremely reduced thickness, virtually eliminating the problem. This procedure was extensively studied by Gummer and Hensman [57] for other components of hydraulic turbines. Moreover, there is no clear report of runner failure caused by von Kármán vortices. For these reasons, this thematic should not be so relevant any more.

However, there are still machines in operation, for which the chamfering procedure was not employed, as it was the case of the turbine studied here. In such situations, the vortex shedding effect can be the source of noise and blade vibrations. For the evaluation of this phenomenon, the procedure presented here could be used. With the dynamic simulation of the fluid flow, the vortex shedding effect could be captured as well as its oscillation amplitude and frequency. The simulation of the vortex shedding as done here should be interpreted as a first approach, since the interaction with the structure might be important for this phenomenon, e.g. in the case of lock-in effects as explained by Blevins [17].

For the simulation of the von Kármán vortex streets behind the runner blades, the LES, DES, SAS and URANS turbulence models were tested. In Figure 7.12, where the main interest was to compare the experimental and the numerically simulated draft tube vortex shape, the pattern of the vortex streets could be observed as well. The numerically simulated vortices displayed the same pattern as during the model test.

The differential pressure oscillation amplitude along the trailing edge calculated with LES, DES, SAS and URANS is found in Figure 7.42 on the left. The difference in the amplitude between the pressure and suction sides are shown along the trailing edge length, starting near to the crown, $v = 0{,}00$, and going till the band, $v = 1{,}00$. Concentrating on the LES results, the pressure oscillation amplitude, due to the vortex shedding effect (VSE), experienced a minimum near to the crown and increased in the direction of the band. The differential pressure oscillation amplitude reached 3,7% near to the crown, passed through a minimum of 1,7% and achieved 6,7% near to the band.

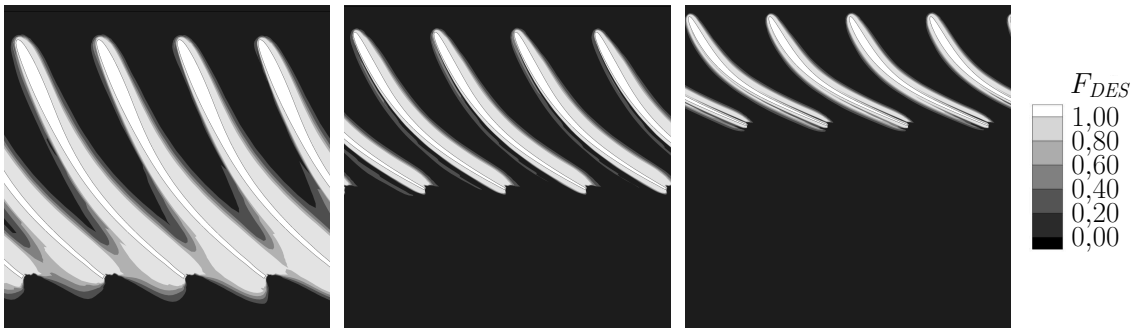

$v = 0{,}20$ $v = 0{,}50$ $v = 0{,}80$

Figure 7.43: Limiter for the SAS model at full load at conformal planes.

The same general pattern could be observed for the frequency, on the right side of Figure 7.42. The vortex generation was asynchronous along the trailing edge, presenting distinct vortex shedding frequencies. The reasons for it were the local blade geometry and flow conditions, as stream velocity, boundary layer thickness and deviation angle. The calculated frequencies varied from around 86 times the runner rotating frequency at the upper third part of the blade to 148 times the runner rotating frequency along the lower half part of the blade.

In contrast to the rotor-stator interaction (RSI), to the draft tube instabilities (DTI) and to the runner channel vortex (RCV) simulations, the hybrid turbulence models were not able to reproduce the results achieved with LES, as seen in Figure 7.42. The pressure oscillation amplitude calculated with the hybrid models was not as large as with LES.

Figure 7.43 brings the probable explanation for this effect. As an example, the DES blending function, F_{DES}, distribution at three conformal planes, $v = 0{,}20$, $v = 0{,}50$ and $v = 0{,}80$, is shown. The values of F_{DES} were near to 1 around the blades, forcing the hybrid turbulence models to assume the URANS behaviour near to the regions of the vortex shedding generation. The damping characteristic of URANS was probably the cause for the reduced amplitudes evaluated with the hybrid turbulence models. It is important to point out that the computational mesh was intentionally not refined in the boundary layer, since the main interest of this study was the numerical simulation of the rotor-stator interaction (RSI), draft tube instabilities (DTI) and runner channel vortex (RCV), which are transient fluid phenomena taking place at the core of the fluid flow and not at the boundary layers. As seen before, for the simulation of these other dynamic effects, SAS and DES were enough accurate.

Figure 7.44 brings the representation of the pressure oscillation amplitude, $\Delta P/(\rho g H)$, induced by the vortex shedding effect (VSE) and calculated with LES at the meridian transform of the runner blades and guide vanes. The right side corresponds to the pressure side and the left side to the suction side. The dynamic pressure distribution on the runner blades could be used for the structural analysis of the dynamic stresses caused by the von Kármán vortices. In the assessment of

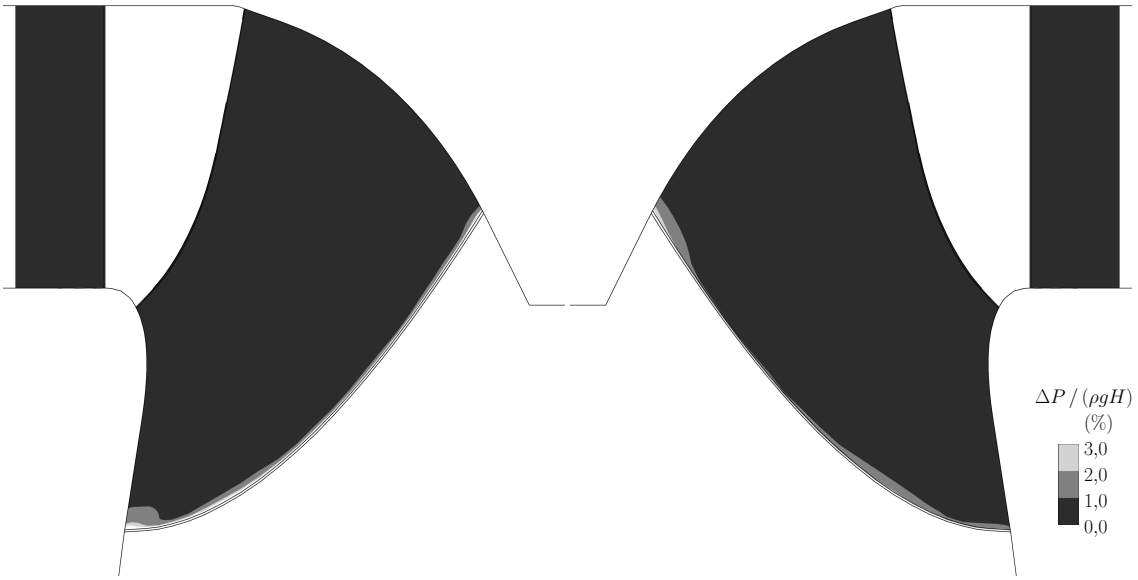

Figure 7.44: Pressure oscillation amplitude at the rated operating point, meridian view.

these mechanical stresses, the lock-in effect due to the fluid-structure interaction should be kept in mind.

The pressure oscillation amplitude caused by the von Kármán vortex streets might be eventually high, when compared to those of other fluid phenomena as rotor-stator interaction (RSI) and draft tube instabilities (DTI). Even though the high amplitudes were limited to small areas at the blade trailing edge, it corresponds to the blade location with the lowest stiffness and with the highest sensibility to mechanical stresses. Therefore, vortex shedding should be avoided in runner design, e.g. with blade chamfering, and its mechanical effects should be further investigated.

7.3.6 Results Summary and Further Considerations

The main objective of the fluid flow computational simulations was the numerical prediction of the transient pressure distribution at the turbine runner. The validation of the presented computation method and relevant turbulence models was achieved through the comparison with the static and dynamic experimental results. Extensive numerical results were produced and part of them is summarised and commented here.

Pressure Oscillation Amplitude and Operating Points

The magnitude of the calculated pressure oscillations was dependent on the driving fluid flow dynamic phenomenon at each selected operating point. The principal flow phenomena in the Francis turbine studied here were the rotor-stator interaction

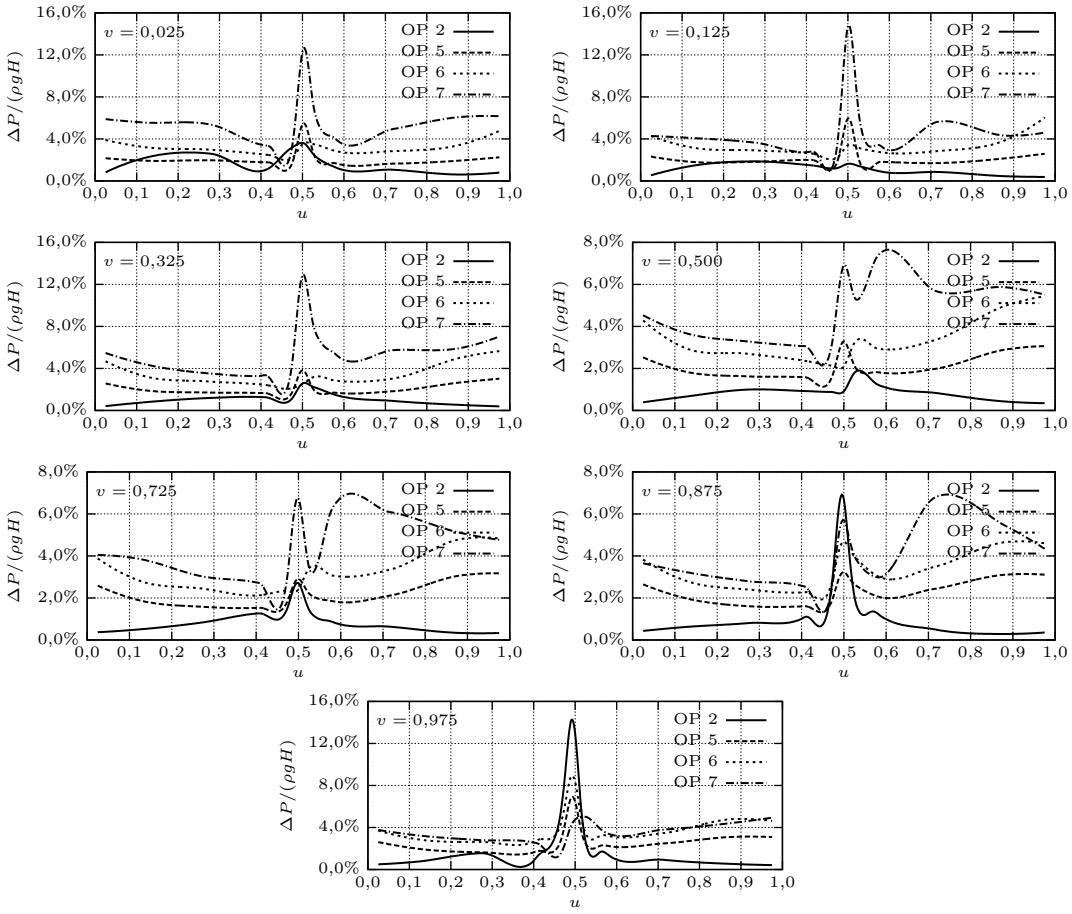

Figure 7.45: Pressure oscillation amplitude at selected conformal planes at rated (OP 2), partial load and high head (OP 5), partial load and low head (OP 6) and deep part load (OP 7).

(RSI), draft tube instabilities (DTI), higher part load (HPL) and runner channel vortex (RCV). These effects could be respectively found at the rated operating point, OP 2, at part load and high head, OP 5, part load and low head, OP 6, and deep part load, OP 7.

The pressure oscillation amplitude at the runner blades at the calculated operating points using the hybrid turbulence models is summarised in Figure 7.45. There, the influence of the several dynamic fluid effects can be seen and compared. As before, seven conformal planes, starting near to the crown, $v = 0{,}025$, passing through the middle of the channel, $v = 0{,}500$, and going up to the band vicinity, $v = 0{,}975$, were employed for representing the pressure oscillation amplitude, $\Delta P/(\rho g H)$, at the runner blades. For each conformal plane, the pressure oscillation amplitude is plotted starting at the trailing edge on the pressure side, $u = 0{,}00$, passing through the leading edge, $u = 0{,}50$, and arriving at the trailing edge on the suction side, $u = 1{,}00$.

It can be seen in Figure 7.45, that in the case of the FT 80 the highest pressure oscillation amplitudes at the runner were reached at deep part load, OP 7, caused

by the runner channel vortex (RCV). Next came the part load and low head, OP 6, dominated by the higher part load (HPL), followed by part load and low head, OP 5, where the draft tube instabilities (DTI) were the driving effect. The pressure oscillation amplitudes at the rated operating point, OP 2, arising from the rotor-stator interaction (RSI), became important only close to the band, at the conformal planes $v = 0{,}875$ and $v = 0{,}975$, where the distance between the runner blades leading edge and the guide vanes became more reduced.

The behaviour of high specific speed Francis machines would be the opposite. The rotor-stator interaction would originate the higher pressure pulsation amplitudes, while the draft tube instabilities, higher part load and runner channel vortex would lose in importance. This behaviour and the corresponding pressure oscillation amplitudes could be calculated in the same way as it was done for the FT 80 with the calculation method presented here.

Figure 7.45 shows that at the rated operating point, OP 2, the pressure oscillations caused by the rotor-stator interaction (RSI) could make themselves noticeable only at the runner blades leading edge, while the amplitudes at the rest of the blade remained low. On the other hand, for the part load operating points, OP 5, OP 6 and OP 7, the pressure pulsation amplitudes remained elevated all over the blade, including the leading edge and the blade body, i.e. pressure and suction sides. Especially the suction side was submitted to the higher pressure oscillation amplitudes, because of the relative position of the rotating vortex rope under the runner, up to the draft tube cone. At deep part load, OP 7, where the calculated values were higher, $\Delta P/(\rho g H)$ was also significantly high at the leading edge, in part due to the runner channel vortex, with its start location near to the leading edge.

The time-averaged velocity profiles, for the radial, tangential and axial velocity components, c_r, c_u and c_m, for the optimum operating point, OP 1, for the rated, OP 2, for part load and high head, OP 5, and part load and low head, OP 6, are found in Figure 7.46. The velocity components were normalised in relation to the runner peripheral velocity at the outer diameter of the blades inlet edge, $U_{1_a} = (D_{1_a}/2)\,\omega$. They were plotted along the normalised radial coordinate, $r/(D_3/2)$, at the runner outlet. Figure 7.46 brings also the distribution of the normalised Euler head at the runner outlet, H_{E_2}/H. The normalised value of the mass-averaged Euler head at the runner outlet, $\overline{H_{E_2}}/H$, is written in the diagrams as well.

At the optimum operating point, OP 1, the velocity distributions were significantly smooth and well balanced. The axial velocity component, c_m, had a nearby constant value at a long extension of the runner outlet. With increasing power and flow, the mass flow was slightly increased near to the runner centre, $r \to 0$, and decreased near to the outer portion of it, $r \to 1$, as seen for the rated operating point, OP 2.

The opposite effect could be observed at the part load, OP 5 and OP 6. The axial velocity, c_m, was considerably increased near to the outer diameter and strongly decreased near to the runner centre. Further reducing the turbine volume flow, Q,

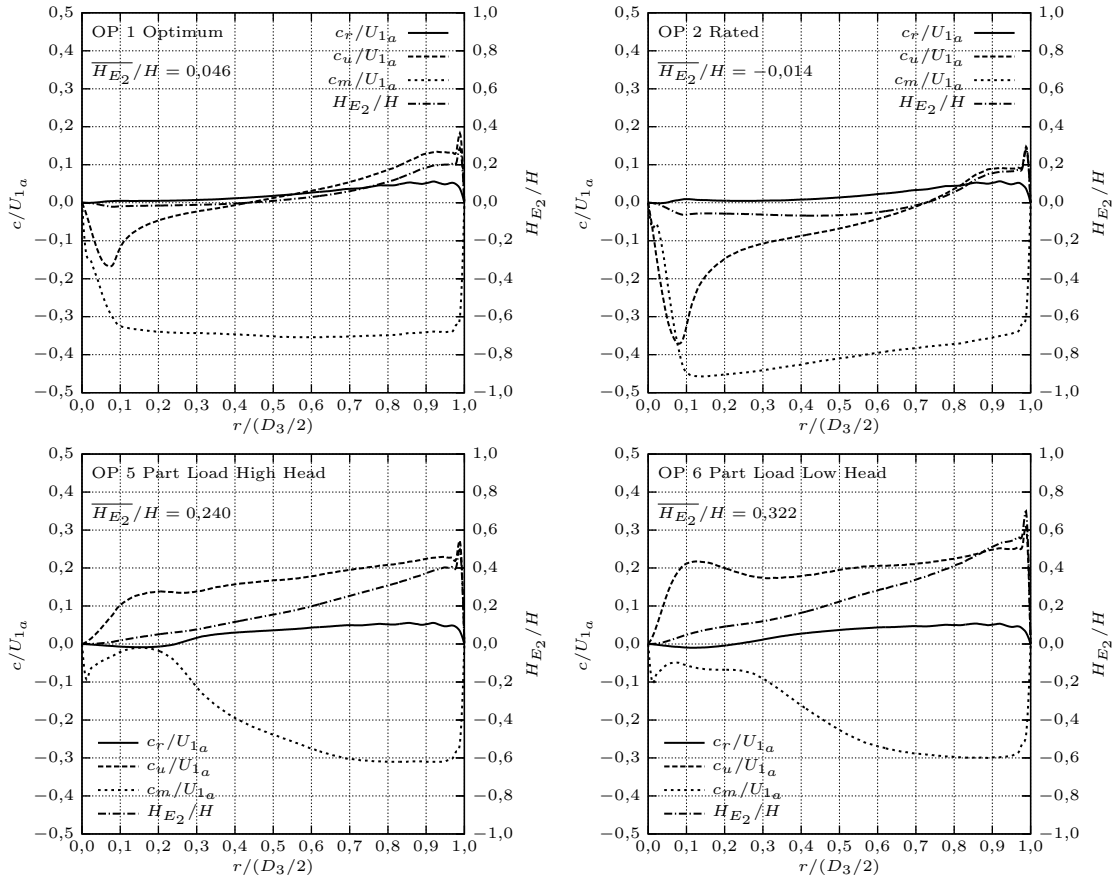

Figure 7.46: Circumferentially averaged velocity and momentum distribution at the runner outlet at optimum (OP 1), rated (OP 2), partial load and high head (OP 5), partial load and low head (OP 6).

and consequently going further into the direction of deep part load and speed-no-load (SNL) would even result into backflow in the central portion of the runner outlet, as it was already almost the case at part load and high head, OP 5.

At Figure 7.46, the relation between the turbine load and the circumferential velocity and Euler head distributions can also be observed. At the optimum operating point, OP 1, the c_u distribution was well balanced along the radius, with regions of similar extension with normal swirl, $c_u > 0$, and counter-swirl, $c_u < 0$. The mass-averaged Euler head at the runner outlet for the optimum was $\overline{H_{E_2}}/H = 4{,}6\%$. In the case of the FT 80, the optimum, OP 1, belongs to the rope free zone and the pressure pulsations in the draft tube cone were considerably low.

At the rated operating point, which corresponded to more volume flow and power than at the optimum, the tendency for counter-swirl became dominant and the mass-averaged Euler head resulted in a negative value, $\overline{H_{E_2}}/H = -1{,}4\%$. The pressure pulsations in the draft tube cone remained considerably low for the rated operating point and the draft tube vortex assumed the torch shape.

Table 7.11: Numerical simulated pressure oscillation amplitude on the runner blades for selected operating points.

Operating Point	$\frac{n'_1}{n'_{1_{opt}}}$ (-)	$\frac{Q'_1}{Q'_{1_{opt}}}$ (-)	$\frac{T'_1}{T'_{1_{opt}}}$ (-)	$\frac{\eta}{\eta_{opt}}$ (-)	$\Delta P/(\rho g H)$ LE (%)	$\Delta P/(\rho g H)$ PS/SS (%)	f/f_n LE (-)	f/f_n PS/SS (-)
OP 2 Rated	1,103	1,229	1,083	0,972	13,7	2,7	24	24
OP 5 Part load high head	1,078	0,797	0,693	0,938	6,6	3,1	24	0,302
OP 6 Part load low head	1,199	0,848	0,644	0,910	8,6	6,0	24	0,282
OP 7 Deep part load	1,043	0,570	0,452	0,828	14,7	7,6	24	0,299

At part load, with decreasing volume flow, the values of c_u were considerably increased along all the radial extension of the runner outlet and there was only normal swirl, $c_u > 0$. The higher values of c_u resulted in considerably higher values of the mass-averaged Euler head, which reached $\overline{H_{E_2}}/H = 24{,}0\%$ and $\overline{H_{E_2}}/H = 32{,}2\%$ for part load and high head, OP 5, and part load and low head, OP 6. These two operating points registered high pressure oscillation amplitudes at the draft tube cone, with even the set-in of higher part load (HPL) at the operating point OP 6. These operating points belonged to the portion of the hill chart, where the rotating vortex rope in the draft tube cone was fully developed.

Pressure Oscillation Amplitude as Design Parameter

The pressure oscillation amplitude, $\Delta P/(\rho g H)$, can be considered as an important parameter for the excitation loads on the runner structure. The values of $\Delta P/(\rho g H)$ could be used as design parameter for the comparison of different runner designs, in relation to their lower or higher potential to dynamically excite the runner structure. They could also be used as driving parameter for the runner mechanical design and structural assessment.

Table 7.11 summarises the numerically predicted pressure oscillation amplitude at the runner and their respective dominating excitation frequency for different operating points. The maximum pressure oscillation amplitude values, $\Delta P/(\rho g H)$, at the runner blades leading edge (LE) and at their body, i.e. pressure and suction sides (PS-SS), can be found in Table 7.11 and the same for the dominating excitation frequency, f/f_n. The values are listed for the operating points corresponding to the important dynamic fluid flow phenomena taking place at the runner, with the rated operating point, OP 2, being representative for rotor-stator interaction (RSI), part load and high head, OP 5, for draft tube instabilities (DTI), part load and low head, OP 6, for higher part load (HPL) and deep part load, OP 7, for runner channel vortex (RCV).

In the case of Francis turbines with high specific speed, as for the FT 80 simulated here, the pressure oscillation amplitude at the blade body should be the more relevant parameter, especially at the operating points OP 5, OP 6 and OP 7,

Table 7.12: Experimental pressure oscillation amplitude at the draft tube for selected operating points.

Operating Point	$\frac{n'_1}{n'_{1_{opt}}}$ (-)	$\frac{Q'_1}{Q'_{1_{opt}}}$ (-)	$\frac{T'_1}{T'_{1_{opt}}}$ (-)	$\frac{\eta}{\eta_{opt}}$ (-)	$\Delta P/(\rho g H)$ HW (%)	90° (%)	TW (%)	270° (%)	$\frac{f}{f_n}$ (-)
OP 2 Rated	1,103	1,229	1,083	0,972	0,36	0,39	0,38	0,40	0,165
OP 5 Part load high head	1,078	0,797	0,693	0,938	4,70	3,65	4,28	5,25	0,302
OP 6 Part load low head	1,199	0,848	0,644	0,910	5,29	4,51	5,71	6,78	0,282
OP 7 Deep part load	1,043	0,570	0,452	0,828	4,54	4,00	4,29	4,95	0,299

where the draft tube instabilities (DTI), higher part load (HPL) and runner channel vortex (RCV) were the driving phenomena. As long as turbines with high specific speed normally present considerable distance between the runner blades leading edge and the guide vanes, the rotor-stator interaction (RSI) should not be able to strongly excite the runner structure and importantly contribute to the fatigue damage, in spite of the higher $\Delta P/(\rho g H)$ values at the blade leading edge at the operating points OP 2 and OP 7. On the other hand, for Francis turbines with low specific speed, the rotor-stator interaction (RSI) should be more determinant for the structural load as the draft tube instabilities (DTI), higher part load (HPL) and runner channel vortex (RCV).

The experimentally determined values of the pressure oscillation amplitudes in the draft tube cone, which were previously used for the validation of the computation method and turbulence modelling, can be found again in Table 7.12. They would be relevant for the dynamic excitation of the draft tube cone, although structural problems related to the draft tube cone were extremely rarely reported. Up to now, values of $\Delta P/(\rho g H)$ in the draft tube cone were used by several turbine owners as parameter for the dynamic loads on the machine, possibly because of the current simplicity to measure them.

However, the pressure oscillation amplitude in the draft tube cone cannot be used as direct indication of the dynamic loads at the runner. The comparison of Tables 7.11 and 7.12 shows that there is no unequivocal direct relationship between the pressure oscillation amplitudes at the runner and at the draft tube cone, just some tendency. The highest pressure pulsations at the draft tube were reached at part load and low head, OP 6, corresponding to higher part load (HPL), while the highest amplitudes at the runner were produced by the runner channel vortices (RCV) at deep part load, OP 7.

Therefore, the values of $\Delta P/(\rho g H)$ at the runner should be employed as indication and as design parameter for the dynamic loads at the runner. In opposition to the pressure oscillation amplitude at the draft tube cone, they cannot be easily obtained experimentally, but the calculation method proposed here made it possible.

The pressure oscillation amplitudes at the runner, presented in Table 7.11 for the FT 80 turbine, can serve as typical values for machines with similar specific speed,

n_q. With the simulation of other machines with similar specific speed, it would be possible to investigate the bandwidth for the typical values. The calculation of turbines with different specific speeds would allow the creation of an extensive database with typical values as function of the machine n_q.

Further Applications

The determination of the dynamic hydraulic total forces and moments at the turbine runner could serve as example of further practical applications for the transient fluid flow simulation at the Francis machine. The dynamic radial total forces and moments at the turbine runner could be employed for the more accurate rotordynamic simulations of the machine shaft line. As in the case of the dynamic pressure field at the runner, the experimental determination of the radial forces and moments at the runner during the model test is not trivial, requires special measuring equipment and offers limited precision, due to the influence of the overall shaft line dynamics of the model machine on the measured forces and moments.

The same methodology presented here could also be employed for the numerical simulation of other operating points and operating conditions dominated by transient effects, as e.g. speed-no-load (SNL) and full load instability (FLI). In the case of speed-no-load, finer meshes at the runner channel would possibly be needed, because of the reduced size of the complex vortical structures, which appear. For full load instabilities (FLI), where the vortex torch under the runner and at the draft tube cone becomes pulsating, cavitation models might be needed.

The procedure presented here could be employed for any other Francis machine as well. Other examples for the application of this method can be found, for example, in Hasmatuchi [63], where it was attempted to better understand the instability of pump-turbines.

Chapter 8

Runner Structural Simulation

After the numerical simulation of the transient fluid flow through the Francis turbine and the numerical prediction of the pressure pulsations in the machine, the secondary objective of this study was the numerical simulation of the mechanical stresses in the turbine runner. The determination of the stresses in the turbine runner allowed the assessment of its structural and fatigue strength. It was also possible to evaluate the stress level caused by the different operating points and the fatigue damage induced by them.

The calculation of the mechanical stresses in the turbine runner was done with the finite element method (FEM), using the transient pressure distribution resulting from the previous CFD analysis. The precise and accurate results from the fluid flow simulation were stored for each calculated time step and used as input for the transient structural analysis. The structural simulation employed the real pressure distribution and made use of no simplifications, approximations or assumptions concerning the dynamic fluid flow. With the availability of the pressure time history at the runner, the finite element (FE) model could be solved through the direct time integration.

This chapter describes the finite element (FE) model and the numerical setup. It also brings the numerical results of the numerical structural simulations.

8.1 Turbine Runner Characteristics

8.1.1 Constructive Aspects

The mechanical stresses of the turbine runner were calculated using the real prototype geometry and in prototype size. The prototype turbine configuration can be seen in Figure 8.1, where the crown, band and shaft coupling designs can be identified. Differently from the turbine fluid flow, which could be calculated or

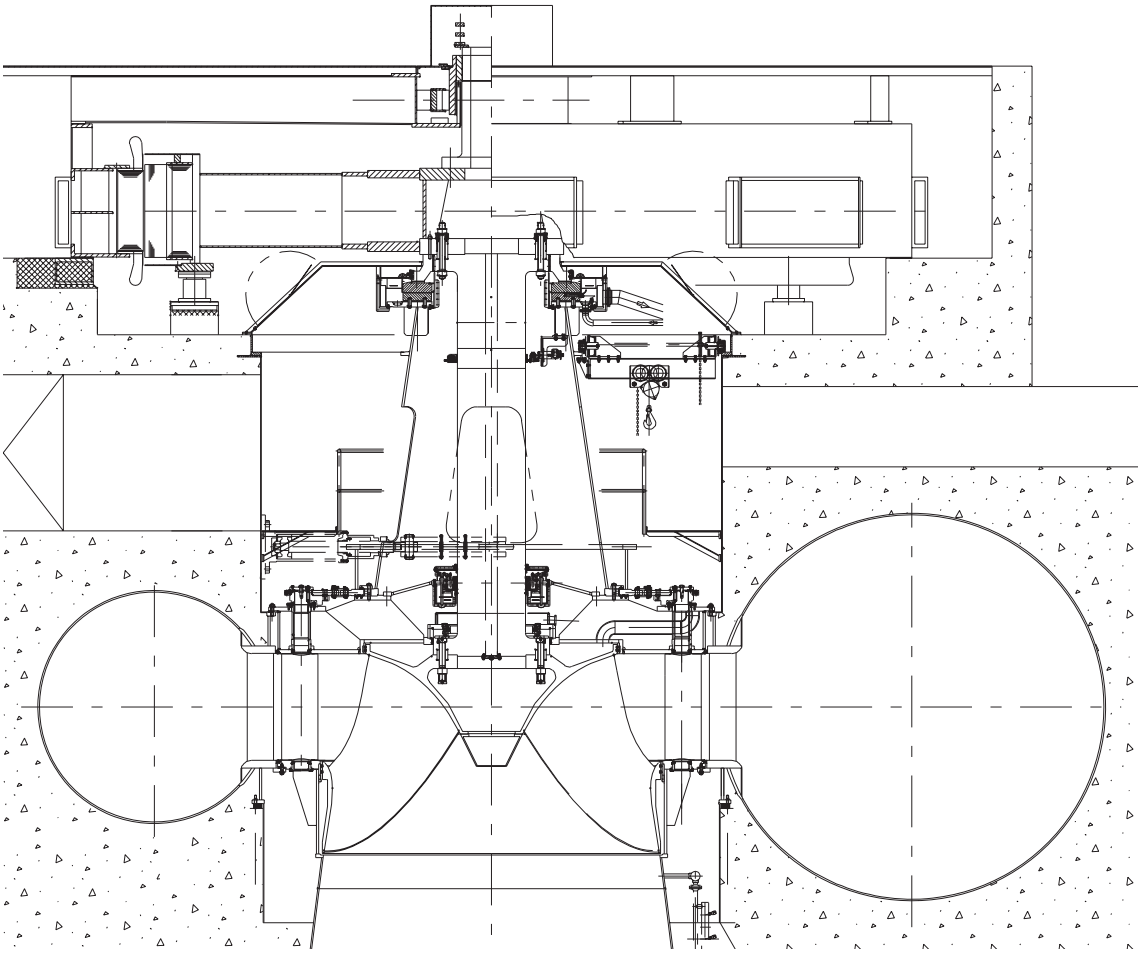

Figure 8.1: Cross-section through the turbine prototype.

measured in the model size and transposed to the prototype, in normal cases the prototype runner in its constructive aspects is not homologous to the model runner. Therefore, mechanical stresses should be computed using the prototype model, as done here.

The main reason for the non-similarity between model and prototype runner is their different geometry. The crown and band designs are normally unique to the prototype being considered, leading also to different geometries for different prototypes derived from the same hydraulic. The shaft coupling position and geometry are also typical from the prototype being analysed. Although not represented in Figure 8.1, the fillet radii between runner blade and crown and band might as well be function of the prototype size, particular constructive restrictions and manufacturing requirements.

The crown and band designs and the shaft coupling for the prototype machine being studied here are shown in Figure 8.1. This configuration and the particular prototype size were considered for the elaboration of the finite element (FE) model used for the numerical computations of the static and dynamic mechanical stresses in the turbine runner.

The real size and geometry for the fillets between blade and crown and band were modelled as well. At the leading edge near to the crown and band, the fillet radii were respectively 0,74% and 0,83% of D_{1_a}. At the trailing edge near to the crown and band, the size of the fillet radii was respectively 0,74% and 0,54% of D_{1_a}. The fillet radius varied along the blade length between the leading and trailing edge, in order to guarantee a smooth transition and an appropriate fillet surface.

The material employed for the runner was the stainless steel ASTM A743 CA-6NM, equivalent to G-X5 CrNi 13.4. For the computation of the dynamic structural behaviour, the complete runner with all its sectors, i.e. with its $z_2 = 13$ blades, was modelled, instead of just one sector, because the transient pressure field did not show any kind of symmetry, e.g. no cyclic symmetry.

8.1.2 Operating Points and Load Cases

The turbine runner was submitted to basically three types of structural loads, the pressure load, centrifugal acceleration load and gravity acceleration load. Other loads due to e.g. the runner unbalance or misalignment were not considered. Transient operating conditions, such as start, stop and load rejection made not part of the scope of this study, even though they could in theory be simulated with the method presented here, but with much higher computational times and costs.

The most important load, in terms of its magnitude and dynamic characteristics, was the pressure load originated from the fluid flow through the hydraulic turbine. The pressure load counted with static and dynamic parts and constituted the source for the runner dynamic excitations. The pressure load was calculated in the previous CFD analysis. The dynamic pressure field at the runner was stored for each time step of the transient fluid flow simulation and used as input for the finite element analysis (FEA).

For the structural analysis, the transient fluid flow was calculated for the operating points defining the boundaries of the operating range. The rated, OP 2, full load and high head, OP 3, full load and low head, OP 4, part load and low head, OP 6, and the deep part load, OP 7, operating points defined the operating range of the machine, as already discussed at the beginning of the previous chapter. In addition to these 5 operating points, part load and high head, OP 5, was also calculated in the finite element analysis (FEA). The location of the operating points and the prototype operating range are again reproduced in Figure 8.2.

For the FT 80 machine, the rotor-stator interaction (RSI) was the dominating dynamic fluid flow effect at the rated point, full load and high head and full load and low head, OP 2, OP 3 and OP 4. At part load and high head, part load and low head and deep part load, OP 5, OP 6 and OP 7, the draft tube instabilities (DTI) became the most important effect. At part load and low head, OP 6, higher part load (HPL) was present. At deep part load, OP 7, the runner channel vortex (RCV) made part of the dynamic fluid flow phenomena.

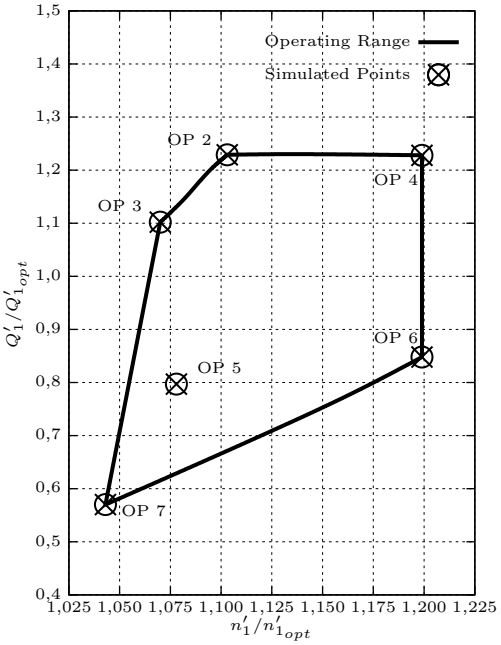

Figure 8.2: Operating range and operating points considered for the structural analysis.

For the application in the finite element analysis (FEA), the pressure field was simulated at the model scale and transposed to the prototype scale using the hydraulic similarity laws for operating points not sensitive to the facility hydraulic circuit dynamics. Considering the same operating point for the model and the prototype, the relation between the model and prototype unit speeds could be observed, $n'_{1_M}/\sqrt{g_M} = n'_{1_P}/\sqrt{g_P}$. At the runner hydraulic surfaces, taken as no slip walls, the local total pressure, $p_t = \rho c^2/2 + p + \rho g z$, was reduced to the piezometric pressure, p_E, and the unit speed expression, $n'_1 = nD/\sqrt{H}$, could be used to determine the prototype runner pressure load.

$$\frac{p_{E_M}}{\rho_M \left(n_M D_M\right)^2} = \frac{p_{E_P}}{\rho_P \left(n_P D_P\right)^2} \tag{8.1}$$

The piezometric pressure of the model machine, at each point, (x, y, z), and at each time step, t, could be obtained from the flow simulation and it contained the static and dynamic parts of the pressure load. The other parameters, model and prototype water density, ρ_M and ρ_P, rotational speeds, n_M and n_P, and characteristic diameters, D_{1a_M} and D_{1a_P}, were previously known. The prototype pressure load, p_{E_M}, could be obtained for each point and time step for all the simulated operating points. It could be applied as pressure load at the hydraulic active surfaces of the prototype runner in the finite element (FE) model.

With the real calculated transient pressure distribution at the turbine runner, there was no need for any hypothetical, fictive or artificial load case and consideration about the pressure field originated from the fluid flow through the hydraulic turbine.

This methodology for the determination of the pressure load can be extended to any other operating point of interest, with no need for simplifications or assumptions. Up to now, no such detailed analysis without simplifications of the transient pressure load on the runner had been carried out for Francis machines, possibly because of the difficulties in simulating the transient volume flow and in dealing with the interface between the finite volume (FV) and the finite element (FE) solver.

Each operating point resulted in a different static and dynamic pressure field at the runner. Normally, different prototypes have distinct operational range and operating points, (n'_1, Q'_1). This constitutes a further reason for performing the mechanical stress calculations for the specific prototype machine being studied.

The runner sensibility to the centrifugal acceleration load is usually calculated with a simple load case, where only the runner rotational speed at runaway is applied as load to the finite element model. This test case was denominated as runaway speed condition and differed from the real runaway condition. At the real runaway condition, the pressure distribution on the runner blades is such that the resulting torque is extremely reduced. The runaway speed load case employed here, as test condition for the numerical setup of the finite element model, included just the centrifugal acceleration load and was just used for test purposes. The normalised maximum turbine runaway speed for the prototype was, $n_D/n = 1{,}733$.

8.2 Structural Simulation Numerical Setup

For the correct evaluation of the static and dynamic stresses in the turbine runner, the finite element model was elaborated corresponding to the real runner characteristics. The numerical aspects of the finite element model were tested, in order to assure that the predicted mechanical stresses reproduce the real stresses in the real runner as precisely as possible.

For the structural assessment, the stress components in the Cartesian components were calculated with the finite element method (FEM) and the principal stress components, σ_1, σ_2 and σ_3, could be derived as well as the von Mises equivalent stress, σ_e.

Geometry

The first basic requirement for the accurate prediction of the mechanical stresses in the runner was that the finite element model geometry could precisely represent the real designed and manufactured geometry. The CAD model, generated with CATIA [30] for the elaboration of the finite element model, reproduced the real geometry of the runner crown, band and blades. It also included the appropriate fillet geometry, along all the fillets extension between the crown and the blades and

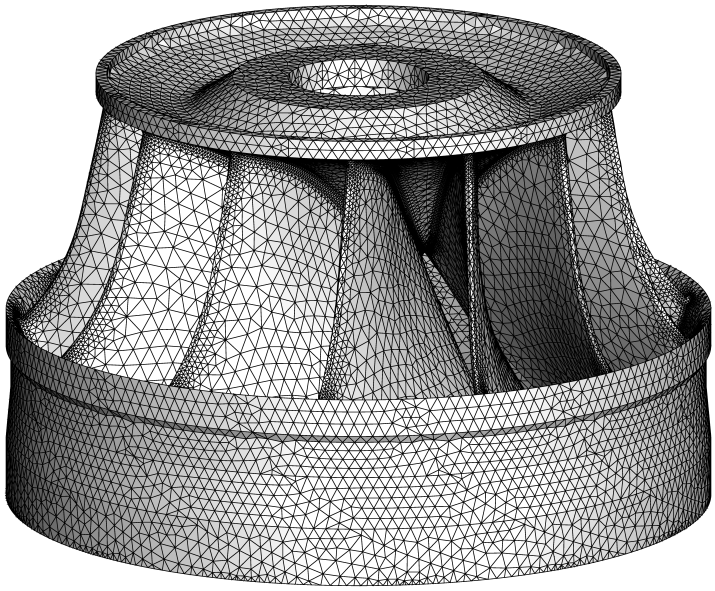

Figure 8.3: Three-dimensional view of the runner mesh for the finite element analysis.

the band and the blades. The fillet geometry at the blades trailing edge was also properly constructed in the computational model. As already mentioned before, the finite element model included the complete runner with all its sectors, i.e. $z_2 = 13$ blades, as long as the instantaneous instationary pressure load did not present any kind of symmetry.

Mesh Generation

The computational grid for the finite element analysis (FEA), was created from the geometric model with the commercial program ANSYS [5]. The mesh was generated using quadratic tetrahedral elements with 10 nodes, one at each vertex and one at the middle of each edge segment. The grid was created for one single sector and copied for the remaining ones. The discretisation of the runner volume was done with an unstructured mesh. Figure 8.3 brings the three-dimensional view of the finite element mesh of the complete runner used for the structural simulation.

In Figure 8.4 the runner mesh can be seen in the meridian view. The details of the mesh at the fillets regions can be observed in Figure 8.5. The fillets regions were discretised with finer grid density. The finer mesh at the fillets was required, as long as they were responsible for stress concentration and for the highest stress gradients, as well as the peak static and dynamic mechanical stresses were located at them. Therefore, the fillets regions had to count with fine grids and high element concentration, in order to provide enough resolution for the computed stress field and to accurately calculate the peak stress values. The fillets regions were of main importance for the structural analysis.

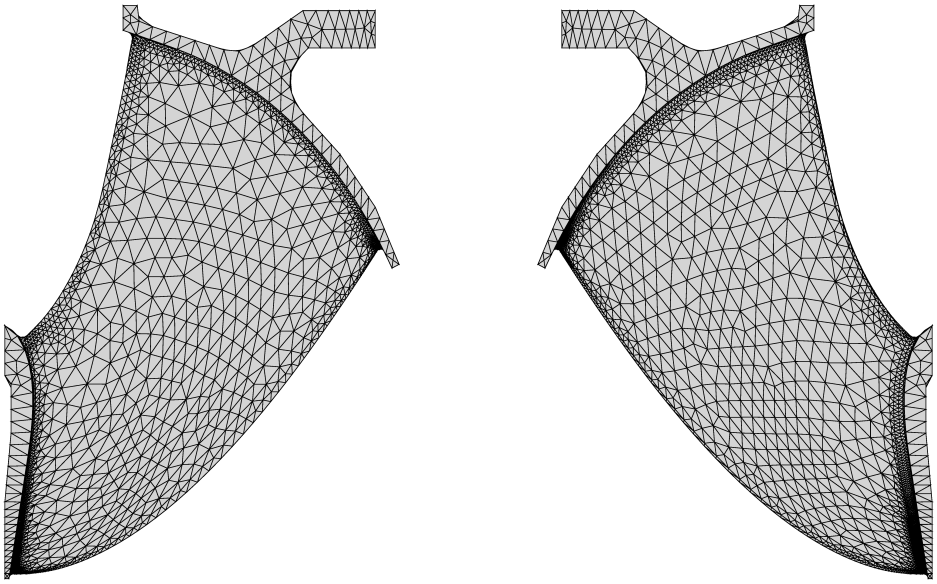

Figure 8.4: Meridian view of the runner mesh for the finite element analysis.

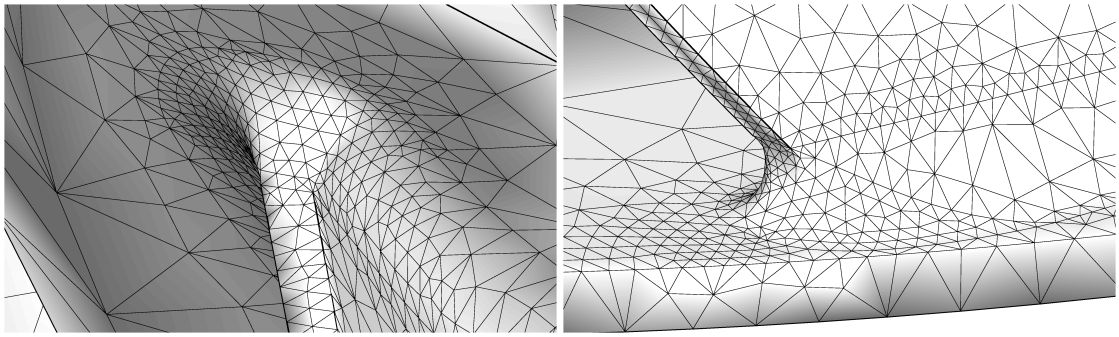

Figure 8.5: Detail view of the fillet mesh at the trailing near to crown (left) and band (right) for the finite element analysis.

In order to reduce the computational costs for the transient analysis, the meshes densities were defined for each runner surface and region, depending on its importance and expected stress gradients and stress level. This offered the possibility to reduce the overall computational grid size in comparison to fully automated meshing algorithms for Francis runners, while keeping the same computation accuracy.

Mesh Density

The general mesh density was the first tested parameter of the numerical model. The same runner geometry was discretised with increasing number of elements and keeping the same mesh topology. The influence of the mesh density on the dynamic behaviour of the simulated runner was tested through the calculation of the first natural frequency of the complete runner with increasing grid density. In Table 8.1,

Table 8.1: Mesh density effect on results. First Natural Frequency.

Number of Nodes per Sector	Number of Elements per Sector	Maximum Edge Length L/D_{1_a} (mm/m)						First Natural Frequency	
		TE, Crown	TE, Band	Fillet Body	Blade Body	Slice Surface	Outer Surface	ω_{n_1}/ω (-)	δ (%)
$31{,}0 \cdot 10^3$	$17{,}1 \cdot 10^3$	2,0	1,0	7,0	20,0	10,0	30,0	12,31	1,2
$66{,}7 \cdot 10^3$	$38{,}5 \cdot 10^3$	1,0	0,6	4,0	20,0	10,0	30,0	12,27	0,9
$102{,}1 \cdot 10^3$	$63{,}7 \cdot 10^3$	1,0	0,6	4,0	10,0	10,0	10,0	12,20	0,3
$186{,}6 \cdot 10^3$	$118{,}6 \cdot 10^3$	1,0	0,6	2,0	10,0	5,0	10,0	12,16	-

it can be found the number of nodes and elements per each sector of the runner, the maximum element edge size for the distinct regions, the calculated first natural frequency and its deviation, δ, in relation to the value obtained with the finest mesh. The element edge size was normalised to the characteristic diameter, L/D_{1_a}, and the first natural frequency to the runner rotational angular speed, ω_{n_1}/ω. In Table 8.1 were listed the maximum element size for the fillets region between the blade trailing edge and the crown and band (TE, Crown and TE, Band), for the remaining fillet and blade surfaces, i.e. for the fillet and blade bodies, for the slice surfaces between the runner sectors and for the outer surfaces not in contact with the main fluid flow.

The values in Table 8.1 show that even the results obtained with the less refined mesh, counting with 17,1 thousand elements per sector, were already very close to those obtained with the finest grid, with 118,6 thousand elements per sector, presenting a maximum deviation of 1,2%. Based on these results, it was assumed that the dynamic behaviour of the runner described by the tested finite element models reached the mesh independency threshold. The reliable simulation of the runner dynamic response could have been done even with the less refined mesh.

The mesh density effect on the stress and displacements results was tested for static load cases. The first one was the centrifugal acceleration at the runaway speed condition and the second one was the time-averaged pressure load at the rated operating point, OP 2. As long as these two conditions were stationary, they were tested in a single runner sector with cyclic symmetry boundary conditions at the slice faces A and B.

$$\mathbf{u}_{\mathrm{B}_x} = \mathbf{u}_{\mathrm{A}_x} \cos\frac{2\pi}{z_2} - \mathbf{u}_{\mathrm{A}_y} \sin\frac{2\pi}{z_2}\,, \quad \mathbf{u}_{\mathrm{B}_y} = \mathbf{u}_{\mathrm{A}_x} \sin\frac{2\pi}{z_2} + \mathbf{u}_{\mathrm{A}_y} \cos\frac{2\pi}{z_2} \tag{8.2}$$

Due to the simplicity in the preparation of the finite element model at the runaway speed condition, several runner mesh densities were tested and the results can be found in Table 8.2. The number of nodes and elements per sector, the normalised extreme values for the total and radial displacements, u_T/D_{1_a} and u_r/D_{1_a}, the normalised equivalent stresses, σ_e/S_y, for the peak value at the blade trailing edge (TE) at the crown and band and the maximum deviation in relation to the finest mesh results are presented in Table 8.2. The yield stress is represented by S_y.

Table 8.2: Mesh density effect on results. Runaway speed.

Number of Nodes per Sector	Number of Elements per Sector	Extreme Value			TE, Crown	TE, Band	Extreme Deviation
		u_T/D_{1_a} (mm/m)	u_r/D_{1_a} (mm/m)	σ_e/S_y (-)	σ_e/S_y (-)	σ_e/S_y (-)	(%)
$31{,}0 \cdot 10^3$	$17{,}1 \cdot 10^3$	0,734	0,417	0,320	0,145	0,320	−2,0
$66{,}7 \cdot 10^3$	$38{,}5 \cdot 10^3$	0,736	0,417	0,325	0,140	0,325	−2,0
$85{,}6 \cdot 10^3$	$50{,}9 \cdot 10^3$	0,759	0,428	0,333	0,140	0,333	1,9
$102{,}1 \cdot 10^3$	$63{,}7 \cdot 10^3$	0,735	0,428	0,327	0,144	0,327	−1,7
$186{,}6 \cdot 10^3$	$118{,}6 \cdot 10^3$	0,748	0,425	0,326	0,142	0,326	-

Table 8.3: Mesh density effect on results. Rated point.

Mesh	Number of Nodes per Sector	Number of Elements per Sector	Extreme Value			TE, Crown	TE, Band
			u_T/D_{1_a} (mm/m)	u_r/D_{1_a} (mm/m)	σ_e/S_y (-)	σ_e/S_y (-)	σ_e/S_y (-)
Normal	$66{,}7 \cdot 10^3$	$38{,}5 \cdot 10^3$	0,972	0,390	0,239	0,118	0,127
Fine	$85{,}6 \cdot 10^3$	$50{,}9 \cdot 10^3$	0,980	0,397	0,236	0,116	0,129
Deviation	δ (%)		−0,8	−1,6	1,4	1,5	−1,8

The results calculated with the different grid densities for the runaway speed condition presented an extreme deviation of −2,0% in relation to those obtained with the finest grid. The reduced deviations associated to no monotonic decreasing tendency of the deviation with the increasing mesh density allowed to assume that mesh independent results were achieved. This behaviour, even with considerably different number of nodes and elements, could possibly be explained with the fact that even with the less refined grid, the overall mesh resolution was enough to reproduce the elastic behaviour of the runner and, at the fillets regions, even the less refined grid counted already with a high node and element concentration.

As already mentioned, the grid density test was also performed for a real load case condition. The time-averaged pressure load at the rated operating point, OP 2, was employed for this verification. Since the preparation of this load case was more demanding than in the case of the runaway speed test condition, two mesh densities were evaluated. The results are presented in Table 8.3.

The extreme deviation between the results simulated with the two different finite element grids remained considerably reduced, with an extreme deviation of −1,8%. This reduced deviation made it acceptable to employ the normal mesh with 66,7 thousand nodes and 38,5 thousand elements for the numerical simulation of the prototype runner, with the advantage of substantial gains regarding the computational costs.

Numerical Approximation Order

The numerical simulation of the runner structure with the finite element method (FEM) was performed using a second-order approximation for the discretisation of the displacement field. This was achieved with the usage of 10-node tetrahedra, which counted with 3 nodes per edge, one at each vertex and one at the middle point of the edges. This kind of element offered quadratic shape functions, allowing an approximation of second-order for the displacements. The second order approximation in the finite element analysis (FEA) offers much higher accuracy, when compared to simple first-order approximations, as already pointed out by Bathe [13] and Zienkiewicz [177], among others. Therefore, the choice for the second-order elements was mandatory, as in the case of any other accurate finite element assessment.

Boundary Conditions

Displacement boundary conditions were used in the finite element analysis of the turbine runner. They modelled the coupling between the runner and the turbine shaft. At the shaft coupling, the runner displacements were restricted, imposing them to be equal to zero. This boundary condition was investigated by Monette, Coutu and Velagandula [106], among others, and was considered adequate for the structural simulation of the turbine runner.

Loads

As mentioned before, the loads considered for the structural simulation of the turbine runner were the hydraulic pressure load, centrifugal acceleration load and gravity acceleration load. Loads originated from the eventual runner unbalance or misalignment were not considered.

From the three considered loads, the hydraulic pressure load was the most important and the responsible for the most part of the total structural load. The pressure field for the hydraulic active surfaces was obtained from the CFD simulation. The centrifugal acceleration and gravity acceleration loads could be represented by simple analytical models incorporated into the finite element (FE) model.

The hydraulic pressure field was dependent from the machine operating point, varied along the surfaces and in relation to the time, $p = (x, y, z, t)$. With the CFD simulation of the transient fluid flow through the complete turbine for different operating points, the transient pressure field in the runner could be determined. The pressure distribution on the runner surfaces was calculated and stored for each time step of the numerical flow simulation and served as input for the finite element analysis (FEA) of the runner structure with the direct time integration method.

Due to the distinct numerical methods and objectives, the finite volume model (FVM) for the fluid flow simulations and the finite element (FE) model for the runner structural calculations counted with different meshes. For each time step, the pressure field calculated with the finite volume mesh was interpolated to the finite element (FE) surface mesh of the runner hydraulic passages. The hydraulic pressure load was applied as surface load in the finite element (FE) model and was allowed to vary at the individual element faces, with different values at the individual elements nodes.

The time-averaged pressure field contributed to the static mechanical stresses in the runner, σ_m. The time-varying portion of the pressure field, caused by the rotor-stator interaction (RSI), draft tube instabilities (DTI), runner channel vortex (RCV) or vortex shedding effect (VSE), depending on the operating point, were responsible by the dynamic mechanical stresses in the runner, σ_a.

The pressure distribution on the runner active hydraulic surfaces, i.e. blade surfaces and crown and band inner surfaces, was provided by the CFD simulation. However, there are other runner surfaces, which were not part of the fluid flow simulation, but which were submitted to less important pressure loads. For the runner, these surfaces were composed by the runner crown and band seals, i.e. labyrinth rotating surfaces, and by the crown and band outer surfaces, i.e. runner side chambers rotating surfaces.

Einzinger [36] describes analytical models commonly used for the modelling of the pressure load at these non-hydraulic active surfaces. Along the seals, the pressure is assumed to decay linearly and the linear pressure drop can be used for the pressure distribution. At the crown and band outer surfaces, the pressure distribution is modelled by employing the steady Euler equations in cylindrical coordinates. With the non-slip condition, the only velocity component at the surfaces in the absolute reference system is $u_\theta = r\omega$. Assuming as well no variation in time or in the tangential direction, the Euler equations yield the pressure distribution on the crown and band outer surfaces. In this case, the pressure distribution is only a function of the radius variation, $\Delta p\,(r) = 1/2\ \rho\omega^2\Delta\,(r^2)$.

The centrifugal and gravity acceleration loads were the other two charges applied to the runner in this study. Both loads were simply applied to the finite element (FE) model as body loads. They were computed through the volume integration of the specific body loads in the finite elements, $f_{i_r} = r\omega^2$ for the centrifugal acceleration in the runner rotating reference system and $f_{i_z} = -g$ for the gravity acceleration.

Model Extension

For all the simulated operating points, the transient pressure field actuating on the runner did not present any kind of symmetry. For the operating points near to the optimum or at full load operating conditions, the dominating dynamic fluid flow effect was the rotor-stator interaction (RSI). Due to e.g. the inhomogeneous pressure

Table 8.4: Model extension effect on results. Runaway speed.

Model Extension	Total Number of Nodes	Total Number of Elements	Extreme Value			TE, Crown	TE, Band
			u_T/D_{1_a} (mm/m)	u_r/D_{1_a} (mm/m)	σ_e/S_y (-)	σ_e/S_y (-)	σ_e/S_y (-)
All sectors	$860{,}8 \cdot 10^3$	$500{,}8 \cdot 10^3$	0,741	0,420	0,328	0,141	0,328
Single sector	$66{,}7 \cdot 10^3$	$38{,}5 \cdot 10^3$	0,736	0,417	0,325	0,140	0,325
Deviation	δ (%)		−0,7	−0,6	−0,7	−0,7	−0,7

distribution at the spiral case, the transient pressure field at the runner was different for each one of its channels. At part load conditions, besides the inhomogeneous spiral case pressure distribution, the rotating vortex rope in the draft tube cone was also responsible for completely different charges at the runner channels for any given instant. Due to the distinct charges actuating simultaneously on the runner sectors, the finite element (FE) model for the transient simulations considered the complete runner.

Some authors, as e.g. Seidel et al. [141], attempted to reduce the transient structural simulation of the runner to only one sector with the usage of the spatial Fourier transformation to model the distinct load in the runner channels. This method simplifies the pressure load to a harmonic spatial wave and do not correspond to the real pressure distribution, which presents a much more complex spatial distribution. Therefore, the direct time integration method, with the complete runner FE model and with the transient pressure load available from the CFD simulation of the complete machine, was the method chosen here to assure the results accuracy.

For the numerical test cases with static load conditions, only one runner sector with cyclic symmetry boundary conditions was used. However, for the structural simulation of the runner, the complete runner geometry with all its sectors was needed, because the transient pressure field for the different operating points did not present any kind of symmetry, as already mentioned. Table 8.4 brings the comparison of the results obtained for the runaway speed condition simulated with one runner sector and with the complete runner.

The marginal deviation was associated to the solver algorithm accuracy. The reduced deviation value allowed the knowledge accumulated with the numerical tests done with the sector model to be extended to the finite element model of the complete runner.

Although the transient pressure loads in the runner did not present any symmetry and the complete runner model was needed for the calculations, each one of the runner sectors experienced successively the same charges and presented successively the same stresses. Therefore, the finer mesh resolution to accurately resolve the stress field was needed in only one arbitrary runner sector. The stresses were watched

Table 8.5: Effect of the combination of coarse and refined sector meshes on results. Runaway speed.

Model Combination	Total Number of Nodes	Total Number of Elements	Extreme Value			TE, Crown	TE, Band
			u_T/D_{1_a} (mm/m)	u_r/D_{1_a} (mm/m)	σ_e/S_y (-)	σ_e/S_y (-)	$\sigma_e/\rho gH$ (-)
All refined	$860{,}8 \cdot 10^3$	$500{,}8 \cdot 10^3$	0,741	0,420	0,328	0,141	0,328
One refined	$432{,}1 \cdot 10^3$	$241{,}0 \cdot 10^3$	0,735	0,417	0,325	0,138	0,325
Deviation	δ (%)		−0,7	−0,7	−0,7	−1,7	−0,7

in this sector during the complete duration of the structural simulation. The grid density in the other runner sectors was required only to be fine enough to deliver the appropriate dynamic properties and internal forces at the boundaries of the watched runner sector.

The previous numerical tests described before showed that even the less refined quadratic mesh, which was investigated, was able to reasonably match the first natural frequency of the runner as well as the displacements and stresses at runaway speed condition. Nonetheless, the structural simulation results of the runner FE model with all refined sectors, with 860,8 thousand nodes and 500,8 thousand elements, were compared to the results obtained with the complete runner mesh, counting with 432,1 thousand nodes and 241,0 thousand elements, where only one sector was refined. The results are presented in Table 8.5.

As seen in Table 8.5, the results obtained with the FE models, where all sectors were refined and where one sector was refined, brought a maximum deviation of −1,7%. With these results, the method was considered valid for the structural assessment of the runner. This approach allowed the reduction of around the half of the computational effort for the transient structural calculations, without the loss of accuracy for the numerical results.

Fluid-Structure Interaction

In the Francis turbine, phenomena of distinct physical nature take place. The dynamic fluid flow through the turbine and the dynamic structural motion of the mechanical components are present. The fluid and structural domains share common interfaces. The walls at the boundaries of the fluid domain correspond to the wet surfaces of the mechanical components. The transient fluid flow through the turbine and the transient structural motion of the runner may affect each other, posing a fluid-structure interaction (FSI) problem. The FSI may be modelled as bidirectional or unidirectional, i.e. one-way or two-way.

For the structural investigation of the turbine runner, the fluid-structure interaction was modelled as unidirectional. The influence of the fluid flow on the runner

structural motion was considered, whereas the runner vibrational motion was not able to modify the primary fluid flow. The instationary simulations of the runner structural motion demonstrated that the maximum oscillation amplitude was not larger than $2{,}4 \cdot 10^{-4}\ D_{1_a}$, being orders of magnitude smaller than the minimum blade thickness and even the boundary layer thickness. In addition, the maximum calculated structural oscillating velocity could not even reach $1{,}9 \cdot 10^{-3}\ U_{1_a}$. For the fluid flow, the runner structural motion was quasi-static and did not affect it.

On the other hand, the pressure oscillations caused by the transient fluid flow were responsible for the dynamic loads at turbine runner and, consequently, for the dynamic displacements and stresses. As mentioned before, the transient pressure distribution originated from the dynamic fluid flow constituted the transient pressure load at the active hydraulic surfaces of the runner structure.

Some authors, as Seidel et Grosse [140], Keck et al. [72], Monette, Coutu and Velagandula [106] and Guillaume et al. [56], extend the interaction between the runner structure and the surrounding fluid to acoustic wave propagation effects. They make use of acoustic fluid elements in the FE structural simulation for representing the fluid. In spite of its growing application to Francis runners structural problems, the acoustic fluid elements count with massive simplifications, as listed by Kinsler [73], that do not correspond to the physical reality in hydraulic turbines.

The acoustic fluid elements formulation assumes no viscosity, no primary flow and no variable mean pressure distribution in the complete fluid domain and no variation of the mean density. This leads to no consideration of the boundary layer effects and no convection. The pressure gradient along the turbine hydraulic passages and their transient variation are ignored as well. When acoustic fluid elements are used in the dynamic structural analysis of the runner, these approximations should be kept in mind and caution is required in the assessment of the simulation results.

Solver

For the numerical solution of the transient motion of the mechanical system, discretised with the finite element method (FEM), the direct time integration method was used. This procedure was explained together with the FEM theory and can be found in Newmark [111]. With the complete time history of the runner pressure distribution obtained from the CFD analysis, the system motion could be solved for each individual time step. The direct time integration method was well suited for this approach.

Moreover, the direct time integration method offered computational benefits. With the method proposed by Newmark [111], the temporal and spatial discretisation of the mechanical system results at each current time step, $n + 1$, in an algebraic matricial equation of the simple form $\mathbf{Ax} = \mathbf{b}$, where the independent term contains information of the previous time step, n. The resulting matricial equation could be

efficiently solved by the preconditioned conjugate gradient (PCG) method. This was an important point for the computational efficiency, as long as the matricial equation had to be solved for each time step. The PCG solver employed for the structural analysis made use of computational double precision for the numerical operations. With one low-end Intel 560J processor with 3,6 GHz and emulated double core, in average 556 time steps, corresponding to around 1,42 runner revolutions, could be solved for the runner structural simulation in one day. The PCG solver was faster than the frontal and sparse solvers and also required less memory and storage space.

The modal superposition method could have been an alternative to the direct time integration method. It would not have imposed any restriction on the modelling of the mechanical system dynamics nor on the temporal and spatial pattern of the pressure load variation. However, in order to assure the accuracy of this method, a higher number of runner natural vibration modes would need to have been previously extracted and stored for the further modal superposition step. With the simple hardware chosen for the structural simulation, the computational memory and storage costs were not attractive and the direct time integration method was preferred thanks to its efficiency. Moreover, there would have been the uncertainty on how many natural vibration modes to extract, in order to assure the accurate description of the system dynamic motion.

Another alternative to the direct time integration method would have been the numerical harmonic analysis of the FE discretised runner structure. The harmonic solution method assumes that the complete structural load varies harmonically with the time. Considering the complex time history, complex spatial distribution and non-synchronous pressure load induced by the dynamic fluid flow, the harmonic solution method would not have been able to accurately describe the system dynamic motion just by considering the pressure oscillation amplitude. More precise results would require the decomposition of the pressure time signal in Fourier series as suggested by Guillaume et al. [56]. The Fourier series expansion would need to be done for each node of the discretised runner surface, employing complex number arithmetic for the punctual pressure oscillation amplitude and phase delay. To assure reasonable accuracy, enough terms would need to be calculated in the Fourier series expansion and each of them would result in a load distribution, whose displacements would have to be calculated by the harmonic solver. After the numerical solution computation, all terms would have to be combined to yield the total dynamic displacement. Once again, the direct time integration was the preferred method, as long as it offered a much simple solution procedure in comparison to the harmonic analysis. With the harmonic analysis, there would also have been an incertitude regarding the number of terms to be calculated in the Fourier series expansion.

Damping

In most mechanical structures, numerous kinds of damping are present. Few theoretical or experimental damping data is available for turbine runners. Therefore,

reference values of structural damping, ζ, taken from the literature were used. According to Aoki [8], typical damping factors for welded structures, as in the case of turbine runners, vary between 0,7% and 2,0%. This range is approximated through the use of proportional or Rayleigh damping, $\mathbf{C} = \alpha\mathbf{M} + \beta\mathbf{K}$.

8.3 Structural Simulation Results

The numerical setup and investigations of the finite element (FE) model allowed the development of a reliable model for the prediction of the dynamic structural behaviour of the turbine runner. The main interest was the estimation of the runner mechanical stresses, static as well as dynamic, at different operating points. The runner structural assessment offered the possibility to identify the critical operating points and to evaluate the runner fatigue strength.

The runner static and dynamic mechanical stresses, σ_m and σ_a, were calculated with the runner FE model, using the direct time integration, for all the operating points, which were previously calculated with CFD. The runner natural frequencies and natural mode shapes were also evaluated, in order to obtain a general overview of the runner vibrational characteristics.

8.3.1 General Dynamic Behaviour, Natural Frequencies and Mode Shapes

An overview of the general dynamic behaviour of the runner could be obtained with the natural frequencies and mode shapes. The runner natural frequencies could be compared with the exciting frequencies predicted by the theory and the distance between them could be evaluated. The mode shapes indicated the vibration pattern of the runner, in case of matching excitation.

As mentioned before, several authors, among them Seidel et Grosse [140], Keck et al. [72], Monette, Coutu and Velagandula [106] and Guillaume et al. [56], extend the fluid-structure interaction effect with the usage of the acoustic fluid elements in the FE model. This condition is often denoted by "runner in water", in opposition to "runner in air", when no acoustic fluid elements are employed. The respective natural frequencies are represented by, f_w and f_a.

It is important to observe that the acoustic fluid elements assume no fluid viscosity, no primary flow, no variable mean pressure distribution and no constant rotational motion of runner. These simplifications do not correspond to the physical reality found in hydraulic turbines. Therefore, the results produced by the modal analysis should be interpreted as no more than an approximation of the dynamic characteristics of the runner in operation. Nevertheless, it can deliver a qualitative impression of the runner dynamic structural characteristic.

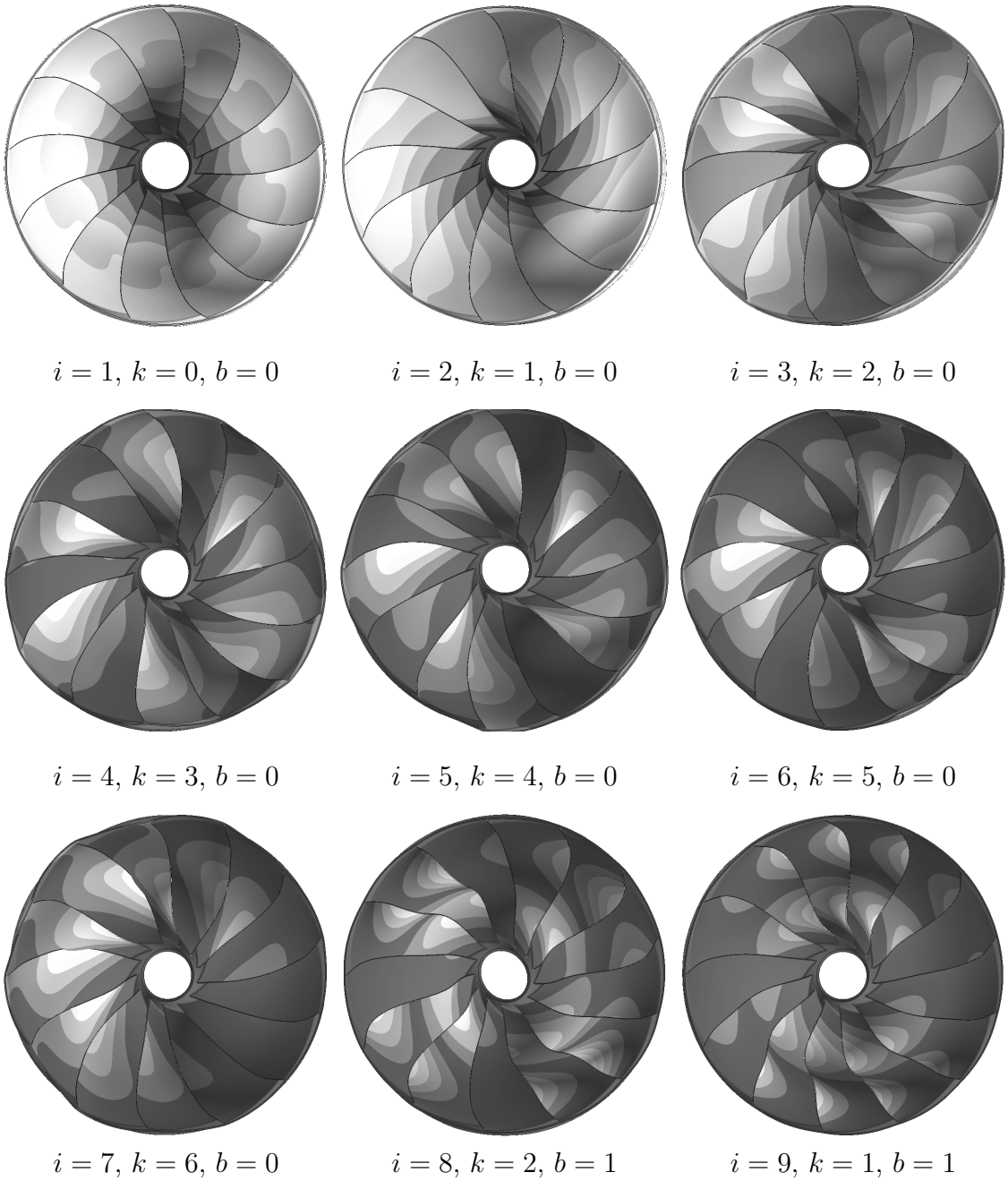

Figure 8.6: Deformed shape and total displacements for the turbine runner natural mode shapes, bottom view.

Figures 8.6 and 8.7 illustrate the first 9 mode shapes extracted for the turbine runner of the FT 80. The deformed shape of the runner, for each of the extracted mode shapes, i, is shown in Figures 8.6 and 8.7. The modal displacements, $\mathbf{\Phi}_i$, were normalised in relation to the mass matrix, $\mathbf{\Phi}_i^{\mathbf{T}}\mathbf{M}\mathbf{\Phi}_i = \mathbf{1}$, and the total modal displacements were coloured with a grey scale.

The runner motion at the first mode shape, $i = 1$, was characterised by a twist motion of the band around the crown. The crown nearly did not move, while the

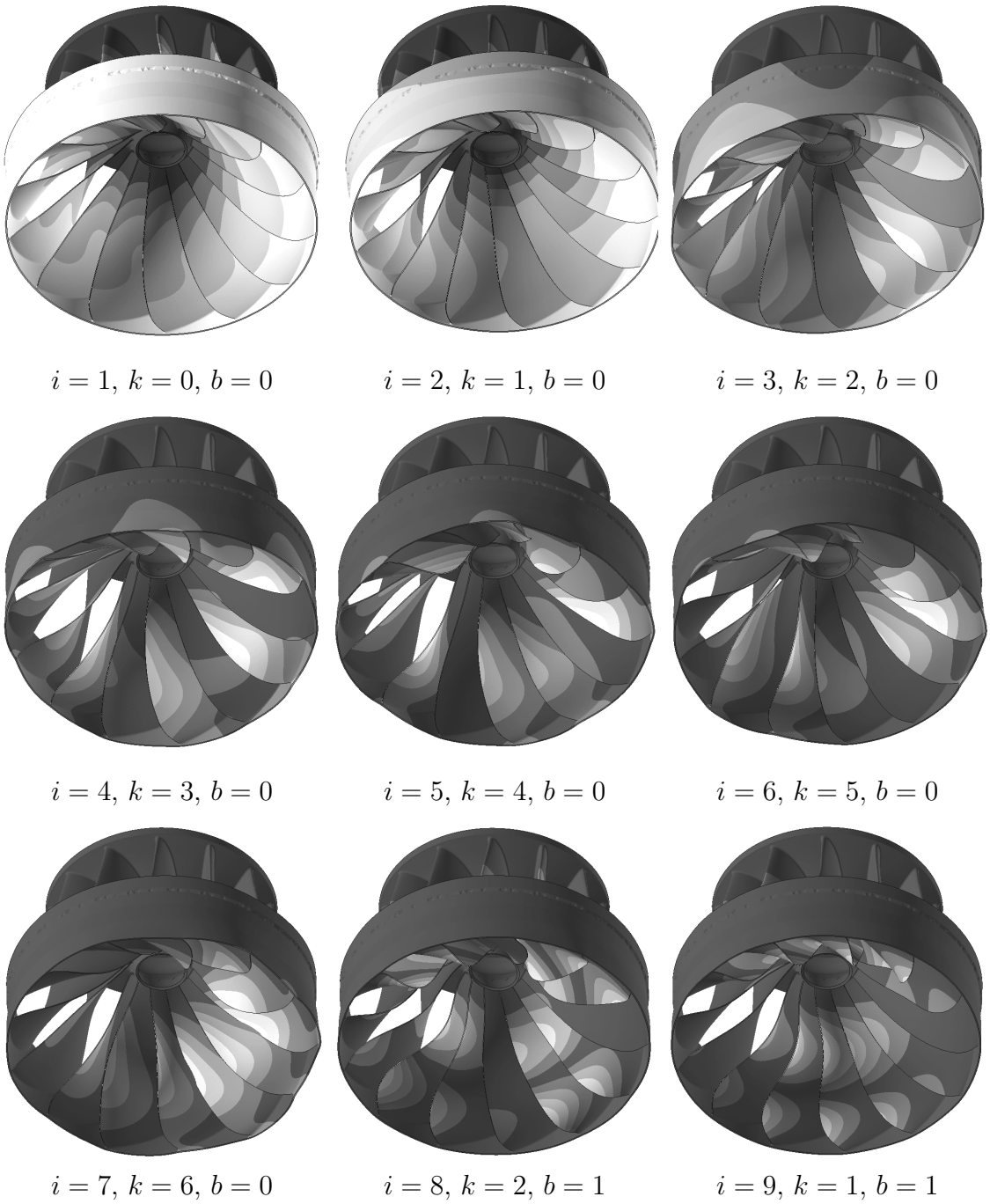

Figure 8.7: Deformed shape and total displacements for the turbine runner natural mode shapes, isometric view.

band rotated around it, in the tangential direction, and moved axially as well, due to the blades elasticity. At the second mode shape, $i = 2$, the runner oscillated like a pendulum around the coupling to the shaft. These two first modes might be influenced by the turbine shaft dynamic characteristics, as discussed by Mehne [97].

At the second mode shape, as well as at the modes of higher order, the runner oscillated in way similar to a thin disc, with diametral lines where the modal

Table 8.6: Runner natural frequencies, natural mode shapes and nearest excitation frequency.

Mode	Mode Shape		Natural Frequency			Excitation		
i (-)	k (-)	b (-)	f_a/f_n (-)	f_w/f_n (-)	f_w/f_a (-)	Type	h (-)	f_e/f_n (-)
1	0	0	12,3	10,2	0,83	SC	5	5
2	1	0	16,9	9,6	0,57	SC	5	5
3	2	0	23,4	13,3	0,57	SC	5	5
4	3	0	36,9	17,8	0,48	GV	1	24
5	4	0	42,8	17,3	0,41	GV	1	24
6	5	0	45,4	16,7	0,37	GV	1	24
7	6	0	46,5	16,2	0,35	GV	1	24
8	2	1	53,1	22,8	0,43	GV	1	24
9	1	1	54,4	23,4	0,43	GV	1	24
10	3	1	56,3	25,9	0,46	GV	1	24
11	4	1	58,5	27,9	0,48	GV	1	24
12	0	1	58,6	25,2	0,43	GV	1	24
13	5	1	60,4	28,7	0,47	GV	1	24
14	1	2	61,3	34,1	0,56	GV	1	24
15	6	1	61,5	28,8	0,47	GV	1	24
16	2	2	63,4	30,0	0,47	GV	1	24
17	0	2	63,7	29,9	0,47	GV	1	24
18	3	2	67,7	32,6	0,48	GV	1	24
19	4	2	69,6	32,4	0,47	GV	1	24
20	5	2	70,8	35,9	0,51	GV	1	24

SC: Unsymmetric pressure distribution, GV: Guide vane passage, DT: Vortex rope.

displacements were near to zero. These lines are often called nodal diameters, as e.g. in Liang et al. [83]. The number of nodal diameters, k, is directly related to the deformation shape of the runner for a given mode shape. For mode shapes of higher order, the blade trailing edge presented nodes similar to the nodes found in vibrating strings or beams. Their number is denoted by, b. The number of nodal diameters, k, and of blade nodes, b, give a precise idea of the mode shape geometry.

Table 8.6 lists the first 20 extracted mode shapes of the runner, with the corresponding number of nodal diameters, k, and blade nodes, b. The natural frequencies calculated with and without acoustic fluid elements, f_w and f_a, normalised to the rotating frequency, f_n, and the reduction factor, f_w/f_a, are also summarised in Table 8.6. The nearest excitation frequency, f_e, its origin and the considered harmonic, h, can also be encountered in Table 8.6.

The most important excitations previewed by the theory in the runner rotating reference frame are the unsymmetric pressure distribution in the spiral case (SC), the guide vanes passage (GV) and the draft tube vortex rope rotation (DT). In the rotating reference frame, the unsymmetric pressure distribution oscillates with the same frequency as the rotating frequency, f_n. The guide vanes passage can excite the runner with the frequency, $z_0\, f_n$. The vortex rope rotates in the same direction

as the runner with a lower frequency, leading to the excitation frequency $f_n - f_{Rh}$ in the runner rotating reference frame, where f_{Rh} is the vortex rope rotating frequency in the absolute reference system. Due to the nature of the modal analysis, the five first harmonics of the excitation frequencies, $h = 1, \ldots, 5$, were also considered.

The modal analysis could also be useful for the qualitative approach proposed by TANAKA [151]. The fluid interaction between guide vanes and runner is approximated by pressure mode shapes, depending on the number of guide vanes, z_0, and runner blades, z_2. With the formula $k = m\,z_0 \pm n\,z_2$, with m and n being integers satisfying the equation, it is searched for runner mode shapes, which could be excited by the runner and guide vanes interaction. A limitation in this qualitative approach is that the inhomogeneous spiral case pressure distribution and the draft tube rotating vortex rope are often ignored, although they can strongly excite the runner. Moreover, with the current capability to numerically simulate the transient pressure field in the Francis machine and use it as input for the finite element analysis (FEA), this methods constitutes no more than a rough approximation.

The modal analysis could give qualitative information about the dynamic characteristics of the runner. However, the modal analysis was not enough for the modern quantitative evaluation of the dynamic mechanical stresses in the runner at different operating conditions. Therefore, the direct time integration method was preferred. Among the advantages of the direct time integration method, there was no need for the natural frequencies and mode shapes extraction. Moreover, the dynamic system response was not truncated to a limited number of mode shapes. No information of how many and which mode shapes contributed to the dynamic motion was necessary. No theoretical representations or simplifications of the pressure distribution and time history were required with the direct time integration method for the assessment of the structural response to the fluid excitation at different operating points.

8.3.2 Full Load and Rotor-Stator Interaction

The mechanical stresses in the runner were calculated for the full load operating conditions with the tested FE model and using the direct time integration method. As mentioned before, the time-averaged pressure distribution from the CFD analysis was used for the calculation of the mean stress, σ_m, and the pressure oscillation time history allowed the computation of the dynamic stress, σ_a.

The simulated points corresponding to the full load operating condition were the rated, OP 2, full load and high head, OP 3, and full load and low head, OP 4. These points defined the turbine upper operating limit. They covered the complete head range, counted with the larger volume flow through the machine, Q, and the transient fluid flow was dominated by the rotor-stator interaction (RSI) effect. They offered the possibility to evaluate the dynamic response of the runner structure to the rotor-stator interaction and the associated mechanical stress level and distribution.

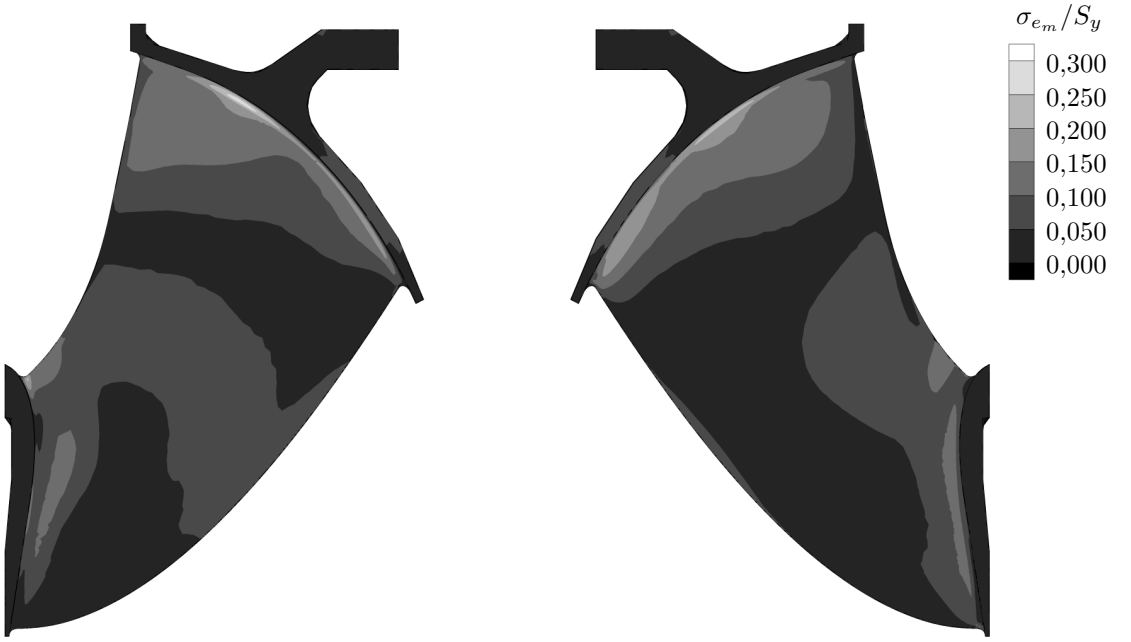

Figure 8.8: Static equivalent mechanical stresses at the rated operating point, meridian view.

As long as the transient flow had the same general pattern at all the points at full load, the rated point, OP 2, was taken as example for the graphics and charts.

Figure 8.8 brings the distribution of the static equivalent stress, σ_{e_m}, in the runner for the rated operating point, OP 2, normalised in relation to the material yield stress, S_y. The contour plot of σ_{e_m} is drawn in the meridian view of the runner, where the blade pressure and suction sides can be respectively found at the right and left sides of the picture.

It can be observed in Figure 8.8 that the highest stresses were located at the fillets regions of the runner. This behaviour was already to be expected, due to the stress

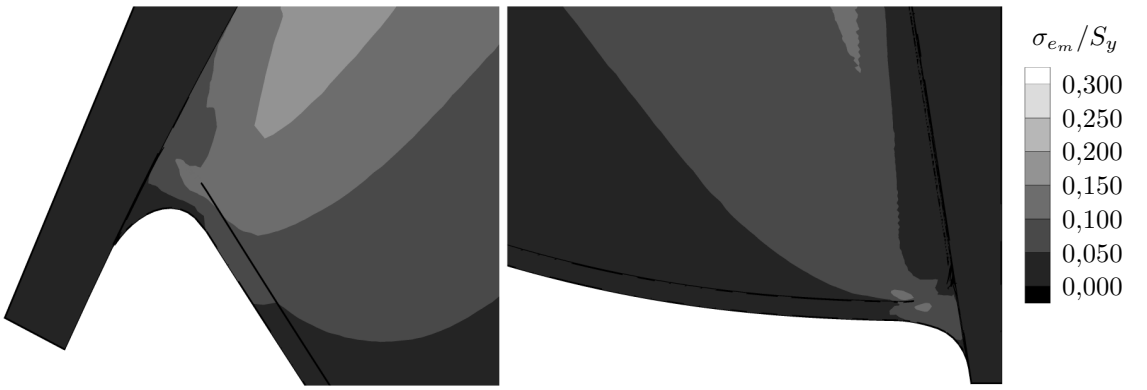

Figure 8.9: Static equivalent mechanical stresses at the rated operating point, detailed view of the trailing edge at crown (left) and band (right).

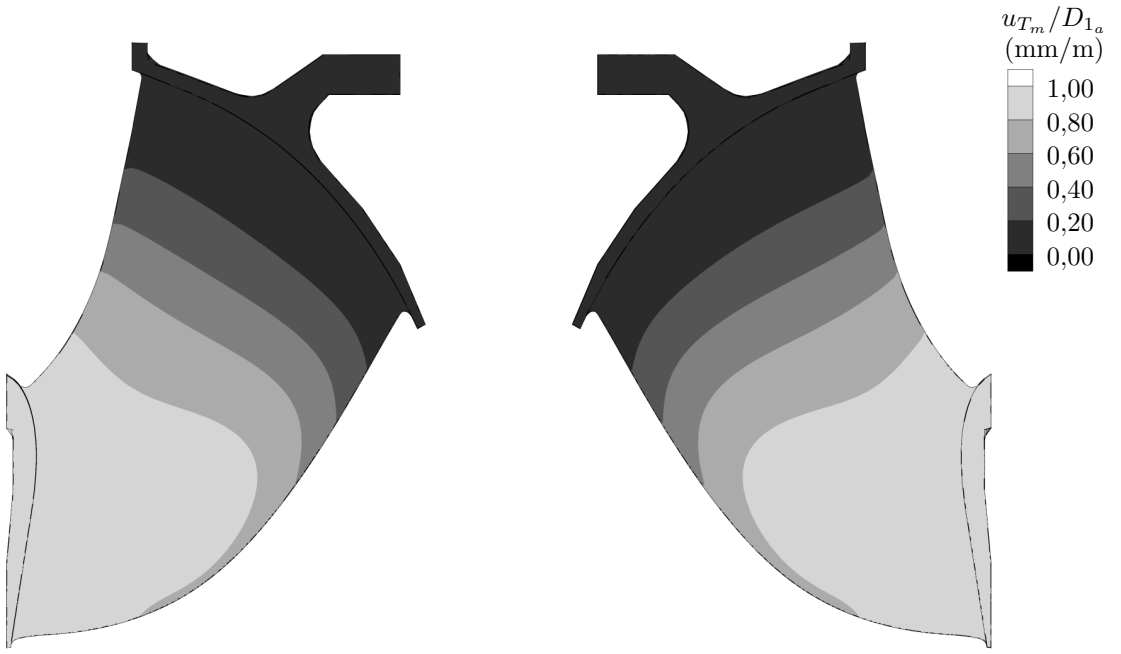

Figure 8.10: Static total displacements at the rated operating point, meridian view.

concentration in the junction of the blades to the crown and band. For the FT 80 and at full load, the highest static stresses took place at the blade to crown fillets at the suction side in its middle portion between the inlet and outlet edges. The maximum value reached for the static stress was $\sigma_{e_m}/S_y = 0{,}245$.

In Figure 8.8 it can be observed that the static stress was also high close to the blade to band fillet region. Static stress peaks could be identified as well at the leading and trailing edges close to the crown and band. The trailing edge regions close to the crown and band were of special interest and can be seen in detail in Figure 8.9. These regions are more prone to cracks, as assessed by Bhave, Murthy and Goyal [15]. At both regions, higher stress spots could be identified.

The total static displacements, u_{T_m}, of the runner structure at the rated point, OP 2, are shown in Figure 8.10. The contour plot for u_{T_m} is represented at the runner meridian view with the blade pressure side on the right side and with the suction side on the left side of the picture. The runner geometry seen in Figure 8.10 is slightly different from the runner nominal geometry and corresponds to the runner deformed shape under the static loads at the rated point. For more visibility, the deformation was increased in the graphical representation.

The total static displacements increased starting from the crown and going in direction to the band. The reason was that the largest portion of u_{T_m} came from the static displacement tangential component. The runner was fixed at the coupling to the shaft at the crown and the static tangential displacement was mainly caused by the pressure difference between the pressure and suction sides of the blade, responsible for the turbine mechanical torque.

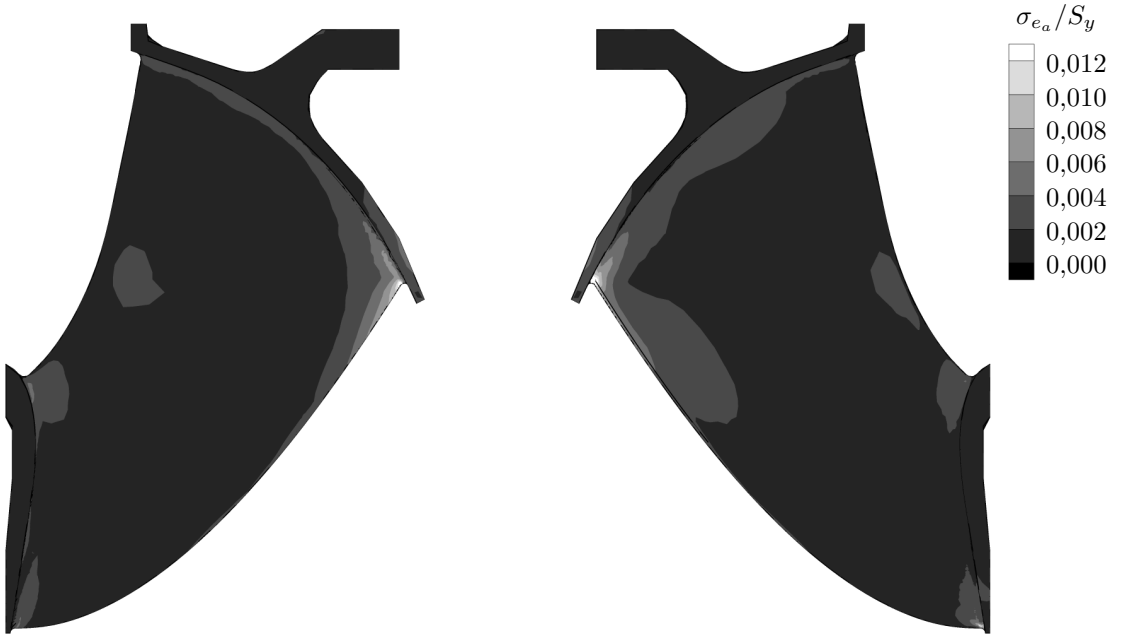

Figure 8.11: Dynamic equivalent mechanical stress amplitude at the rated operating point, meridian view.

One of the points of greatest interest in the structural assessment of the turbine runner was the determination of the dynamic mechanical stresses. Combined to the static mechanical stresses, they might importantly influence the expected runner fatigue life. Figure 8.11 shows the calculated dynamic equivalent stress amplitude, σ_{e_a}, for the FT 80 runner at the rated point, OP 2, normalised to the material yield stress S_y. As in the previous figures, the σ_{e_a} contour plot is drawn at the meridian view with the pressure and suction sides ordered as before. To improve the visualisation of the dynamic stresses, the contour colour scale was limited to an upper cut-off value of $\sigma_{e_a}/S_y = 0{,}012$.

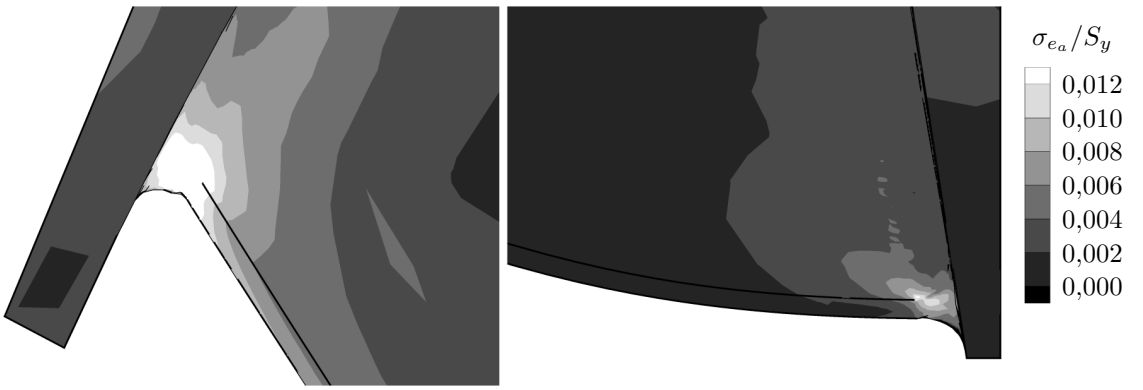

Figure 8.12: Dynamic equivalent mechanical stress amplitude at the rated operating point, detailed view of the trailing edge at crown (left) and band (right).

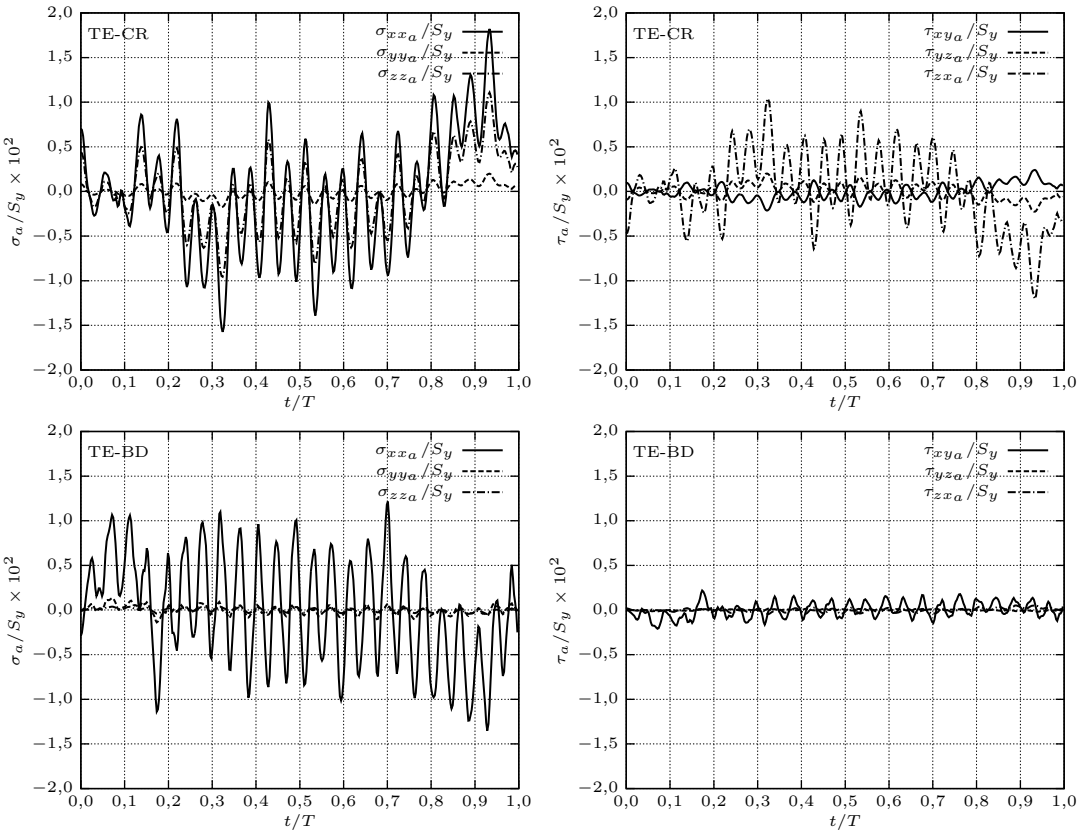

Figure 8.13: Time history of the dynamic stress components at the trailing edge near to the crown (top) and band (bottom) at the rated operating point.

At the middle of the blade and at the inlet, the dynamic mechanical stresses remained low. The stress peaks were very pronounced at the blade trailing edge near to the crown and band. The highest dynamic stresses were observed in the blade trailing edge region near to the crown. This region of high stress extended in a moderate degree along the trailing edge and along the fillet between blade and crown. The highest dynamic stress was $\sigma_{e_a}/S_y = 0{,}0277$, located at the blade trailing edge at the crown. High dynamic stresses were also found at the blade trailing edge at the band and at its surrounding region, reaching the maximum local value of $\sigma_{e_a}/S_y = 0{,}0132$.

The trailing edge region near to the crown and band, where the highest stresses took place at the rated operating point, OP 2, can be seen in detail in Figure 8.12. The stress concentration at the fillet region at the trailing edge can be clearly identified. The peak stresses were located in the region at the end of the fillets, where the blade assumed its nominal thickness.

Figure 8.13 brings the time history of the dynamic stresses at the runner trailing edge near to the crown and band, where the highest dynamic stress peaks were located. The dynamic portion of all stress tensor components, normalised to the yield stress, are plotted along the time, t, normalised to the machine rotation period, T. The x and y directions for the decomposition of the dynamic stress tensor were arbitrary

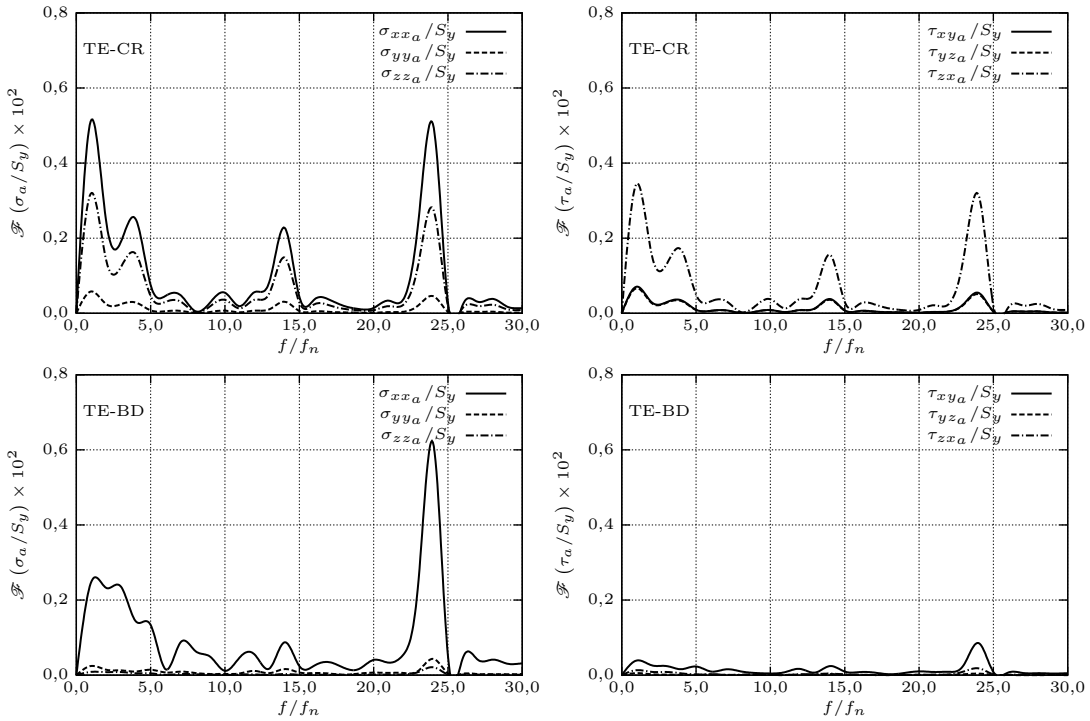

Figure 8.14: Fourier transform of the dynamic stress components at the trailing edge near to the crown (top) and band (bottom) at the rated operating point.

chosen, while the z direction corresponded to the machine rotation axis. The upper two plots refer to the dynamic stress components at the trailing edge near to the crown and the two lower ones to those at the trailing edge near to the band.

At the time history plot, two dominating vibration frequencies could be identified: the slower one caused by the excitation through the inhomogeneous pressure field in the spiral case and the faster one corresponding to the excitation from the guide vanes passing frequency. The runner structural response related to the spiral case pressure distribution excitation revealed a complex shape, while the response to the guide vanes excitation presented a nearly sinusoidal shape.

The Fourier transform of the time signal, in Figure 8.14, could point out the dominating runner structural response frequencies. The first one, corresponding to the slower vibration, was concentrated around $f/f_n = 1{,}0$, where f_n denotes the machine rotation frequency. Due to the complex shape of the excitation related to the spiral case pressure distribution, the frequency spectrum was considerably dispersed around the characteristic frequency, $f/f_n = 1{,}0$, and its harmonics were very pronounced. The guide vanes passing frequency, $f/f_n = 24$, could also be identified in the dynamic stress frequency spectrum. In the case of the response to the guide vanes excitation, the spectrum amplitude was less dispersed around the characteristic frequency, because of the nearly sinusoidal form of the excitation.

The Fourier transform could also qualitatively reveal the participation of the excitations arising from the spiral case and from the guide vanes in the runner

Table 8.7: Mean and dynamic equivalent stresses at full load.

Operating Point	Mean Equivalent Stress σ_{e_m}/S_y (-)				
	LE, Crown	LE, Band	TE, Crown	TE, Band	Fillet, CR
OP 2 Rated	0,134	0,208	0,118	0,127	0,239
OP 3 Full load high head	0,132	0,186	0,130	0,111	0,226
OP 4 Full load low head	0,093	0,169	0,097	0,108	0,176
Operating Point	Dynamic Equivalent Stress σ_{e_a}/S_y (-)				
	LE, Crown	LE, Band	TE, Crown	TE, Band	Fillet, CR
OP 2 Rated	0,0033	0,0047	0,0277	0,0132	0,0040
OP 3 Full load high head	0,0027	0,0032	0,0229	0,0133	0,0027
OP 4 Full load low head	0,0028	0,0038	0,0205	0,0127	0,0039
Operating Point	Stress Ratio $\sigma_{e_a}/\sigma_{e_m}$ (%)				
	LE, Crown	LE, Band	TE, Crown	TE, Band	Fillet, CR
OP 2 Rated	2,5	2,2	23,4	10,4	1,7
OP 3 Full load high head	2,0	1,7	17,7	11,9	1,2
OP 4 Full load low head	3,0	2,2	21,1	11,8	2,2

structural response. Considering all dynamic stress components, the larger portion of the dynamic stresses came from the guide vanes excitation. Nonetheless, it could be observed that, in the case of the FT 80 at full load, the spiral case excitation contributed strongly to the dynamic mechanical stresses as well.

The runner structural response to the fluid dynamic excitation was also computed for the other points of interest located at the full load part of the hill chart. At these operating points, the driving dynamic effect was the rotor-stator interaction (RSI). The rated, OP 2, the full load and high head, OP 3, and the full load and low head, OP 4, operating points showed very similar dynamic behaviours. The variations in the dynamic stress values were influenced by the different head, volume flow and guide vane opening, which changed the distance between the guide vanes trailing edge and the runner blades leading edge. At the operating points at full load, the dynamic excitation mechanism was the same, arising from the rotor-stator interaction (RSI).

Table 8.7 summarises the calculated static and dynamic stress values for the full load operating points at the most important locations of the runner. The stress values are listed for the leading edge (LE) at the crown and band, for the trailing edge (TE) at crown and band and for the middle of the blade at the crown (CR) fillet, where the highest static stresses were found. Also the ratio between the dynamic and static mechanicals stresses, $\sigma_{e_a}/\sigma_{e_m}$, can be encountered in the table.

All three calculated full load operating points had the same behaviour regarding the dynamic mechanical stresses in the runner. The equivalent dynamic stress

amplitude, σ_{e_a}, presented the same tendency in relation to the observed locations in the runner and the calculated values for a given location were in the same order of magnitude for all points at full load. The table shows that the trailing edge near to the crown and band, with peak stresses of respectively $\sigma_{e_a}/S_y = 0{,}0277$ and $\sigma_{e_a}/S_y = 0{,}0133$, were the most important locations for the dynamic and strength assessment of the runner structure. The middle of the fillet region between the crown and the blade, in spite of its higher static mechanical stress, $\sigma_{e_m}/S_y = 0{,}127$, showed out to be irrelevant for the dynamic evaluation, due to its low dynamic mechanical stress, $\sigma_{e_a}/S_y = 0{,}0040$.

Another interesting parameter in Table 8.7 is the ratio of the dynamic to the static equivalent mechanical stress, $\sigma_{e_a}/\sigma_{e_m}$. In the case of the FT 80 at full load conditions, the maximum ratio at the trailing edge near to the crown was reached at the rated operating point, OP 2, with $\sigma_{e_a}/\sigma_{e_m} = 23{,}4\%$. At the trailing edge near to the band, the maximum ratio was $\sigma_{e_a}/\sigma_{e_m} = 11{,}9\%$ at full load and high head, OP 3. The ratio $\sigma_{e_a}/\sigma_{e_m}$ constitutes an important parameter for the fatigue analysis. Part of the reason for these high ratios at full load was possibly the low static stresses present in the runner.

8.3.3 Part Load and Draft Tube Instabilities

The part load operating conditions were characterised by important transient fluid flow phenomena in the draft tube cone. At part load, the rotating vortex rope could be observed in the draft tube cone. Significant pressure pulsations were associated to the vortex rope rotational motion, which reached the runner blades. The vortex rope motion and the associated transient dynamic pressure field were calculated, as already discussed before, and the stored pressure time history was used as input for the dynamic finite element analysis (FEA). The time-averaged pressure field was employed for the determination of the static stress, σ_m. As before, the direct time integration method was used for the transient runner finite element (FE) simulation.

For the analysis of the influence of the draft tube instabilities (DTI) on the mechanical stresses in the runner, the part load and high head operating point, OP 5, was chosen. This operating point was characterised by the ordinary part load operation, with the presence of the rotating vortex rope in the draft tube cone, no higher part load (HPL) effects and no runner channel vortices (RCV).

Figure 8.15 shows the calculated normalised equivalent static stresses, σ_{e_m}/S_y, in the turbine runner at part load and high head, OP 5. The blade pressure and suction sides are respectively found at the right and left sides of the meridian view in Figure 8.15. The contour plot scale for the equivalent static stress was limited in the picture for better visualisation purposes.

The equivalent static stress distribution at part load and high head, OP 5, assumed a shape similar to the one obtained at the full load operating conditions. However, the general static stress was lower, reaching the maximum value of $\sigma_{e_m}/S_y = 0{,}118$

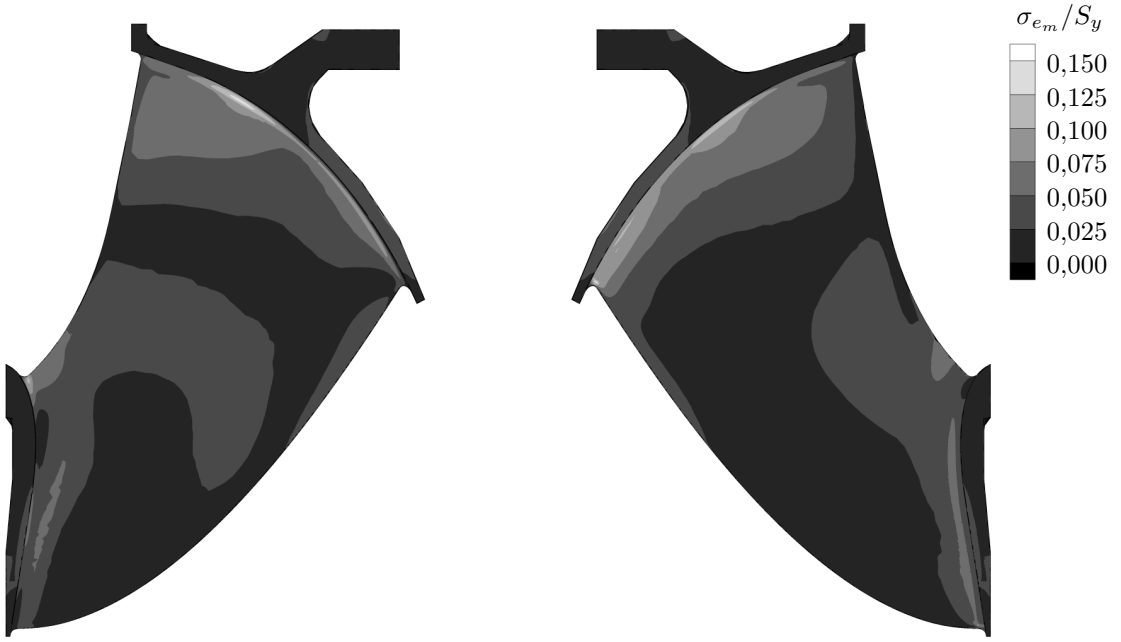

Figure 8.15: Static equivalent mechanical stresses at the part load and high head operating point, meridian view.

at the middle of the fillet between crown and blade. Figure 8.16 shows in detail that local equivalent static stress peaks could again be observed at the blade trailing edge near to the crown and band. This could negatively impact the runner fatigue life.

The total static displacements, u_{T_m}, at the part load and high head operating point are depicted in Figure 8.17. The normalised contour plots made use of the runner meridional representation. The observed displacement distribution was again similar to the one calculated for the full load operating points. The reason was that the static displacements were dominated by the tangential displacement, which arose from the torque applied to the runner blades by the time-averaged pressure load.

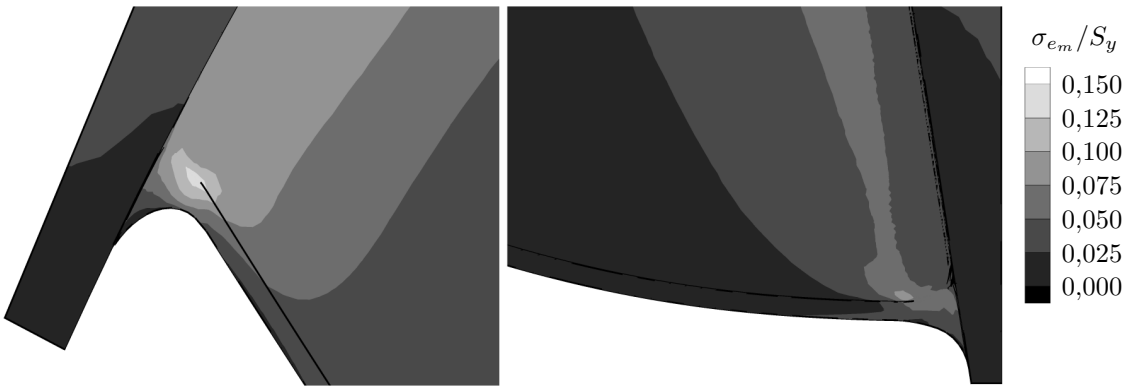

Figure 8.16: Static equivalent mechanical stresses at the part load and high head operating point, detailed view of the trailing edge at crown (left) and band (right).

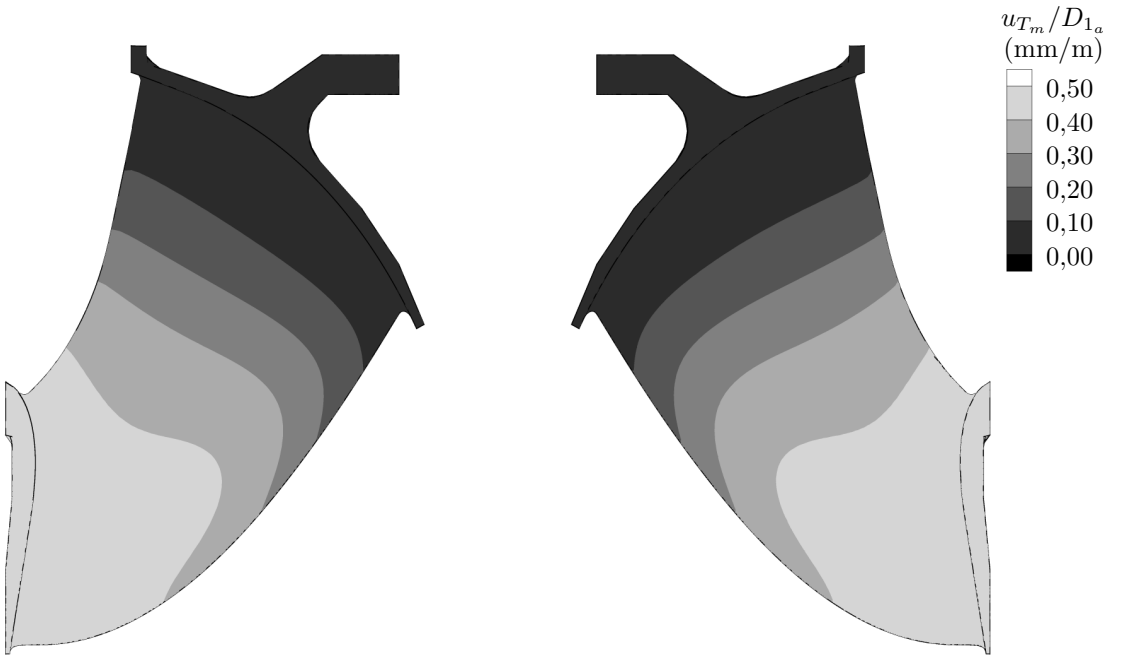

Figure 8.17: Static total displacements at the part load and high head operating point, meridian view.

At part load, the power and runner torque are considerably lower than at full load and the displacements at part load were consequently lower as well.

The topic of greater interest in the study of the influence of the draft tube instabilities (DTI) on the runner structure was the analysis of the dynamic mechanical stresses, as long as they might strongly impact the runner fatigue life. Figure 8.18 presents the equivalent dynamic mechanical stresses, σ_{e_a}, in the runner, normalised to the yield stress, S_y. The contour plot presented at the meridian view had its grey scale limited to $\sigma_{e_a}/S_y = 0{,}030$, in order to improve the visibility of the stress levels.

The largest portion of the blade showed low dynamic stress levels. The highest equivalent dynamic mechanical stresses, σ_{e_a}, were again located at the trailing edge near to the crown and band. The extension of the high stress regions was considerably limited and small high stress spots were associated to the peak stress locations, due to the stress concentration at the trailing edge fillets. Figure 8.19 shows in detail the stress distribution at the trailing edge near to the crown and band. The absolute stress maximum was reached at the trailing edge near to the band, with $\sigma_{e_a}/S_y = 0{,}0333$. It was significantly higher than the local stress peak at the trailing edge near to the crown, where its value achieved $\sigma_{e_a}/S_y = 0{,}0142$. At the part load and high head operating condition, OP 5, the trailing edge near to the band was the critical location from the point of view of the dynamic stresses.

The time history of the dynamic stress tensor components can be found in Figure 8.20. The stress components normalised to the yield stress were plotted

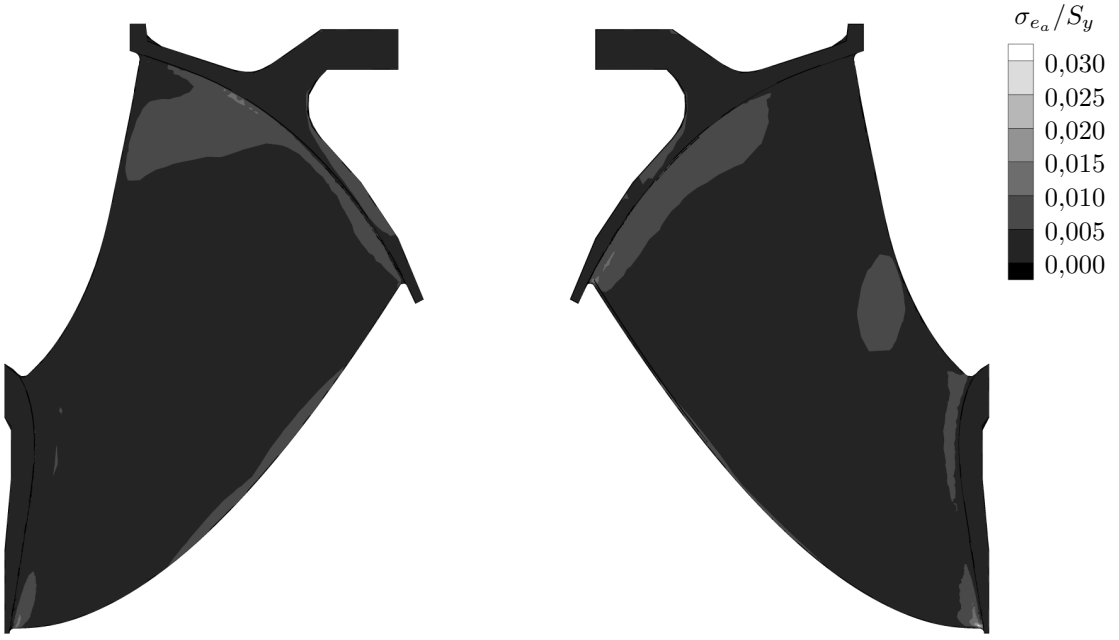

Figure 8.18: Dynamic equivalent mechanical stress amplitude at the part load and high head operating point, meridian view.

as function of time normalised to the runner rotation period. The upper and lower parts of the figure show respectively the dynamic stress components at the blade trailing edge near to the crown and band. The x and y directions for the tensor decomposition were took arbitrarily. The Fourier transform of the dynamic stress tensor components was plotted in Figure 8.21.

The pressure oscillation coming from the vortex rope rotation was expected to be the driving phenomenon in the runner excitation at part load. In order to identify the vortex rope effect on the dynamic mechanical stresses with help of the time history and Fourier transform plots, its frequency had to be converted to the runner

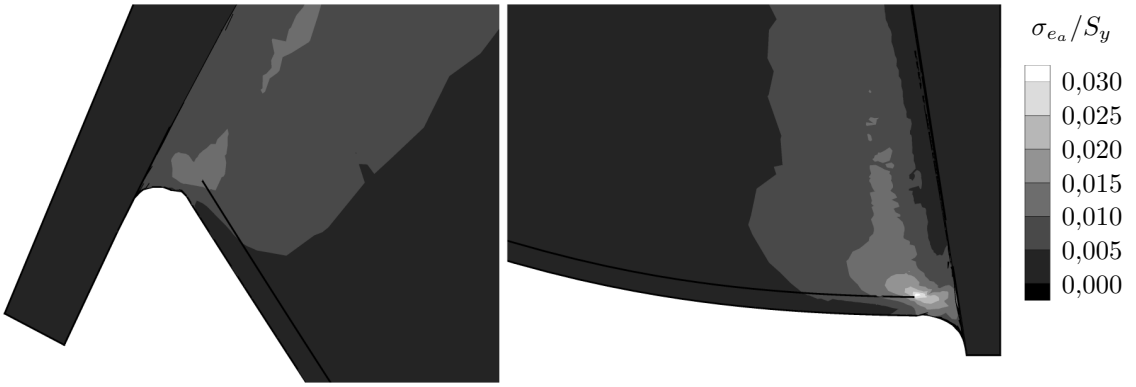

Figure 8.19: Dynamic equivalent mechanical stress amplitude at the part load and high head operating point, detailed view of the trailing edge at crown (left) and band (right).

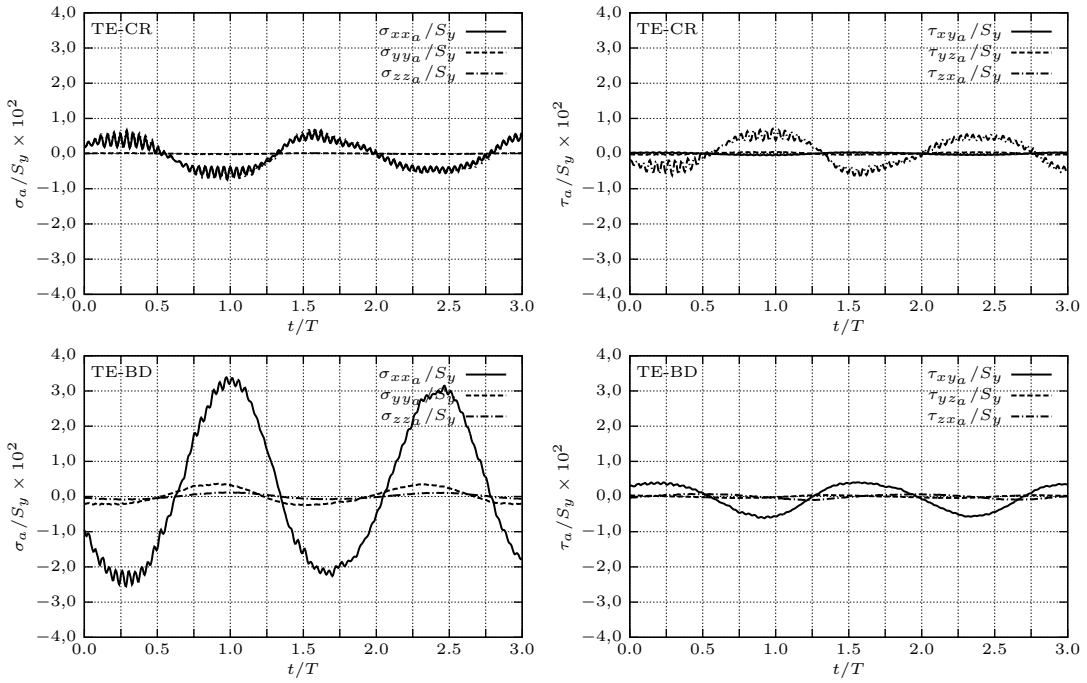

Figure 8.20: Time history of the dynamic stress components at the trailing edge near to the crown (top) and band (bottom), at the part load and high head operating point.

rotating reference frame. At the absolute reference frame, the runner rotated with the frequency f_n, while the vortex rope at high part load and high head, OP 5, rotated with the Rheingans frequency of $f_{Rh} = 0{,}302 f_n$. This means that the vortex rope rotation was slower than the runner revolution, so that, in the runner rotating reference frame, the vortex rope frequency had to be converted to $f/f_n = 1 - f_{Rh}/f_n$, resulting in $f/f_n = 0{,}698$.

Considering the vortex rope rotating frequency in the runner rotating reference frame, its effect on the runner structural response and, consequently, on the dynamic mechanical stress could be identified in the time history and Fourier transform, in Figures 8.20 and 8.21. The slower vibration movement was originated from the vortex rope excitation, while the faster one was due to the guide vane passage with $f/f_n = 24$. Especially at the trailing edge near to the crown, the time signal of the dynamic stress components presented a complex shape, differing from pure sinusoidal curves.

The time history analysis of all stress components showed that the vortex rope was, as expected, the most important effect for the dynamic stresses at part load, as seen in Figure 8.20. The amplitude of the fast stress oscillations, corresponding to the guide vanes passage, was considerably lower, being almost negligible. This can also be qualitatively observed in the Fourier transform, where the amplitude of the first peak at low frequency, $f/f_n = 0{,}698$, related to the vortex rope rotation, was significantly higher than the second one at high frequency, $f/f_n = 24$, coming from the guide vane passage. These considerations show that the high dynamic stress

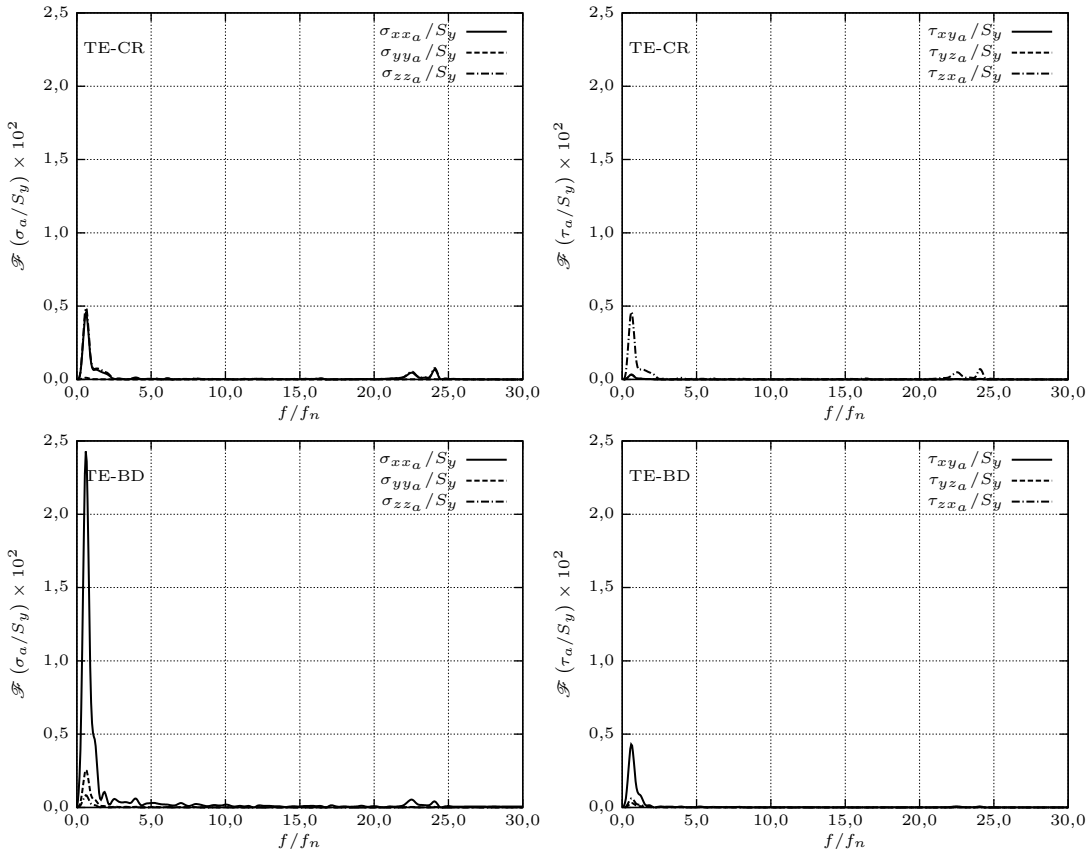

Figure 8.21: Fourier transform of the dynamic stress components at the trailing edge near to the crown (top) and band (bottom), at the part load and high head operating point.

levels at part load at the trailing edge near to the crown and band were induced by the draft tube instabilities (DTI).

Table 8.8 summarises the runner structural analysis at part load and high head, OP 5, with the calculated stress values at the blade leading edge (LE) near to the crown and band, at the middle of the runner fillets between crown (CR) and blade and at the blade trailing edge (TE) near to the crown and band. The normalised equivalent static stress, σ_{e_m}/S_y, the normalised equivalent dynamic stress, σ_{e_a}/S_y, and the stress ratio, $\sigma_{e_a}/\sigma_{e_m}/S_y$, were listed in Table 8.8.

As already discussed, the highest dynamic equivalent stresses, σ_{e_a}, were located at the blade trailing edge near to the crown and band. The maximum value was reached

Table 8.8: Mean and dynamic equivalent stresses at part load and high head.

Equivalent Stress			LE, Crown	LE, Band	TE, Crown	TE, Band	Fillet, CR
Mean	σ_{e_m}/S_y	(-)	0,068	0,106	0,133	0,093	0,118
Dynamic	σ_{e_a}/S_y	(-)	0,0055	0,0070	0,0142	0,0333	0,0115
Ratio	$\sigma_{e_m}/\sigma_{e_a}$	(%)	8,1	6,5	10,6	35,7	9,8

near to band, in opposition to the full load condition, where the critical location was near to the crown. The evaluated dynamic stress levels were considerably higher than at full load, showing that, for high specific speed machines, the part load operating condition is determinant for the runner dynamic behaviour and for the fatigue life.

8.3.4 Higher Part Load and Draft Tube Instabilities

Besides the ordinary part load operating condition, the so called higher part load (HPL) phenomenon may take place in the hydraulic turbine in specific regions of the turbine hill chart. As already explained, at higher part load (HPL), the vortex rope in the draft tube cone assumes a pronounced elliptical cross-sectional shape and, due to its self-rotation, the pressure pulsations at part load are increased. The interest here was to verify, if the higher part load (HPL) effect, which could be clearly observed during the model tests as well as in the fluid flow simulation, could have a distinct influence on the runner dynamic structural behaviour, when compared to the ordinary part load operating condition.

The numerical fluid flow simulation of the higher part load condition (HPL) was successfully carried out for the part load and low head operating point, OP 6. The transient pressure oscillation distribution on the runner blades was stored and used as pressure load for the direct time integration of the runner finite element (FE) model. The part load and low head operating point, OP 6, was also important for the structural assessment of the runner, because it belonged to the boundary of the machine operating range, being the vertex point between the minimum head and minimum power limits.

The mean equivalent stress, σ_{e_m}, and the mean total displacement, u_{T_m}, distributions at the runner were extremely similar to the ones obtained previously at part load and high head, OP 5. They presented exactly the same shape. Therefore, they were not repeated here for the part load and low head operating point, OP 6. This similarity was already expected, since the time-averaged pressure distribution at the runner should not be significantly different from part load and high head, OP 5, to part load and low head, OP 6.

The dynamic equivalent stress distribution at part load and low head, OP 6, was also similar to the one observed at part load and low head, OP 5, with the difference that the dynamic stress peaks were more pronounced. The normalised σ_{e_a} distribution can be found in Figure 8.22, with the detail of the blade trailing edge near to crown and band in Figure 8.23. There, the contour plot scale was limited to $\sigma_{e_a}/S_y = 0{,}030$ for better visualisation. The runner blade pressure side can be found on the right side of the meridian view and the suction side on the left side.

As observed for the previously analysed operating points, the contour plot of σ_{e_a}/S_y at part load and low head, OP 6, counted with the peak stress locations at the trailing edge near to the crown and band. The reached values were respectively, $\sigma_{e_a}/Sy = 0{,}0183$ and $\sigma_{e_a}/Sy = 0{,}0407$. These values were close to the ones obtained

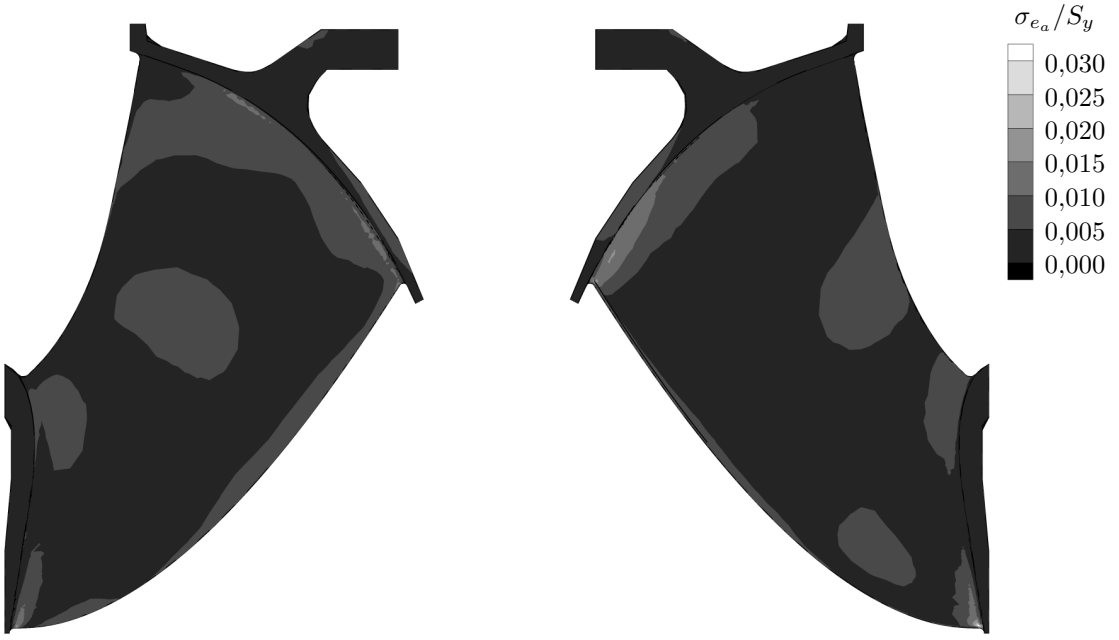

Figure 8.22: Dynamic equivalent mechanical stress amplitude at the part load and low head operating point, meridian view.

previously at part load and low head, OP 5, but somewhat higher, even though in the same order of magnitude. The higher part load (HPL) effect seemed not to decisively influence nor significantly increase the level of the dynamic mechanical stress values. The time history and the Fourier transform of the dynamic stress components in Figures 8.24 and 8.25 were able to better identify the excitation mechanism and clarify the corresponding runner structural response.

The pattern of the normalised stress components time history in Figure 8.24, associated to the runner structural response to the fluid flow pressure fluctuations at higher part load (HPL), did not show any qualitative difference to the ordinary part

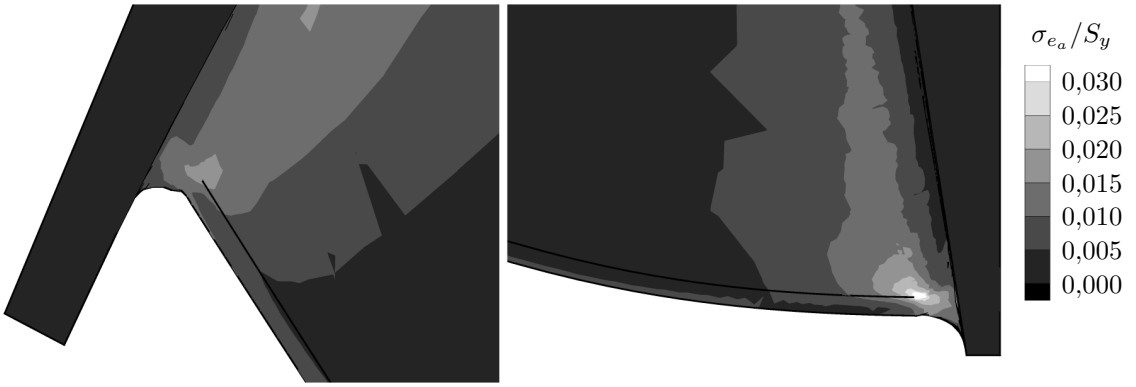

Figure 8.23: Dynamic equivalent mechanical stress amplitude at the part load and low head operating point, detailed view of the trailing edge at crown (left) and band (right).

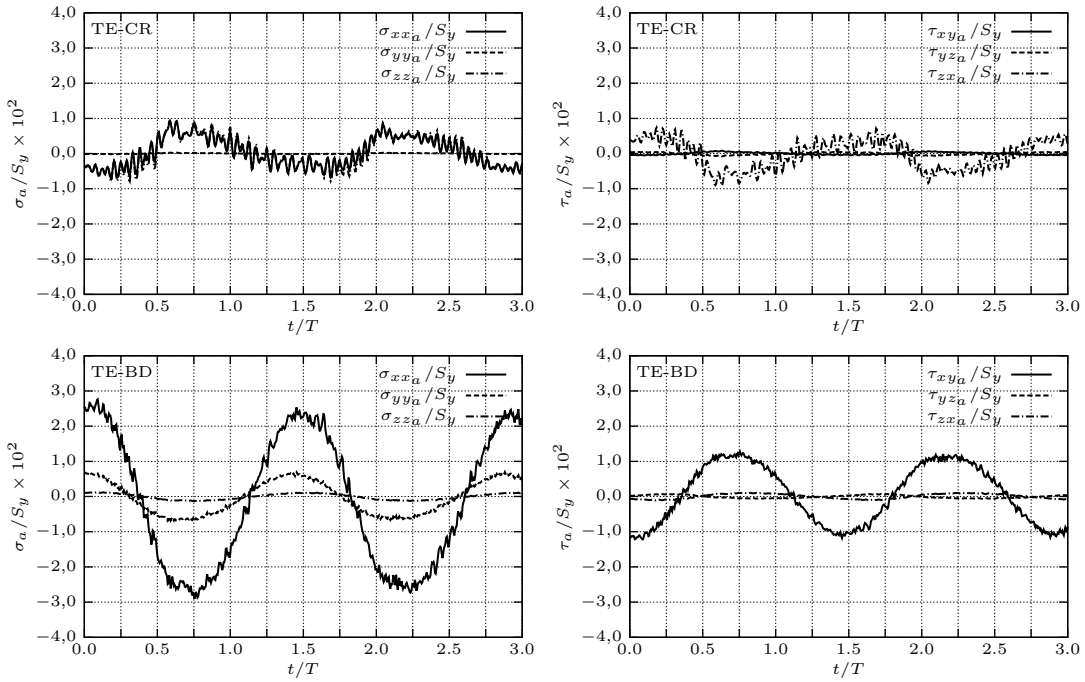

Figure 8.24: Time history of the dynamic stress components at the trailing edge near to the crown (top) and band (bottom), at the part load and low head operating point.

load operating condition. The frequency spectrum at higher part load in Figure 8.25 also did not contain any qualitative difference in relation to normal part load.

As discussed before in the analysis of the effect of the higher part load (HPL) phenomenon on the fluid flow pressure pulsations, a higher oscillating frequency related to the vortex rope self-rotation was present in its frequency spectrum. However, this higher frequency was not found again in the Fourier transform of the dynamic stress components in the turbine runner. There could be drawn the conclusion that the higher part load phenomenon in the turbine flow could not excite the runner structure in any special or specially critical manner. The runner structural response to the draft tube instabilities at higher part load (HPL), for the FT 80 turbine, was not different from its response to normal part load excitation.

The possible explanation would be that the portion of the pressure oscillations exclusively related to the higher part load (HPL) could not importantly excite the runner natural vibration modes and that the excitation due to the vortex rope rotation around the machine axis was the far stronger effect. The only noticeable effect of the higher part load (HPL) was that they slightly increased the pressure pulsation level at part load and low head, OP 6, in relation to part load and high head, OP 5, and this slight increase could also be found in the dynamic mechanical stresses in the turbine runner.

In the time history and in the Fourier transform of the dynamic stress tensor components seen in Figures 8.24 and 8.25, the Rheingans frequency of the rotating

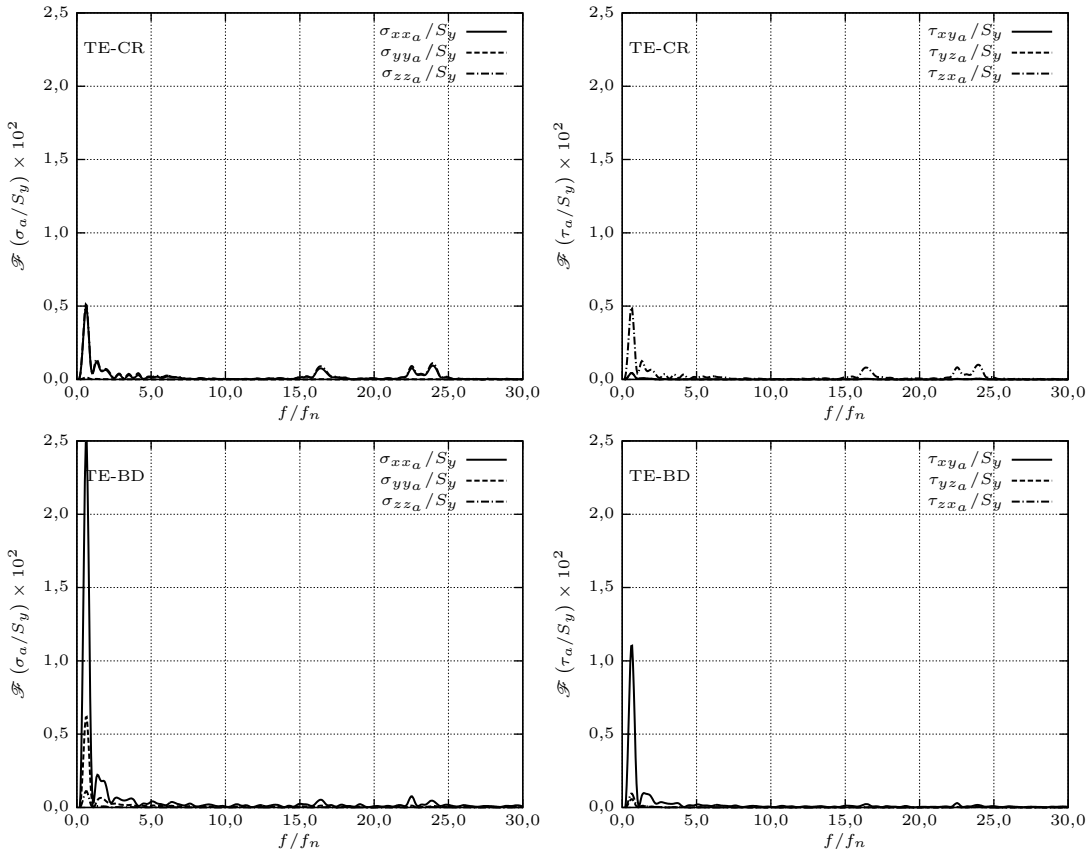

Figure 8.25: Fourier transform of the dynamic stress components at the trailing edge near to the crown (top) and band (bottom), at the part load and low head operating point.

vortex rope could be identified. The Rheingans frequency of $f_{Rh} = 0{,}282 f_n$ in the stationary reference frame, corresponding to $f/f_n = 0{,}718$ in the runner rotating reference frame, could be observed in the numerically calculated dynamic stress components. The guide vane passing frequency, $f/f_n = 24$, could be noticed as well, but, as in the case of part load and high head, OP 5, its contribution to the dynamic mechanical stresses in this high specific speed Francis turbine was almost negligible in comparison to the dynamic stress portion related to the vortex rope rotation.

Table 8.9 shows the summary of the static and dynamic mechanical stresses in the runner at part load and low head, OP 6, and the ratio between them. The static mechanical stresses were slightly lower than at part load and high head, OP 5,

Table 8.9: Mean and dynamic equivalent stresses at part load and low head.

Equivalent Stress			LE, Crown	LE, Band	TE, Crown	TE, Band	Fillet, CR
Mean	σ_{e_m}/S_y	(-)	0,040	0,090	0,113	0,094	0,080
Dynamic	σ_{e_a}/S_y	(-)	0,0049	0,0102	0,0183	0,0407	0,0123
Ratio	$\sigma_{e_m}/\sigma_{e_a}$	(%)	12,1	11,4	16,3	43,4	15,4

possibly because of the smaller head. As already mentioned, in the same way as for the previously analysed operating points, the highest dynamic stresses were located at the trailing edge near to the crown and band. These two locations were again the more important for the dynamic assessment of the runner structural response and for the fatigue life evaluation. The other locations, in spite of relatively high static stresses, were not relevant from the point of view of the dynamic stresses. The high stress ratios were partially due to the low static stresses, but also to the strong vortex rope excitations. These high ratios might have significant impact on the runner fatigue damage.

8.3.5 Deep Part Load and Channel Vortex

The runner mechanical stresses were of special interest at deep part load. This operating condition was expected to be extremely demanding for the runner structure, due to the large magnitude of the fluid flow pressure oscillations and because of the presence of the runner channel vortices. The deep part load operating point, OP 7, was chosen for the study of transient fluid flow phenomena. It counted with the rotating vortex rope, with the runner channel vortices and no relevant cavitation effects. From all numerically calculated operating points, the deep part load, OP 7, showed the highest pressure oscillation amplitudes. The dynamic pressure field of each simulated time step was used as load for the direct time integration solution of the runner finite element (FE) model.

The calculated static equivalent mechanical stress distribution in the turbine runner, arising from the deep part load, OP 7, pressure load, was qualitatively very similar to the one obtained at part load. This can be observed in Figure 8.26, where the contour plot for the normalised σ_{e_m} values is shown with the meridional transformation. One more time, local stress peaks were located at the blade trailing edge near to the crown and band, as seen in detail in Figure 8.27. However, they reached considerably higher levels at the trailing edge near to the crown and band, with respectively $\sigma_{e_m}/S_y = 0{,}144$ and $\sigma_{e_m}/S_y = 0{,}124$. The total static displacements of the runner, u_{T_m}, did not brought any special feature and did not show any qualitative difference in relation to the other operating points and, due to its limited interest, its graphical representation was omitted here.

Of greater interest at deep part load, OP 7, were the dynamic mechanical stresses at the turbine runner. The normalised dynamic equivalent stress distribution can be found in Figure 8.28, with the runner blade pressure side on the right side of the meridian view and the suction side on the left side. The highest dynamic stresses were located once more at the trailing edge near to the crown and band, as viewed in detail in Figure 8.29. Besides from the stress concentration at these locations, it could be noticed that relatively high stresses were distributed along the whole blade trailing edge. Moreover, the peak stresses at the trailing edge near to the crown and band reached significantly higher values in comparison to the other evaluated operating points, with respectively $\sigma_{e_a}/S_y = 0{,}0462$ and $\sigma_{e_a}/S_y = 0{,}0640$. These

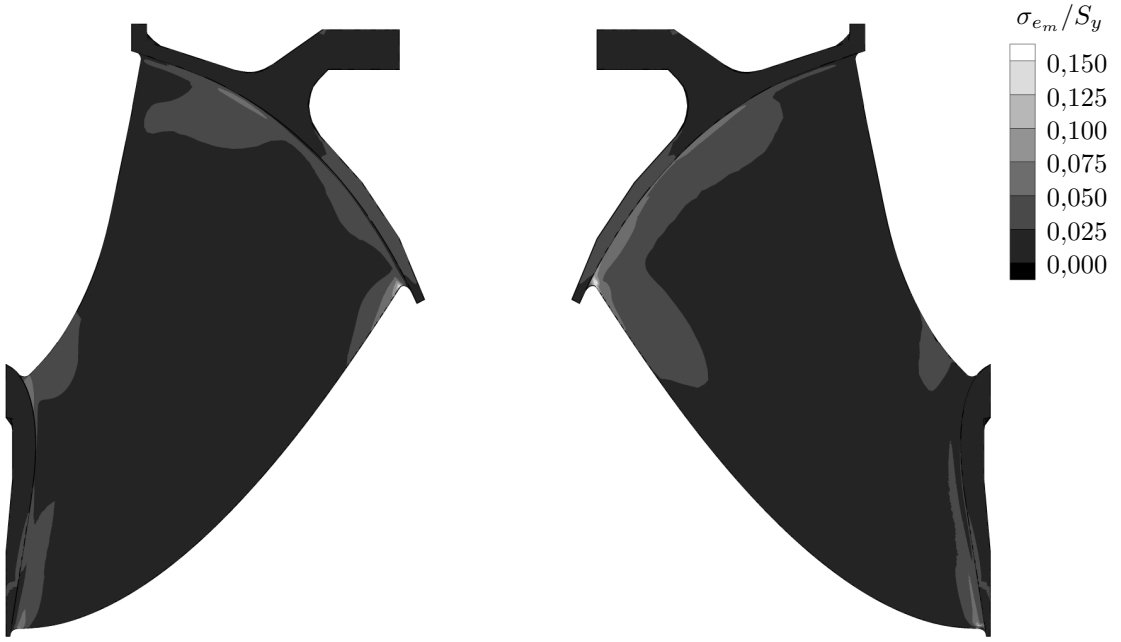

Figure 8.26: Static equivalent mechanical stresses at the deep part load operating point, meridian view.

results could shed light on the strong influence of deep part load on the runner dynamic stresses and showed its importance for the dynamic structural assessment of the runner and its fatigue life. At the deep part load operating point, OP 7, besides the high absolute dynamic stress peak at the trailing edge near to the band, the local stress peak at the trailing edge near to the crown was very pronounced as well. Both locations were nearly of same importance for the fatigue damage analysis from the point of view from the deep part load operating point, OP 7.

The time history and its Fourier transform for the normalised dynamic stress tensor components can be encountered in Figures 8.30 and 8.31. The time evolution of the stress components showed a complex periodical shape, produced by the vortex rope

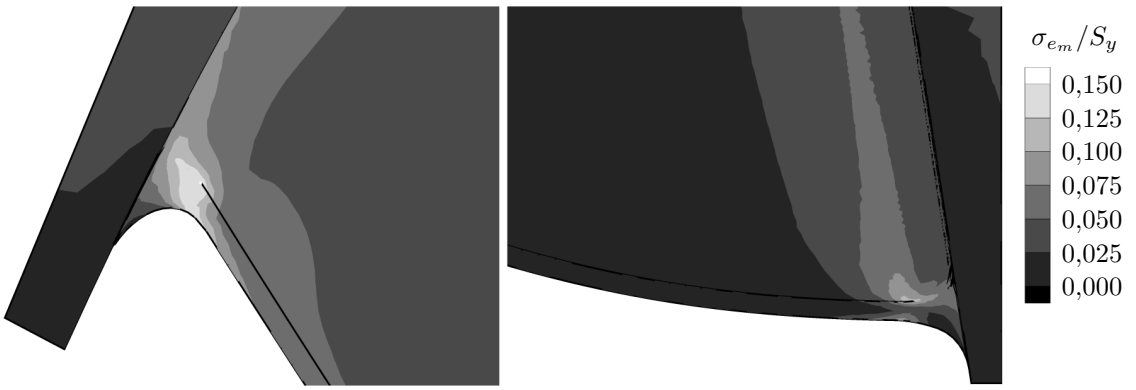

Figure 8.27: Static equivalent mechanical stresses at the deep part load operating point, detailed view of the trailing edge at crown (left) and band (right).

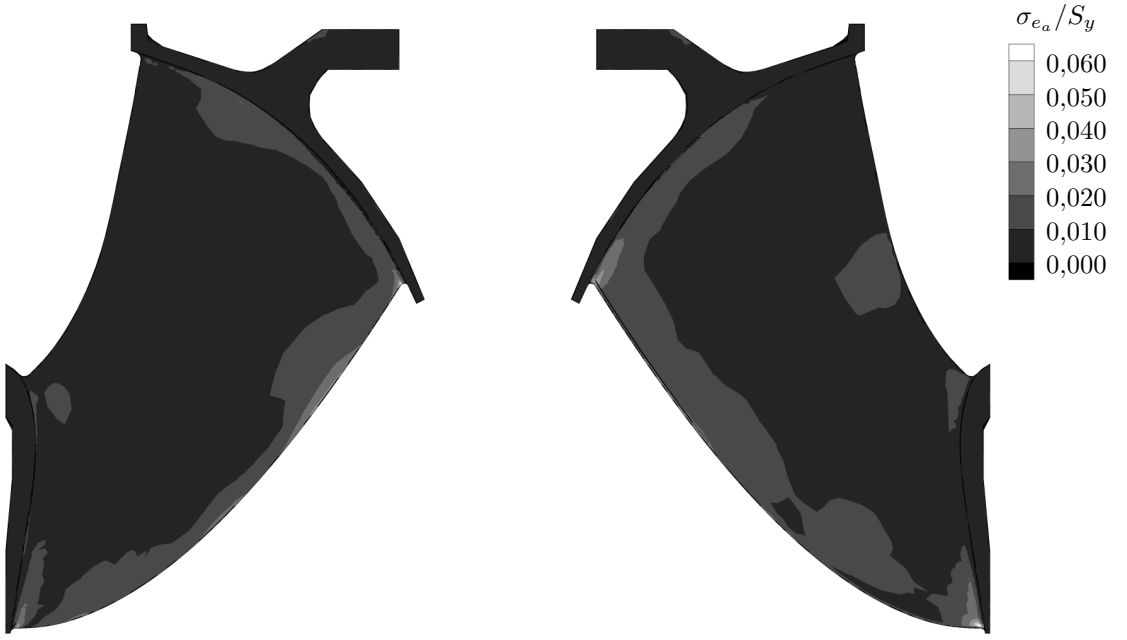

Figure 8.28: Dynamic equivalent mechanical stress amplitude at the deep part load operating point, meridian view.

rotation at deep part load and by the runner channel vortex. The time signal and the frequency spectrum were strongly dominated by slow vibrations corresponding to the Rheingans frequency. The frequency in the stationary reference frame, $f_{Rh} = 0{,}299$, could be found in the runner rotating reference frame, corresponding to $f/f_n = 0{,}701$. The guide vane passing frequency could be identified in the time history and in the frequency spectrum, but only in extremely limited extension for this high specific speed hydraulic turbine. Its contribution to the dynamic mechanical stresses in the FT 80 at deep part load, OP 7, was negligible in comparison to the vortex rope rotation effect.

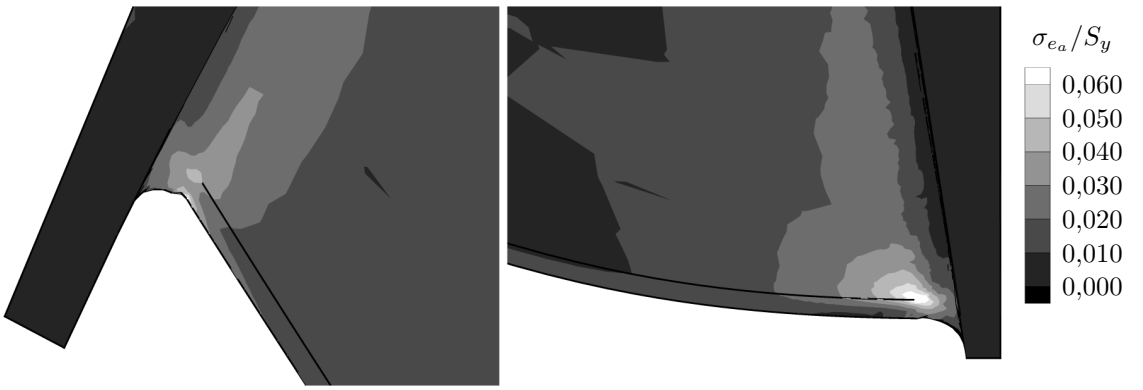

Figure 8.29: Dynamic equivalent mechanical stress amplitude at the deep part load operating point, detailed view of the trailing edge at crown (left) and band (right).

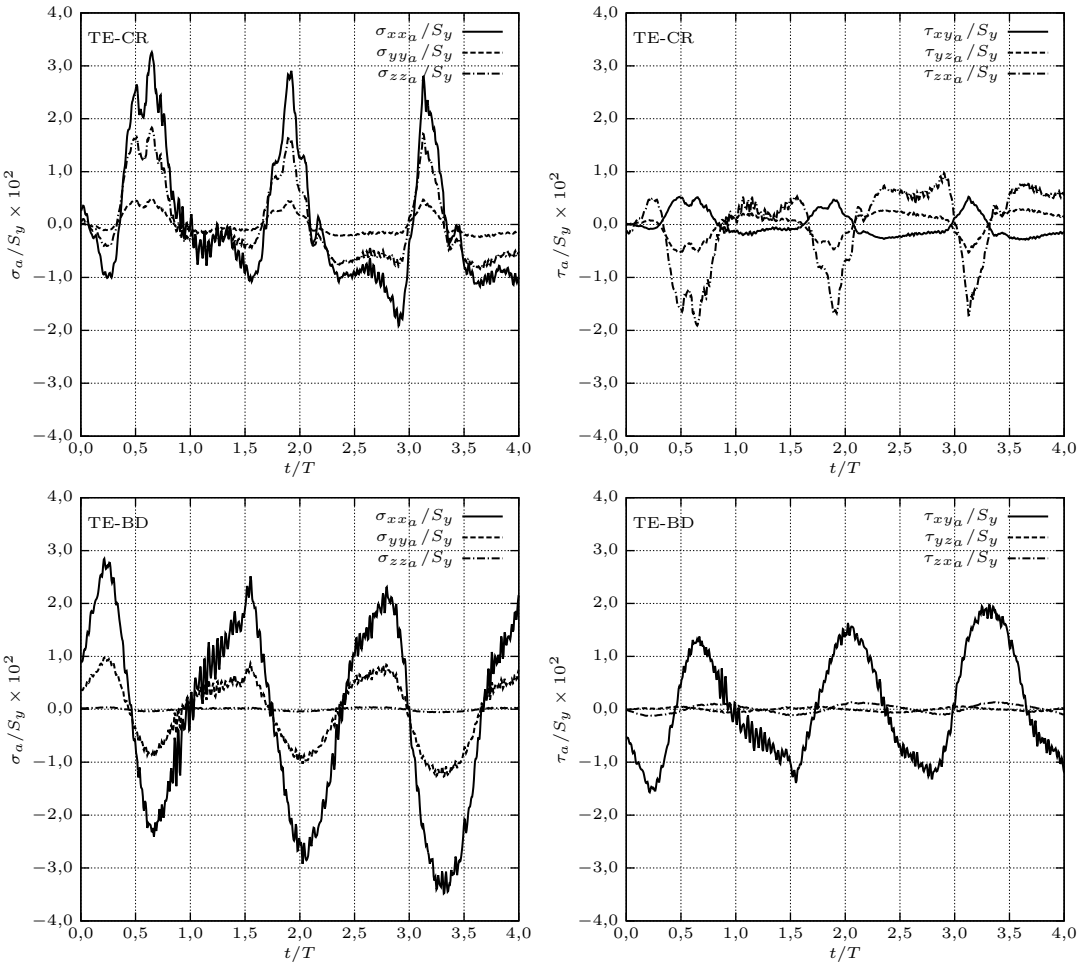

Figure 8.30: Time history of the dynamic stress components at the trailing edge near to the crown (top) and band (bottom), at the deep part load operating point.

The static and dynamic equivalent stresses in the runner and their ratio were listed in Table 8.10, with the values for the locations at the leading edge (LE) near to the crown and band, at the trailing edge (TE) near to the crown and band and at the middle of the fillet between blade and crown (CR). The trailing edge near to the crown and band presented high static as well as dynamic equivalent stresses and, in addition to it, their ratios of 32,1% and 51,5% were importantly high. This made the deep part load operating point, OP 7, a strong potential contributor for the fatigue damage at the trailing edge near to the crown and band.

Table 8.10: Mean and dynamic equivalent stresses at deep part load.

Equivalent Stress			LE, Crown	LE, Band	TE, Crown	TE, Band	Fillet, CR
Mean	σ_{e_m}/S_y	(-)	0,028	0,067	0,144	0,124	0,054
Dynamic	σ_{e_a}/S_y	(-)	0,0071	0,0088	0,0462	0,0640	0,0131
Ratio	$\sigma_{e_m}/\sigma_{e_a}$	(%)	25,1	13,2	32,1	51,5	24,1

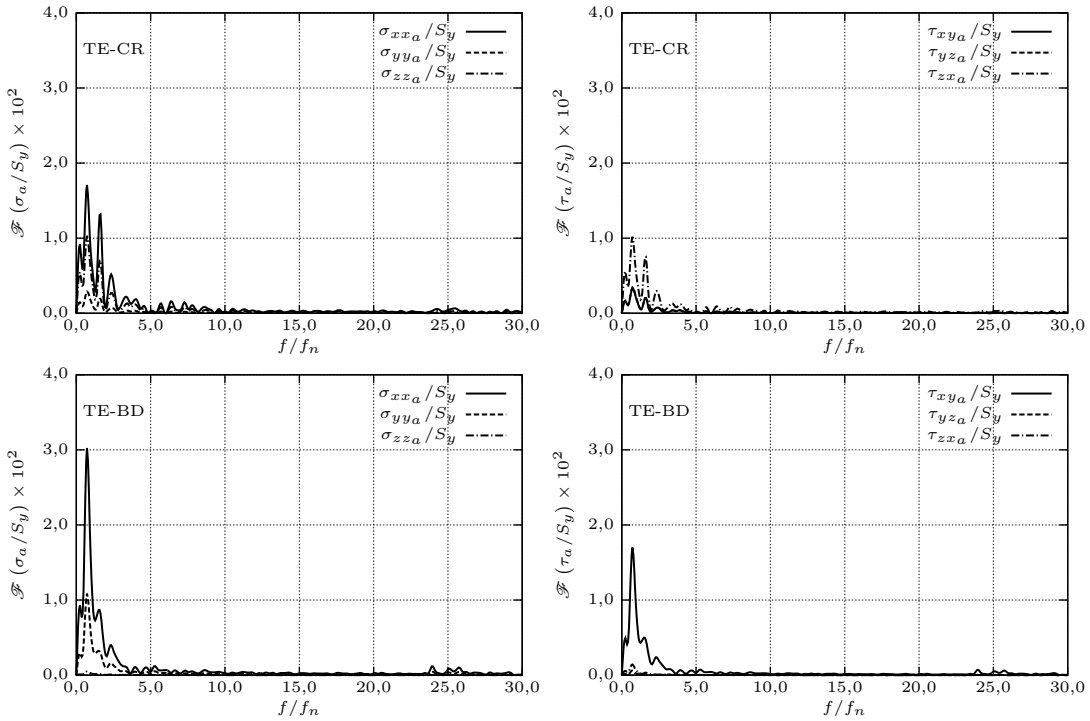

Figure 8.31: Fourier transform of the dynamic stress components at the trailing edge near to the crown (top) and band (bottom), at the deep part load operating point.

8.3.6 Results Summary and Further Considerations

The dynamic mechanical stresses in the Francis runner were calculated with the finite element method (FEM) and using the direct time integration method. The time history of the previously numerically simulated oscillating pressure field in the hydraulic turbine was used as input, constituting the transient pressure load for the finite element analysis (FEA).

The evaluation of the dynamic mechanical stresses at the rated operating point, OP 2, full load and high head, OP 3, full load and low head, OP 4, part load and high head, OP 5, part load and low head, OP 6, and deep part load, OP 7, offered the possibility to understand and characterise the runner dynamic response to distinct transient fluid phenomena as rotor-stator interaction (RSI), draft tube instabilities (DTI), higher part load (HPL) and runner channel vortices (RCV).

Table 8.11 summarises the computed mean and alternate equivalent mechanical stresses, σ_{e_m} and σ_{e_a}, and their ratio, at the runner critical stress locations for the chosen operating points. The stress values were normalised in relation to the material yield strength, S_y. They were listed for the leading edge (LE) near to the crown and band, for the trailing edge (TE) near to the crown and band and for the middle of the fillet between blade and crown (CR).

Table 8.11: Mean and dynamic equivalent stresses for the simulated operating points.

Operating Point	Mean Equivalent Stress σ_{e_m}/S_y (-)				
	LE, Crown	LE, Band	TE, Crown	TE, Band	Fillet, CR
OP 2 Rated	0,134	0,208	0,118	0,127	0,239
OP 3 Full load high head	0,132	0,186	0,130	0,111	0,226
OP 4 Full load low head	0,093	0,169	0,097	0,108	0,176
OP 5 Part load and high head	0,068	0,106	0,133	0,093	0,118
OP 6 Part load and low head	0,040	0,090	0,113	0,094	0,080
OP 7 Deep part load	0,028	0,067	0,144	0,124	0,054
Operating Point	Dynamic Equivalent Stress σ_{e_a}/S_y (-)				
	LE, Crown	LE, Band	TE, Crown	TE, Band	Fillet, CR
OP 2 Rated	0,0033	0,0047	0,0277	0,0132	0,0040
OP 3 Full load high head	0,0027	0,0032	0,0229	0,0133	0,0027
OP 4 Full load low head	0,0028	0,0038	0,0205	0,0127	0,0039
OP 5 Part load and high head	0,0055	0,0070	0,0142	0,0333	0,0115
OP 6 Part load and low head	0,0049	0,0102	0,0183	0,0407	0,0123
OP 7 Deep part load	0,0071	0,0088	0,0462	0,0640	0,0131
Operating Point	Stress Ratio $\sigma_{e_a}/\sigma_{e_m}$ (%)				
	LE, Crown	LE, Band	TE, Crown	TE, Band	Fillet, CR
OP 2 Rated	2,5	2,2	23,4	10,4	1,7
OP 3 Full load high head	2,0	1,7	17,7	11,9	1,2
OP 4 Full load low head	3,0	2,2	21,1	11,8	2,2
OP 5 Part load and high head	8,1	6,5	10,6	35,7	9,8
OP 6 Part load and low head	12,1	11,4	16,3	43,4	15,4
OP 7 Deep part load	25,1	13,2	32,1	51,5	24,1

The highest mean equivalent stresses, σ_{e_m} were found at the middle of the fillet between blade and crown. However, this location was revealed to be irrelevant for the dynamic analysis and for the fatigue assessment, because of its low alternate stresses, σ_{e_a}. The trailing edge near to the crown and near to the band were the locations, where the maximum dynamic mechanical stresses, σ_{e_a}, were found for all operating points. Moreover, high static mechanical stresses, σ_{e_m}, were found at these locations as well. The trailing edge near to the crown and near to the band were also characterised by elevated $\sigma_{e_a}/\sigma_{e_m}$ ratios. For these reasons, the trailing edge near to the crown and band could be pointed out as critical for the runner dynamic structural analysis. They constituted the points with more risks for structural damages, as confirmed by numerous field observations, e.g. by Fisher et al. [44]. Therefore, the trailing edge near to the crown and band were the points of interest for the fatigue assessment.

The correlation between the dynamic stresses and the operating points showed that, in the case of the FT 80 turbine, the rotor-stator interaction (RSI), associated to

the full load operating conditions, OP 2, OP 3 and OP 4, were responsible for moderated σ_{e_a} values. For low specific speed Francis turbines, the dynamic stresses related to the rotor-stator interaction (RSI) would have been much higher, because of the higher pressure oscillation amplitudes induced by the tight distance between guide vanes trailing edge and runner blades leading edge in this kind of machines.

The analysis of the operating points and the calculated dynamic stresses revealed that, for the FT 80, the vortex rope rotation associated to the draft tube instabilities (DTI) at part load, OP 5, OP 6 and OP 7, produced high σ_{e_a} values at the observed locations. This behaviour brought in evidence the impact of the high pressure oscillation amplitudes at part load on the dynamic mechanical stresses for high specific speed machines, like the FT 80. Low specific speed machines, where the pressure oscillation amplitudes in the draft tube cone are considerably lower, should have their structure much less influenced by the vortex rope rotation.

The higher part load (HPL) phenomenon, at part load and low head, OP 6, did not caused any qualitatively different response of the runner structure to the pressure oscillations, when compared to ordinary part load, as in the case of part load and high head, OP 5. The higher dynamic mechanical stresses calculated at OP 6 in comparison to OP 5 came from the higher pressure oscillation amplitudes and not from qualitatively distinct dynamic phenomena. At deep part load, OP 7, the presence of the runner channel vortex (RCV), together with the rotating vortex rope, induced the highest dynamic mechanical stresses in the runner.

These numerically obtained results confirmed the common perception that the endurance of high specific speed Francis turbines are negatively impacted by part load and deep part load operation, where the rotating vortex rope coming from the draft tube instabilities (DTI) is present. On the other hand, low specific speed Francis runners would be strongly sensible to the rotor-stator interaction (RSI).

8.4 Fatigue Assessment

Francis runners submitted to though operating conditions, counting with not optimised mechanical design or manufactured without high quality processes might be subjected to mechanical failures, with the occurrence and propagation of fatigue cracks. There are numerous reports on the occurrence of fatigue cracks in Francis runners, as discussed among others by e.g. Fisher et al. [44], Coutu et al. [28], Brekke [21] and Bhave, Murthy and Goyal [15]. Under these circumstances, the fatigue analysis of the runner structure gains on relevance, in order to prevent the mechanical failure of this important turbine component.

The chosen approach in this study was to evaluate how the different turbine operating conditions could contribute to the runner fatigue damage. The pressure distribution over the turbine runner actuated as structural loads on it. The time-averaged pressure field was responsible for the static loads, while the pressure

oscillations generated the dynamic loads. The static loads resulted in the mean mechanical stresses and the transient loads in the dynamic mechanical stresses. The combination of both stress components originated the runner fatigue damage.

Interesting here was to investigate how the pressure pulsations associated to the distinct transient fluid flow phenomena, as rotor-stator interaction (RSI), draft tube instabilities (DTI) and runner channel vortices (RCV), could influence the runner fatigue damage and fatigue life. With this objective, the operating points studied before, rated, OP 2, full load and high head, OP 3, full load and low head, OP 4, part load and high head, OP 5, part load and low head, OP 6, and deep part load, OP 7, were also used for the fatigue assessment of the FT 80 runner.

Procedure

The mean and alternate mechanical stresses from the runner finite element analysis (FEA), performed using the pressure time history from the transient fluid flow numerical simulation, were taken as input for the runner fatigue assessment. More precisely, the calculated stress time history could be employed as input for the fatigue calculations. The runner structural analysis carried out previously showed that the trailing edge near to the crown and near to the band were the locations, where the highest dynamic stresses were found and, at the same time, they counted with high mean stress levels. In addition, field test observations, as reported by Fisher et al. [44], pointed out the occurrence of cracks at these locations. Therefore, the trailing edge near to the crown and near to band were the relevant and chosen locations for the fatigue analysis. The investigation of the fatigue models and methodology themselves did not belong to the scope of this study. The relevant elements of the fatigue theory were just applied in the analysis of the turbine runner, with the exclusive practical objective to estimate the contribution of the distinct machine operating conditions to the runner damage and their influence on the fatigue life.

Fatigue Models

The results from the finite element analysis (FEA) revealed a multiaxial stress state at the trailing edge near to the crown and near to the band. At both locations, the multiaxial stress state was present for all simulated operating points. The time history plots of the mechanical stress components indicated that they were mostly in phase, but that they were not proportional to each other. This means that the directions of the principal stresses varied constantly over the time. Under these stress conditions, more elaborated fatigue models were needed for the assessment of the runner, as the critical plane principle described by Fatemi-Socie [40] or the micro-crack approach proposed by Wang and Brown [164].

For the runner fatigue analysis, high cycle fatigue (HCF) was considered. Taking a typical machine rotational speed of $n_P = 150$ rpm as example, after 8 000 hours of operation, the excitations arising from the inhomogeneous spiral case pressure distribution would have imposed $7{,}2 \cdot 10^7$ fatigue cycles to the runner, the guide vane passage $1{,}7 \cdot 10^9$ cycles and the vortex rope rotation approximately $2{,}2 \cdot 10^7$ cycles. The high number of cycles in this typical example, together with the ASME [3] recommendation for welded structures, justified the adoption of high cycle fatigue (HCF). The NEUBER [110] rule had to be adapted to the multiaxial stress state with e.g. the procedure from GLINKA AND BUCZYNSKI [54].

The runner dynamic structural analysis showed that the time variation of the dynamic stress components could not be approximated by simple analytic functions. However, their time history was made available by the transient numerical structural simulation of the runner with the finite element method (FEM), as if it were experimental measured stress data. This offered the possibility to employ the rainflow method to determine the alternate stress amplitude and the associated number of cycles. The original rainflow counting algorithm from MATSUISHI AND ENDO [95] had to be substituted by one, which could deal with the multiaxial stress state. The modification introduced by WANG AND BROWN [164] was chosen for this study for being suitable for the application to stress data obtained with the finite element method (FEM).

For the fatigue analysis, the material properties are of great importance. For more accurate results, material data from specific fatigue strength tests are needed. Turbine manufacturers normally carry out these tests for their runner material. In the case of the FT 80, the runner material was the stainless steel ASTM A743 CA-6NM, equivalent to G-X5 CrNi 13.4, for which specific fatigue properties were available, as for example from TVFA WIEN AND LBF INSTITUT [152] research activities.

The manufacturing process might introduce residual stresses in mechanical components and affect their fatigue life. In the case of Francis runners, which were not stress relieved, the residual stress magnitude at the blade trailing edge near to crown and band might even reach the material yield strength, S_y. Due to the ductile nature of stainless steel, the stress level is reduced to 10% up to 20% of the yield strength after commissioning, as reported by SABOURIN ET AL. [133], and tends to be completely eliminated during long-term operation as formulated by ZAHAVI AND TORBILO [176].

Uncertainties

The static and dynamic stresses actuating in the turbine at different operating points could be accurately estimated with the procedure presented in this study, using the transient fluid flow simulation and the transient structural analysis. The uncertainties related to the loads at stable operating conditions were not more than

those inherent to the CFD and FEA in general. The dynamic stresses in the runner at transitory operating conditions, as e.g. start and stop or load rejection, could be estimated by the approximation proposed by Huth [66]. Alternatively, they could have been estimated by the same numerical procedure employed here for the operating points or determined experimentally.

The fatigue analysis itself brings some uncertainties with it. For example, the fatigue life of a test specimen examined at the laboratory should be interpreted as a statistical result and means a high probability, usually over 90%, that the specimen fails after a given number of cycles. This statistical character of the fatigue analysis should be kept in mind, especially because of the high deviation in the material fatigue properties. Another point of inherent uncertainty in the fatigue analysis is related to the fatigue damage models, which attempt to predict the material useful life. Even if these models are based on experimental observations, they rely on mathematical representations of the material behaviour regarding the crack initiation mechanism.

The magnitude of the residual stresses and the way, in which they are reduced along the machine operation, are based on field test observations from e.g. Sabourin et al. [133] and on the mathematical model proposed by Zahavi and Torbilo [176]. This limited approach might lead to some inaccuracy. The uncertainty related to the influence of residual stresses on the fatigue life might be minimised by a sensitivity analysis. Moreover, residual stresses should not importantly modify the relative contribution of each analysed operating point to the runner fatigue damage.

The fatigue life of the Francis runner depends on how the machine is operated, i.e. the combination and frequency of operating points, also known as load spectrum. In the design phase, the load spectrum can only be assumed and tries to reproduce how the machine will be run, when in commercial operation. The evaluation of different possible scenarios for the load spectrum can minimise the uncertainties related to it. Still, the relative fatigue damage, caused by each operating point during the same normalised time period, is not affected by the load spectrum.

Considering the uncertainties in the fatigue assessment of turbine runners, the fatigue analysis should be understood as an orientation in the design of Francis runners, which shall be complemented by experience and engineering judgment. Nonetheless, more important here was the investigation of the effect of the distinct operating conditions on the runner fatigue life. This objective could be reached anyway, as long as the relative damage originated by each operating condition was little sensible to the uncertainties in the fatigue analysis.

8.4.1 Fatigue Damage and Operating Points

The effect on the runner fatigue of the distinct studied operating conditions, i.e. rotor-stator interaction (RSI), draft tube instabilities (DTI), higher part load (HPL) and runner channel vortex (RCV), was assessed through the determination of the

Table 8.12: Fatigue damage and operating points.

Operating Point		Cumulated Damage after 1 000 hours D (-)	
		TE-CR	TE-BD
OP 2	Rated	$5{,}0 \cdot 10^{-6}$	$8{,}3 \cdot 10^{-5}$
OP 3	Full load and high head	$2{,}9 \cdot 10^{-6}$	$9{,}3 \cdot 10^{-5}$
OP 4	Full load and low head	$1{,}6 \cdot 10^{-6}$	$2{,}7 \cdot 10^{-5}$
OP 5	Part load and high head	$4{,}2 \cdot 10^{-7}$	$5{,}1 \cdot 10^{-4}$
OP 6	Part load and low head	$6{,}1 \cdot 10^{-7}$	$1{,}1 \cdot 10^{-4}$
OP 7	Deep part load	$1{,}4 \cdot 10^{-4}$	$6{,}9 \cdot 10^{-4}$
	Vortex shedding effect	$7{,}7 \cdot 10^{-8}$	$1{,}3 \cdot 10^{-7}$

fatigue damage caused by each simulated operating point. The fatigue damage, D, associated with each operating point was determined by n/N, based on the Palmgren-Miner [115, 104] concept, where n was the number of load cycles during a reference time and N the corresponding number of cycles until fatigue failure for this load. For example in the case of the draft tube instabilities (DTI), the number of load cycles, n, would be the number of vortex rope rotations during the reference period and the number of cycles until failure, N, would be the required number of vortex rope rotations until the crack initiation.

Results

For the comparison of the relative fatigue damage under same conditions, the number of cycles at each operating point was determined for a reference operating duration of 1 000 hours. This means that for the determination of the fatigue damage the stress history associated to each operating point was multiaxially rainflow counted during 1 000 hours of operation and D was calculated with the chosen fatigue model. For the evaluation of the individual D values, the Palmgren-Miner [115, 104] rule was employed together with the rainflow counting method applied to the stress history of the individual operating point being analysed.

Table 8.12 lists the fatigue damage at the blade trailing edge near to the crown (TE-CR) and band (TE-BD) for each simulated operating point. The fatigue damage was calculated taking into account the multiaxial stress state, using the rainflow counting method and assuming a residual stress of $\sigma_0/S_y = 0{,}20$.

There could be observed that the fatigue damage was larger at the blade trailing edge near to the band than near to the crown, being fast one up to two orders of magnitude greater, depending on the operating point. For the operating points OP 2 to OP 7, D went from $4{,}2 \cdot 10^{-7}$ up to $1{,}4 \cdot 10^{-4}$ at the trailing near to the crown and from $8{,}3 \cdot 10^{-5}$ up to $6{,}9 \cdot 10^{-4}$ near to the band.

At the full load operating conditions, the blade trailing edge near to the band was mainly submitted to the high frequent dynamic stresses arising from the guide vane

passage. The dynamic stresses at the trailing edge near to the crown were rather dominated by the low frequent spiral case inhomogeneous pressure distribution. At part load operation, the nature of the excitation at the trailing edge near to the crown and band was the same, coming from the vortex rope rotation, still with significantly higher dynamic mechanical stresses at the trailing edge near to the band than near to the crown. These were the main reasons for the greater calculated fatigue damage at the trailing edge near to the band than near to the crown.

From the values in Table 8.12, the critical fatigue location for the FT 80 runner was the trailing edge near to the band. Other machines, depending on their design, geometry, mean and dynamic stress levels and excitation frequencies could, in theory, experience more fatigue sensitivity at the trailing edge near to the crown.

At the trailing edge near to the crown, the larger fatigue damage was caused by the deep part load, OP 7, with $D = 1{,}4{\cdot}10^{-4}$, followed by the full load operating points, OP 2, OP 3 and OP 4, and after by the part load operating points, OP 5 and OP 6. The origin of the larger fatigue damage amount was mainly the dynamic stress component. At the trailing edge near to the crown, the influence of the rotating vortex rope on σ_a was not as significant as at the trailing edge near to the band.

Considering the critical fatigue location for the FT 80, the trailing edge near to the band, the greatest fatigue damage, $D = 6{,}9{\cdot}10^{-4}$, came from deep part load, OP 7, due to the high dynamic stresses generated by the draft tube instabilities (DTI) and by the runner channel vortex (RCV).

After deep part load, OP 7, the larger D values were reached by part load and high head, OP 5, and low head, OP 6, with respectively $D = 5{,}1{\cdot}10^{-4}$ and $D = 1{,}1{\cdot}10^{-4}$. Again, the greater contribution for the fatigue damage came from the high dynamic stresses, originated from the proximity of the band-near portion of the blade to the rotating vortex rope. Although the pressure pulsations and dynamic stresses were higher at part load and low head, the fatigue damage was larger at part load and high head, OP 5, possibly because of the higher mean stresses induced by the higher head. The presence of higher part load (HPL) at part load and low head (OP 6) did not noticeably influence the fatigue damage amount.

At the trailing edge near to the band, the lower fatigue damage was generated by the full load operating conditions, OP 2, OP 3 and OP 4, as long as the rotor-stator interaction (RSI) produced the lower pressure pulsations for the FT 80.

This behaviour was typical from high specific speed machines, where the part load operating points with the presence of the draft tube instabilities (DTI) are responsible for the higher pressure oscillation amplitudes, for the higher dynamic mechanical stresses and, as just seen, for the higher fatigue damage at the runner structure critical location. At low specific speed machines, the draft tube instabilities (DTI) become less important and the rotor-stator interaction assumes the role of the driving dynamic phenomenon. At low n_q hydraulic turbines, the larger amount of fatigue damage is expected to be produced by the full load operating conditions, because of the strong presence of rotor-stator interaction.

The approach presented here, with the transient fluid flow simulation and the subsequent transient finite element analysis (FEA) of the runner structure, could be repeated for any other operating point or any other Francis machine for the estimation of the corresponding fatigue damage.

The fatigue damage results for the FT 80 showed that reducing the machine output to part load and deep part load created the most demanding conditions from the point of view of fatigue life. If not clearly required by energy generation and grid regulation strategies, this operating range could be avoided, resulting in the extension of the machine useful life. There should be drawn attention to the point that especially operating points with high alternate stress amplitudes, caused by the fluid flow pressure pulsations, could lead to significantly higher fatigue damage.

Table 8.12 brought as well the estimated fatigue damage produced by the structural excitation through the vortex shedding effect (VSE). As discussed before, the vortex shedding CFD and FEA computations should be interpreted in this study just as a qualitative approach. For this reason, the exact computed values for the fatigue damage coming from the vortex shedding effect (VSE) had no relevant meaning. However, it could serve as estimation of the order of magnitude of D, caused by the vortex streets at the runner blades trailing edge. With values of D in the order of magnitude of $7{,}7 \cdot 10^{-8}$ at the trailing edge near to the crown and $D = 1{,}3 \cdot 10^{-7}$ near to the band, the vortex shedding effect did not appear as a relevant phenomenon for the fatigue assessment of the runner and would have been negligible.

Transient Operating Conditions

For the completeness of the fatigue assessment, not only the accurately simulated operating points were considered, but also transient operating conditions as start, stop, load variation, load rejection and runaway. These transient operating conditions could have been numerically calculated with the method presented here. However, for simplicity, their associated stresses were estimated with the approach proposed by Huth [66].

For the fatigue assessment here, the start, stop and load change were taken into account. Experimental surveys from Gagnon et al. [49] show that the transient stress levels in Francis turbines during the start phase depend on the start sequence. Slow start regimes reduce the facility responsiveness, but keep the dynamic stresses at low levels. Fast starts are associated to higher dynamic stresses.

Based on the observations of Gagnon et al. [49] and Sabourin et al. [133], four start regimes were considered, soft start, slow start, normal start and fast start. For each of them, stress amplification factors were assumed in relation to the mean stresses, respectively taking the values 1,0, 1,3, 1,6 and 2,0. The stop condition was chosen to be comparable to a soft start. Two load change conditions were considered, from part load to optimum operating range and from the latter to full load, taking into account the mean stress variation, as suggested by Huth [66].

Table 8.13: Fatigue damage and operating conditions.

Operating Condition	Cumulated Damage after 1 000 cycles D (-)	
	TE-CR	TE-BD
Soft Start	$9{,}7 \cdot 10^{-8}$	$3{,}9 \cdot 10^{-8}$
Slow Start	$9{,}0 \cdot 10^{-7}$	$2{,}4 \cdot 10^{-7}$
Normal Start	$3{,}9 \cdot 10^{-6}$	$8{,}5 \cdot 10^{-7}$
Fast Start	$4{,}7 \cdot 10^{-5}$	$1{,}5 \cdot 10^{-5}$
Stop	$9{,}7 \cdot 10^{-8}$	$3{,}9 \cdot 10^{-8}$
Part load to optimum	$< 1{,}0 \cdot 10^{-12}$	$< 1{,}0 \cdot 10^{-12}$
Optimum to full load	$< 1{,}0 \cdot 10^{-12}$	$1{,}1 \cdot 10^{-10}$

Table 8.13 lists the fatigue damage for the considered transient operating conditions, calculated for the multiaxial stress state, using the rainflow counting method and assuming a residual stress of $\sigma_0/S_y = 0{,}20$. As reference for the fatigue damage computation, 1 000 cycles were imposed for each condition.

There can be seen in Table 8.13, that, in the case of the FT 80, the critical fatigue location for the transient operating conditions was once more the blade trailing edge near to the band. It could be confirmed that more aggressive start sequences were responsible for larger fatigue damage, with $D = 3{,}9 \cdot 10^{-8}$ at the trailing edge near to the band for the soft start and $D = 1{,}5 \cdot 10^{-5}$ for the fast start. Between the soft and fast start procedures, the fatigue damage was increased with a much faster rate than the dynamic mechanical stresses. For more safety towards fatigue, smooth start sequences should be preferred, when acceptable from the point of view of the facility operational strategy.

In the case of pump-turbines, where the start, stop and operating mode reversal are subjected to tougher dynamic solicitations, because of the flow dynamics and also often due to the operational strategy, the participation of the transient conditions in the total fatigue damage becomes of main importance.

For Francis machines at transient operating conditions, the accurate pressure oscillations and induced dynamic mechanical stresses in the runner can be simulated with the CFD and FEA approaches proposed here, with the benefit of offering a more precise fatigue assessment, as done here for the operating points associated to rotor-stator interaction (RSI), draft tube instabilities (DTI), higher part load (HPL) and runner channel vortices (RCV).

Counting Method

The rainflow method took the advantage of counting with the stress time history obtained from the runner transient finite element (FE) simulation, offering the possibility to evaluate the fatigue damage as if experimental multiaxial data were available. When the stress time history is not known, the analytic method idealising

Table 8.14: Fatigue damage and counting method.

Operating Point	Cumulated Damage after 1 000 hours D (-)			
	TE-CR		TE-BD	
	Analytic	Rainflow	Analytic	Rainflow
OP 2 Rated	$1{,}4{\cdot}10^{-5}$	$5{,}0{\cdot}10^{-6}$	$4{,}6{\cdot}10^{-6}$	$8{,}3{\cdot}10^{-5}$
OP 3 Full load and high head	$7{,}8{\cdot}10^{-6}$	$2{,}9{\cdot}10^{-6}$	$4{,}5{\cdot}10^{-6}$	$9{,}3{\cdot}10^{-5}$
OP 4 Full load and low head	$4{,}8{\cdot}10^{-6}$	$1{,}6{\cdot}10^{-6}$	$3{,}8{\cdot}10^{-6}$	$2{,}7{\cdot}10^{-5}$
OP 5 Part load and high head	$2{,}1{\cdot}10^{-7}$	$4{,}2{\cdot}10^{-7}$	$6{,}4{\cdot}10^{-6}$	$5{,}1{\cdot}10^{-4}$
OP 6 Part load and low head	$5{,}4{\cdot}10^{-7}$	$6{,}1{\cdot}10^{-7}$	$1{,}6{\cdot}10^{-5}$	$1{,}1{\cdot}10^{-4}$
OP 7 Deep part load	$5{,}5{\cdot}10^{-5}$	$1{,}4{\cdot}10^{-4}$	$2{,}7{\cdot}10^{-4}$	$6{,}9{\cdot}10^{-4}$

the alternate stress as a sinusoidal function of time is often employed. Here, as long as the multiaxial time history was available, there was no reason not to use the rainflow counting method. However, for investigative interest, the fatigue damage results obtained with the multiaxial rainflow counting method from Wang and Brown [164] were compared to those, which used the analytical sinusoidal approximation. The fatigue damage for the distinct operating points obtained with both counting methods, combined to the multiaxial stress-state and a residual stress of $\sigma_0/S_y = 0{,}20$, can be found in Table 8.14.

Table 8.14 shows that, with exception of the fatigue damage at the trailing edge near to the crown at full load, the values of D computed with the rainflow counting method were higher than those using the analytic approximation. The sophisticated approach of the rainflow counting method, dividing the alternate stresses in classes, offered the possibility to more accurately evaluate their amplitude and frequency. The analytical method was not able to appropriately resolve the complex time signal and precisely reproduce the stress variations.

In the case of part load, OP 5, OP 6 and OP 7, with the complex time signal shape caused by the draft tube instabilities (DTI), the analytic counting method resulted in too low fatigue damage values in comparison to the rainflow counting method. For example, the fatigue damage computed with the analytic counting method at the trailing edge near to the band at deep part load, OP 7, was $D = 2{,}7{\cdot}10^{-4}$ and with the rainflow method $D = 6{,}9{\cdot}10^{-4}$.

On the other hand, at full load, OP 2, OP 3 and OP 4, the fatigue damage predicted with the analytic counting method at the trailing edge near to the crown was higher than with the rainflow counting. The probable reason for it was the superposition of the slow stress variation coming from the inhomogeneous pressure distribution in the spiral case with the fast variation caused by the guide vanes passage. For the FT 80 at the trailing edge near to the crown, the contribution of the guide vane passage was in the reality not so important as the inhomogeneous spiral case pressure distribution, but, with the combination of both, the former was overestimated by the analytic counting method.

Table 8.15: Fatigue damage and stress state.

Operating Point	Cumulated Damage after 1 000 hours D (-)			
	TE-CR		TE-BD	
	Uniaxial	Multiaxial	Uniaxial	Multiaxial
OP 2 Rated	$7{,}1 \cdot 10^{-6}$	$5{,}0 \cdot 10^{-6}$	$1{,}2 \cdot 10^{-6}$	$8{,}3 \cdot 10^{-5}$
OP 3 Full load and high head	$3{,}8 \cdot 10^{-6}$	$2{,}9 \cdot 10^{-6}$	$1{,}5 \cdot 10^{-6}$	$9{,}3 \cdot 10^{-5}$
OP 4 Full load and low head	$2{,}1 \cdot 10^{-6}$	$1{,}6 \cdot 10^{-6}$	$3{,}9 \cdot 10^{-7}$	$2{,}7 \cdot 10^{-5}$
OP 5 Part load and high head	$6{,}4 \cdot 10^{-7}$	$4{,}2 \cdot 10^{-7}$	$4{,}1 \cdot 10^{-6}$	$5{,}1 \cdot 10^{-4}$
OP 6 Part load and low head	$7{,}6 \cdot 10^{-7}$	$6{,}1 \cdot 10^{-7}$	$1{,}7 \cdot 10^{-6}$	$1{,}1 \cdot 10^{-4}$
OP 7 Deep part load	$2{,}0 \cdot 10^{-4}$	$1{,}4 \cdot 10^{-4}$	$7{,}1 \cdot 10^{-6}$	$6{,}9 \cdot 10^{-4}$

Nevertheless, the results produced with both methods shared the same order of magnitude, so that if the more accurate rainflow counting results were not available, the analytic method could have been an approximation for the fatigue damage with still tolerable loss of accuracy. If the stress time history is available, the rainflow counting method should be preferred.

Fatigue Model

The fatigue life prediction relies on fatigue models, which idealise the material behaviour in relation to mean and cyclic stresses regarding the initiation of cracks. For the estimation of the fatigue damage caused by the different operating points and transient fluid flow phenomena presented before, the micro-crack approach from Wang and Brown [164] was selected. This method could take into account the multiaxial stress at the trailing edge near to the crown and band, whose dynamic stress components were not in phase. When compared to uniaxial models, this procedure should provide more accurate results for considering the general stress state and for not restricting the independent time evolution of the stress components.

For the estimation of the gain of accuracy with general multiaxial fatigue models in relation to uniaxial approaches, the Wang and Brown [164] multiaxial method was compared to the Smith, Watson and Topper [144] uniaxial model. The calculated values with both methods, considering the rainflow counting method and a residual stress of $\sigma_0/S_y = 0{,}20$, are seen in Table 8.15.

The estimated values of D revealed that the uniaxial model delivered higher fatigue damage amounts at the trailing edge near to the crown than the multiaxial method. Still, the values predicted by both models for this location were similar. At the trailing edge near to the band, the values obtained by the Smith, Watson and Topper [144] uniaxial model were too low in comparison to the Wang and Brown [164] multiaxial micro-crack approach. The probable reason for the deviations between both methods was the very pronounced multiaxial stress state at the trailing edge near to the crown and band and the nature of the stress tensor

Table 8.16: Fatigue damage and residual stress.

Operating Point		Cumulated Damage after 1 000 hours D (-)					
		TE-CR			TE-BD		
		$\frac{\sigma_0}{S_y} = 0{,}0$	$\frac{\sigma_0}{S_y} = 0{,}2$	$\frac{\sigma_0}{S_y} = 1{,}0$	$\frac{\sigma_0}{S_y} = 0{,}0$	$\frac{\sigma_0}{S_y} = 0{,}2$	$\frac{\sigma_0}{S_y} = 1{,}0$
OP 2	Rated	$2{,}2{\cdot}10^{-6}$	$5{,}0{\cdot}10^{-6}$	$2{,}3{\cdot}10^{-5}$	$3{,}9{\cdot}10^{-5}$	$8{,}3{\cdot}10^{-5}$	$3{,}7{\cdot}10^{-4}$
OP 3	Full load and high head	$1{,}4{\cdot}10^{-6}$	$2{,}9{\cdot}10^{-6}$	$1{,}2{\cdot}10^{-5}$	$4{,}3{\cdot}10^{-5}$	$9{,}3{\cdot}10^{-5}$	$4{,}0{\cdot}10^{-4}$
OP 4	Full load and low head	$8{,}3{\cdot}10^{-7}$	$1{,}6{\cdot}10^{-6}$	$6{,}8{\cdot}10^{-6}$	$1{,}3{\cdot}10^{-5}$	$2{,}7{\cdot}10^{-5}$	$1{,}1{\cdot}10^{-4}$
OP 5	Part load and high head	$4{,}0{\cdot}10^{-7}$	$4{,}2{\cdot}10^{-7}$	$1{,}1{\cdot}10^{-6}$	$1{,}9{\cdot}10^{-4}$	$5{,}1{\cdot}10^{-4}$	$6{,}5{\cdot}10^{-3}$
OP 6	Part load and low head	$2{,}5{\cdot}10^{-7}$	$6{,}1{\cdot}10^{-7}$	$2{,}2{\cdot}10^{-6}$	$4{,}9{\cdot}10^{-5}$	$1{,}1{\cdot}10^{-4}$	$7{,}1{\cdot}10^{-4}$
OP 7	Deep part load	$6{,}0{\cdot}10^{-5}$	$1{,}4{\cdot}10^{-4}$	$8{,}9{\cdot}10^{-4}$	$2{,}7{\cdot}10^{-4}$	$6{,}9{\cdot}10^{-4}$	$7{,}3{\cdot}10^{-3}$

time history, where its components were not in phase. The larger deviations in the fatigue damage values at the trailing edge near to the band, when compared to those near to the crown, were related to the higher alternate stresses at the former, increasing the importance of the dynamic component in the fatigue calculation.

If multiaxial stress data is available for the runner, it would be recommended that multiaxial stress models were used. Alternative fatigue models could be used, as the Fatemi-Socie [40] critical plane principle or other multiaxial methods as listed, for example, by Papuga [116].

Residual Stress

As discussed before, the residual stress in the turbine runner represents a source of uncertainty in the prediction of the fatigue damage. Residual stress measurements in prototype runners were already performed, as done e.g. by Sabourin et al. [133]. Though, they are still limited to a very reduced number of especial cases. Although the reported residual stress range of $\sigma_0/S_y = 0{,}10$ until $\sigma_0/S_y = 0{,}20$ seems reasonable, material properties scattering and dependency on the manufacturing process should be expected.

In order to investigate the sensibility of the fatigue damage amount to the residual stress, the fatigue evaluation was repeated for three different residual stress levels, $\sigma_0/S_y = 0{,}10$, $\sigma_0/S_y = 0{,}20$ and $\sigma_0/S_y = 1{,}00$. The results of the fatigue calculations with variable σ_0, with the rainflow counting method and with the multiaxial stress state are presented in Table 8.16.

The residual stress could significantly increase the fatigue damage amount, as it could be seen, for example, at the trailing edge near to the band at deep part load, OP 7, with values of $D = 2{,}7{\cdot}10^{-4}$, $D = 6{,}9{\cdot}10^{-4}$ and $D = 7{,}3{\cdot}10^{-3}$ for the increasing values of σ_0. There could also be identified a stronger dependency of D on σ_0 for locations and operating points with high dynamic mechanical stresses, σ_a, here at the trailing edge near to the band at part load, OP 5, OP 6 and OP 7.

With the objective of reducing the uncertainty of the residual stress in the estimation of the fatigue life, sensibility analysis towards σ_0 as done here could be integrated in the fatigue assessment process of Francis runners.

8.4.2 Turbine Operation Scenarios and Fatigue

The fatigue damage, D, caused by the different operating points and distinct transient fluid flow phenomena, can be compared between each other, with the objective to identify the most critical conditions for the considered hydraulic turbine runner. The fatigue damage can also serve as a comparison parameter in the evaluation of the relative fatigue endurance of new runner designs in relation to other alternatives or to already existing machines. The fatigue damage for different operating points and conditions can be employed as well in the estimation of the runner fatigue life.

Besides the uncertainties in the calculation of the fatigue damage as analysed before, the evaluation of the runner fatigue life brings additional sources of inaccuracy. They consist basically in the incertitude about how the hydraulic turbine will be operated when in real commercial use. Depending on the operating and energy production strategy, the machine can be submitted to very varied regimes of operation.

As example here for the estimation of the runner fatigue life, based on the numerical simulation of the transient fluid flow, transient runner structural response and fatigue damage calculation, multiple turbine operation scenarios were considered. They could illustrate the proposed procedure and provide a qualitative assessment on how the FT 80 would behave in commercial operation.

Three distinct operation scenarios were initially considered. They took into account the total operation time per year, the amount of operating hours at several operating points and the occurrence frequency of transient operating conditions.

The first scenario, described as base energy generation, reproduced typical operating conditions for a hydraulic turbine participating in the stable slightly varying energy generation as base for the electrical grid. Under this condition, the machine would be in operation almost continuously along the year, the operation at full load would be far more frequent than at part load and starts, stops and load changes would not be frequent.

The second scenario considered the turbine in operation for energy demand regulation. The hydraulic turbine would be used to quickly respond to daily variations in the electrical energy consumption. The turbine would still be most of the time of the year in operation, but with regular downtimes, when the demand would be lower. Due to energy regulation aspect, the turbine would be mainly operated at full load, but with an increasing participation of part load. Starts, stop and load changes would also be more frequent.

Table 8.17: Turbine operation scenarios for fatigue assessment.

Load Condition	Scenario 1 Base Energy Generation	Scenario 2 Energy Demand Regulation	Scenario 3 Grid Stability Regulation
Operating time per year	8 000 h	7 000 h	6 000 h
Full load participation	90%	70%	40%
OP 2 Rated	30%	20%	10%
OP 3 Full load and high head	10%	30%	25%
OP 4 Full load and low head	50%	20%	5%
Part load participation	10%	30%	60%
OP 5 Part load and high head	3%	10%	15%
OP 6 Part load and low head	5%	15%	10%
OP 7 Deep part load	2%	5%	35%
Starts and stops per day	1	2	3
Part load to optimum per day	2	4	22
Optimum to full load per day	6	12	26

The third scenario put the turbine in operation for grid stability regulation. With this operation philosophy, the hydraulic turbine would be used not only for energy demand regulation, but also for providing ancillary services to assure the electrical grid stability. The turbine would also be operated in a similar way, if used for maximising financial gains in the spot energy market. In this scenario, the turbine would count with longer downtime periods, with even longer operation at part load, especially at deep part load, and would count with numerous starts, stops and load changes. Pump-turbines are often used for this kind of scenario as well, even under more demanding conditions.

Table 8.17 lists the typical values assumed for each one of the idealised scenarios, showing the amount of operating hours per year, the participation of the different operating points in the total operating time, the number of starts and stops per day and the number of load changes from part load to optimum and from optimum to full load per day. Vortex shedding effects were considered only at full load operating conditions, in accordance with the model test observations for the FT 80. Scenario 1 counted with slow start procedure, Scenario 2 with normal and Scenario 3 with fast.

The previous fatigue damage results could be combined to estimate the total fatigue damage, D_T, for each scenario. With the Palmgren-Miner [115, 104] rule and with the operation duration or frequency for each operating point or condition, the total fatigue damage could be obtained from the combination of the individual fatigue damage, D, results. This procedure could be repeated for any other operational scenario, provided the individual fatigue damages were known. If the operational regime would be precisely known, the values taken for the scenario could be simply substituted by the actual figures and the new total fatigue damage could be evaluated.

The fatigue damage values for each operating point and operating condition were the previously calculated with the rainflow counting method, multiaxial stress state and

$\sigma_0/S_y = 0{,}20$. In the estimation of the fatigue life, the PALMGREN-MINER [115, 104] principle assumes that crack initiation occurs, when $\Sigma\, n_i/N_i = C$. For the Francis runner being analysed, the constant in the rule was taken as $C = 0{,}3$. With the total fatigue damage per year and considering the maximum admissible value of C, the expected fatigue life could be estimated.

Table 8.18 brings for Scenarios 1, 2 and 3 the fatigue damage, D, at the trailing edge near to the crown and band, originated from one year of operation under the corresponding scenario conditions for each operating point and operating condition. The participation, D/D_T, of each of them for the total fatigue damage can also be seen in Table 8.18. The total fatigue damage per year, D_T, and the expected amount of years in operation until the initiation of cracks can be found in Table 8.18 as well.

It could be observed for this high specific speed machine that, with the increasing participation in the turbine operation of part load and especially from deep part load, the total fatigue damage became considerably larger. The high participation of the deep part load operating point, OP 7, with respectively 50,9%, 71,7 and 83,3 of the total damage, D_T, at the trailing edge near to the crown and 16,8%, 22,7 and 66,3 near to the band for Scenarios 1, 2 and 3, allowed detecting that operating points with high dynamic mechanical stresses arising from high pressure pulsations in the turbine runner could severely reduce its fatigue life. Even at Scenario 1, where the participation of full load was more important and part load operation was very limited, the contribution of deep part load, OP 7, to the total fatigue damage was considerably elevated. In the case of low specific speed machines, the tendency of the total fatigue damage to be dominated by the most critical operating point would remain. However for low n_q hydraulic turbines, the critical effect for the fatigue endurance would be the rotor-stator interaction (RSI), especially at full load, and not the draft tube instabilities (DTI) at part load, as observed for the FT 80.

For the FT 80, the start procedure could reach 14,2% in the total damage participation at the trailing edge near to the crown in Scenario 3, where starts and stops were more frequent and where the fast start procedure was assumed. Scenarios 1 and 2 showed that reduced number of starts and stops as well as smoother start procedures could limit its associated total damage participation at this runner location to respectively 0,7% and 4,1%. Turbines and pump-turbines with even more unfavourable start procedures would have their runner fatigue life even more significantly affected by the fatigue damage caused by the start procedure. The remaining transient operating conditions, i.e. stop and load change, contributed only marginally to D_T. The vortex shedding effect had limited participation in the total fatigue damage as well, being not critical for the fatigue endurance.

At first glance, the amount of years in operation until crack initiation in the turbine runner was quite elevated, going from 453 years at the trailing edge near to the band at Scenario 1 down to 136 years at Scenario 3. Again, it could be observed how the operating conditions with high dynamic mechanical stresses could reduce the runner fatigue endurance. The fatigue life calculations counted with the uncertainties relative to the fatigue analysis and assumed the hypothesis of healthy

Table 8.18: Fatigue damage and fatigue life for different scenarios.

Trailing Edge at Crown		Cumulated Damage per Year					
		Scenario 1 Base Energy Generation		Scenario 2 Energy Demand Regulation		Scenario 3 Grid Stability Regulation	
		D (-)	D/D_T (%)	D (-)	D/D_T (%)	D (-)	D/D_T (%)
OP 2	Rated	$1{,}2{\cdot}10^{-5}$	27,0	$7{,}0{\cdot}10^{-6}$	10,1	$3{,}0{\cdot}10^{-6}$	0,8
OP 3	Full load and high head	$2{,}4{\cdot}10^{-6}$	5,3	$6{,}2{\cdot}10^{-6}$	8,9	$4{,}4{\cdot}10^{-6}$	1,2
OP 4	Full load and low head	$6{,}3{\cdot}10^{-6}$	14,0	$2{,}2{\cdot}10^{-6}$	3,2	$4{,}7{\cdot}10^{-7}$	0,1
OP 5	Part load and high head	$1{,}0{\cdot}10^{-7}$	0,2	$2{,}9{\cdot}10^{-7}$	0,4	$3{,}8{\cdot}10^{-7}$	0,1
OP 6	Part load and low head	$2{,}4{\cdot}10^{-7}$	0,5	$6{,}4{\cdot}10^{-7}$	0,9	$3{,}6{\cdot}10^{-7}$	0,1
OP 7	Deep part load	$2{,}3{\cdot}10^{-5}$	50,9	$5{,}0{\cdot}10^{-5}$	71,7	$3{,}0{\cdot}10^{-4}$	83,3
	Start	$3{,}3{\cdot}10^{-7}$	0,7	$2{,}8{\cdot}10^{-6}$	4,1	$5{,}1{\cdot}10^{-5}$	14,2
	Stop	$3{,}5{\cdot}10^{-8}$	0,1	$7{,}1{\cdot}10^{-8}$	0,1	$1{,}1{\cdot}10^{-7}$	$\ll 0{,}1$
	Part load to optimum	$7{,}3{\cdot}10^{-13}$	$\ll 0{,}1$	$1{,}5{\cdot}10^{-12}$	$\ll 0{,}1$	$8{,}0{\cdot}10^{-12}$	$\ll 0{,}1$
	Optimum to full load	$2{,}2{\cdot}10^{-12}$	$\ll 0{,}1$	$4{,}4{\cdot}10^{-12}$	$\ll 0{,}1$	$9{,}5{\cdot}10^{-12}$	$\ll 0{,}1$
	Vortex shedding effect	$5{,}6{\cdot}10^{-7}$	1,2	$3{,}8{\cdot}10^{-7}$	0,5	$1{,}9{\cdot}10^{-7}$	0,1
Total Damage, D_T (-)		$4{,}5{\cdot}10^{-5}$		$6{,}9{\cdot}10^{-5}$		$3{,}6{\cdot}10^{-4}$	
Years until crack initiation		6 704		4 319		836	

Trailing Edge at Band		Cumulated Damage per Year					
		Scenario 1 Base Energy Generation		Scenario 2 Energy Demand Regulation		Scenario 3 Grid Stability Regulation	
		D (-)	D/D_T (%)	D (-)	D/D_T (%)	D (-)	D/D_T (%)
OP 2	Rated	$2{,}0{\cdot}10^{-4}$	30,1	$1{,}2{\cdot}10^{-4}$	10,8	$5{,}0{\cdot}10^{-5}$	2,3
OP 3	Full load and high head	$7{,}5{\cdot}10^{-5}$	11,3	$2{,}0{\cdot}10^{-4}$	18,3	$1{,}4{\cdot}10^{-4}$	6,4
OP 4	Full load and low head	$1{,}1{\cdot}10^{-4}$	16,4	$3{,}8{\cdot}10^{-5}$	3,5	$8{,}1{\cdot}10^{-6}$	0,4
OP 5	Part load and high head	$1{,}2{\cdot}10^{-4}$	18,6	$3{,}6{\cdot}10^{-4}$	33,5	$4{,}6{\cdot}10^{-4}$	20,9
OP 6	Part load and low head	$4{,}5{\cdot}10^{-5}$	6,8	$1{,}2{\cdot}10^{-4}$	11,0	$6{,}8{\cdot}10^{-5}$	3,1
OP 7	Deep part load	$1{,}1{\cdot}10^{-4}$	16,8	$2{,}4{\cdot}10^{-4}$	22,7	$1{,}5{\cdot}10^{-3}$	66,3
	Start	$8{,}8{\cdot}10^{-8}$	$\ll 0{,}1$	$6{,}2{\cdot}10^{-7}$	0,1	$1{,}6{\cdot}10^{-5}$	0,7
	Stop	$1{,}4{\cdot}10^{-8}$	$\ll 0{,}1$	$2{,}9{\cdot}10^{-8}$	$\ll 0{,}1$	$4{,}3{\cdot}10^{-8}$	$\ll 0{,}1$
	Part load to optimum	$7{,}3{\cdot}10^{-13}$	$\ll 0{,}1$	$1{,}5{\cdot}10^{-12}$	$\ll 0{,}1$	$8{,}0{\cdot}10^{-12}$	$\ll 0{,}1$
	Optimum to full load	$2{,}4{\cdot}10^{-10}$	$\ll 0{,}1$	$4{,}9{\cdot}10^{-10}$	$\ll 0{,}1$	$1{,}1{\cdot}10^{-9}$	$\ll 0{,}1$
	Vortex shedding effect	$9{,}6{\cdot}10^{-7}$	0,1	$6{,}5{\cdot}10^{-7}$	0,1	$3{,}2{\cdot}10^{-7}$	$\ll 0{,}1$
Total Damage, D_T (-)		$6{,}6{\cdot}10^{-4}$		$1{,}1{\cdot}10^{-3}$		$2{,}2{\cdot}10^{-3}$	
Years until crack initiation		453		280		136	

material, i.e. free of manufacturing defects. As exemplified by Brekke [21], Francis runners might fail after few hours of operation in the case of critical crack growth conditions, associated to poor manufacturing and aggressive design. To minimise the probability of failures, the calculated expected fatigue life of new runner designs could be compared to those of proofed existing designs. Anyway, the absolute value of the predicted fatigue life can give an indication of the risk of crack failure during the runner projected life.

To investigate the sensibility of the runner fatigue life to the stress levels, three additional scenarios were considered. Scenarios 4, 5 and 6 were based on the intermediate Scenario 2, energy demand regulation. Scenario 4 investigates the influence of the residual stress, σ_0, on the fatigue damage and fatigue life. With $\sigma_0/S_y = 0{,}50$, it simulates the effect of poor manufacturing processes on the runner fatigue endurance. Scenarios 5 and 6 respectively considered mean and alternate stresses 1,5 times larger than those actually actuating in the FT 80. Both simulated the impact of aggressive design on the fatigue damage. The higher dynamic mechanical stresses in Scenario 6 could have been produced by low structural strength of the runner or by elevated pressure oscillation amplitudes. Besides the investigation of these conditions, Scenarios 4, 5 and 6 could also be interpreted as sensibility analysis for the stress parts towards uncertainties.

The fatigue assessment results for Scenarios 4, 5 and 6 can be found in Table 8.19. The table is analogous to the one with the results for Scenarios 1, 2 and 3.

In Scenarios 4 and 5, the residual stress and the static mechanical stress, produced by the time-averaged pressure load, had the effect of increasing the mean stress, σ_m. It could be noticed that the dominance of the operating points with higher alternate stress, σ_a, here part load and high head, OP 5, and deep part load, OP 7, was increased in the total damage participation.

More important was the effect of the increased stress on the total fatigue damage and expected fatigue life. The expected amount of years until crack initiation was clearly reduced in all three additional scenarios. In Scenario 5, the increase of the static mechanical stresses, induced by the time-averaged pressure load, had limited influence on reducing the fatigue life, when compared to the other stress parts. It showed that the higher static pressure levels on the runner blades could not importantly reduce its fatigue endurance. The increase of the residual stress, σ_0, in Scenario 4, was responsible for significantly reducing the runner fatigue life. At the trailing edge near to the band, the expected fatigue life would have been shortened to 30 years, which would be often lower than the desired useful life of hydraulic turbines. There could be seen that low quality material or manufacturing processes might negatively impact the runner fatigue endurance. Scenario 6, considered higher dynamic mechanical stresses, σ_a, with the effect of importantly reducing the runner fatigue life. At the trailing edge near to the band, the critical location, the expected amount of years until crack initiation dropped to no more than 17 years. This value would not be acceptable for the turbine commercial operation. Scenario 6, could emphasise the decisive effect of high dynamic mechanical stresses, caused by high pressure pulsations in the runner or by low-strength runner structures, on the reduction of the runner useful life. This kind of sensibility analysis, together with the fatigue assessment procedure, could be incorporated in the fatigue assessment of Francis runners.

Possible critical conditions would be, for example, the combination of Scenarios 4 and 6, i.e. the occurrence of high residual stress and high dynamic mechanical stress. This would represent, among others, the association of poor manufacturing process

Table 8.19: Fatigue damage and fatigue life for additional scenarios.

Trailing Edge at Crown		Cumulated Damage per Year					
		Scenario 4 High Residual Stress		Scenario 5 High Mean Stress		Scenario 6 High Alternate Stress	
		D (-)	D/D_T (%)	D (-)	D/D_T (%)	D (-)	D/D_T (%)
OP 2	Rated	$3{,}2{\cdot}10^{-5}$	8,0	$9{,}3{\cdot}10^{-6}$	9,1	$4{,}1{\cdot}10^{-5}$	7,5
OP 3	Full load and high head	$2{,}5{\cdot}10^{-5}$	6,3	$8{,}0{\cdot}10^{-6}$	7,8	$3{,}3{\cdot}10^{-5}$	5,9
OP 4	Full load and low head	$9{,}5{\cdot}10^{-6}$	2,4	$2{,}7{\cdot}10^{-6}$	2,6	$1{,}4{\cdot}10^{-5}$	2,6
OP 5	Part load and high head	$7{,}6{\cdot}10^{-7}$	0,2	$2{,}9{\cdot}10^{-7}$	0,3	$9{,}3{\cdot}10^{-7}$	0,2
OP 6	Part load and low head	$2{,}3{\cdot}10^{-6}$	0,6	$7{,}8{\cdot}10^{-7}$	0,8	$2{,}9{\cdot}10^{-6}$	0,5
OP 7	Deep part load	$3{,}1{\cdot}10^{-4}$	78,6	$8{,}0{\cdot}10^{-5}$	77,9	$4{,}4{\cdot}10^{-4}$	79,7
	Start	$1{,}1{\cdot}10^{-5}$	2,9	$9{,}2{\cdot}10^{-7}$	0,9	$1{,}2{\cdot}10^{-5}$	2,2
	Stop	$8{,}5{\cdot}10^{-7}$	0,2	$1{,}1{\cdot}10^{-7}$	0,1	$1{,}1{\cdot}10^{-6}$	0,2
	Part load to optimum	$3{,}4{\cdot}10^{-10}$	$\ll 0{,}1$	$1{,}5{\cdot}10^{-12}$	$\ll 0{,}1$	$1{,}5{\cdot}10^{-12}$	$\ll 0{,}1$
	Optimum to full load	$5{,}7{\cdot}10^{-10}$	$\ll 0{,}1$	$4{,}4{\cdot}10^{-12}$	$\ll 0{,}1$	$4{,}4{\cdot}10^{-12}$	$\ll 0{,}1$
	Vortex shedding effect	$3{,}7{\cdot}10^{-6}$	0,9	$5{,}7{\cdot}10^{-7}$	0,6	$6{,}8{\cdot}10^{-6}$	1,2
Total Damage, D_T (-)		$4{,}0{\cdot}10^{-4}$		$1{,}0{\cdot}10^{-4}$		$5{,}5{\cdot}10^{-4}$	
Years until crack initiation		756		2 934		544	

Trailing Edge at Band		Cumulated Damage per Year					
		Scenario 4 High Residual Stress		Scenario 5 High Mean Stress		Scenario 6 High Alternate Stress	
		D (-)	D/D_T (%)	D (-)	D/D_T (%)	D (-)	D/D_T (%)
OP 2	Rated	$5{,}1{\cdot}10^{-4}$	5,2	$1{,}6{\cdot}10^{-4}$	10,4	$6{,}9{\cdot}10^{-4}$	3,9
OP 3	Full load and high head	$8{,}4{\cdot}10^{-4}$	8,5	$2{,}6{\cdot}10^{-4}$	17,1	$1{,}1{\cdot}10^{-3}$	6,4
OP 4	Full load and low head	$1{,}6{\cdot}10^{-4}$	1,6	$4{,}8{\cdot}10^{-5}$	3,2	$2{,}2{\cdot}10^{-4}$	1,2
OP 5	Part load and high head	$4{,}6{\cdot}10^{-3}$	46,5	$5{,}1{\cdot}10^{-4}$	34,0	$9{,}8{\cdot}10^{-3}$	55,0
OP 6	Part load and low head	$7{,}5{\cdot}10^{-4}$	7,6	$1{,}5{\cdot}10^{-4}$	10,3	$1{,}4{\cdot}10^{-3}$	7,8
OP 7	Deep part load	$2{,}6{\cdot}10^{-3}$	26,1	$3{,}7{\cdot}10^{-4}$	24,9	$4{,}6{\cdot}10^{-3}$	25,6
	Start	$2{,}7{\cdot}10^{-6}$	$\ll 0{,}1$	$2{,}6{\cdot}10^{-7}$	$\ll 0{,}1$	$3{,}0{\cdot}10^{-6}$	$\ll 0{,}1$
	Stop	$2{,}3{\cdot}10^{-7}$	$\ll 0{,}1$	$4{,}0{\cdot}10^{-8}$	$\ll 0{,}1$	$4{,}6{\cdot}10^{-7}$	$\ll 0{,}1$
	Part load to optimum	$2{,}4{\cdot}10^{-10}$	$\ll 0{,}1$	$1{,}5{\cdot}10^{-12}$	$\ll 0{,}1$	$1{,}5{\cdot}10^{-12}$	$\ll 0{,}1$
	Optimum to full load	$1{,}5{\cdot}10^{-9}$	$\ll 0{,}1$	$6{,}3{\cdot}10^{-10}$	$\ll 0{,}1$	$7{,}3{\cdot}10^{-9}$	$\ll 0{,}1$
	Vortex shedding effect	$4{,}3{\cdot}10^{-4}$	4,4	$9{,}1{\cdot}10^{-7}$	0,1	$1{,}1{\cdot}10^{-5}$	0,1
Total Damage, D_T (-)		$9{,}9{\cdot}10^{-3}$		$1{,}5{\cdot}10^{-3}$		$1{,}8{\cdot}10^{-2}$	
Years until crack initiation		30		200		17	

to aggressive runner mechanical or hydraulic design. In unfavourable cases, it could lead to rapid runner fatigue crack failures. High quality manufacturing, stress relief, conservative design and accurate numerical design process, as proposed here, could positively contribute to more safety for new runner designs towards useful life and reliable operation.

Chapter 9

Conclusion

The pressure oscillations induced by the transient fluid flow through Francis turbines are at the origin of mechanical stresses in the runner, which in extreme cases may lead to structural failures through fatigue crack initiation and propagation, affecting the machine reliable operation. This study could successfully propose a procedure to numerically calculate the pressure pulsations in Francis turbines and the mechanical stresses in the runner caused by them, offering the basis for the fatigue life prediction. As example for the proposed methodology, a real high specific speed Francis machine, FT 80, that has been in operation since years, was chosen together with full load, part load and deep part load operating conditions.

The accuracy in the numerical simulation of the transient fluid flow was of main importance for the reliable estimation of the dynamic mechanical stresses and fatigue damage in the runner. The employed finite volume (FV) model for the numerical calculations of the fluid flow through the Francis turbine considered the complete machine and made use of hybrid turbulence models, as detached eddy simulation (DES) and scale adaptive simulation (SAS). The numerical results could be compared with available model test data and were able to offer very tight agreement with the experimental values, concerning basic performance data and pressure oscillation amplitude.

The numerical fluid flow investigations showed that the turbulence models were of great importance for accurate transient simulations. The DES and SAS turbulence models could deliver much superior numerical results than the unsteady Reynolds-averaged Navier-Stokes (URANS) equations, when compared to the experimental data. These more sophisticated turbulence models, DES and SAS, were able to avoid the introduction of excessive artificial dissipation through the turbulent viscosity in the fluid flow. In the case of draft tube instabilities (DTI), this allowed the large vortical structures under the runner and in the draft tube cone to properly develop in the transient simulation. As long as the dynamic fluid flow effects were responsible for the pressure pulsations and consequently for the dynamic mechanical stresses, the more precise numerical flow calculation with DES and SAS could improve the accuracy of the complete process.

In the simulations carried out here, the DES and SAS turbulence models presented similar precision when confronted to the large eddy simulation (LES), with the important advantage for industrial applications of being computationally more efficient, with much shorter simulation times. The DES and SAS turbulence models delivered results with similar accuracy between them for the investigated hydraulic turbine. Both models require knowledge of the fluid flow problem being analysed, in order to assure accuracy and reasonable computational costs. The application of the DES and SAS turbulence models to the transient fluid flow computations allowed precisely reproducing the rotor-stator interaction (RSI), draft tube instabilities (DTI), higher part load (HPL) and runner channel vortices (RCV) for the FT 80.

The time-averaged and transient pressure fields at the runner obtained by the CFD analysis were used as input for the finite element analysis (FEA) of the runner structure, with the objective of determining the static and dynamic mechanical stresses. The dynamic pressure field from the CFD analysis was stored for each individual calculated time step and could be used as pressure load at each time step of the finite element analysis (FEA). This offered the possibility to avoid all kind of simplifications, regarding the dynamic pressure load produced by the pressure pulsations, in the runner transient structural simulation. With the pressure time history available for every location at every time step, the direct time integration method could be employed. This brought the advantage of suppressing all restrictions in the dynamic behaviour of the runner structure.

The availability of accurate CFD data for every time step could improve the precision in the prediction of the dynamic mechanical stresses. The runner finite element analysis (FEA) with reliable pressure load input could deliver absolutely new knowledge about the influence of dynamic fluid flow phenomena, as rotor-stator interaction (RSI), draft tube instabilities (DTI), higher part load (HPL) and runner channel vortex (RCV), on its structural response and dynamic mechanical stresses. This allowed the gain of dynamic mechanical information about the FT 80 runner at full load, part load and deep part load operating conditions.

The precise transient structural evaluation of the runner produced more accurate data for the fatigue analysis. The static and dynamic mechanical stresses from the finite element (FE) computations were used as data for the fatigue assessment. The fatigue analysis counts with inherent uncertainties, due to its statistical nature, material models and scattering of material properties. The procedure carried out here could reduce the uncertainties regarding the mean and alternate stresses. Still, other types of incertitude remained, as the residual stress level in the runner and the real operation history of the hydraulic turbine when in commercial operation. Parameter sensibility analysis and the consideration of different turbine operation scenarios could reduce the importance of these shortcomings.

The fatigue analysis showed that especially high residual and alternate stress levels could significantly reduce the runner fatigue endurance. High residual stresses might be the consequence of poor manufacturing processes, while high alternate stresses might have their origin at high pressure oscillation amplitudes and low-strength

runner structure, as result of much too aggressive design. The combination of these critical conditions could explain part of the fatigue crack failures reported in Francis turbines. High quality manufacturing processes and material, sensible hydraulic and mechanical design as well as accurate analysis procedures, as presented here, can increase the operational safety of Francis turbine runners.

Further Developments

The developments achieved here in the transient simulation of the fluid flow through Francis hydraulic turbines can serve as base for additional advances in the numerical study of dynamic phenomena in hydraulic turbines. The procedure presented here for the FT 80 at full load, part load and deep part load could be repeated for any other Francis machine and operating point. Especially interesting would be the simulation of extreme operating conditions as speed-no-load (SNL). With the increment of computational power, this methodology could be incorporated in the future into the industrial analysis and design of Francis turbines. The application range of this method in the numerical prediction of transient fluid flow effects could be extended to other reaction-type hydraulic machines as pumps and pump-turbines. In the case of pumps and pump-turbines, this procedure could increase the accuracy in the prediction of pump and S-shape instabilities.

The application range of the method proposed here could be extended and its accuracy even further improved with the introduction of cavitation models. This could increase the precision in the simulation of operating points with significant cavitating regions in the fluid flow, as for example in off-design operating conditions as e.g. speed-no-load. The introduction of cavitation models would be necessary for the computational simulation of overload operating conditions, where full load instability takes place, arising from the pulsating cavitating vortex torch.

The numerical flow calculation of transient operating conditions, as start and stop procedures, load rejection and load change, could be carried out with the usage of moving meshes for the fluid volume mesh around the guide vanes.

New possibilities in the operation of Francis turbines, more precisely the active flow control, could be numerically tested, employing the procedure used here, before the application in the prototype. The study of the active flow control in Francis machines was already initiated by Wunderer and Schilling [171] and Magnoli and Schilling [91, 90] and could be the base for new developments.

Concerning the numerical structural calculations, the accuracy in the prediction of the runner dynamic mechanical stresses could be further improved with the adoption of the two-way coupled fluid-structure interaction (FSI) for the turbine runner. The method discussed here for the determination of the dynamic loads caused by the fluid flow and their application in the fatigue assessment could be extended to other hydraulic turbine components subjected to transient fluid flow phenomena.

Bibliography

[1] Algifri, A. H., Bhardwaj, R. K., and Rao, Y. V. N. Eddy viscosity in decaying swirl flow in a pipe. *Applied Scientific Research 45*, 4 (1988), 287–302.

[2] Alligné, S., Maruzewski, P., Dinh, T., Wang, B., Fedorov, A., Iosfin, J., and Avellan, F. Prediction of a Francis turbine prototype full load instability from investigations on the reduced scale model. In *Proceedings of the 25th IAHR Symposium* (Timisoara, Romania, 2010).

[3] American Society of Mechanical Engineers (ASME). *ASME Boiler and Pressure Vessel Code, Section VIII, Division 3.* ASME, New York, NY, USA, 2010.

[4] ANSYS, Inc. ANSYS-CFX Release 11.0, 2006.

[5] ANSYS, Inc. ANSYS-Structural Release 11.0, 2006.

[6] ANSYS, Inc. ICEM-CFD Release 11.0, 2006.

[7] Antonsen, Ø. Ustabile driftsområder for Francisturbiner. Tech. rep., Norges Teknisk- Naturvitenskaplige Universitet, Trondheim, Norway, 2005.

[8] Aoki, S. Dynamic characteristic of welded structures. *Nuclear Engineering and Design*, 160 (1996), 379–385.

[9] Arora, P., Goyal, S., Gupta, S. K., Khan, M. A., Bhasin, V., Sivaprasad, S., Tarafdar, S., Vaze, K. K., Ghosh, A. K., and Kushwaha, H. S. Multiaxial Non-Proportional Fatigue and Ratcheting Studies on PHT Piping Material of Indian PHWRs. In *36th MPA-Seminar* (Stuttgart, Germany, 2010).

[10] Ausoni, P. Etude du mécanisme de génération des tourbillons de von Kármán et de leurs interactions avec la structure. Tech. rep., Ecole Polytechnique Fédérale de Lausanne, Lausanne, Switzerland, 2004.

[11] Avellan, F. Introduction to Cavitation in Hydraulic Machinery. In *6th International Conference on Hydraulic Machinery and Hydrodynamics* (Timisoara, Romania, 2004).

[12] Avellan, F., Etter, S., Gummer, J. H., and Seidel, U. Dynamic Pressure Measurements on a Model Turbine Runner and their Use in preventing Runner Fatigue Failure. In *Proceedings of the 20th IAHR Symposium* (Charlotte, North Carolina, USA, 2000).

[13] Bathe, K. J. *Finite Element Procedures*. Prentice-Hall, Englewood Cliffs, New Jersey, USA, 1996.

[14] Benigni, H., Jaberg, H., Lampl, J., and Franz, E. Transient numerical simulation of a horizontal shaft tube bulb turbine. In *HYDRO 2007* (Granada, Spain, 2007).

[15] Bhave, S. K., Murthy, C. B., and Goyal, S. K. Investigation into blade failures of Francis turbines. *International Water Power and Dam Construction 38*, 1 (1986), 37–39.

[16] Bjørndal, H., Moltubakk, T., and Aunemo, H. Flow induced stresses in a medium head Francis runner – Strain gauge measurements in an operating plant and comparison with Finite Element Analysis. In *10th International Meeting of the Work Group on the Behaviour of Hydraulic Machinery under steady oscillatory conditions* (Trondheim, Norway, 2001).

[17] Blevins, R. D. *Flow-induced vibration*, 2nd ed. Krieger Publishing Co., Malabar, Florida, USA, 1990.

[18] Bosch, G., and Rodi, W. Simulation of vortex shedding past a square cylinder with different turbulence models. *International Journal for Numerical Methods in Fluids 28*, 4 (1998), 601–616.

[19] Boussinesq, J. Théorie de l'écoulement Tourbillant. *Mémoires présentés par Divers Savants à l'Académie des Sciences de l'Institut de France*, 23 (1877), 46–50.

[20] Brandt, A. Multigrid techniques: 1984 guide with applications to fluid dynamics. Tech. Rep. GMD-Studien Nr. 85, Gesellschaft für Mathematik und Datenverarbeitung (GMD), Bonn, Deutschland, 1984.

[21] Brekke, H. Life time and safety of hydro turbines. In *HYDRO 2009* (Lyon, France, 2009).

[22] Brekke, H. Performance and safety of hydraulic turbines. In *Proceedings of the 25th IAHR Symposium* (Timisoara, Romania, 2010).

[23] Chakravarthy, S. R., and Osher, S. High resolution applications of the OSHER upwind scheme for the Euler equations. Tech. Rep. Paper 83-1943, AIAA, San Diego, California, USA, 1983.

[24] Chapman, D. R., and Kuhn, G. D. The limiting behaviour of turbulence near a wall. *Journal of Fluid Mechanics*, 170 (1986), 265–292.

[25] Chen, Y. S., and Kim, S. Computation of the turbulent flows using an extended k-ϵ turbulence closure model. Tech. Rep. CR-179204, NASA, 1987.

[26] Chien, K. Y. Predictions of Channel and Boundary-Layer Flows with a Low-Reynolds-Turbulence Model. *AIAA Journal 20*, 1 (1982), 33–38.

[27] Ciocan, G. D., Mombelli, H. P., and Avellan, F. Instabilités des Turbines Francis: Essais et Mesures détaillés sur modèle réduit. In *Conférence Internationale Énergie-Environnement, CIEM 2003* (Bucarest, Romania, 2003).

[28] Coutu, A., Proulx, D., Coulson, S., and Demers, A. Dynamic Assessment of Hydraulic Turbines. In *Proceedings of HydroVision 2004* (Montréal, Québec, Canada, 2004).

[29] Cowper, G. R. Gaussian quadrature formulas for triangles. *Int. J. Num. Mech. Eng. 7*, 3 (1973), 405–408.

[30] Dassault Systèmes. CATIA V5 Release 16, 2005.

[31] Davidson, L. Evaluation of the SST-SAS Model: Channel Flow, Asymmetric Diffuser and Axi-symmetric Hill. In *European Conference on Computational Fluid Dynamics ECCOMAS CFD 2006, Egmond aan Zee, The Netherlands* (Delft, Netherlands, 2006), P. Wesseling, E. Oñate, and J. Périaux, Eds., TU Delft.

[32] Deardorff, J. W. A Numerical Study of Three-Dimensional Turbulent Channel Flow at Large Reynolds Numbers. *Journal of Fluid Mechanics*, 41 (1970), 453–480.

[33] Demirdžić, I., Lilek, Ž., and Perić, M. A colocated finite volume method for predicting flows at all speeds. *International Journal of Numerical Methods in Fluids*, 16 (1993), 1029–1050.

[34] Demuren, A. O. Calculation of Turbulence-Driven Secondary Motion in Ducts with Arbitrary Cross Section. *AIAA Journal 29*, 4 (1991), 531–537.

[35] Dörfler, P. On the phase role of phase resonance in vibrations caused by blade passage in radial hydraulic turbomachines. In *Proceedings of the 12th IAHR Symposium* (Stirling, UK, 1984), pp. 227–241.

[36] Einzinger, J. *Numerische Simulation der Fluid-Struktur-Interaktion in Turbomaschinen* . PhD thesis, Technische Universität München, Lehrstuhl für Hydraulische Maschinen und Anlagen, 2006.

[37] Ergatoudis, J. G., Irons, B. M., and Zienkiewicz, O. C. Curved, isoparametric, quadrilateral elements for finite element analysis. *Int. J. Solids Struct.*, 4 (1968), 31–42.

[38] Farhat, M., Avellan, F., and Seidel, U. Pressure Fluctuation Measurements in Hydro Turbine Models. In *Proceedings of the 9th Symposium on Transport Phenomena and Dynamics of Rotating Machinery* (Honolulu, Hawaii, USA, 2002).

[39] Farhat, M., Natal, S., Avellan, F., Paquet, F., Lowys, P. Y., and Couston, M. Onboard Measurements of Pressure and Strain Fluctuations in a Model of low Head Francis Turbines. In *Proceedings of the 21st IAHR Symposium* (Lausanne, Switzerland, 2002).

[40] Fatemi, A., and Socie, D. F. A critical plane approach to multiaxial fatigue damage including out-of-phase loading. *Fatigue and Fracture of Engineering Materials and Structures 11*, 3 (1988), 149–165.

[41] Favré, A. Equations des Gaz Turbulents Compressibles. *Journal de Mécanique 4*, 3 (1965), 361–390.

[42] Ferziger, J. H. Large Eddy Numerical Simulations of Turbulent Flows. Tech. Rep. Paper 76-347, AIAA, San Diego, California, USA, 1976.

[43] Ferziger, J. H., and Perić, M. *Computational Methods for Fluid Dynamics*, 3rd ed. Springer-Verlag, Berlin, Germany, 2002.

[44] Fisher, R., Seidel, U., Grosse, G., Gfeller, W., and Klinger, R. A Case Study in Resonant Hydroelastic Vibration: The Causes of Runner Cracks and the Solutions Implemented for the Xiaolangdi Hydroelectric Project. In *Proceedings of the 21st IAHR Symposium* (Lausanne, Switzerland, 2002).

[45] Flurl, B. *Ein modulares Verfahren zur Simulation von Mehrfeldproblemen in Strömungsmaschinen*. PhD thesis, Technische Universität München, Lehrstuhl für Hydraulische Maschinen und Anlagen, 2011.

[46] Franc, J. P., Avellan, F., Belhadji, B., Billard, J. Y., Marjolet, L. B., Fréchou, D., Fruman, D. H., Karimi, A., Kueny, J. L., and Michel, J. M. *La Cavitation: Mécanismes Physiques et Aspects Industriels*. Presse Universitaires de Grenoble, Grenoble, France, 1995.

[47] Fröhlich, J., and Rodi, W. *Introduction to Large-Eddy Simulation of turbulent flows*. Cambridge University Press, 2000, ch. 8, pp. 267–298.

[48] Gagné, J.-L., and Coulson, D. M. Measurement of turbine runner strains on a high specific speed Francis unit in service. In *Proceedings of the 14th IAHR Symposium* (Trondheim, Norway, 2004).

[49] Gagnon, M., Tahan, S. A., Bocher, P., and Thibault, D. Impact of startup scheme on Francis runner life expectancy. In *Proceedings of the 25th IAHR Symposium* (Timisoara, Romania, 2010).

[50] Gaskell, P. H., and Lau, A. K. C. Curvature-compensated convective transport: SMART, a new boundedness-preserving transport algorithm. *International Journal of Numerical Methods in Fluids 8*, 6 (1988), 617–641.

[51] Gatski, T. B., and Speziale, C. G. On explicit algebraic stress models for complex turbulent flows. *Journal of Fluid Mechanics*, 254 (1993), 59–78.

[52] Geradin, M., and Kill, N. A new approach to finite element modelling of flexible rotors. *Engineering Computations*, 1 (1984), 52–64.

[53] Germano, M., Piomelli, U., Moin, P., and Cabot, W. A Dynamic Subgrid-Scale Eddy Viscosity Model. *Physics of Fluids A*, 3 (1991), 1760.

[54] Glinka, G., and Buczynski, A. Elastic-plastic stress-strain analysis of notches under non-proportional cyclic loading paths. In *Proceedings of the 5th International Conference on Biaxial/Multiaxial Fatigue and Fracture* (Cracow, Poland, 1997).

[55] Grimes, R. G., Lewis, J. G., and Simon, H. D. A Shifted Block Lanczos Algorithm for Solving Sparse Symmetric Generalized Eigenproblems. *SIAM Journal Matrix Analysis Applications 15*, 1 (1996), 228–272.

[56] Guillaume, R., Deniau, J. L., Scolaro, D., and Colombet, C. Influence of the rotor-stator interaction on the dynamic stresses of Francis runners. In *Proceedings of the 26th IAHR Symposium* (Beijing, China, 2012).

[57] Gummer, H., and Hensman, P. C. A review of stayvane cracking in hydraulic turbines. *Water Power and Dam Construction*, 44 (1992), 32–42.

[58] Guo, D., Chu, F. L., and Zheng, Z. C. The Influence of rotation on vibration of a thick cylindrical shell. *Journal of Sound and Vibration*, 242 (2001), 487–505.

[59] Hackbusch, W. Parabolic multi-grid methods. In *Computing Methods in Applied Sciences and Engineering* (Amsterdam, Netherlands, 1984), R. Glowinski and J. R. Lions, Eds., North-Holland.

[60] Haigh, B. P. Report on alternating stress tests of sample of mild steel. Tech. rep., British Association Stress Committee, Manchester, UK, 1915.

[61] Hammer, P. C., Marlowe, O. P., and Stroud, A. H. Numerical integration over simplexes and cones. *Math. Tables Aids Comp. 10*, 55 (1956), 130–137.

[62] Harten, A. High resolution schemes for hyperbolic conservation laws. *Journal of Computational Physics 49*, 3 (1983), 357–393.

[63] Hasmatuchi, V., and Avellan, F. Hydrodynamics of a Pump-Turbine Operation at Off-Design Conditions in Generating Model. In *SimHydro 2012 – New frontiers of simulation* (Nice, France, 2012).

[64] Henry, P. *Turbomachines hydrauliques: Choix illustré de réalisations marquantes*, 1st ed. Presses Polytechniques et Universitaires Romandes, Lausanne, Suisse, 1992.

[65] Huang, P. G., Coleman, G. N., and Bradshaw, P. Compressible turbulent channel flows. *Journal of Fluid Mechanics*, 305 (1995), 185–218.

[66] Huth, H. J. *Fatigue Design of Hydraulic Turbine Runners*. PhD thesis, Norges Teknisk- Naturvitenskaplige Universitet, Trondheim, Norway, 2005.

[67] International Electrotechnical Commission (IEC). *Hydraulic turbines, storage pumps and pump-turbines – Model acceptance tests*, 2nd ed. IEC, Genf, Schweiz, 1999.

[68] Issa, R. I. Solution of implicitly discretized fluid flow equations by operator-splitting. *Journal of Computational Physics*, 62 (1986), 40–65.

[69] Jeong, J., and Hussain, F. On the Identification of a Vortex. *Journal of Fluid Mechanics*, 285 (1995), 69–94.

[70] Jones, W. P., and Launder, B. E. The Prediction of Laminarization with a Two-Equation Model of Turbulence. *International Journal of Heat and Mass Transfer*, 15 (1972), 301–314.

[71] Keck, H., Drtina, P., and Sick, M. A Breakthrough – CFD Flow Simulation for a Complete Turbine. *Sulzer Technical Review*, 1 (1997).

[72] Keck, H., Weiss, T., Michler, W., and Sick, M. Recent Developments in the Dynamic Analysis of Water Turbines. In *2nd IAHR International Meeting of the Workgroup on Cavitation and Dynamic Problems in Hydraulic Machinery and Systems* (Timisoara, Romania, 2007).

[73] Kinsler, E. L. *Fundamentals of Acoustics*. John Wiley & Sons, New York, NY, USA, 1982.

[74] Koutnik, J., Faigle, P., and Moser, W. Pressure Fluctutations in Francis Turbines – Theoretical Prediction and Impact on Turbine. In *Proceedings of the 24th IAHR Symposium* (Foz do Iguaçu, Brazil, 2008).

[75] Koutnik, J., Krüger, J., Pochlý, F., Rudolf, P., and Habán, V. On cavitating vortex rope form stability during Francis turbine part load operation. In *1st Meeting of the IAHR International Workgroup on Cavitation and Dynamic Problems in Hydraulic Machines and Systems* (Barcelona, Spain, 2006).

[76] Kroll, N. Berechnung von Strömungsfeldern um Propeller und Rotoren im Schwebeflug durch die Lösung der Euler-Gleichungen. Forschungsbericht 89-37, Deutsche Forschungsanstalt für Luft- und Raumfahrt, Institut für Entwurfsaerodynamik, Braunschweig, Germany, June 1989.

[77] Kuntz, M., Garcin, H., Guedes, A., Menter, F., Parkinson, E., and Kueny, J. L. Developments of CFX-TASCflow for unsteady rotor-stator simulations in the frame of the European project HPNURSA. In *CFX Users Conference 2000* (Munich, Germany, 2000).

[78] Lam, C. K. G., and Bremhorst, K. A. Modified form of the k-ϵ Model for Predicting Wall Turbulence. *ASME Journal of Fluids Engineering*, 103 (1981), 456–460.

[79] Launder, B. E., and Sharma, B. I. Application of the Energy Dissipation Model of Turbulence to the Calculation of Flow Near a Spinning Disc. *Letters in Heat and Mass Transfer 1*, 2 (1974), 131–138.

[80] Launder, B. P., and Spalding, D. B. The numerical computation of turbulent flows. *Computer Methods in applied mechanics and engineering*, 3 (1974), 269–289.

[81] Leonard, A. Energy Cascade in Large-Eddy Simulations of Turbulent Fluid Flows. *Advances in Geophysics*, 18A (1974), 237–248.

[82] Leonard, B. P. A stable and accurate convection modelling procedure based on quadratic upstream interpolation. *Computer methods in applied mechanics and engineering*, 19 (1979), 59–98.

[83] Liang, Q. W., Rodriguez, C. G., Egusquiza, E., Escaler, X., and Avellan, F. Numerical simulation of fluid added mass effect on a Francis turbine runner. *Computers & Fluids 36*, 6 (2007), 1106–1118.

[84] Lien, F. S., Chen, W. L., and Leschziner, M. A. Low-Reynolds-number eddy-viscosity modelling based on non-linear stress-strain/vorticity relations. In *Proceedings of the 3rd Int. Symposium on Engineering Turbulence Modelling and Experiments, Crete, Greece* (Amsterdam, Netherlands, 1996), W. Rodi, Ed., Elsevier, pp. 91–100.

[85] Liess, C. Zur Druckwellen-Resonanz im schaufellosen Raum von Francisturbinen. Tech. Rep. 7623, Voith Hydro, Heidenheim an der Brenz, Deutschland, 1981.

[86] Liess, C., Nordmann, R., Dietzen, F. J., Simon, F., and Braun, D. Determination of Leakage Flow and Dynamic Behavior of Labyrinth Seals for Hydraulic Machines. In *Proceedings of the 15th IAHR Symposium* (Belgrade, Yugoslavia, 1990).

[87] Lilek, Ž., Muzaferija, S., Perić, M., and Seidl, V. An implicit finite-volume method using nonmatching blocks of structured grid. *Numerical Heat Transfer, Part B*, 32 (1997), 385–401.

[88] Magnoli, M. V. Numerical simulation of pressure oscillations in Francis turbine runners. In *JASS 2009 – Joint Advanced Student School* (St. Petersburg, Russia, 2009).

[89] Magnoli, M. V., Galvani, C., and Poll, H. CAD / CAE Considerations, Fluid-Structure Interaction and Topological Optimization for hydrogenerators rotating components design. In *Proceedings of the XII Finite Element Seminar and ANSYS Users Meeting* (São Paulo, Brazil, 2002).

[90] Magnoli, M. V., and Schilling, R. Active Flow Control in Francis Turbines. In *HYDRO 2011 – Practical Solutions for a Sustainable Future* (Praha, Czech Republic, 2011).

[91] Magnoli, M. V., and Schilling, R. Increase of the Annual Energy Output in Hydraulic Powerplants through Active Flow Control. In *ICREPQ'11* (Las Palmas, Spain, 2011).

[92] Magnoli, M. V., and Schilling, R. Möglichkeiten und Grenzen der numerischen Simulation bei der Weiterentwicklung von Wasserkraftmaschinen. In *Praktikerkonferenz Wasserkraft* (Graz, Österreich, 2011).

[93] Magnoli, M. V., and Schilling, R. Numerical Simulation of Pressure Pulsations in Francis Turbines. In *Proceedings of the 26th IAHR Symposium* (Beijing, China, 2012).

[94] Magnoli, M. V., and Schilling, R. Numerical Simulation of Pressure Pulsations in Francis Turbines. In *SimHydro 2012 – New frontiers of simulation* (Nice, France, 2012).

[95] Matsuishi, M., and Endo, T. Fatigue of metals subjected to varying stress. In *In Proceedings of the Japan Society of Mechanical Engineers* (Fukuoka, 1968).

[96] Mauri, S. *Numerical Simulation and Flow Analysis of an Elbow Diffuser*. PhD thesis, Ecole Polytechnique Fédérale de Lausanne, Lausanne, Switzerland, 2002.

[97] Mehne, S. Idealisierung der Kopplung von Laufrad und Wellenstrang zur Berechnung des gemeinsamen Schwingungsverhaltens. Master's thesis, Berufsakademie Heidenheim, 2002.

[98] Meirovitch, L. *Elements of Vibration Analysis*. McGraw-Hill, New York, NY, USA, 1986.

[99] Menter, F. R. Tow-Equation Eddy-Viscosity Turbulence Models for Engineering Applications. *AIAA Journal 32*, 8 (1994), 1598–1605.

[100] Menter, F. R., and Egorov, Y. A Scale-Adaptive Simulation Model using Two-Equation Models. Tech. Rep. Paper 2005-1095, AIAA, Reno, Nevada, USA, 2001.

[101] Menter, F. R., Kuntz, M., and Bender, R. A Scale-Adaptive Simulation Model for Turbulent Flow Predictions. In *41st Aerospace Sciences Meeting and Exhibit* (Reno, Nevada, USA, 2003), AIAA, Ed., vol. Paper 2003-0767.

[102] Menter, F. R., and M. Kuntz, M. Adaptation of Eddy-Viscosity Turbulence Models to Unsteady Separated Flow Behind Vehicles. In *Proc. Conf. The Aerodynamics of Heavy Vehicles: Trucks, Busses and Trains* (Asilomar, California, USA, 2002).

[103] Miller, K. J. An experimental linear cumulative-damage law. *The Journal of Strain Analysis for Engineering Design 5*, 3 (1970), 177–184.

[104] Miner, M. A. Cumulative Damage in Fatigue. *Journal of Applied Mechanics 67*, 12 (1945), A159–A164.

[105] Moin, P. Numerical and physical issues in large eddy simulation of turbulent flows. *JSME Int. J. Series B, 41*, 2 (1998), 454–463.

[106] Monette, C., Coutu, A., and Velagandula, O. Francis Runner Natural Frequency and Mode Shape Predictions. In *Waterpower XV* (Chattanooga, Tennessee, USA, 2007).

[107] Morrow, J. Low Cycle Fatigue Behaviour of Quenched and Tempered SAE 1045 Steel. Tech. Rep. 277, British Association Stress Committee, Illinois, USA, 1915.

[108] Muzaferija, S. *Adaptive finite volume method for flow predictions using unstructured meshes and multigrid approach.* PhD thesis, University of London, 1994.

[109] Nennemann, B., Vu, T. C., and Farhat, M. CFD prediction of unsteady wicket gate-runner interaction in Francis turbines: A new standard hydraulic design procedure. *Waterpower XIV* (2005).

[110] Neuber, H. Theory of stress concentration for shear-strained prismatical bodies with arbitrary non-linear stress-strain law. *Journal of Applied Mechanics*, 28 (1961), 544–550.

[111] Newmark, N. M. A Method of Computation for Structural Dynamics. *ASCE Journal of Engineering Mechanics Division*, 85 (1959), 67–94.

[112] Nicolet, C., Zobeiri, A., Maruzewski, P., and Avellan, F. On the upper part load vortex rope in Francis turbine: experimental investigation. In *Proceedings of the 25th IAHR Symposium* (Timisoara, Romania, 2010).

[113] Ogarevic, V. V., and Aldred, J. An Implementation of Low-Cycle Multiaxial Fatigue Methods. In *ECCM-2001* (Cracow, Poland, 2001).

[114] Ogor, I. B., Gyllenram, W., Ohlberg, E., Nilsson, H., and Ruprecht, A. An Adaptive Turbulence Model for Swirling Flow. In *Conference on Turbulence and Interactions TI2006* (Pourquerolles, France, 2006).

[115] Palmgren, A. G. Die Lebensdauer von Kugellagern. *VDI Zeitschrift 68*, 14 (1924), 339–341.

[116] Papuga, J. *Mapping of Fatigue Damages – Program Shell of FE-Calculation.* PhD thesis, Czech Technical University in Prague, 2005.

[117] Patankar, S. *Numerical heat transfer and fluid flow.* Hemisphere, New York, NY, USA, 1980.

[118] Pfleiderer, C. *Die Wasserturbinen.* Wolfenbütteler Verlagsanstalt, 1947.

[119] Piomelli, U., Moin, P., and Ferziger, J. H. Model consistency in large eddy simulation of turbulent channel flows. *Phys. Fluids*, 31 (1988), 1884–1891.

[120] Reynolds, O. On the Dynamical Theory of Incompressible Viscous Fluids and the Determination of the Criterion. *Philosophical Transactions of the Royal Society of London*, 186 (1895), 123.

[121] Rheingans, W. J. Power Swings in Hydroelectric Power Plants. *Transactions of the ASME 62*, 174 (1940), 171–184.

[122] Rhie, C. M., and Chow, W. L. A numerical study of the turbulent flow past an isolated airfoil with trailing edge separation. *AIAA Journal*, 21 (1983), 1525–1532.

[123] Riedel, N. *Rotor-Stator Wechselwirkung in hydraulischen Maschinen.* PhD thesis, Technische Universität München, Lehrstuhl für Hydraulische Maschinen und Anlagen, 1997.

[124] Ritz, W. Über eine neue Methode zur Lösung gewissen Variations – Problem der Mathematischen Physik. *J. reine angew. Math.*, 135 (1909), 1–61.

[125] Rodi, W. *The prediction of free turbulent boundary layers by use of a two-equation model of turbulence.* PhD thesis, University of London, 1972.

[126] Rodi, W. A new algebraic relation for calculating the Reynolds stress. *Z. angewandte Mathematik und Mechanik*, 56 (1976), T219–T221.

[127] Rodi, W. *Turbulence Models and Their Application in Hydraulics – A state of the art review*, 3rd ed. Balkema, Delft, The Netherlands, 1993.

[128] Rodriguez, C. G., Egusquiza, E., Escaler, X., Liang, Q. W., and Avellan, F. Experimental Investigation of added mass effects on a Francis turbine runner in still water. *Journal of Fluids and Structures*, 22 (2006), 699–712.

[129] Rotta, J. C. *Turbulente Strömungen*. Teubner Verlag, Stuttgart, Germany, 1972.

[130] Ruprecht, A., Helmrich, T., Aschenbrenner, T., and Scherer, T. Simulation of Vortex Rope in a Turbine Draft Tube. In *Proceedings of the Hydraulic Machinery and Systems 21st IAHR Symposium* (Lausanne, Switzerland, 2002).

[131] Ruprecht, A., Kirschner, O., Lippold, F., and Buntić, I. Noise reduction in a small Francis turbine caused by vortex shedding at the trailing edge, numerical analysis and field test. In *IAHR 11th International Meeting of the Work Group on the behaviour of hydraulic machinery under steady oscillatory conditions* (Stuttgart, Germany, 2003).

[132] Ruprecht, A., and Maihöfer, M. Massively parallel computation of the flow in hydro turbines. In *Proceedings of the 21st IAHR Symposium* (Lausanne, Switzerland, 2002).

[133] Sabourin, M., Gagné, J.-L., Giroux, S., St.-Hilaire, A., and Bruère-Terreault, J. Mechanical Loads and Fatigue Analysis of a Francis Runner. In *Proceedings of HydroVision 2004* (Montréal, Québec, Canada, 2004).

[134] Sagaut, P. *Large eddy simulation for incompressible flows*, 2nd ed. Springer-Verlag, Berlin, Germany, 2004.

[135] Sarkar, S., Erlebacher, G., Hussaini, M. Y., and Kreiss, H. The analysis and modeling of dilatational terms in compressible turbulence. *Journal of Fluid Mechanics*, 227 (1991), 474–493.

[136] Sarpkaya, T. On Stationary and Travelling Vortex Breakdowns. *Journal of Fluid Mechanics*, 45 (1971), 545–559.

[137] Schilling, R. Strömung in Radseitenräumen von Kreiselpumpen. *Strömungsmech. Strömungsmasch.*, 27 (1979).

[138] Schilling, R., Ernst, H.-P., Watzelt, C., and Knapp, W. Investigation of the incidence and deviation angles in high specific speed Francis Turbine. In *Proceedings of the 16th IAHR Symposium* (São Paulo, Brazil, 1992), vol. 2, pp. 779–788.

[139] Segoufin, C., Mazzouji, F., Couston, M., Lowys, P. Y., and Deniau, J. L. Influence of the rotor-stator interaction on the dynamic stresses of Francis runners. In *Proceedings of HydroVision 2006* (Portland, Oregon, USA, 2006).

[140] Seidel, U., and Grosse, G. New approaches to simulate the dynamic behavior and dynamic stresses of Francis and pump turbine runners. In *2nd IAHR Internaltional Meeting of the Workgroup on Cavitation and Dynamic Problems in Hydraulic Machinery and Systems* (Barcelona, Spain, 2006).

[141] Seidel, U., Hübner, B., Löfflad, J., and Faigle, P. Evaluation of RSI-induced stresses in Francis runners. In *Proceedings of the 26th IAHR Symposium* (Beijing, China, 2012).

[142] Skoda, R. *Numerische Simulation abgelöster und transitionaler Strömungen in Turbomaschinen*. PhD thesis, Technische Universität München, Lehrstuhl für Hydraulische Maschinen und Anlagen, 2003.

[143] Smagorinsky, J. General Circulation Experiments with the Primitive Equations. I. The Basic Experiment. *Mon. Weather Rev.*, 91 (1963), 99–164.

[144] Smith, K. N., Watson, P., and Topper, T. H. A Stress-Strain Function for the Fatigue of Metals. *Journal of Materials 5*, 4 (1970), 767–778.

[145] Spalart, P. R. Strategies for turbulence modelling and simulations. *International Journal of Heat and Fluid Flow*, 21 (2000), 252–263.

[146] Spalart, P. R., and Allmaras, S. A one-equation turbulence model for aerodynamic flows. Tech. Rep. Paper 92-0439, AIAA, Reno, Nevada, USA, 1992.

[147] Spalart, P. R., Deck, S., Shur, M. L., Squires, K. D., Strelets, M. K., and Travin, A. A new version of detached-eddy simulation, resistant to ambiguous grid densities. *Theor. Comput. Fluid Dyn. 20*, 3 (2006), 181–195.

[148] Spalart, P. R., Jou, W. H., Strelets, M., and Allmaras, S. R. Comments on the feasibility of LES for wings, and on a hybrid RANS/LES approach. In *Advances on DNS/LES, Proceedings of the First AFOSR International Conference on DNS/LES, Ruston, Louisiana, USA* (Columbus, Ohio, USA, 1997), C. Liu and Z. Liu, Eds., Greyden Press, pp. 137–147.

[149] Strelets, M. Detached Eddy Simulation of Massively Separated Flows. In *39th Aerospace Sciences Meeting and Exhibit* (Reno, Nevada, USA, 2001), AIAA, Ed., vol. Paper 2001-0879.

[150] Strutt (Lord Rayleigh), J. W. On the theory of resonance. *Trans. Roy. Soc.*, A161 (1870), 77–118.

[151] Tanaka, H. Vibration behaviour and dynamic stress of runners of very high head reversible pump turbines. In *Proceedings of the 15th IAHR Symposium* (Belgrade, Yugoslavia, 1990).

[152] Technische Versuchs- und Forschungsanstalt GmbH (TVFA Wien), and Fraunhofer-Institut für Betriebsfestigkeit und Systemzuverlässigkeit (LBF). Stahlguss 83. Tech. Rep. V6700/a20, TVFA Wien, Wien, Austria, 1999.

[153] Tennekes, H., and Lumley, J. L. *A First Course in Turbulence*. MIT Press, Cambridge, Massachusetts, USA, 1983.

[154] Timoshenko, S., and Goodier, J. N. *Theory of Elasticity*, 2nd ed. McGraw-Hill, New York, NY, USA, 1951.

[155] Travin, A., Shur, M., Strelets, M., and Spalart, P. R. Physical and numerical upgrades in the detached-eddy simulation of complex turbulent flows. In *412 EUROMECH Colloquium on LES of Complex transitional and turbulent flows* (München, Germany, 2000).

[156] Truckenbrodt, E. *Strömungsmechanik, Grundlagen und technische Anwendungen*, 1st ed. Springer-Verlag, Berlin, 1968.

[157] Ulith, P. Francisturbinen – ihre Dimensionierung, ihr Betriebsverhalten sowie Aspekte für die Ausführung von besonders großen Einheiten. In *Vortragsveranstaltung an der Fachhochschule München, Fachbereich 03* (München, Deutschland, 1978).

[158] Van Doormal, J. P., and Raithby, G. D. Enhancements of the SIMPLE method for predicting incompressible fluid flows. *Numerical Heat Transfer*, 7 (1984), 147–163.

[159] Van Driest, E. R. On Turbulent Flow Near a Wall. *Journal of the Aeronautical Sciences*, 23 (1956), 1007.

[160] Viano, M. Pertes dans les labyrinthes cylindriques lisses. *La Houille Blanche*, 1 (1970).

[161] Vieser, W., Esch, T., and Menter, F. Heat Transfer Prediction using Advanced Two-Equation Turbulence Models. Tech. Rep. CFX Technical Memorandum CFX-VAL10/0602, ANSYS, Inc., 2002.

[162] Voith Hydro. Francis Turbines. Heidenheim an der Brenz, Deutschland, 2007.

[163] Von Kármán, T. Über den Mechanismus des Widerstandes, den ein bewegter Körper in einer Flüssigkeit erfährt. *Math.-Phys.*, K1 (1911), 509–517.

[164] Wang, C. H., and Brown, M. W. Inelastic deformation and fatigue under complex loading. In *Proceedings of the 12th International Conference on Structural Mechanics in Reactor Technology* (Stuttgart, Germany, 1997), Elsevier, pp. 159–170.

[165] Wickström, A. Structural analysis of francis turbine runners using ADINA. *Computers and Structures 64*, 5-6 (1997), 1087–1095. Proceedings of the 11th ADINA Conference.

[166] Wilcox, D. C. Reassesment of the Scale-Determining Equation for Advanced Turbulence Models. *AIAA Journal 26*, 11 (1988), 1299–1310.

[167] Wilcox, D. C. *Turbulence Modeling for CFD*, 2nd ed. DCW Industries, Inc., La Cañada, California, USA, 1993.

[168] Wöhler, A. Über die Festigkeitsversuche mit Eisen und Stahl. *Zeitschrift für Bauwesen*, 20 (1870), 73–106.

[169] Wunderer, R. Aktive Strömungsbeeinflussung. Tech. rep., Forschungsinitiative Kraftwerke des 21. Jahrhunderts (KW 21), 2007.

[170] Wunderer, R. *Aktive Strömungsbeeinflussung.* PhD thesis, Technische Universität München, Lehrstuhl für Hydraulische Maschinen und Anlagen, 2009.

[171] Wunderer, R., and Schilling, R. Numerical Simulation of Active Flow Control in Hydro Turbines. In *The 12th International Symposium on Transport Phenomena and Dynamics of Rotating Machinery* (Honolulu, Hawaii, USA, 2008).

[172] Xingqi, L., Pengcheng, G., Weili, L., Xiaobo, Z., and Peng, L. Vibration damping of hydraulic turbine unit – Case study for Yantan Hydropower Plant. In *Proceedings of the 4th WSEAS International Conference on Fluid Mechanics and Aerodynamics* (Elounda, Greece, 2006), pp. 309–314.

[173] Yan, J., Koutnik, J., Seidel, U., Hübner, B., and Scherer, T. Compressible Simulation of Rotor-Stator-Interaction in a Pump-Turbine. In *3rd Meeting of the IAHR International Workgroup on Cavitation and Dynamic Problems in Hydraulic Machines and Systems* (Brno, Czech Republic, 2009).

[174] Yan, J., Koutnik, J., Seidel, U., Hübner, B., and Scherer, T. Compressible Simulation of Rotor-Stator-Interaction in a Pump-Turbine. In *Proceedings of the 25th IAHR Symposium* (Timisoara, Romania, 2010).

[175] Young, F. R. *Cavitation.* McGraw-Hill, New York, NY, USA, 1989.

[176] Zahavi, E., and Torbilo, V. *Fatigue Design, Life Expectancy of machine parts.* CRC Press, New York, NY, USA, 1969.

[177] Zienkiewicz, O. C. *The Finite Element Method.* McGraw-Hill Company, London, UK, 1977.

[178] Zienkiewicz, O. C., and Newton, R. E. Coupled Vibrations of a Structure Submerged in a Compressible Fluid. In *Proceedings of the Symposium on Finite Element Techniques* (Stuttgart, Deutschland, 1969).